Mechanics of alkali-silica reaction in concrete across scales

Emil GALLYAMOV

Abstract

Alkali-silica reaction occurs in concrete between the alkalis contained in the pore solution and silica in the aggregates. Generation of ASR products gives rise to the internal pressures that cause expansion and cracking. Due to its deleterious effect on concrete, ASR poses a major threat to the safety and operability of the concrete infrastructure worldwide.

Recent experimental advances obtained in the scope of the multi-disciplinary Sinergia project entitled "Alkali-silica reaction in concrete" of Swiss research institutes shed new light on ASR. Being part of Sinergia, the research conducted in the scope of the present thesis had a goal to fill in the knowledge gap on the ASR mechanics. Therefore, analytical and numerical models facilitated by the novel experimental data have been developed.

One of the Sinergia experimental studies showed that the initial ASR products accumulate between the crystal grains of aggregates. We are using this knowledge together with an estimate of the volumetric increase of a typical ASR product to evaluate the crack-growing potential of a single region filled with ASR products. This is done by employing a semi-analytical model of an expanding inclusion of nanometre-size encircled by a disk-shaped crack. The role of the expansion value and the inclusion's size and shape on the resulting crack length is investigated. The analytical findings are confirmed by a finite element model.

Another experimental Sinergia study produced a time-series of X-ray tomograms of the ASR-affected concrete, which resolved the evolution of the deformation field, the crack growth and the accumulation of ASR products. This unique set of data is used in the current thesis to study the growth of ASR-crack networks and their role in the macroscopic behaviour of concrete. A novel cohesive elements-based meso-scale model capable of predicting the stable growth of numerous cracks is developed. Several hypotheses on the ASR-loading and cracking mechanisms are proposed and tested by including them in the model. Statistical comparison of the numerical and experimental crack networks provide new insights into ASR-cracking physics.

The continuous-damage approach is adopted to improve the efficiency and stability of the meso-scale model. The physics of the model is enriched by accounting for the orthotropic behaviour of damaged elements and the self-contact in cracks. This development allows reproduction of the macroscopic expansion of the concrete samples under

Abstract

substantial uniaxial load, which was not feasible by the earlier isotropic-damage models. Moreover, the role of creep on the ASR in concrete is investigated by combining viscoelasticity with strain-softening.

The last subject treated in this thesis is the macroscopic behaviour of ASR-affected structures. A computational multi-scale model of concrete is developed, validated and used to investigate the long-term behaviour of a real ASR-affected dam. The latter was facilitated by the availability of actual field measurements. This approach combines the meso-scale model with the orthotropic damage and the elastic macro-scale model of the dam. The model allows us to relate the macroscopic expansion of concrete to its state at the meso-scale, which comprises the crack network, its openings and orientations, and expansions of individual ASR sites. Coupling of the mechanical model with the transient heat analysis permits to evaluate the role of temperature variations on the ASR expansion across the dam.

Key words: alkali-silica reaction, fracture mechanics, computational homogenisation, Eshelby problem, cohesive zone model, crack network.

Résumé

La réaction alcali-granulat (RAG) se produisant dans le béton est due à la réaction entre la silice hétérogène contenue dans les granulats et les ions alcalins contenus dans la solution de pore du ciment. Le produit généré par cette réaction augmente la pression interne du béton engendrant une expansion de ce dernier et la création de fissures. L'effet néfaste de la réaction alcali-granulat sur le béton représente une menace pour la sécurité et la maintenance de nombreuses infrastructures en béton dans le monde entier.

Le projet multidisciplinaire Sinergia intitulé "La réaction alcali-silice dans le béton" des instituts de recherche suisses à récemment apporté un nouvel éclairage sur la réaction alcali-granulat. Cette thèse fait partie du projet Sinergia et a donc pour objectif d'analyser et de comprendre les mécanismes de la RAG à l'aide de modèles analytiques et numériques développés sur les bases de données expérimentales provenant de divers laboratoires partenaires.

Une étude expérimentale conduite dans le cadre de Sinergia a démontré que le produit primaire de la RAG s'accumule dans les grains cristallographiques des granulats. Cette connaissance ainsi que l'estimation de l'augmentation de la différence entre le volume des réactifs et des produits de la RAG, nous permettent d'évaluer la probabilité d'évolution d'une fissure dans le cas d'une simple poche RAG. Afin de réaliser cette estimation nous considérons un modèle composé d'une inclusion de taille nanométrique entourée d'une fissure en forme de disque. L'expansion de l'inclusion provoque la croissance de la fissure. Nous étudions le rôle de la valeur d'élargissement, la taille et la forme de l'inclusion sur la longueur de la fissure. Les valeurs analytiques seront confirmées par un modèle aux éléments finis.

Une seconde étude conduite dans le cadre du project Sinergia fournit une série d'images radiographiques réalisée à l'aide de rayons X sur un béton affecté par la RAG. Cette étude permet de résoudre l'évolution de la déformation, de l'élargissement de la fissure et de l'accumulation du produit de la RAG. Ces données ont été utilisées pour étudier l'évolution du ensemble de fissures dues à la RAG et son rôle sur le comportement mécanique du béton à l'échelle macroscopique. Un nouveau modèle aux éléments finis incluant des éléments cohésifs a été développé. Ce modèle développé à l'échelle mésoscopique permet de simuler une évolution stable d'un ensemble de fissures. Plusieurs hypothèses sur le chargement du béton par les produits de la RAG et le mécanisme

de fissuration sont proposées et testées. La comparaison statistique entre les résultats du modèle numérique et les données expérimentales disponibles a permis de fournir un nouvel éclairage sur les mécanismes physiques à l'œuvre dans la RAG.

Afin d'améliorer l'efficacité et la stabilité du modèle à l'échelle mésoscopique, une approche basée sur un endommagement continu est étudiée. Dans le but de s'approcher des observations expérimentales, un endommagement orthotropique et la récupération de la rigidité sont intégrés au modèle. Cette amélioration du modèle permet de capturer l'élargissement macroscopique du béton soumis à une charge uniaxiale. De plus, le rôle du fluage de la pâte de ciment sur la fissuration RAG est étudiée en combinant le caractère viscoélastique avec l'adoucissement par tension.

Le dernier sujet abordé dans cette thèse est le caractère macroscopique des structures affectées par les fissures RAG. Un modèle multiéchelle du béton est développé, validé et utilisé pour étudier le comportement à long terme d'un barrage affecté par des fissures RAG. Le développement de ce modèle est facilité par la mise à disposition de mesures expérimentales réalisées sur le barrage. Ce modèle combine le modèle mésoscopique à endommagement orthotropique et le modèle élastique macroscopique du barrage. Ce modèle permet de lier l'expansion macroscopique du béton à son état mésoscopique. Ceci inclut l'extension de l'endommagement, l'ouverture et l'orientation des fissures, ainsi que l'expansion des sites RAG individuels. Le couplage du modèle mécanique avec l'analyse thermique permet d'évaluer le rôle de la variation de température sur l'expansion liée à la RAG le long du barrage.

Mots clefs : réaction alcali-granulat, mécanique des fractures, homogénéisation computationnelle, problème d'Eshelby, modèle de zone cohésive, ensemble de fissures.

Резюме

Щелочно-кремнеземная реакция (ЩКР) происходит в бетоне и является результатом взаимодействия ионов щелочи, содержащихся в цементной пасте, и диоксидом кремния, содержащимся внутри заполнителя. Образование продуктов реакции приводит к росту внутреннего давления на бетон, ведущего, в свою очередь, к его расширению и растрескиванию. Из-за своих пагубных последствий ЩКР представляет собой существенную угрозу безопасности и функционированию бетонных сооружений по всему миру.

Недавние экспериментальные разработки, проведенные в рамках междисциплинарного проекта Sinergia "Щелочно-кремнеземная реакция в бетоне" рядом швейцарских исследовательских институтов, позволили сделать новые открытия в области ЩКР. Будучи частью проекта Sinergia, исследования, проведенные в рамках данной диссертации, имели целью устранить имеющиеся пробелы в понимании механики ЩКР. Для исследования этой тематики автором данной диссертации были разработаны аналитические и численные методы, основанные на недавних экспериментальных наблюдениях.

Одно из исследований в проекте Sinergia показало, что изначальные продукты ЩКР накапливаются между кристаллическими зернами заполнителя. Это наблюдение вместе с численной оценкой увеличения объёма продуктов ЩКР по сравнению с реагентами были использованы для определения возможности трещинообразования вокруг отдельно взятого очага формирования продуктов ЩКР. Это исследование было осуществлено посредством использования полуаналитической механической модели расширяющегося наноскопического включения, опоясанного дискообразной трещиной. Были исследованы роли величины расширения, а также формы и размера включения на рост трещины и ее размер. Аналитические выводы были подтверждены результатами конечно-элементной модели.

Исследователям из другого подпроекта удалось получить временное развитие трехмерных томограмм подверженного ЩКР бетона. Эти томограммы позволяют отслеживать развитие деформаций в образцах, рост трещин и накопление продуктов ЩКР в пространстве и во времени. Этот уникальный набор данных был использован автором диссертации для изучения роста ЩКР-трещин и их влияния на макроскопическое поведение бетона. Была разработана трехмерная мезоскопическая численная модель, основанная на когезивных интерфейс-элементах. Преимуществом этой модели является возможность одновременного роста множества трещин сложной формы внутри одного образца. Был сформулирован

ряд гипотез касаемо природы внутренней нагрузки, а также механизма трещинообразования, который позже был протестирован за счет включения его в модель. Сравнение статистических показателей экспериментальных и численных результатов позволили сделать выводы, касающиеся физики трещинообразования в результате ЩКР.

Для улучшения эффективности и стабильности мезоскопических вычислений была также разработана двухмерная модель на основе теории непрерывного разрушения. Реалистичность модели была повышена за счет включения ортотропного поведения разрушаемых элементов, а также контакта между стенками захлопывающихся трещин. Эти разработки позволили воспроизвести макроскопическое расширение бетонных образцов, подверженных существенной одноосной сжимающей нагрузке, что было невыполнимо ранее предложенными моделями с изотропным разрушением. Более того, за счет включения в модель вязкоупругости было изучено влияние ползучести бетона на динамику ЩКР.

Последняя тема, представленная в диссертации, касается макроскопического поведения конструкций, подверженных ЩКР. Автором была разработана двумерная мультимасштабная термо-механическая модель бетона, которая была использована для исследования поведения одной из швейцарских платин, подверженных ЩКР на протяжении последних 70 лет. История деформаций платины, а также полевые измерения температуры и колебания уровня воды были предоставлены компанией-оператором. Предложенный подход совмещает мезоскопическую модель бетона на основе ортотропного разрушения с упругой макроскопической моделью платины. Деформации на макро-уровне связаны с состоянием бетона на мезо-уровне, где последнее включает в себя уровень растрескивания бетона, степерь раскрытия и преобладающая ориентация трещин, а также расширение отдельных очагов ЩКР. Термо-механическое сопряжение модели позволяет оценить роль сезонных перепадов температур на разницу в расширении бетона в зависимости от его положения в плотине.

Ключевые слова: щелочно-кремнеземная реакция, механика трещин, вычислительная гомогенизация, задача Эшелби, когезивная зона, сеть трещин.

Acknowledgements

My deepest gratitude goes to my Ph.D. advisor Prof. Jean-François Molinari. I am very thankful for the chance he gave me to conduct my Ph.D. research at EPFL. Not only he provided the valuable guidance, but also taught me multiple things: to build a scientific line of reasoning, to prioritise the tasks and to distinguish between the definite and indefinite articles in English. The personality traits that I always admired are his enthusiasm and passion, which keep the mood in the lab vibrant and dynamic.

I own special acknowledgement to Prof. Brice Lecampion, president of the defence jury, as well as other thesis committee members: Prof. Karen Scrivener, Prof. Fabrice Gatuingt and Dr. Michele Griffa.

My Ph.D. research was part of the interdisciplinary Sinergia project and it involved collaboration with several other laboratories from Swiss universities. I would like to thank all my collaborators and in particular the head of the project Andreas Leemann. Moreover, a special thanks goes to Prof. Barbara Lothenbach, Mahdieh Shakoori Oskooie and Michele Griffa for our collective work.

The four years of my Ph.D. I was privileged to spend in the computational solid mechanics laboratory (LSMS). The inter-institutional and international ties of the lab permitted me to meet the numerous brilliant researchers. Among them, I especially wish to thank Prof. Mauro Corrado, with whom I had a fruitful collaboration. His generous help and technical guidance were highly appreciated in the challenging moments.

I express my gratitude to Nicolas Richart for bringing me to the world of computer science and for all his time and patience dedicated to me. I also want to thank Guillaume Anciaux for structuring my programming knowledge and discussing the numerical aspects of my work.

I would also like to thank all my past and present colleagues: Manon Voisin-Leprince, Thibault Roch, Angelos Mikelis, Mohit Pundir, Yulin Sun, Sacha Wattel, Parissa Alavi, Son Pham-Ba, Jacopo Biloto, Antoine Lucchetta, Joaquin Garcia, Gianluca Costagliola, Enrico Milanese, Lucas Frerot, Lucas Bernardini, Roozbeh Rezakhani, Tobias Brink, Fatima Fekak and Fabian Barras. We did a lot of fun activities together, had some interesting scientific and philosophic discussions over the lunch, learned about each other's cultures and cuisines. Extra credits go to Manon Voisin-Leprince and Sarah Bouassida for translating and proofreading the abstract of this thesis into French.

I own special acknowledgement to Birgitte Seem, Anne-Françoise Suter and Martina Keddouh for their administrative support. Moreover, I want to thank Emma Sorrentino

for our French-Russian language tandem. Although she has succeeded to teach me the basic French, I have completely failed as the Russian teacher.

I would also like to express my gratitude to the few professional connections I have made while doing the research. First, I thank Markus Schwager for always willing to help and for giving me the chance to present my research in the Swiss Federal Office of Energy. Next, I thank Jonathan Fauriel and Olivier Valloton for our collaboration on the study of Salanfe dam.

I am very thankful to all my friends outside the lab. First acknowledgement goes to Maxim Norkin, who was not only a permanent companion for all the hikes and ski sessions, but also introduced me to the world of genetics and molecular biology. I thank Sarah Bouassida, Loup Serraille, Alkistis Tsirogianni, Markus Schwager and Sandra Bodmer for all the discussion, funny moments and trips we had together. I also thank Yury Alkhimenkov for our scientific exchange as well as for instilling my craving for the gym.

I would also like to thank all the Russian-speaking friends whom I met in Lausanne: Maiia Bragina, Natalia Yalovenko, Sergey Arzoyan, Anna Rozenblit, Evgenii Glushkov and Dmitry Loginov. I have genuinely enjoyed our lunches together and participation in the Association of Russian-speaking Students at EPFL.

Many thanks to my friends from the Netherlands: Alexey Ilyushkin, Maria Zamiralova, Mark and Alina Khait. The fact of being surrounded by the Ph.D. students in Delft finally motivated me to become one myself.

More gratitude goes to my M.Sc. thesis advisers Denis Voskov and Timur Garipov for introducing me to the world of fracture mechanics and C++ programming, which ended up being the core subject of my dissertation.

Of course, this thesis would not be possible without the endless support of my wife Irina. Not only she motivated me throughout these four years, helped to overcome different challenges, but also discussed science-related topics and proofread some parts of the manuscript. I would also like to thank someone who is not yet able to read this text - my son Timur. His arrival brought a lot of motivation, joy and sense to my life.

The last part of the acknowledgements is in Russian language.

Благодарности

В первую очередь я хотел бы от всего сердца поблагодарить свою семью: папу Рината Мукатдасовича - за те деревянные кубики, которые привили пространственное мышление и любовь к конструкциям; маму Рузалию Салимуловну - за то, что терпеливо проверяла домашние задания и научила тонко чувствовать; брата Вадима - за искреннюю дружбу. Без вашей любви и безусловной поддержки эта работа была бы невозможна.

Кроме того, я выражаю глубокую признательность своим школьным учителям: Галине Анатольевне Беловоусовой, Анастасии Николаевне Тазетдиновой, Любови Михайловне Огуречниковой, Гузели Мансафовне Яхиной, Венере Закиевне Гимрановой, Марине Валентиновне Горшениной и Зульфие Ириковне Юнусовой за то, что дали прекрасное обра-

зование и привили любовь к точным наукам, хорошей литературе и иностранным языкам.

Еще я благодарен своим университетским преподавателям: Сергею Леонидовичу Штаневу за введение в сопротивление материалов, которое стало тематикой моей будущей диссертации, Владимиру Николаевичу Сорокину за курс теоретической механики, который многое прояснил в этой жизни, а также Ринату Рашидовичу Сахибгарееву за первое знакомство с научной работой.

Lausanne, February 4, 2022 Emil Rinatovich Gallyamov

Contents

Contents

List of Figures

List of Tables

1 Introduction

1.1 Motivation

The alkali-silica reaction (ASR) is the most common type of alkali-aggregate reaction, which is the generic term for reactions between the alkaline concrete pore solution and certain mineral phases within the aggregates. At the scale of an aggregate, the ASR manifests itself in the form of local silica dissolution, growth of micro-cracks, their filling with ASR products, and the overall expansion of the aggregates, the cement paste and concrete in general as shown in Fig. 1.1. The expansion and cracking caused by the ASR has a major negative impact on the civil engineering infrastructure worldwide. Coping with the ASR consequences in such large structures as dams, bridge piers and sea walls requires considerable expenditure of funds. To prevent the ASR manifestation in the new structures and reduce the severity of its consequences in the existing ones, substantial scientific effort is dedicated to the ASR.
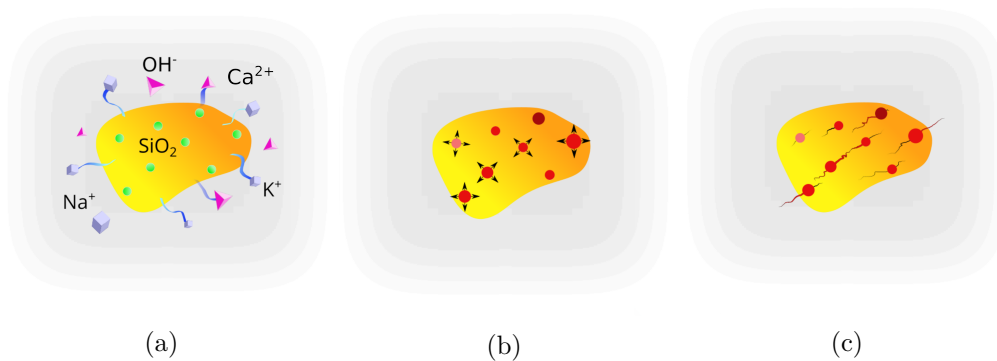
Figure 1.1: Stages of concrete damaging due to the ASR: (a) alkalis from cement paste diffuse into aggregates and react with amorphous silica; (b) resulting ASR products exert internal pressure on aggregates; (c) cracks open and grow inside aggregates and cement paste.

The formation of ASR products starts in the aggregates close to the interface with the cement paste. With ongoing reaction, the formation of ASR products continuously moves toward the interior of the aggregate. Fig. 1.2 shows three adjacent quartz grains in a reactive quartzite aggregate of a concrete doped with caesium nitrate (Leemann, 2021). The contact zone of the three grains is lined with a thin film of ASR products exhibiting a high back-scattering contrast due to the incorporation of caesium. Although the collective form of the ASR products reflects the one of the pre-existing cracks and voids as shown in Fig. 1.2, the newly formed ASR products precipitate as clusters of alkali-silicate gel in the size of $1 - 100$ nm (Gaboriaud et al., 2002). These newly formed clusters can be regarded as "pockets". They form between adjacent mineral grains within the reactive aggregates close to the border with the cement paste (Leemann et al., 2016; Leemann and Münch, 2019). Later on, the same pattern of ASR products accumulation inside grain boundaries is observable also in aggregate inner regions. The primary ASR
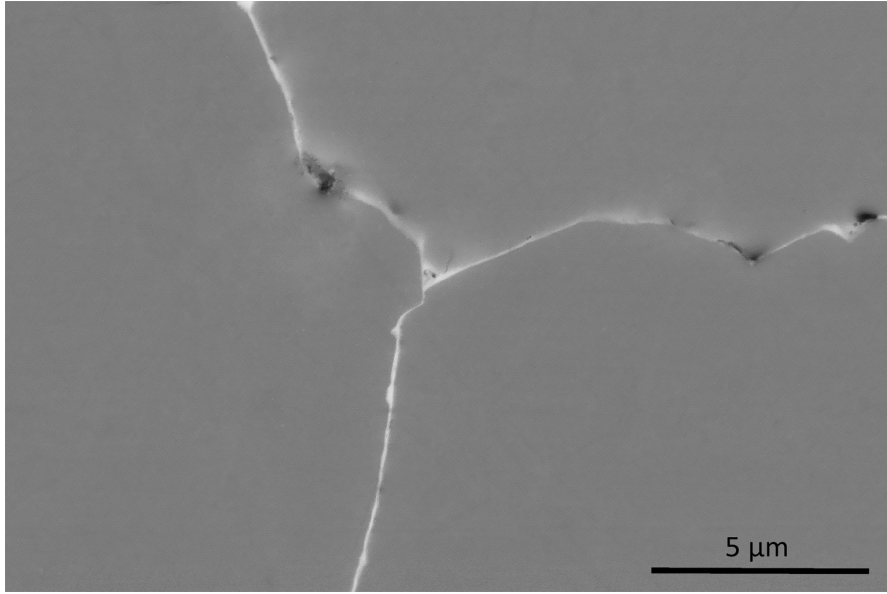
Figure 1.2: Three adjacent quartz grains lined with a thin film of bright ASR products with a thickness between $50 - 300$ nm in a yet uncracked concrete aggregate. The brightness is caused by the doping of the concrete with caesium and its incorporation in the ASR products. Scanning electron image in the back-scattering mode adapted from (Leemann, 2021).

product yields internal loading on the aggregates leading to cracking. The resulting cracks originate in the aggregates and extend into the cement paste. Crack openings could be much larger than the initial ASR product size and the openings of the pre-existing cracks. As the reaction advances, the alkali front moves inwards the aggregates, producing more ASR sites. The newly formed cracks start to fill with the secondary ASR products.

At the meso-scale of concrete, micro-cracks are homogeneously distributed. They

align with the direction of the prevailing load (Larive, 1997; Hilaire et al., 2017; Dunant and Scrivener, 2012); typical crack patterns vary from randomly oriented to co-directional cracks. Another phenomenon triggered by the deviatoric loading is the so-called "stress-induced anisotropy", i.e. the reduction of the chemical expansion in the direction of the compressive load and its partial transfer to perpendicular directions (Larive, 1997; Multon and Toutlemonde, 2006; Gautam and Panesar, 2016; Dunant and Scrivener, 2012). Highly compressed specimens show negligible expansion in the loading direction. Further opening and percolation of the micro-cracks lead to the appearance of the large fissures detectable at the macro-scale. Cracking reduces the tensile strength by $50-70\%$, the compressive strength by $25-60\%$ and the elastic material properties by $60-70\%$ (Swamy, 2003; SCD, 2017).

At the macroscopic scale, the ASR manifests itself in form of continuous concrete expansion and cracking. As the high relative humidity and the increased temperature accelerate the ASR, the most affected structures are the ones in a direct contact with water, such as dams, bridge piers and sea walls. According to the recent study conducted by the Swiss Committee on Dams (SCD, 2017), roughly 50% out of 154 Swiss dams are concerned by this problem. When discussing macroscopic effects of the ASR, the main focus will be on dams as the engineering structures of a great economical importance. Charlwood and Sims (2017), in their comprehensive review of the affected dams and hydro-projects around the world, emphasise the following typical effects of the ASR expansion:

- upstream, downstream and vertical deformation;

- map cracking on the surfaces;

- structural cracks;

- movements causing interference with gates and equipment;

- movement and leakage at the horizontal lift joints;

- deformations affecting stability, etc.

Field observations also suggest that the ASR expansions can be highly inhomogeneous within a dam (Gunn et al., 2017). This ASR zonation could be caused by material, structural and environmental effects. On the material side, the cementitious content of a dam varies spatially, having higher values closer to the surface and along galleries. Volume fraction of aggregates (also their mineralogy, size and shape) may also differ. Since ASR is a process that is strongly dependent on the concrete micro-structure and its chemical composition, its manifestation is expected to vary between zones with different material properties.

Possible environmental sources of the non-uniform ASR expansion are the variations of the relative humidity and the temperature within a structure. Both scalar fields are changing in a dam due to the daily/yearly fluctuations of the surrounding temperature, reservoir level, precipitation rate, exposure to the direct sunlight, etc. In many of the examined dams, the Swiss Committee on Dams (SCD, 2017) identified significant differences in concrete swelling between warm and slender upper wall areas and cold massive lower parts. Moreover, the presented data suggests a certain link between the horizontal drift and the orientation of the dam axis with respect to the South.

The experimental data and the field observations reveal a complex combination of different phenomena happening simultaneously during ASR. This reaction involves multiple scales and couples chemical, structural and environmental aspects. To understand the nature of this complex system and predict its future behaviour, the numerical modelling is an indispensable tool.

1.2 Objectives

A multidisciplinary, collaborative Sinergia project "Alkali-silica reaction in concrete" took advantage of the recent improvements in the investigation techniques and increased computational capacities. The research was conducted by the laboratories from three Swiss institutes: École Polytechnique Fédérale de Lausanne (EPFL), Swiss Federal Laboratories for Materials Science and Technology (Empa) and Paul Scherrer Institut (PSI). The project was financed by the Swiss National Science Foundation through grant CR-SII5_17108. The goal of the project was to fill the existing knowledge gaps on ASR and thus to support in the future the development of engineering countermeasures. The proposed comprehensive approach encompassed a wide range of scales from nanometre to the size of a structure. It included studies on the chemical, structural and mechanical ASR aspects. The Sinergia project consisted of six sub-projects, each one handling a particular ASR phenomenon, e.g. initial dissolution of SiO_2, analysis of the composition of the initial ASR products, studying the structure of ASR products by synchrotron-based techniques, prediction of the ASR kinetics by the thermodynamic modelling, monitoring of the crack formation by non-destructive 3D analysis. The work presented in this thesis was done within the scope of the Sinergia Sub-project VI. Its goal was to improve the understanding of the ASR by mechanical modelling based on the realistic micro-structures provided by the 3D analysis of the crack formation from the Sub-project V. During the overall Sinergia project's evolution, collaborations with other sub-projects also emerged. Benefiting from the multidisciplinary expertise of the colleagues and the availability of their new data, in the Sub-project VI we have considered the complexity of the ASR physics at a wide range of scales. Not only each scale is considered separately, but the material behaviour at one scale is enriched by the information obtained at a different scale. Like-wise, the objectives of this research are categorised per considered scale in ascending order.

While the ASR-expansion mechanisms have been studied intensively over the decades, there is still no final agreement on the principal cause. The ASR-expansion mechanism and the growth of the primary cracks at the nanometre scale are investigated. Sinergia Sub-project II gave an estimate of the volumetric difference between the reactants and the typical ASR products. One aim of this thesis is to understand if this volumetric difference is sufficient for the initiation and propagation of the primary cracks. Moreover, the role of the size and shape of a typical ASR pocket on its potential to grow a crack is investigated.

To facilitate understanding of the ASR mechanics, cutting-edge experiments were recently performed by the colleagues from the Sinergia Sub-project V. Shakoorioskooie (2021); Shakoorioskooie et al. (2021a,b) conducted accelerated ASR experiments on concrete specimens under free-expansion conditions. Time-lapse characterisation by means of X-ray micro-tomography allowed the researchers to capture the temporal evolution of cracks and ASR products. To distinguish ASR products from its surroundings, caesium (Cs) was added to the concrete mix as a contrast agent. The segmented tomograms give access to the concrete meso-structure, positions and geometrical features of the cracks and the pockets of ASR products. The aim of the current thesis done within the Sub-project VI is to explain the physics behind the expansion and cracking captured by this tomography data. While doing this, this study aims to identify the driving forces responsible for crack growth and the way they affect the crack statistics and the macroscopic behaviour of a specimen.

Researchers have previously made attempts to predict realistic deterioration of concrete at its meso-scale due to ASR. A group of works succeeded in reproducing the natural crack patterns and chemical expansion under free boundary conditions (Dunant and Scrivener, 2010; Cuba Ramos et al., 2018). Although the proposed approach allowed capturing the reduction in the chemical expansion under moderate uniaxial loading, it predicted some non-realistic specimen shrinkage under higher uniaxial loading. In the current study, it is suggested that such numerical deficiency was caused by the simplistic numerical treatment of cracks and one aim of this work was to improve this model.

Another observation made by Cuba Ramos et al. (2018) on their mesoscopic model concerns the elevated amounts of damage in comparison to the laboratory observations. As one of the possible reasons, the authors suspected the absence of the viscous dissipation in the cement paste. This thesis aims to estimate the role of stress relaxation in the cement paste on concrete expansion and cracking.

Finally, at the macro-scale, the knowledge obtained in the previous studies is used to model the macroscopic behaviour of an ASR-concerned dam. The objective is to develop a model of a dam that would explicitly use the information on the mesoscopic state of the ASR-damaged concrete. By employing this model on a real-dam case, this study aims to understand the interplay between the state of stress and deformations in

the structure and the meso-scale concrete state. The latter accounts for the reaction state, the amount of cracks, their connectivity, width and orientations. By linking these two scales, this study aims to explain the origin of the ASR anisotropy. In addition, it aims to distinguish the areas of a dam that are the most susceptible to develop such anisotropy. Finally, the role of the seasonal temperature variations on the ASR-related deformations is investigated.

1.3 Approach

Several strategies are adopted to fulfil the above objectives. These strategies comprise both analytical and numerical methods.

To study the nature of the ASR mechanics at the nano-scale, a semi-analytical model was employed. It combines a well-known analytical solution of an expanding inclusion embedded in a matrix and an interpolated semi-analytical solution for a disk-shaped crack encircling this inclusion. The former problem is also known as the Eshelby problem. Here, the inclusion represents a single pocket of ASR products and the matrix is the aggregate. This model allows evaluation the role of the ASR volumetric expansion and the size and shape of the inclusion on the crack growing potential.

To confirm the findings of the analytical model and to reproduce the crack network from the tomography data of Shakoorioskooie et al. (2021a,b), a finite-element numerical model is used. The finite-element method is chosen due to its computational efficiency and ease of implementation. Cracks are modelled by the cohesive elements - zero-thickness interface elements inserted between the solid ones. The cohesive zone model suggests the existence of a finite zone in the vicinity of the crack tip that dissipates energy upon opening and percolation of micro-cracks, as was independently proposed by Dugdale (1960); Barenblatt (1962). Like-wise, the cohesive elements dissipate energy by generating the closing traction, which reduces with increasing opening. Cohesive elements form a network of thin cracks that could be easily compared to the crack network coming from the tomography data.

Use of the cohesive elements becomes computationally expensive when numerous simulations have to be performed simultaneously. As the multi-scale model of a dam requires running hundreds of the meso-scale simulations, an alternative method had to be used. This alternative is the continuous damage approach (Kachanov, 1986), according to which the integrity of a material point is described by a damage parameter d increasing from zero to one. As the crack within a single element becomes more pronounced, the damage parameter increases and the elastic properties reduce. The continuous damage approach permits efficient modelling of a complex crack network. The finite-element approach is employed with the continuous-damage representation of cracks to develop a realistic meso-scale model. The realism of the model encompasses its

ability to reproduce both the free- and loaded-expansion ASR experiments by developing a qualitatively similar crack network and exhibiting a quantitatively similar macroscopic expansion. Such a model is obtained by introducing the orthotropic continuous damage law with the stiffness recovery upon crack closure. This phenomenon is also described by the term "self-contact of a crack". A simple isotropic version of this model is employed to study the effect of the visco-elasticity in the cement paste.

The improved efficiency and the good match of the meso-scale model with the laboratory experiments enables its usage for the macro-scale analysis of a dam. As the concrete state at the meso-scale evolves with the macroscopic deformations of a structure, a model coupling these two scales is necessary. Such functionality is offered by the multi-scale approach based on the computational homogenisation (Renard, 1987; Miehe et al., 1999; Feyel and Chaboche, 2000; Kouznetsova et al., 2001). Its idea is to have two boundary value problems, one at each scale, and solve them simultaneously, in a fully nested manner. This procedure allows evaluation the macroscopic effects of the fine-scale processes in an explicit manner. Both scales are modelled by the finite-element approach. At the fine scale, the previously-implemented meso-scale model with orthotropic continuous damage is employed. The macroscopic stress and stiffness are obtained by the homogenisation of the fine scale boundary value problem. Moreover, the transient heat transport equation is solved to compute the temperature variations at the structural level. The information on the temperature is used to estimate the expansion rates of the ASR products at the meso-scale.

The numerical frameworks and constitutive models developed during this thesis are implemented in the open-source FEM library Akantu [Richart and Molinari 2015; Vocialta et al. 2017, akantu.ch].

1.4 Outline

The following chapters are organised as follows:

Chapter 2 starts with the review of the ASR-expansion and cracking mechanisms suggested in the literature. Further, the existing models for concrete deterioration due to ASR at different scales are described and categorised.

Chapter 3 describes a study on the potential of a single expanding ASR pocket of a nano-to-micrometre size to grow a crack. The findings are confirmed by the numerical model based on the cohesive elements.

Chapter 4 introduces a tomography-based numerical model with the cracks represented by the cohesive elements. The model is calibrated by matching the statistical basis of the tomography data as well as the macroscopic behaviour of a sample. By modelling different internal and external loading scenarios, the hypotheses on the crack

loading and extension mechanism are tested. In addition, the role of the external loading on the growth of cracks, their opening and orientation is investigated.

In **Chapter 5**, a meso-scale numerical model with the orthotropic continuous damage treatment of cracks is introduced. The model is calibrated to match the free-expansion laboratory experiments. The importance of the orthotropic damage and the self-contact in cracks in reproducing the loaded ASR experiments is demonstrated. In a sub-study, the effect of the stress relaxation on the crack growth is evaluated by adding viscoelasticity to the strain-softening behaviour of the cement paste.

Chapter 6 describes a thermo-mechanical multi-scale numerical model. Its validity is verified on a simple test case. Further, it is applied on the case of an ASR-affected concrete gravity dam in Switzerland. Model parameters are calibrated to match the real dam's displacements. Finally, the conclusions concerning the structural consequences of the ASR as well as the role of the temperature variations on the difference in the ASR state are derived.

The thesis is concluded by the summary of the main results and an outlook on the possible further developments.

2 State of the art

Concrete can be considered as a multi-scale material comprising macro-, meso-, micro-, and nano-scales as shown in Fig. 2.1. At the macro-scale, concrete is considered homogeneous. At the meso-scale (also called structural), concrete is assumed to be a three-phase composite material consisting of coarse aggregates, mortar, and interfacial transition zone. Meso-scale modelling of concrete permits the investigation of initiation, propagation and percolation of micro-cracks and their contribution to the failure of concrete. The micro-scale covers the heterogeneous structure of mortar and distinguishes cement paste, sand particles and ITZ. Finally, the nano-scale considers mineral grains and their boundaries within a single aggregate. Further, we will discuss the possible ASR-expansion mechanisms and the numerical models used to predict the ASR-affected concrete behaviour at the different scales.
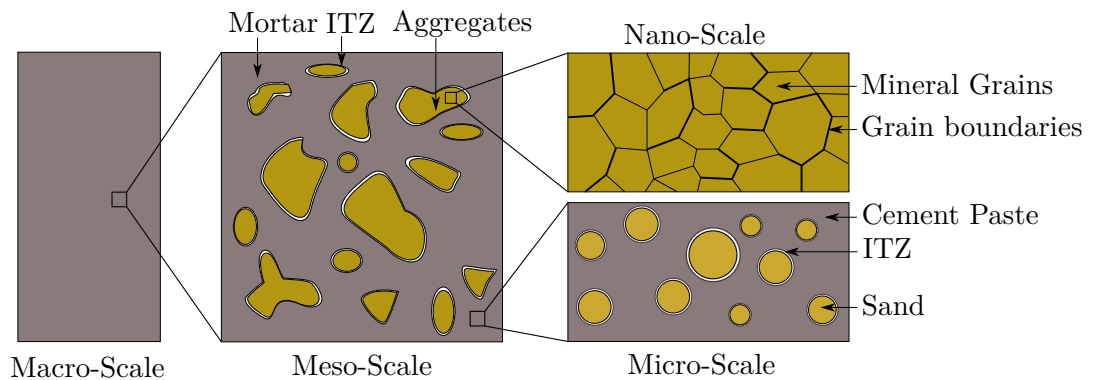
Figure 2.1: Multiple scales of concrete. Inspired by Thilakarathna et al. (2020)

2.1 Nano-scale

Most of the ASR-expansion mechanisms proposed in the literature suggest that the expansion originates at the nano-scale. The most widely reported hypothesis for the ASR expansion is swelling of the ASR products due to the uptake of water - the so-called theory of imbibition or osmotic pressure (Glasser, 1979; Diamond, 1989; Poole, 1992). Recent water uptake measurements on the synthetic ASR products, however, indicate a very limited water uptake (Shi et al., 2019). This suggests that the ASR expansion is not caused by the water-related swelling of the ASR products but by alternative mechanisms. Dron and colleagues (Dron, 1990; Dron et al., 1998) proposed a theory explaining the ASR expansion by the crystallisation pressure that appears due to over-saturation of the surrounding solution. Chatterji and Thaulow (Chatterji, 1989; Chatterji and Thaulow, 2000) proposed the theory of ion diffusion and argued that the expansion is caused by the difference in the fast inward diffusion of alkali ions into the reaction sites and slow outward diffusion of silica ions. Within the ion diffusion theory, Wang and Gillott (1991) suggested that $Ca(OH)_2$ is responsible for maintaining a high concentration of OH^- ions in solution and providing Ca^{2+} ions that exchange for Na^+ and K^+ ions. The latter are released to continue the damaging reaction. Ichikawa and Miura (2007) modified the ion diffusion theory by suggesting that the reaction creates an insoluble tight and rigid reaction rim that allows the penetration of alkaline solution but prevents the leakage of viscous alkali silicate. The latter accumulates in the aggregates and produces the expansive pressure. Jones (1988) has attributed swelling to the dispersion of gel. Prezzi et al. (1997) and Rodrigues et al. (1999) suggested that the electrical double-layer repulsion forces forming on the charged surfaces of the gel particles are responsible for the ASR expansion. Garcia-Diaz et al. (2006) established experimental relationships between the apparent volume variation of flint aggregate skeleton and micro-mortar swelling consecutive to the ASR degradation. While ignoring the internal product stoichiometry, the authors postulated that the Q4-Q3 silica tetrahedron transition, which has 30% of volume difference, is the origin of swelling. All of these models explain some parts of the experimental results, but fail to explain the others (Garcia-Diaz et al., 2006).

Even though the underlying mechanism for the expansion is not exactly known, it is clear that the formation of ASR products, which incorporates, in addition to SiO_2, also ions (K^+, Ca^{2+}, OH^-) and water from the pore solution, leads to the increase in solid volume. ASR products, commonly reported in the literature, precipitate as an amorphous gel. However, it has been shown that in addition to the amorphous ASR product, the one present in large cracks within aggregates could be crystalline (Cole and Lancucki, 1983; De Ceukelaire, 1991; Dähn et al., 2016; Leemann et al., 2020). Presence of ASR products of different morphology complicates understanding of the mechanism of concrete expansion and cracking.

Mechanics of the ASR at the nano-scale is not a common subject of numerical modelling. Until recently, it has been widely assumed that the cracking starts from the ASR

gel filling up either the interfacial transition zone or pores. Researchers would consider a group of pre-existing cracks and apply homogenisation principles to obtain macroscopic response (e.g. Lemarchand et al., 2005; Esposito and Hendriks, 2016; Iskhakov et al., 2019). Recent findings by Leemann and Münch (2019) showed that the initial ASR products accumulate between the aggregate grains at the nano-scale. To the author's knowledge, there is no study on the ASR cracking at this scale available in the literature. A possible reason for that is the difficulty to make observations and moreover to take the experimental measurements of the local internal pressure.

2.2 Meso-scale

ASR meso-scale models resolve the structure of concrete at the level of the aggregates and of the cement paste. Here, they are categorised in several types.

The first type is the reaction rim model. Its idea is to attribute the expansion and cracking of concrete to the expansion of external rims of the aggregates. These models assume that the alkalis are diffusing into the aggregates in the form of a smooth front, which defines a boundary between the reacted and non-reacted silica. An example of the reaction rim model would be the lattice discrete particle model by Alnaggar et al. (2013), where each aggregate is represented by a discrete particle. Cracks in this model can only propagate on the surfaces of the polyhedral aggregates.

Different reaction-rim models were proposed by Suwitoa et al. (2003) and Multon et al. (2009). Both models compute the depth of ion diffusion into the aggregate and estimate the amount of resulting ASR products. In the former model, the whole loading is applied at the interfacial transition zone and the macroscopic elastic expansion is evaluated. The latter model applies the loading within the body of an aggregate and advances cracks, which are modelled by the continuum damage approach (Kachanov, 1986).

The second model type assumes that the expansive sites are randomly distributed inside aggregates. A typical example of such model is the one proposed by Schlangen and Copuroglu (2010). It is a lattice model with explicitly represented aggregates, cement paste and ITZ. The ASR expansion is applied as the eigenstrain at the ASR sites randomly chosen inside the aggregate material. Upon damage, the elements are removed from the lattice.

A similar approach but with 2D finite elements was proposed by Dunant and Scrivener (2010) and later expanded for the needs of high-performance computing by (Cuba Ramos et al., 2018). The pockets of ASR gel are represented by the finite elements randomly distributed within aggregates. The continuous damage approach, adopted to represent cracking, allowed reproduction of realistic crack networks. The model qualitatively cap-

tured the stress-induced anisotropy. It however failed at the high uniaxial loads by predicting specimens' contraction along the loading direction, which is never the case in the loaded ASR experiments (Larive, 1997; Multon and Toutlemonde, 2006; Gautam and Panesar, 2016). Such limitation of the model is attributed to not accounting for the self-contact in cracks. The model was complemented by Giorla et al. (2014, 2015) by adding the visco-elasticity to the cement paste and studying its stress relaxation effect.

Rezakhani et al. (2021) used the continuous damage approach with explicit representation of the ASR pockets to model the free expansion of ASR-affected concrete in 3D. The authors coupled Mazars' damage model and visco-elasticity of cement paste. Explicit dynamics analysis was called to avoid convergence issues. The authors have shown that the biggest part of the macroscopic expansion comes from the propagation and opening of cracks and not from the elastic expansion of ASR sites.

An interesting study comparing the reaction-rim and the gel-pockets models was conducted by Miura et al. (2021). The authors have modelled the two mechanisms by means of a 3D-rigid body spring model and applied them to the case of a single spherical inclusion and multiple ones. The results showed that the gel-pockets model produces some sharp radial cracks penetrating both the aggregates and the cement paste. The reaction-rim model at first develops the onion skin cracks that propagate inside the aggregates along their boundaries. Further, the radial cracks start to grow towards the cement paste. The authors concluded that the reaction-rim model is well-suited for highly reactive aggregates, such as glassy andesite. The gel-pockets model, in turn, provides the most accurate description for the moderate and slowly reactive aggregates, such as schist.

A different three-dimensional model of the concrete micro-structure undergoing ASR was proposed by Comby-Peyrot et al. (2009). The main difference is that the internal loading is represented by swelling of the entire aggregates. The continuous damage approach was used to model the deterioration of cement paste only. The model qualitatively reproduces crack patterns on the concrete faces, but does not allow cracking within the aggregates.

A different approach on modelling the ASR mechanics was recently proposed by Liaudat et al. (2020). A meso-scale model of the ASR-affected soda-lime glass concrete couples chemistry and mechanics. First, the diffusion-reaction problem accounts for the concentrations of aqueous silicate, calcium and alkalis in the pore solution. Progress of the reaction leads to accumulation of ASR products, eventually leading to the development of internal pressures. The latter serves as the driving forces to open discontinuities in the mechanical part of the model. These discontinuities comprise the cracks in the aggregates, cement paste, and ITZ. The mesh incorporates zero-thickness interface elements exhibiting strain-softening behaviour. These discontinuities are pre-inserted along all the aggregate-paste contacts and some predefined paste-paste and aggregate-

aggregate inter-elements boundaries representing potential crack paths. The alkali-silica reaction is assumed to occur only at the glass-cement interfaces and within the opened cracks. Hence, the accumulated ASR products directly lead to the generation of pressures applied at the discontinuity faces. Simulation of a 2D specimen with a single circular aggregate results in a crack pattern and a macroscopic expansion that fairly match the experimental observations. Being very advanced in the chemo-mechanical coupling, the proposed model is advantageous for the early stages of the ASR with few short cracks developed. However, efficient modelling of a 3D concrete meso-structure by the proposed method may be complicated, mainly because of the crack-path uncertainty, which would require pre-insertion of the interface elements everywhere. The latter would substantially rise the computational cost of the model.

Modelling damage in concrete at the meso-scale is a tedious task. All the described models lose their efficiency when a realistic tomography-based mesh has to be considered. Huang et al. (2015) made an attempt to predict ASR-unrelated damage in a tomography-based concrete model by using the compressive damage plasticity model in ABAQUS. By simulating the uniaxial tension and compression tests, the authors achieved fair agreement with the experiments and developed a network of localised thin cracks. No information on the computational efficiency was reported. Yang et al. (2019) applied a phase-field regularised cohesive zone model to predict deterioration of concrete. Simulations of the three- and four-point bending tests were conducted on a 2D tomography-based geometry. The authors managed to predict several cracks growing in the specimen. Extension of this model to 3D is complicated due to the extreme computational cost of the phase-field model.

A model simulating the ASR expansion in a tomography-based mesh was recently proposed by Pan et al. (2018). A centimetre-scale mesh of concrete was used to model diffusion of alkalis from cement paste into the aggregates, dissolution of silica and its reaction with alkalis. Volume of the reactants was transformed into the strains that were later used to obtain the elastic stresses according to Hooke's law. The authors have matched the macroscopic expansion with experimental data from the literature. The fact that the model is purely elastic and does not allow cracking, makes it suitable only for the early ASR stages.

2.3 Macro/structural scale

The ASR is most commonly detected in the large concrete structures exposed to water, such as sea walls, bridge piers and dams. Several macro-scale models that address the consequences of the ASR directly at the structural level are available in the literature. These models, calibrated on the historical measurements, aim to predict future behaviour of a structure. Such predictions are important in order to avoid significant reduction in the service life and hence help to alleviate the economical effects. In the macro-scale

models, concrete is considered as a homogeneous material and the underlying concrete structure comprising aggregates and cement paste is not resolved. As the explicit representation of aggregates and cement paste at this scale would yield to computational models of unacceptable size, a simplified material description is inevitable.

One large subgroup of macro-scale models is based on a phenomenological approach (Larive, 1997; Capra and Bournazel, 1998; Ulm et al., 2000; Saouma and Perotti, 2006; Martin et al., 2012; Omikrine Metalssi et al., 2014, etc.). These models compute directly the macroscopic ASR strain by extrapolating results from laboratory measurements to the field conditions. These phenomenological models require extensive experimental studies to determine all the input parameters needed for the simulations.

Another group of macro-scale ASR models incorporates the principles of poromechanics, according to which concrete is considered as a solid skeleton permeated by open porosity (Capra and Sellier, 2003; Bangert et al., 2004; Comi et al., 2009; Grimal et al., 2010; Pignatelli et al., 2013; Multon and Sellier, 2016; Esposito and Hendriks, 2016). Constitutive laws for the macro-scale simulations are derived from homogenisation principles. The ASR-induced damage is typically assumed to be isotropic. The solid phase does not distinguish between aggregates and cement paste, which causes a uniform damage distribution inside the concrete skeleton.

In recent work, Vo et al. (2021) proposed a macroscopic ASR model considering reinforced concrete in a homogenised manner. The particularity of this poroelastic model is its ability to take into account interactions between steel rebars and concrete. Moreover, the damage of concrete is modelled by a continuous damage approach with three possible crack directions. The model predicts anisotropic swelling induced by the effects of the reinforcement-caused constraints and the external loading.

Another group of macro-scale models considers propagation of the micro-cracks within a representative volume element (RVE) of concrete. An RVE represents the heterogeneous concrete structure at a smaller length scale. Esposito and Hendriks (2016) modelled the macroscopic expansion as a consequence of ASR-induced propagation of the pre-existing cracks in the cement paste. The aggregates were modelled as spherical inclusions. Three orthogonal families of penny-shaped cracks in the cement paste were considered. The crack growth was governed by linear elastic fracture mechanics. The effective stiffness tensor of an RVE is evaluated through the Mori-Tanaka homogenisation scheme (Benveniste, 1987). Iskhakov et al. (2019) advanced the previous model by adding an independent crack family within the aggregates as well as ring-shaped cracks around them. Being an elegant solution for the early stage ASR cracking, the discussed models can not predict stiffness loss after the interconnection threshold - a critical volume fraction of the micro-cracks, at which they form a connected network.

Recently, due to the advancement of high-performance computing, the first numer-

ical multi-scale models have been proposed for ASR mechanics. These models couple numerical computations at the large and fine scales in a single simulation. A computational multi-scale approach is advantageous because the consequences of the ASR at a larger scale can be computed directly from the reaction advancement inside the underlying RVEs. A model by Puatatsananon and Saouma (2013) accounts for the diffusion processes and the ASR-gel swelling at the level of the aggregates. Wu et al. (2014) proposed a model that couples gel production and expansion in micro-pores of hardened cement paste to its manifestation at the meso-scale. Nonetheless, both models are lacking an explicit representation of the ASR-induced cracks, which could help to reproduce the ASR anisotropy. Almenar et al. (2017) developed a thermo-poro-mechanical multi-scale model that accounts for the concrete degradation. The resulting damage profile inside RVEs has a rather diffused character, which poses a constraint on a realistic representation of the concrete stiffness. A 3D multi-scale model by Rezakhani et al. (2019) couples the lattice discrete-particle model at the meso-scale to a standard FE model at the macro-scale. The authors approximated swelling of single ASR pockets by the overall expansion of the aggregates. Their model captures the anisotropic ASR expansion under loading and produces localised crack patterns. On the other hand, cracks are only allowed to develop along the planes delimited by the aggregates centres, which is not the case of a real ASR-affected concrete.

The discussed numerical models succeed in capturing certain ASR phenomena: macroscopic expansion, expansion of individual aggregates, concrete cracking, water and ion diffusion, growth of ASR products, etc. While some of the models are more interested in reproducing one part of the ASR physics, they may ignore the rest. Capturing all of the ASR features at all the scales simultaneously does not seem expedient and furthermore is hardly possible due to the underlying complexity of the problem. Moreover, our limited knowledge of the responsible mechanisms implies including certain empirical laws in the developed models. The emergence of the new experimental data and field measurements helps to improve the existing models by replacing some of the assumptions by the data. A similar work is done in this thesis.

3 ASR-crack nucleation at the nano-scale

Recent experimental studies on the different ASR products suggest that the volume increase between the reactants and the products could reach up to 100%. Taking place inside the aggregates, newly formed ASR products impose internal pressure on the surrounding material. In the current chapter, the possibility of crack growth due to such internal loading is studied. Based on the responsible chemical reaction, the increase in the volume of the products over the reactants could be computed. A semi-analytical mechanical model for an expanding ASR pocket encircled by a pre-existing micro-crack is formulated. The inclusion represents a single pocket of the expanding ASR products surrounded by the aggregate matrix. The crack extension is predicted for the ASR pocket of different sizes, shapes and expansion values. Theoretical predictions are confirmed by a numerical model based on the combination of the finite-element method and the cohesive zone model. The results of this study are currently under review with the preprint available in (Gallyamov et al., 2021b).

3.1 Chemical reaction

A typical ASR formation reaction could be written as

$$\underset{\text{solid}}{4\,\text{SiO}_2} + \text{K}^+ + \text{Ca}^{2+} + 3\,\text{OH}^- + 2\,\text{H}_2\text{O} \longrightarrow \underset{\text{ASR product}}{\text{KCa}[\text{Si}_4\text{O}_9(\text{OH})]\cdot 3\,\text{H}_2\text{O}} \tag{3.1}$$
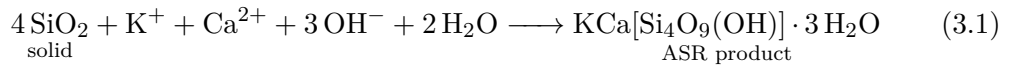
that describes the formation of the ASR product with molar ratios K/Si and Ca/Si of 0.25. These ratios correspond to the elemental ratios observed in ASR products in the field samples as well as to those observed in laboratory synthesised ASR products, although they vary to a certain extent (Leemann and Lura, 2013; Shi et al., 2019, 2020; Iskhakov et al., 2021). All calculations presented here refer to the idealised composition given in Eq. (3.1).

Assuming quartz or amorphous SiO_2 as a silica source, it is possible to calculate

the increase of solid volume if the ASR product is formed within the space originally occupied by SiO_2. Note that other species (K^+, Ca^{2+}, OH^-, and H_2O), needed to form ASR products, are assumed to diffuse into the aggregate from the cement pore solution, such that their volume is not considered. Based on the molar volume of quartz (22.6 cm^3/mol), and the molar volume of the crystalline ASR product K-shlykovite, $KCa[Si_4O_9(OH)] \cdot 3\,H_2O$, of 183 cm^3/mol (Geng et al., 2020) (or 45.7 cm^3/mol if normalised to 1 silica: $K_{0.25}Ca_{0.25}[SiO_{2.25}(OH)_{0.25}] \cdot 0.75\,H_2O$) the increase in solid volume by a factor of two is obtained, and a ratio between the additional volume ($45.7 - 22.6 = 23.1$) and the initial volume is $23.1/22.6 \approx 1.0$, thus leading to 100% expansion. For the amorphous ASR products, the molar volume has not been measured but based on the extensive analysis performed by Leemann et al. (2020), the amorphous ASR product with a composition of $Na_{0.1}K_{0.2}Ca_{0.2}SiO_{2.3}(OH)_{0.1} \cdot 1.1\,H_2O$ indicates a similar or even higher volume increase (≈ 2.3) as for the crystalline ASR product. The duplication of the initial volme due to the precipitation of the ASR product could potentially lead to the formation of cracks within aggregates. This hypothesis was studied in detail based on a semi-analytical mechanical model of an inclusion-crack system within an infinite medium.

3.2   Analytical model of expanding ASR pockets

The dependence of the possible crack growth on the size and the shape of ASR products is studied by exploring a semi-analytical mechanical model that consists of two components. The first one is a purely analytical model for an inclusion expanding within an infinite medium. The second one is a semi-analytical model of a ring-shaped crack encircling the previously described inclusion. The resulting model yields stress concentrations at the external crack tip that are used to evaluate the crack growth. A pocket of an ASR product is assumed to have a spheroidal shape since the latter comprises a wide range of shapes with central symmetry (e.g. spheres, oblate spheroids, disks, etc).

The departing point of the analytical model is the Eshelby problem (Eshelby, 1959) that describes an expanding ellipsoidal inclusion embedded in an infinite medium. The term "inclusion" implies that its elastic properties differ from the ones of the matrix. The inclusion represents a single pocket of an ASR product surrounded by the aggregate. In this study, a spheroid is considered - a type of an ellipsoid with a circular cross-section. Here, we assume a relatively small ASR pocket, which is positioned sufficiently far from the aggregate's boundary not to cause any mechanical influence, thus justifying the "infinite surrounding medium" condition. Given the known expansion of the inclusion, the elastic properties of the ASR product, its shape and size, the stress and strain fields could be determined. The problem was solved by Eshelby (1959, 1957) for general eigen strains. The solutions for the inclusion and the matrix are different. Later Mura (1987) provided explicit equations for the Eshelby tensor $\mathbb{S}$ for different shapes of an ellipsoid at the interior points. Ju and Sun (1999, 2001) gave the first explicit formulas
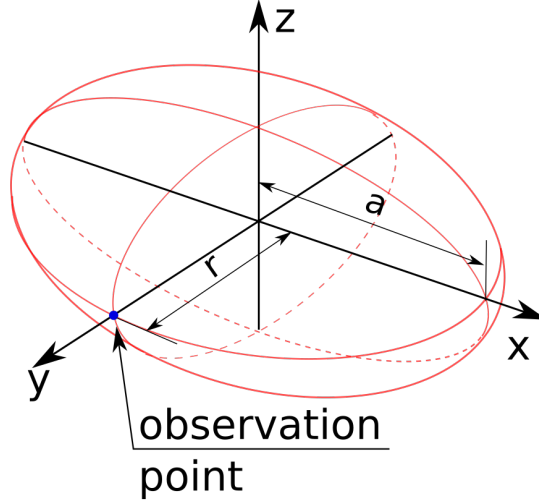
Figure 3.1: Geometry of a spheroidal inclusion. Further in the text, stresses are evaluated either in the observation point or along the y-axis

for computing the Eshelby tensor in the surrounding matrix. Healy (2009) developed a MATLAB^{TM} code with the Eshelby solution in 3D both inside and outside the inclusion.

A spheroidal inclusion with the semi-axis a and the equatorial radius r (shown in Fig. 3.1) is embedded in a matrix. Variation of the semi-axis a allows considering different geometries: 1) a sphere ($a = r$); 2) a needle ($a >> r$); 3) a penny (or a disk) ($a << r$). The expansion is applied at the inclusion in the form of the eigenstrain $\boldsymbol{\varepsilon}_{eig}$ - a strain causing zero stress under no confinement. The eigenstrain is linked to the elastic strain $\boldsymbol{\varepsilon}_{el}$ as

$$\boldsymbol{\varepsilon} = \boldsymbol{\varepsilon}_{el} + \boldsymbol{\varepsilon}_{eig} \tag{3.2}$$

where $\boldsymbol{\varepsilon}$ is the total strain. 100% volumetric expansion of the ASR product is applied in the form of the isotropic eigenstrain $\boldsymbol{\varepsilon}_{eig} = 1$.

The matrix is an infinite body with the remote stress $\boldsymbol{\sigma}^0$ or strain $\boldsymbol{\varepsilon}^0$ applied at infinity. In the current study, a stress-free body with $\boldsymbol{\sigma}^0$ and $\boldsymbol{\varepsilon}^0$ equal to zero is assumed. The effect of external loading on the ASR was previously studied by several authors (e.g. Larive, 1997; Multon and Toutlemonde, 2006; Dunant and Scrivener, 2012).

The solution for the strain and stress inside the inclusion was given by Ju and Sun (2001)

$$\begin{aligned}
\boldsymbol{\varepsilon} &= \boldsymbol{\varepsilon}^0 + \mathbb{S} : \boldsymbol{\varepsilon}_{eig} \\
\boldsymbol{\sigma} &= \boldsymbol{\sigma}^0 + \mathbb{C}^0[\mathbb{S} - \mathbb{I}] : \boldsymbol{\varepsilon}_{eig}
\end{aligned} \tag{3.3}$$

where $\mathbb{S}$ is the 4th-order Eshelby tensor for the interior points, $\mathbb{C}^0$ the matrix stiffness

tensor and $\mathbb{I}$ the identity tensor. The particular property of the Eshelby problem is that the stress and the strain fields at the interior points are uniform and the Eshelby tensor $\mathbb{S}$ is independent of the position within the inclusion.

Oppositely, for the corresponding fields outside the inclusion, the strain and the stress at a point depend on the position of the latter:

$$
\begin{aligned}
\boldsymbol{\varepsilon}(\boldsymbol{x}) &= \boldsymbol{\varepsilon}^0 + \mathbb{G}(\boldsymbol{x}) : \boldsymbol{\varepsilon}_{eig} \\
\boldsymbol{\sigma}(\boldsymbol{x}) &= \boldsymbol{\sigma}^0 + \mathbb{C}^0 \mathbb{G}(\boldsymbol{x}) : \boldsymbol{\varepsilon}_{eig}
\end{aligned}
\tag{3.4}
$$

where $\mathbb{G}(\boldsymbol{x})$ is a 4th-order Eshelby tensor for the exterior points.

Explicit formulas for the components of $\mathbb{S}$ and $\mathbb{G}(\boldsymbol{x})$, available in (Ju and Sun, 2001) and (Healy, 2009), yield the values of $\boldsymbol{\varepsilon}$ and $\boldsymbol{\sigma}$ at any point of space.

3.3 Semi-analytical model with a ring-shaped crack

Griffith (1921) in his fundamental work showed that the material strength at the macro-scale is largely affected by the presence of microscopic flaws. For an expanding inclusion, to grow a crack from its surface, there should be an initial micro-fissure that would facilitate the crack propagation. A higher expansion would be required if such an inclusion would be surrounded by a sound material with no flaws in it. Pre-existing defects in the form of microcracks are common in rocks (Anders et al., 2014).

A crack is added to the Eshelby problem as shown in Fig. 3.2. It has the shape of a flat ring in the yz-plane. While the inner crack tip lays exactly on the equator of the spheroid, the outer one extends by the distance l. r and R denote the internal and external crack radii correspondingly. An additional y'-axis was introduced for computation purposes: it is a y-axis with the origin shifted to the surface of the spheroid. The crack is opening in mode I. Keeping the expansion value fixed, a different alignment of a crack would reduce the probability of its extension.

According to the adopted model, the inclusion is always expanding as a solid body. When the crack extends, the ASR product does not flow inside. Therefore this model represents the ASR product in its mature stage. Accounting for the gel fluidity would require an extended analytical model including the mass conservation and the pressure redistribution.

Aggregates are composed of a brittle material that fractures abruptly without undergoing significant softening. Such behaviour is well reproduced by linear elastic fracture mechanics (LEFM) that serves as a base for the further analytical developments. The internal load $\varepsilon_{eig} = 1$ is based on the expansive potential of the ASR product (see Section 3.1). Such a high expansion induces large strains that could not be sustained by the
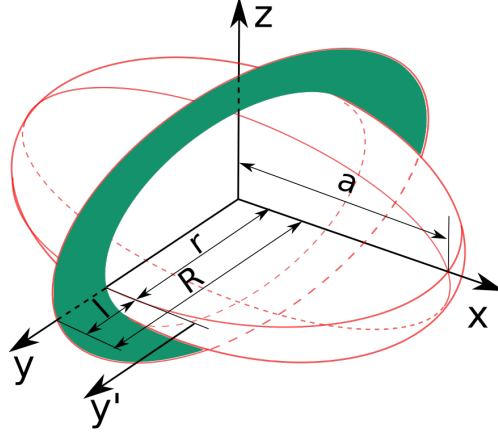
Figure 3.2: Spheroid with the pre-existing disk-shaped crack in the yz-plane.

aggregate material. Instead, it would yield such second-order effects as micro-cracking around the inclusion and alteration of the LEFM-based crack shape and length. Predicting such behaviour is a challenging task. Here, a first-order qualitative prediction is aimed.

To evaluate the crack growth, one has to know K_I - the stress intensity factor (SIF) in mode I for the external crack tip. The principle of superposition states that applying $\boldsymbol{\sigma}(\boldsymbol{x})$ on the crack faces is similar to loading the cracked body with the loads that cause $\boldsymbol{\sigma}(\boldsymbol{x})$ in the absence of a crack (Petroski and Achenbach, 1978). To find K_I, the problem of a crack loaded by a spheroidal inclusion is replaced by a crack whose faces are loaded by the stresses caused by the expanding inclusion in the absence of the crack. The latter ones are known from the solution of the Eshelby problem.

Literature has few analytical solutions for computing K_I for ring-shaped cracks under simple loading, e.g. (Tada et al., 2000). Unfortunately, a solution for a general stress distribution is not available. Instead, this problem could be solved using weight functions, as proposed by Bueckner (1970) and Rice (1972). These authors suggested using the known crack face displacement $u(l, x)$ and the known stress intensity factor K_I^0 for a symmetrical load system on a cracked body to compute unknown K_I for any other symmetrical load system. The equation for SIF reads as

$$K_I = \int_0^l \sigma(y')h(l, y')dy' \tag{3.5}$$

where $h(l, y')$ is a weight function defined as

$$h(l, y') = H\frac{\partial u}{\partial l}/K_I^0 \tag{3.6}$$

21

In Eqs. (3.5) and (3.6), l is the crack length equal to the difference between the external and internal radii $(R-r)$, H is a material parameter, $\sigma(y')$ is the stress distribution along the crack plane in the unflawed body under the load associated to K_I. Integration is carried out along the crack surface only. Fett and Rizzi (2007) computed weight functions for a ring-shaped crack by the interpolating procedure. The latter is the reason for the solution being "semi-analytical". The weight function for the outer crack tip reads as

$$h(l,y')\sqrt{l} = \frac{2}{\sqrt{\pi(1-y'/l)(l/r+1)}}\left(\frac{1+y'/r}{\sqrt{2+l/r+y'/r}} - \frac{1-\sqrt{y'/l}}{\sqrt{l/r+2}}\right) \qquad (3.7)$$

Plugging Eq. (3.7) and the stresses from Eq. (3.4) into Eq. (3.5) and integrating it numerically results in the required values of K_I. A similar approach was previously used by Iskhakov et al. (2019) within a multi-scale model.

3.4   Numerical validation

Analytical and semi-analytical predictions are validated through the numerical modelling. Two components of the final solution are verified. The first component is the elastic stress in the inclusion's surroundings in the absence of a crack. The second component is the actual crack radius for different inclusion shapes and sizes. The numerical model is based on the finite element method (FEM).

The latter is briefly summarised for a body Ω with its boundary Γ, which comprises both the external and the crack surfaces Γ_t and Γ_c correspondingly. The variational form of Eq. (4.1) is

$$\int_\Omega \boldsymbol{\sigma} : \boldsymbol{\varepsilon}(\partial \mathbf{u})\ d\Omega + \int_{\Gamma_c} \mathbf{T} \cdot \partial \mathbf{u}\ d\Gamma - \int_{\Gamma_t} \mathbf{t} \cdot \partial \mathbf{u}\ d\Gamma = 0 \qquad (3.8)$$

where $\partial \mathbf{u}$ the vector of virtual displacements, $\mathbf{t}$ is the vector of external boundary forces, and $\mathbf{T}$ is the vector of cohesive tractions. The equilibrium above is the basis of the finite-element method. Discretisation of the continuous displacement field $\partial \mathbf{u}$ by finite-element interpolants and integration of Eq. (3.8) yields a system of the form:

$$\mathbb{K}\mathbf{u} = \mathbf{f}_{\text{ext}} \qquad (3.9)$$

where $\mathbb{K}$ is the global stiffness tensor and $\mathbf{f}_{\text{ext}}$ is the vector of external forces. When a non-linear material behaviour is considered, the system above also becomes non-linear. Its solution is obtained by employing the Newton-Raphson iterative solver. All implementations are done using the C++ open-source finite element library Akantu [Richart and Molinari 2015; Vocialta et al. 2017, akantu.ch].

The geometry used for the numerical model is shown in Fig. 3.3. It comprises one-
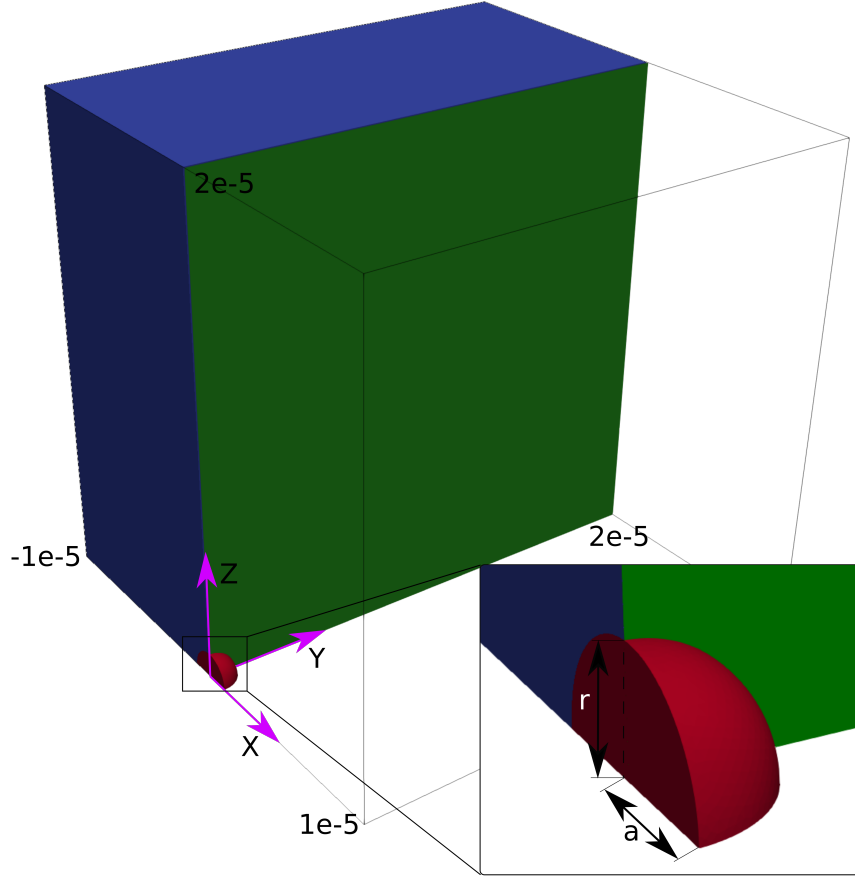
Figure 3.3: Geometry of the numerical model used for the verification study. Red colour corresponds to the ASR product, blue to the surrounding aggregate, green to the predefined crack plane. The second half of the aggregate is omitted for visualisation of the crack plane. The dimensions are given in meters.

quarter of the full space. Symmetry over the xz- and xy-planes is established by imposing zero out-of-plane displacements. The simulated block comprises one-quarter of the inclusion-matrix system. The equatorial radius of the spheroid is 1 μm, while the dimensions of the full block are $20 \times 20 \times 20$ μm^3. The behaviour of the bulk materials (the aggregate and the inclusion) is linear elastic. The loading is prescribed at the inclusion in the form of the isotropic eigenstrain $\varepsilon_{eig} = 1$ that represents a 100% volumetric expansion of the ASR product.

For verification of the maximum crack radius, the crack plane is added to the FE model along the yz-plane. The discontinuity is modelled by cohesive elements that are inserted along the pre-defined plane during the mesh generation. The cohesive zone approach yields to dissipation of the fracture energy by the interface (or cohesive) elements placed between the neighbouring solid elements (see Fig. 3.4a). When two solid elements are being pulled apart, a cohesive element in-between resists by generating the

(a)

(b)
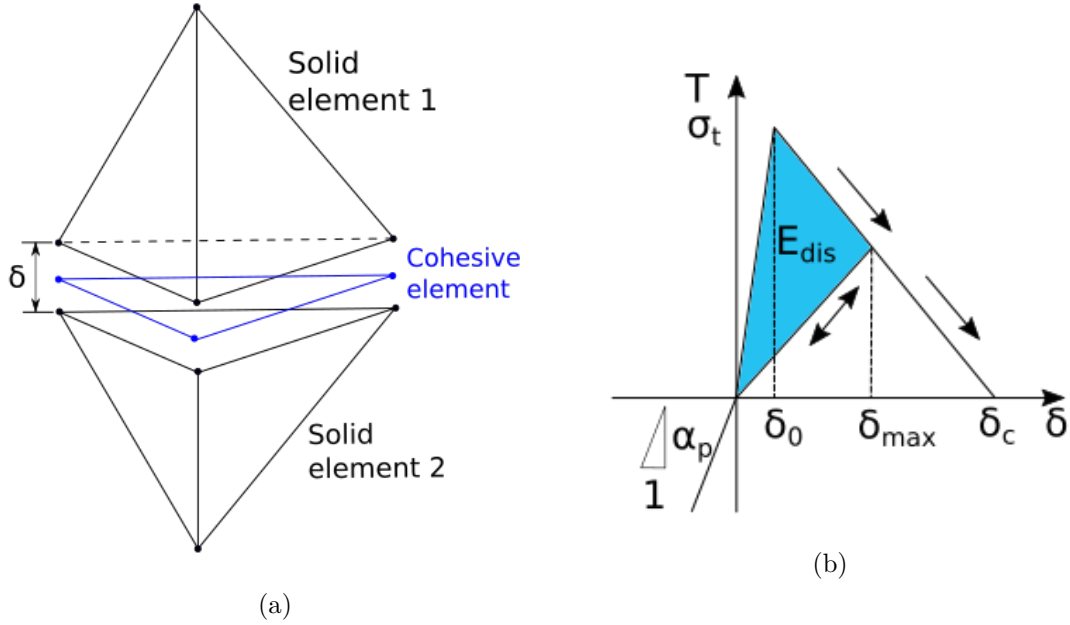
Figure 3.4: a) Sketch of a first-order 2D cohesive element between 3D solid elements. b) Illustration of the bi-linear cohesive law.

inwards traction whose amplitude depends on the opening displacement value. Cohesive elements represent the non-linear process zone (or cohesive zone) at the crack tip, as originally proposed by Dugdale (1960) and Barenblatt (1962).

Behaviour of a cohesive fracture is postulated by a cohesive law - a relation between tractions **T**, effective displacements $\boldsymbol{\delta}$ and cohesive energy density ϕ:

$$\mathbf{T} = \frac{\partial \phi}{\partial \boldsymbol{\delta}} \tag{3.10}$$

For the current study, the bi-linear traction-separation law, shown in Fig. 3.4b, is employed. For the cohesive opening δ below the elastic limit δ_0, a cohesive element behaves in a linear elastic manner. The effective displacement is defined as

$$\delta = \sqrt{\beta^2 \Delta_t^2 + \Delta_n^2} \tag{3.11}$$

where Δ_t and Δ_n are respectively the tangential and normal components of the opening displacement vector $\boldsymbol{\Delta}$ at the cohesive elements. The empirical parameter β couples normal and tangential displacements. As the considered problem is symmetric with respect to the crack plane, the effective displacements of the cohesive elements have only

normal component ($\delta = \Delta_n$). The tractions are computed based on the opening δ:

$$\mathbf{T}(\delta, \delta_{\max}) = \begin{cases} \frac{\sigma_t \delta}{\delta_0} \mathbf{n} & \text{for } \delta_{\max} \leq \delta_0 \\ \sigma_t \left(1 - \frac{\delta}{\delta_c}\right) \mathbf{n} & \text{for } \delta = \delta_{\max} > \delta_0 \\ \frac{T_{\max}}{\delta_{\max}} \mathbf{n} & \text{for } \delta < \delta_{\max} > \delta_0 \\ \alpha_p \delta & \text{for } \delta < 0 \\ 0 & \text{for } \delta \geq 0 \text{ and } \delta_{\max} \geq \delta_c \end{cases} \tag{3.12}$$

where $\mathbf{n}$ is the unity vector normal to the crack surface, σ_t is the local material strength and δ_c is the critical normal opening at which full decohesion happens. After the traction T reaches the material strength in tension σ_t, it starts to decrease linearly reproducing material softening. The latter takes place up to a moment when the opening reaches its critical value δ_c. Then the element is fully broken. If the loading is removed while the element is in the softening stage ($\delta < \delta_c$), its behaviour becomes elastic again within the window $0 \leq \delta \leq \delta_{max}$. Under compression, cohesive elements behave elastically with a penalty coefficient α_p. The initial elastic opening of a cohesive element is a numerical artefact: ideally, the interface should be fully rigid up to the point where it reaches the tensile strength σ_t and the softening starts. To minimise the artificial effect of the pre-inserted cohesive elements on the behaviour of the bulk material, the elastic opening δ_0 should be kept very small, so that the initial stiffness of the cohesive element is higher than the one of the bulk material. Opening of a cohesive element dissipates energy E_{dis}. The maximum value that can be dissipated upon reaching the critical opening δ_c equals the fracture energy G_C according to

$$\delta_c = 2 \frac{G_C}{\sigma_t} \tag{3.13}$$

where G_C could be computed from the fracture toughness K_{IC} as

$$G_C = \frac{K_{IC}^2}{E} \tag{3.14}$$

where E is the Young's modulus of the surrounding material.

While the LEFM-based semi-analytical solution assumes that the material undergoes brittle failure, the cohesive zone model suggests that it undergoes softening that is contained in the process zone next to the crack tip. The length of this zone, l_z, depends on the adopted model. According to Hillerborg et al. (1976), it can be estimated as

$$l_z = \frac{E G_C}{\sigma_t^2} \tag{3.15}$$

To make the cohesive zone model match the LEFM solution, the process zone l_z should be big enough to accommodate several finite elements, but smaller than any other model

Material properties	ASR product*	Aggregate †	Cohesive material
Young's modulus E [GPa]	10	60	-
Poisson's ratio ν [-]	0.3	0.3	-
Fracture toughness K_{IC} [MPa$\sqrt{\text{m}}$]	-	2	-
Fracture energy G_C [J/m^2]	-	-	66.7
Tensile strength σ_t [MPa]	-	-	$4.5 \cdot 10^3$
Elastic opening δ_0 [nm]	-	-	1
Critical opening δ_c [nm]	-	-	29.6

Table 3.1: Material properties of the ASR product and the aggregate matrix, and parameters of the bi-linear cohesive law. * Based on the micro-indentation tests by (Leemann and Lura, 2013). † Taken from (Alehossein and Boland, 2004).

length scale (the size of the inclusion, the crack, and the domain). For an inclusion of 1 μm radius and a domain of 20 μm size, a 0.2 μm cohesive zone was chosen. The crack plane was meshed with the element size of 0.03 μm, which allowed having several elements within the cohesive zone. In Eq. (3.15), E and G_C are the material properties, while σ_t is treated as a calibration parameter. To make l_z equal to 0.2 μm, the tensile strength σ_t was assigned 4.5 GPa (see Table 3.1). Such a high value is adopted to make the cohesive zone model comply with the principles of LEFM. The values of σ_t, δ_0 and δ_c are given in Table 3.1.

3.5   Results

The theoretical predictions of stresses and crack radii are computed for different inclusion shapes and sizes. The theory is then validated by comparing with the numerical model.

3.5.1   Stresses in the bulk

To compute the stresses, material properties given in Table 3.1 are used. Due to the unavailability of the mechanical properties of the amorphous ASR product, those of the crystalline state are taken.

The analytical solution for the stresses inside and outside the inclusion is given in Fig. 3.5. The x-, y- and z-directions coincide with the directions of the principal stresses. Stresses at the interior points are independent of the point's position. Stresses in the matrix are plotted at the intersection point between the y-axis and the surface of the spheroid (see the observation point in Fig. 3.1). The semi-axis a is varied from almost zero to five times the equatorial radius r, changing from a penny to a sphere and finally to a needle. Stresses inside the inclusion are always compressive, becoming hydrostatic ($\sigma_{xx} = \sigma_{yy} = \sigma_{zz}$) in the spherical configuration. When approaching the disk limit, the stress in the direction normal to the disk plane tends towards zero. The stress state in
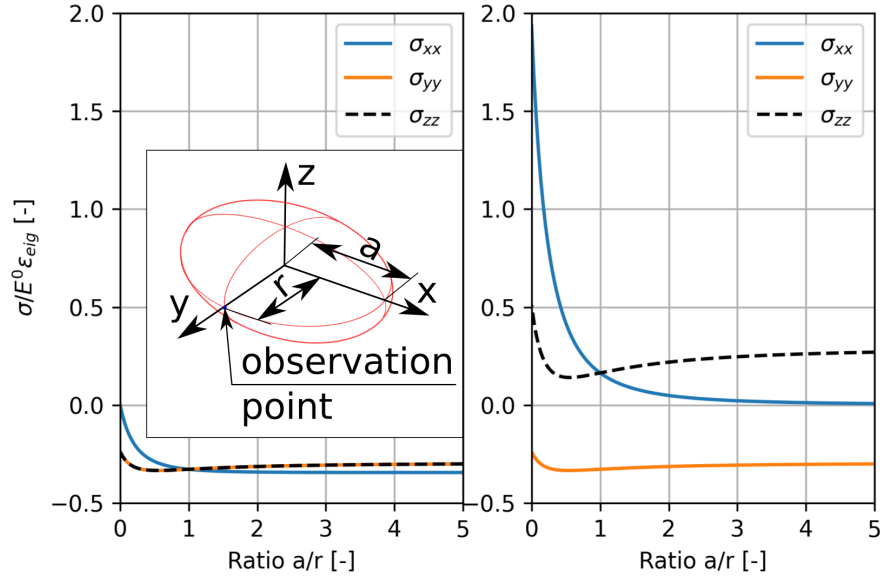
Figure 3.5: Stresses inside (on the left) and outside the inclusion (on the right) at the observation point for a varying inclusion's shape. Stresses are normalised by a product of the matrix's Young's modulus E^0 and the eigenstrain scalar ε_{eig}. The semi-axis a is normalised by the equatorial radius r.

the matrix is different. While the stress in the y-direction is still compressive, the other two stresses are either null or tensile. This creates the necessary premises for the crack nucleation. In the spherical setup, the tensile stresses in the x- and y-directions are equal, which makes any plane passing through the y-axis suitable for the crack growth. In the penny-shape limit $(a/r \to 0)$, σ_{xx} intensifies making the yz-plane preferable for a crack to grow. Since the gel inclusions are expected to have a flat shape, the analysis is limited to the cases where the ratio a/r changes from zero to one.

The analytical solution for the stresses along the y-axis for three different inclusion shapes is plotted in Fig. 3.6. Although the disk has a tensile stress at the border much larger than the one of a sphere, it decays much faster. For a spherical configuration $(a = r)$, the stress drops with the rate of r^3/y^3, which matches a well-known analytical solution (Timoshenko and Goodier, 1951, p. 417). A particularity of the Eshelby solution is its size independence: both the small and the large inclusions will generate similar stress and strain fields under the same expansion value.

The numerical solution for the stress σ_{xx} along the y-axis fairly matches the analytical predictions. A comparison between the two sets of results is plotted in Fig. 3.7. At this stage, no crack is present in the simulation. The only difference between the two methods is observed at the inclusion's boundary, where FEM cannot represent the stress peak for the oblate shapes. The numerical solution could be improved by the mesh refinement. The stress decay further from the inclusion surface is perfectly resolved.

27
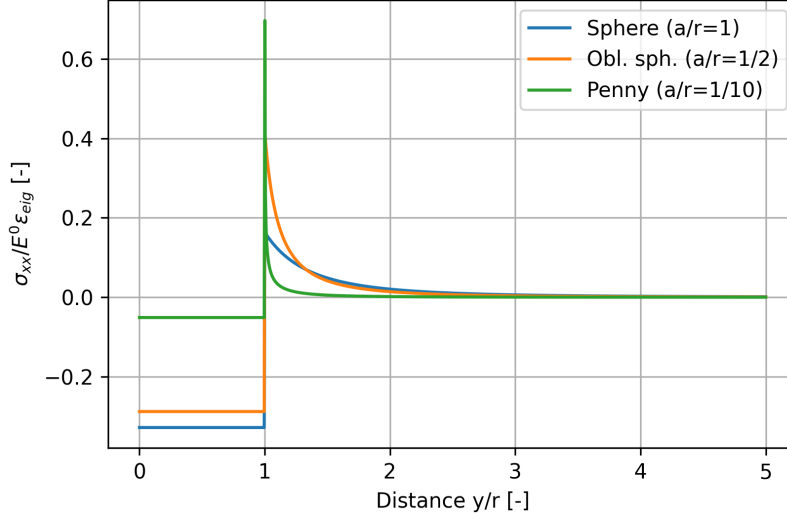
Figure 3.6: Stress σ_{xx} for three different inclusion shapes plotted along the y-axis. Its value is normalised by a product of the matrix's Young's modulus E^0 and the eigenstrain scalar ε_{eig}. The distance y is normalised by the equatorial radius r.
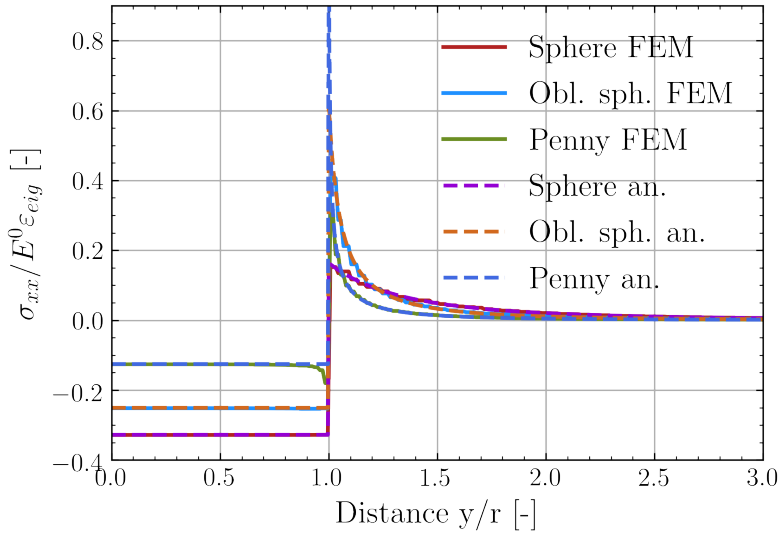
Figure 3.7: Comparison of the stress σ_{xx} along the y-axis from the analytical model and FE simulation
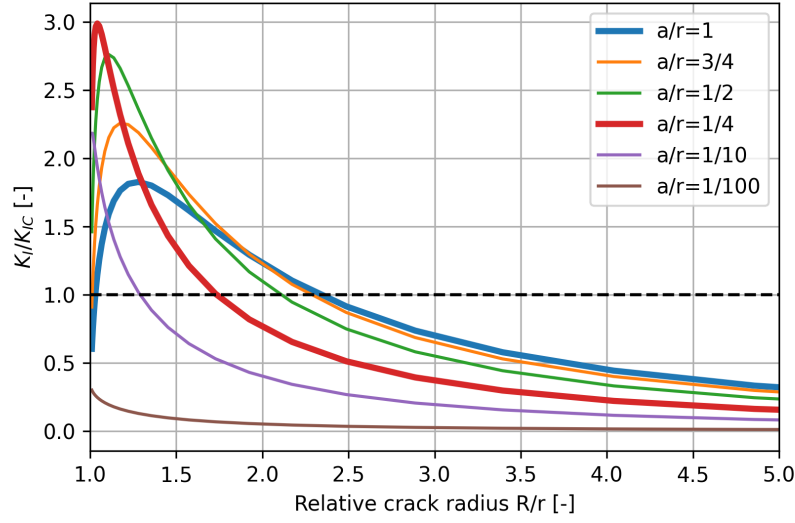
Figure 3.8: K_I/K_{IC} depending on the aspect ratio of the spheroid a/r and the external crack radius R/r for a spheroid with the fixed equatorial radius $r = 1 \ \mu m$ under the expansion of 100% .

3.5.2 Crack radius

The crack is added to the numerical problem employing the cohesive elements. The parameters of the cohesive law are listed in Table 3.1. To have a small l_z and preserve the fracture energy G_C, the tensile strength σ_t had to be assigned a high value and the critical opening δ_c had to be adjusted.

Expansion of the inclusion leads to the concentration of stresses at the crack tip. The intensity of this concentration is characterised by the stress intensity factor. The analytical solution for K_I depending on the spheroid's shape and the crack radius are plotted in Fig. 3.8. The equatorial radius of the inclusion in this plot equals 1 μm. K_I normalised by the fracture toughness K_{IC} serves as an indicator for crack growth. While the values of K_I/K_{IC} above one suggest that the crack will extend, a strict equality indicates the crack radius at which growth will cease. Cracking due to the ASR is happening in a quasi-static regime. The expansion value of 100% is not applied at once but is gradually increased. The process of crack growth is illustrated for the case of a spherical inclusion in Fig. 3.9. The cracking starts at a value that is lower than the final load. More specifically, the first crack extension happens when K_I at the peak of the curve becomes equal to K_{IC} (point 1 of Fig. 3.9). After the first crack growth event, any further infinitesimal increase in the load would lead to an increase in the crack length (point 2). At all times, the stress intensity factor K_I is strictly equal to the fracture toughness K_{IC}, and the crack propagation is stable. Finally, the load reaches its final value, and the crack growth arrests at point 3.
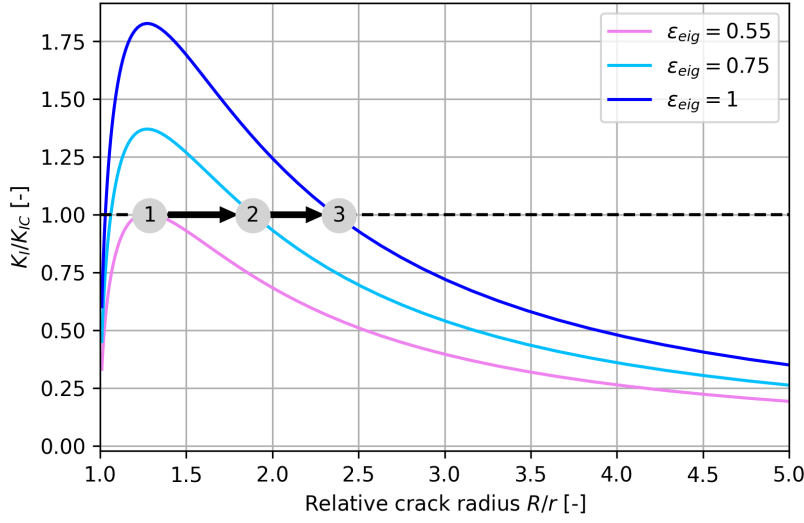
Figure 3.9: Illustration of the crack growth process around a spherical inclusion. Point 1 denotes the lowest value of expansion at which the crack extension begins. Point 2 corresponds to some intermediate expansion value at which the crack propagates in a stable mode ($K_I = K_{IC}$). Crack growth stops upon reaching the final ε_{eig} at point 3.

All the curves in Fig. 3.8 have unimodal distribution shape. At the extreme values of R, zero and ∞, K_I tends towards zero. In physical terms, it means that for a crack to grow, a pre-existing fissure of a finite length must exist. Otherwise, the problem transitions from being toughness-controlled to strength-controlled (Bažant, 1984; Ritchie, 2011). Overcoming material strength in the absence of micro-fissures would require higher expansion values of the ASR pocket. In contrast, a sufficiently large size of the pre-existing crack encircling the inclusion facilitates its further growth.

The curves in Fig. 3.8 are ascending up to the K_I peak value and later descend to zero. Such behaviour of K_I is not typical for the majority of the classical fracture mechanical problems. Normally, K_I is monotonously growing or reducing, e.g. a semi-infinite body under tension or a penny-shaped crack under a pair of forces applied at its centre. One may wonder why, in the case of the expanding inclusion, K_I has a peak, while in the case of a remote tensile load, it does not. The difference in K_I profiles stems from the different nature of loads. For the remote tensile load, the crack tip always "feels" the tensile stress applied at infinity. For the expanding inclusion, the stresses in the matrix in the absence of the crack are not constant. For simplicity, a spherical case is considered. In Fig. 3.10, the normalised stress σ_{xx} and stress intensity factor K_I are plotted along the distance y' given in logarithmic scale. The stress intensity factor was computed for the geometry where the crack size l equals the distance y'. The stress is constant up to $y'/r = 10^{-3}$ after which it starts to drop. While the stress is constant, K_I is monotonously growing (similar to the remote tension case). When the stress reduces, so
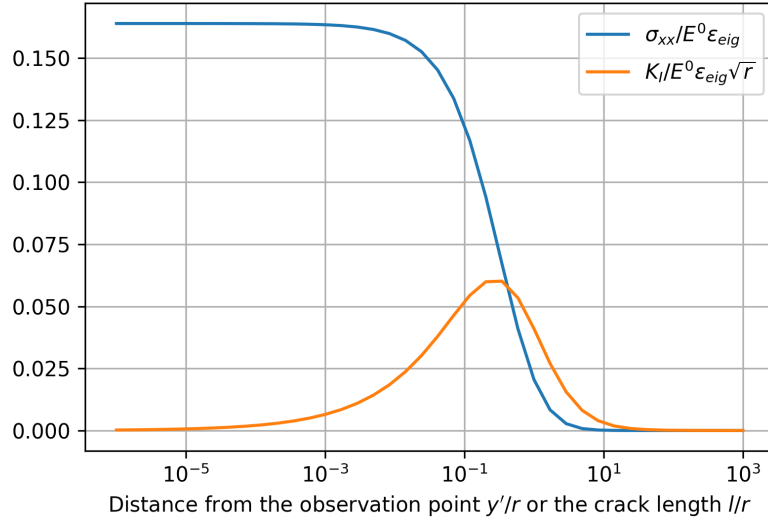
Figure 3.10: Stress σ_{xx} along the y'-axis in an unflawed configuration and SIF K_I for a crack of length $l = y'$. Values are normalised by a product of the matrix's Young's modulus E^0 and the eigenstrain scalar ε_{eig}. An extra normalisation term $1/\sqrt{r}$ is applied to K_I. The distances y' and l are normalised by the equatorial radius r.

does K_I, which results in a peak.

The K_I peak position and its height vary for different shapes of the inclusion. The highest K_I corresponds to an oblate spheroid with an aspect ratio $a/r = 1/4$, which makes it the most critical case for high fracture toughness. A sphere $(a/r = 1)$ has a lower peak value but its maximum crack length is the largest. Consequently, a sphere and a 1/4-spheroid are the two most critical geometries with regards to the K_I intensity and the maximum crack length correspondingly.

For the current equatorial radius of a spheroid $r = 1$ μm, any aspect ratio $1/10 \leq a/r \leq 1$ leads to the fracture growth. Flattening of the shape of the inclusion would reduce its potential to grow a crack. For instance, a penny with thickness $a = 0.01$ μm is not expected to develop a crack. The maximum crack radius for all possible spheroids with 1 μm radius is 2.35 μm, which is more than twice as big as the ASR pocket itself.

Although the stress solution of the Eshelby problem does not depend on the size of the inclusion, the solution for the stress intensity factor does. This is demonstrated in Fig. 3.11. The two most critical shapes (a sphere and a 1/4 spheroid) of different radii were tested: 0.1 μm, 1 μm, and 10 μm. The previous expansion value was applied. One can observe a gradual increase in both the peak SIF value and the maximum crack length for bigger inclusions. This allows concluding that the size of the ASR pocket has a direct effect on the crack propagation: larger ASR inclusions have a higher chance to
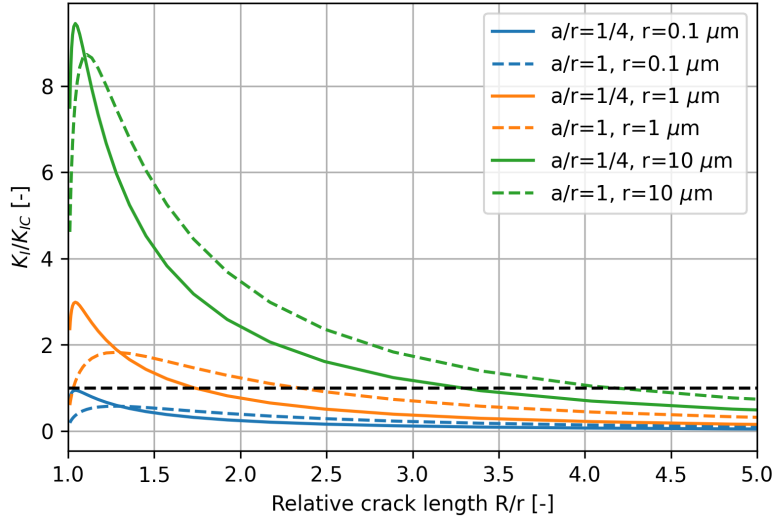
Figure 3.11: K_I/K_{IC} for a sphere and a 1/4-spheroid of different radii and a constant expansion of 100%.

damage the surrounding aggregate and thus cause a longer crack. Another important observation is that, irrespective of its shape, an inclusion of 0.1 μm size or smaller does not trigger the crack growth. This observation suggests that there is a critical value of the spheroid's radius below which no crack extension will happen for the expansion values of 100% and the chosen material properties. This critical radius lays in the range between 0.1 μm and 1 μm.

To study how the inclusion size is related to the maximum developed crack radius, an additional parametric study was performed. Its results are presented in Fig. 3.12. Two previously highlighted shapes (a sphere and a 1/4-spheroid) were increased in size from hundreds of nanometers to a few centimetres and the corresponding maximum crack radii were measured. Such a wide range was chosen for purely illustrative purposes and does not have any physical implications. The expansion values of 100% and 200% were applied. The maximum crack radius shows a power-law dependence on the inclusion size. The power law has an exponent of 4/3. The plot also shows that the same power-law exponent holds for different expansion values.

Numerical validation of the analytical solution is given in Fig. 3.13. Here, white dotted lines represent the semi-analytical predictions for three spheroids, while the coloured background comprises three numerical crack profiles. The final positions of the numerical cracks can be interpreted through the damage colours: brown corresponds to the fully damaged cohesive elements, blue to the intact ones. The rainbow-coloured regions correspond to the cohesive zones at the external crack radii. The radius of the crack next to a sphere is about 2.4 μm, which is almost equal to the analytically predicted
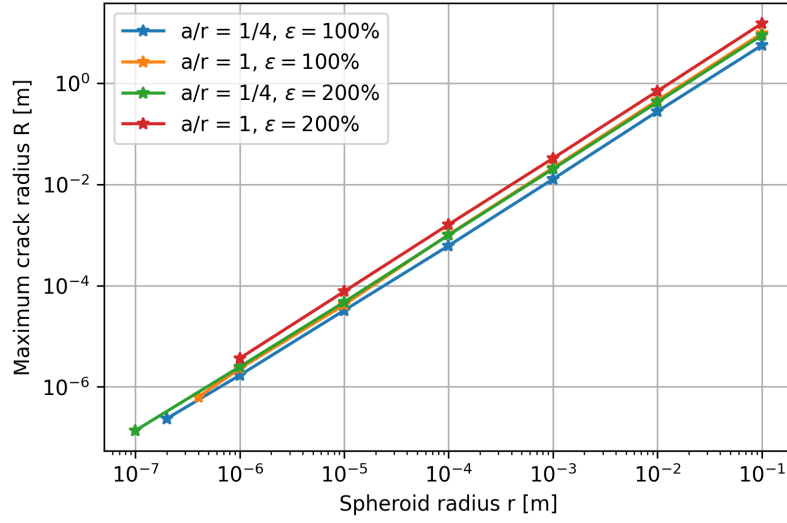
Figure 3.12: Maximum crack radii for the spheroidal inclusions of different sizes under two different expansion values. Results are plotted in log-log scale.

radius of 2.35 μm. For a 1/4-spheroid, the numerically-grown crack measures 1.6 μm, which is 8.5% smaller than the analytical value of 1.75 μm. Finally, a penny has not developed a crack and just slightly opened a rim of elements while its analytical prediction is 1.27 μm. The reason for the underdeveloped crack is believed to be the interference coming from the inclusion that is too close-by. Except for this last case, the numerical model fairly reproduces the semi-analytical predictions.

3.6 Conclusions

In this study, the potential of ASR pockets of different sizes and shapes to cause cracking of surrounding aggregates due to their volumetric increase of 100% was estimated. For this, a semi-analytical model consisting of the expanding spheroidal inclusion and a ring-shaped crack encircling it was employed. The inclusion represented a pocket of an ASR product at its mature solid state. A prerequisite for such a model was the presence of pre-existing fissures, which are abundant in rocks. First, the stresses in the matrix were computed by an analytical solution. Later, the product of the computed stresses and the specific weight function was integrated over the surface of the crack to obtain the stress intensity factor for mode I. The latter characterises the crack potential to grow. The distance at which the stress intensity factor normalised by the fracture toughness equals one rendered the maximum crack length.

The resulting solution strongly depended on the inclusion's shape and size. Flat shapes concentrated higher tensile stresses on their sharp edges. At the same time,
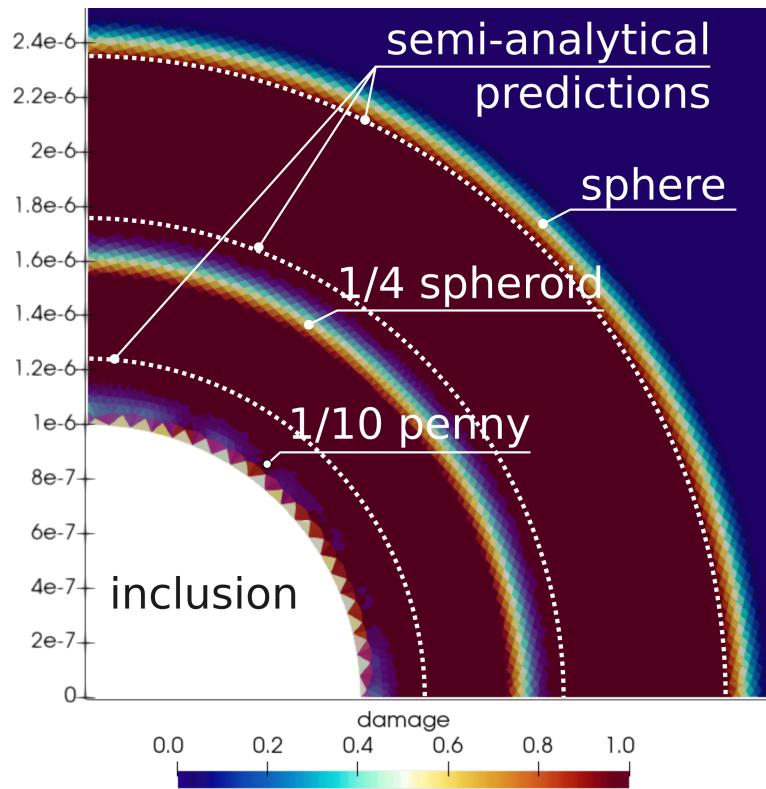
Figure 3.13: Final values of damage in the numerical simulations for three spheroids with the radius 1 μm and the expansion of 100%. The dotted lines denote the semi-analytical predictions of the maximum crack radii presented in Fig. 3.8. The dimensions are given in meters.

these stresses decayed much faster further away from the inclusion. While the stress intensity factor for mode I was the highest for an oblate spheroid with an aspect ratio of 1/4, the longest crack was caused by a spherical shape. It made the 1/4-spheroid and the sphere the two most critical shapes, either for reaching the high values of the fracture toughness or for growting the longest crack.

The size of the inclusion played a crucial role on the crack-growing potential. For an inclusion of 1 μm radius under the expansion of 100%, all the spheroidal shapes with the aspect ratios above 1/10 were likely to grow a crack. Flatter shapes would cause either short cracks ($R/r \leq 1.25$) or no crack at all. The study indicated the existence of a critical inclusion radius in the range between 0.1 μm and 1 μm below which no crack growth is expected for the current combination of K_{IC} and ε_{eig}. Consistently, an increase in the inclusion's size yielded higher values of K_I and longer cracks.

Further increase in the inclusion size, as well as in the expansion value, suggested a power-law dependence between the radius of a spheroid and the maximum crack radius. Independently of the spheroidal shape or the expansion value, the power-law exponent was about 4/3.

The results of the analytical and semi-analytical predictions were confirmed by the numerical model. For verification of the stresses in the bulk in the absence of the crack, a purely elastic finite element model was assembled. To validate the predicted maximum crack length, this model was enriched with cohesive elements. Both the elastic stresses and the crack lengths obtained numerically had a good match with the semi-analytical results.

4 Tomography-based meso-scale ASR model

After studying the origins of the ASR expansion at its finest scale, we proceed to the scale above. At the meso-scale, the ASR manifests itself in the form of expanding aggregate regions, micro-cracking, accumulation of the secondary ASR products in cracks, pores and ITZ. If in the previous chapter a single growing crack was considered, at the meso-scale multiple cracks grow simultaneously, branch and percolate, creating a complex network. Understanding how these networks evolve and their role on the macroscopic behaviour should improve the overall understanding of the ASR. For this purpose, some researchers have conducted the *post-mortem* microscopy analysis of the damaged specimens, which allowed building the damage maps of a single specimen (Ben Haha, 2006). However, reconstruction of the entire crack network was still not feasible.

Recent advances in this direction were done by the researchers from the Sinergia Sub-project V. Shakoorioskooie et al. (2021a,b) conducted an accelerated ASR experiment where the concrete blocks were regularly scanned with X-ray tomography. Addition of a contrasting agent in the concrete mixture allowed distinguishing the aggregates, cement paste, cracks and voids, and ASR products as individual phases. The resulting time-series of tomograms gave access to time-evolving deformation fields, crack maps and their occupancy by ASR products. The tomography scans were accompanied by the macroscopic measurements of expansion, stiffness, compressive and flexural strength.

The acquired data is aimed to help in understanding the processes that lead to expansion and cracking processes. Visual study of the data allows making qualitative evaluations and build hypotheses. A more quantitative approach is by using numerical models. Hypotheses on the ASR nature could be included into these models and be tested by comparing the results of the simulations with the experimental data. As the numerical models are sufficiently flexible, multiple hypotheses could be tested in a short period of time. This approach is adopted to study mechanics of the ASR in the current chapter.

The aim of the current chapter is to better understand the mechanisms behind the

meso-scale concrete expansion and cracking guided by the X-ray tomography data. This study aims to investigate how the growth of cracks and evolution of their patterns affect the macroscopic behaviour of concrete. An additional goal is to develop a numerical model that would predict realistic growth of multiple cracks while preserving the physics.

To meet these goals, a novel numerical model of the meso-scale concrete undergoing the ASR is developed. The novelty of the approach is built on the combination of the cohesive zone model with the sequential linear solution, which improves the numerical stability, and of a crack extension algorithm, which ensures the cracks' smoothness. The proposed numerical approach permits explicit representation of multiple localised thin cracks in a stable and controlled manner. Having these characteristics is crucial for the comparison with the experimental data. Two main hypotheses on the nature of the ASR loading and associated cracking are tested. First, the hypothesis of a pointwise loading of cracks by ASR products that is sufficient to lead to a realistic crack network is discussed. Second, the hypothesis that cracks elongate from the pre-existing micro-cracks, instead of continuous nucleation, is tested. The rest of the chapter is organised as follows. First, a theoretical background of the model is given in Section 4.1. In Section 4.2, the numerical implementation (e.g. mesh generation, solution scheme, crack treatment) as well as the hypotheses and modelling assumptions are discussed. Section 4.3 describes a test case that is used for the validation. The laboratory experiments and the tomography-based model are described in Section 4.4. The simulation results, their comparison with the experiments and evaluation of the hypotheses are discussed in Section 4.5. The chapter is concluded with the summary of the main findings.

4.1 Governing equations

4.1.1 Solid mechanics

The slow progression of the ASR justifies use of momentum conservation as the governing equation:

$$\nabla \cdot \boldsymbol{\sigma} = 0 \tag{4.1}$$

where $\boldsymbol{\sigma}$ is the Cauchy stress tensor. The latter is related to the infinitesimal strain tensor $\boldsymbol{\varepsilon}$ by a constitutive law:

$$\boldsymbol{\sigma} = \mathbb{C} : \boldsymbol{\varepsilon} \tag{4.2}$$

where $\mathbb{C}$ is the fourth order stiffness tensor. Following the hypothesis of small displacements, the strain tensor $\boldsymbol{\varepsilon}$ is defined as

$$\boldsymbol{\varepsilon} = \frac{1}{2} \left[\nabla \boldsymbol{u} + (\nabla \boldsymbol{u})^T \right] \tag{4.3}$$

where $\nabla \boldsymbol{u}$ is the displacement gradient vector.

4.1.2 ASR product growth

During the accelerated ASR experiments, the concrete specimens were submerged in an alkali solution. As its concentration was kept constant, an infinite supply of alkalies is assumed. Although, the amount of amorphous silica and quartz are limited by their availability within aggregates, it is sufficient to keep the reaction going during the experiment as indicated by the continuous expansion of concrete. It is assumed that the concentration of reactants is constant during the whole experiment, which implies the constant reaction rate v.

The latter leads to the linear increase in the concentration of the ASR products with time:

$$v = \frac{1}{a} \frac{\partial [\text{ASR products}]}{\partial t} \tag{4.4}$$

In the above equation, a represents the stoichiometric coefficient and [X] is the concentration of species X. As there is no clear understanding on the nature of ASR loading, proportionality between the concentration of ASR products and the internal ASR pressure is assumed.

4.1.3 Crack growth

Similar to the previous chapter, cracks are modelled by cohesive elements, the behaviour of which is postulated by a cohesive law :

$$\mathbf{T} = \frac{\partial \phi}{\partial \boldsymbol{\delta}} \tag{4.5}$$

with $\mathbf{T}$ being tractions, $\boldsymbol{\delta}$ the effective displacements and ϕ the cohesive energy density. In this study, a simplified version of the linear irreversible cohesive law by Camacho and Ortiz (Camacho and Ortiz, 1996) is adopted. The cohesive law is illustrated in Fig. 4.1. While a single crack loaded by the internal ASR pressure would open in pure tension, the interaction between multiple cracks could provoke their closure and evolution of frictional forces. Friction is omitted by equating the effective cohesive displacement and the normal component of the opening $\delta = \Delta_n$. Although this is done to improve the solution scheme, it ignores an important mechanical aspect and should be addressed in the future work. The tractions are computed as follows:

$$\mathbf{T}(\delta, \delta_{\max}) = \begin{cases} \sigma_t \left(1 - \frac{\delta}{\delta_c}\right) \mathbf{n} & \text{for } \delta = \delta_{\max} \\ \frac{T_{\max}}{\delta_{\max}} \mathbf{n} & \text{for } \delta < \delta_{\max} \\ \alpha_p \delta & \text{for } \delta < 0 \\ 0 & \text{for } \delta \geq 0 \text{ and } \delta_{\max} \geq \delta_c \end{cases} \tag{4.6}$$
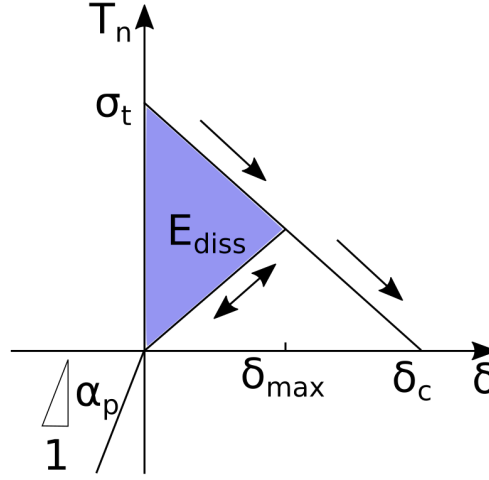
Figure 4.1: Illustration of the linear cohesive law.

where $\mathbf{n}$ is the unity vector normal to the crack surface, σ_t is the local material strength and δ_c is the critical opening at which full decohesion happens. To avoid interpenetration of crack surfaces, a simple penalty contact law with the penalty parameter α_p is employed. Dissipated energy can be defined as

$$E_{\text{diss}} = \frac{1}{2}\sigma_t\delta_{\max} \tag{4.7}$$

The equality $E_{\text{diss}} = G_C$ is established upon full decohesion. The critical opening δ_c is defined by the fracture energy G_C and the insertion stress σ_t as

$$\delta_c = 2G_C/\sigma_t \tag{4.8}$$

4.2 Numerical implementation

Similar to the model described in the previous chapter, the finite element method was employed. Its theory was briefly summarised in Section 3.4 and is not repeated here.

4.2.1 Crack front treatment

Cracks are resolved by zero-thickness cohesive elements exhibiting traction-separation law from Eq. (4.6). They are inserted continuously during the simulation (extrinsic approach of Camacho and Ortiz (1996)). A cohesive element is introduced at the place of a facet that complies with the insertion criteria. The latter is based on stress: the normal tensile traction on a facet T_n has to overcome the local material strength σ_t.

The cohesive zone of concrete is few-centimetres wide. This is larger than the size
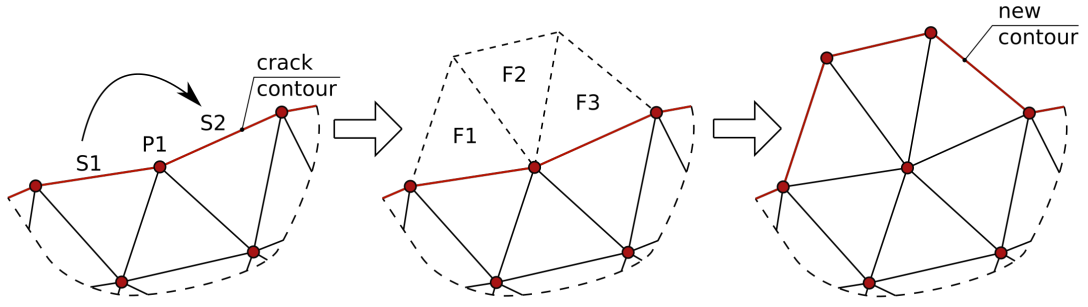
Figure 4.2: Illustration of the crack insertion procedure. At each point $P1$ of a crack contour, two neighbouring segments $S1$ and $S2$ are identified. The shortest facet path from $S1$ to $S2$ is searched for. The path consisting of the facets $F1$, $F2$ and $F3$ complies with the insertion and the smoothness criteria. Cohesive elements are inserted at the positions of $F1$, $F2$ and $F3$ and the crack contour is updated.

of the tomograms used for the model construction. Such a large size causes diffused micro-cracking, which is characterised by some weakly-opened micro-cracks spread all over the specimen. The tomography data used in this work distinguishes cracks after certain width while the features thinner than the tomography resolution could not be detected. This discards most of the thin crack of nano- to micrometre width expected in the diffused cracking regime.

To make the numerical model develop only localised cracks similar to the ones observed in the tomograms, three additional measures were taken. First, to reduce the cohesive zone size, the value of the tensile strength σ_t was taken one order of magnitude higher than the ones reported in the literature (e.g. Alehossein and Boland, 2004). The second measure was to scatter the tensile strength σ_t according to a statistically representative distribution. This measure aims to represent the natural micro-fissures which facilitate crack propagation. Details on the specific choice of the material properties and the distribution parameters are given in Section 4.4.

The third measure called to develop localised cracks is the enforcement of the smooth crack extension from its contour. Only the cohesive elements forming a continuous path between two neighbouring segments of a crack contour could be inserted. The procedure for crack extension is illustrated in Fig. 4.2. It can be split into three steps. The first one is to pick a node on the current crack contour (P1) and define a pair of neighbouring contour segments S1 and S2. The next step is to identify the shortest path from S1 to S2 consisting of facets containing the node P1. The final step is to verify the insertion criteria and the smoothness of the loop. The latter is ensured by discarding the facets forming sharp angles with any of their loop neighbours. Given that the facets in the loop comply with all the necessary conditions, cohesive elements are inserted and the crack contour is updated. The initial cracks are necessary as a starting point for the future crack growth. For this purpose, closed loops of cohesive elements are randomly

placed within the aggregate material during the mesh generation. Later, these cohesive loops are used for the load application. The procedures of the cracks pre-insertion and extension are given in Algorithms 1 and 2, correspondingly.

Algorithm 1 Insertion of N pre-existing cracks

1: **procedure** INSERTCRACKS(N)
2:     Create an empty set of visited nodes $\mathbf{U}$
3:     **while** number of inserted cracks $< N$
4:         Randomly pick a node P_i within the aggregate material
5:         Create an empty list of the crack facets $\mathbf{V}$
6:         **if** node P_i already belongs to a crack
7:             Add node P_i to the set $\mathbf{U}$
8:             **go to** 4
9:         Randomly pick a segment S_i and a facet F_i adjacent to node P_i
10:        Define segment S_i as a starting one S_0
11:        Add facet F_i to $\mathbf{V}$
12:        **repeat**
13:            Consider the last facet F_l from $\mathbf{V}$
14:            Identify its bordering segment S_b
15:            Find a facet containing S_b and forming the largest obtuse angle with F_l
16:            Add the identified facet to $\mathbf{V}$
17:        **until** the identified facet contains the starting segment S_0
18:        **if** a closed loop was not identified
19:            **go to** 4
20:        Insert cohesive elements according to the list $\mathbf{V}$

All these measures were taken to produce localised smooth cracks similar to what is qualitatively observed in the ASR experiments. Cracks merging and branching remains possible within this workflow. By adopting this modelling approach, the hypothesis that the ASR cracks start from the pre-existing micro-flaws and later elongate from their contours is made. This hypothesis eliminates the possibility for new cracks to nucleate. Moreover, it discards the development of cracks that are not loaded by the ASR products from inside (e.g. shear cracks).

4.2.2 Parallelism

The efficient parallel implementation of an FE model with dynamic insertion of cohesive elements was presented by Vocialta et al. (2017). Efficient parallel execution of the model was enabled by the message passing interface (MPI). In contrast to that model, where cohesive elements could be inserted everywhere, in the current study cracks are only allowed to elongate. Therefore, additional treatment is required when a crack is crossing the border between two domains handled by different processors. In such a case, the same contour segments of a crack could be handled by both processors simultaneously.

Algorithm 2 Crack extension algorithm

1: **procedure** EXTENDEXISTINGCRACKS
2:     **for** every crack
3:         **for** every node P_i of the crack's contour
4:             Create an undirectional graph $\mathbb{G}$ ▷ Using Boost Graph Library
5:             Find two segments S_1 and S_2 of the contour adjacent to node P_i
6:             **for** facet F_j containing node P_i ▷ Excepting the facets of the crack
7:                 Check the insertion criteria
8:                 **if** $t_{n,j} \geq \sigma_{t,j}$
9:                     Find two segments S_k and S_l of facet F_l that share node P_i
10:                   Add segments S_k and S_j as vertices to $\mathbb{G}$
11:                   Add facet F_l as a corresponding edge to $\mathbb{G}$
12:             Within $\mathbb{G}$, compute the shortest facet path between vertices S_1 and S_2
13:             **if** path does not exist
14:                 move to the next contour node P_{i+1}
15:             **for** each pair of two consequent facets of the path
16:                 **if** angle between two facets is sharp
17:                     Delete problematic facet from $\mathbb{G}$
18:                     **go to** 12
19:             Insert cohesive elements at the identified path

---

As each processor decides independently whether to extend a crack, there is a possibility of artificial crack branching. To avoid this, the stress communication between processors is established during each cohesive insertion event. During these communications, two neighbouring processors decide whose bordering facets are the most stressed.

4.2.3 ASR loading

The internal ASR loading is applied at the nodes of the pre-existing cracks in aggregates (see Fig. 4.3). Loading applied at a single crack is represented by a pair of splitting forces with equal amplitudes but opposite directions. The loading is applied at the duplicated nodes of cohesive elements. Even when the crack extends and more nodes are duplicated, loading is kept at the original nodes (see Fig. 4.3b). The orientation of the forces is based on the normals of associated cohesive elements. The amplitude of the loading is growing linearly with time in accord with Section 4.1.2:

$$F_{n+1} = F_n + \dot{F}\Delta t \tag{4.9}$$

where $\dot{F}$ is the constant loading increase rate, F_n and F_{n+1} are the loading values at two subsequent steps, and Δt is the time step. The equation above does not take into account the temperature as the reference experiments were conducted under constant environmental conditions. The linear loading increase is a modelling assumption. Any other loading profile could be used based on the experimental evidence.
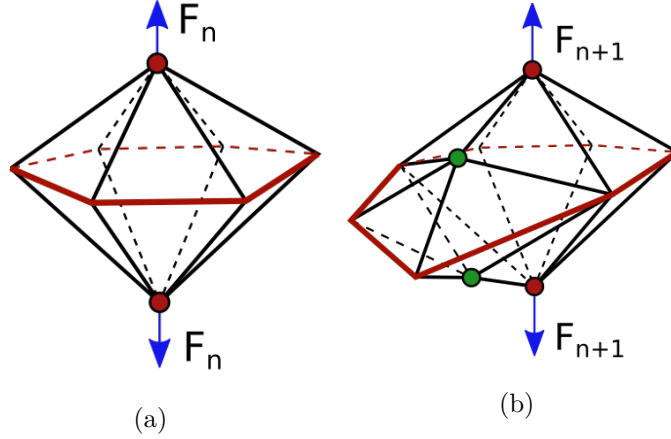
Figure 4.3: Illustration of the loading applied at an ASR site. a) Loading at the initial configuration with a single duplicated node pair. b) Loading of the extended crack with several duplicated node pairs. In both cases, the loading is applied at the initial duplicated node pair only.

4.2.4 Sequential solution

Computation of failure in brittle and quasi-brittle materials by means of the classical non-linear finite element method is often prone to numerical instabilities. In particular, for problems characterised by the simultaneous propagation of multiple cracks, as in the case of the ASR, the solution of the system is likely to diverge and hence a completely different approach becomes necessary.

This problem is circumvented by the algorithmic elimination of the non-linearity in the constitutive behaviour. The latter is done by linearizing the cohesive law with a treatment similar to the sequentially linear analysis (SLA) proposed by Rots (2001); Rots and Invernizzi (2004); Rots et al. (2008). The idea of this method is to replace the incremental solution of the strain-softening behaviour by a sequence of linear elastic steps with the step-wise reduced stiffness. The loading is not applied all at once, but in small increments that bring a single element to its failure envelope. In this way, negative tangent stiffness is avoided and the convergence check becomes unnecessary. The SLA procedure is illustrated in Fig. 4.4. Application of SLA to interfacial elements with friction was previously demonstrated by Pari et al. (2021).

Cuba Ramos et al. (2018) have shown that the use of SLA allows capturing the complex crack networks inside the aggregates and the mortar. The load increments are chosen in such a way that for each imposed load increment, exactly one integration point (IP) undergoes softening and all other IPs remain below their failure criterion. The development of this method has been inspired by lattice models, in which the continuum is replaced by a lattice of beams. In lattice models, divergence problems do not occur because the solution is obtained from a sequence of linear analyses. In every step of the
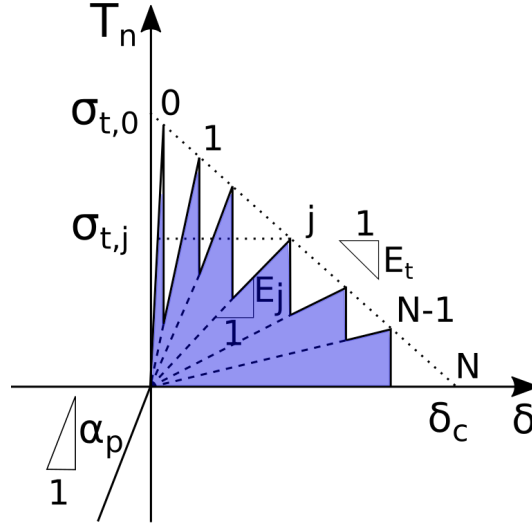
Figure 4.4: Illustration of the sequentially linear analysis.

analysis, the beam with the highest load is detected and subsequently removed. The SLA transfers this approach to the continuum modelling. Consequently, in every step, the IP with the highest load is detected, and if the damage criterion is satisfied, the stiffness and strength at this IP are reduced according to the current damage value d_i, which is defined as

$$d_i = 1 - \frac{1}{a^i} \tag{4.10}$$

where the empirical reduction constant a, is brought to the power i, which is the number of the reduction step. In the following simulations, $a = 2$ and $i_{max} = 10$, which are chosen as a compromise between the computational time and the high resolution of the strain-softening curve.

Resolving each damaging event brings excessive computational cost. In order to overcome this complication and speed up the computations, the classical SLA scheme was altered by two modifications. First, the loading increase was fixed to a constant sufficiently small value that is still reasonable from the computational time perspective. By the second modification, all the IPs stressed above their tensile limit are permitted to be damaged within one iteration. The summary on the adopted workflow is given in Algorithm 3.

Compared to the lattice models, an advantage of SLA is that the concept of strength, elasticity and fracture energy remain meaningful at the macro-scale. As SLA does not use the tangent stiffness, numerical instabilities do not arise and, during the analysis, the equilibrium path of the material degradation is always followed. Another advantage is that due to the controlled increase of damage, jumps over the structural response do not occur. However, the major drawback of this method is its high computational cost. It results from the fact that a new solution has to be computed after each damaging

---

Algorithm 3 Linearisation of the cohesive law

1: **for** every time step t_j
2:     **while** cohesive elements are damaged
3:         Apply the full load $\mathbf{F} = \mathbf{F}(t_j)$
4:         Obtain the elastic solution $\mathbf{u}$
5:         **for** every cohesive element k
6:             Compute normal traction T_n
7:             Note its current reduction step i and tensile strength $\sigma_{t,i}$
8:             **if** $T_n \geq \sigma_{t,i}$
9:                 Damage the cohesive element k and update its properties:

$\bullet$ Reduction step : $i \mathrel{+}= 1$

$\bullet$ Damage : $d_i = 1 - \dfrac{1}{a^i}$

$\bullet$ Secant stiffness : $E_i = E_0(1 - d_i)$

$\bullet$ Tensile strength : $\sigma_{t,i} = \delta_c E_i \dfrac{E_t}{E_i + E_t}$

with $E_t = \dfrac{\sigma_{t,0}}{\delta_c - \sigma_{t,0}/E_0}$

---

event. Consequently, the total number of computations is significantly larger than in a non-linear finite element approach. A more detailed description of the application of SLA to the meso-scale ASR problem can be found in (Cuba Ramos, 2017).

4.3   Model validation

The proposed numerical approach is validated by matching a well-known analytical solution. The validation problem comprises a penny-shaped crack in the infinite medium loaded in Mode I by a pair of equal, oppositely-oriented forces F applied at the crack centre, as depicted in Fig. 4.5. Such setup was chosen due to its similarity to the modelled ASR problem. The solution to this problem based on linear elastic fracture mechanics (LEFM) can be found in classical cracks handbooks (e.g. Tada et al., 2000). The stress intensity factor K_I is

$$K_I = \frac{F}{(\pi a)^{3/2}} \tag{4.11}$$

where F is the force magnitude and a is the crack radius. Given the constant loading F, as the crack becomes larger, the stress intensity at the crack tip reduces and K_I is subject to power-law decay. The value of a at which K_I becomes equal to the material toughness K_{Ic} corresponds to the maximum crack radius for this configuration. It can be computed as

$$a = \frac{\sqrt[1.5]{F/K_{Ic}}}{\pi} \tag{4.12}$$
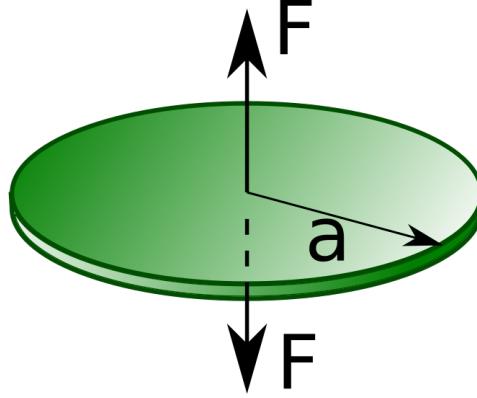
Figure 4.5: Validation case of a penny-shaped crack loaded by a pair of forces.

Model parameter	Value
Domain sizes D, W, H [µm]	20
Loading $F/4$ [Pa]	$1.45 \cdot 10^{-2}$
Fracture toughness K_{Ic} [MPa$\sqrt{\text{m}}$]	2*
Tensile strength σ_t [GPa]	4.5
Bulk Young's modulus E [GPa]	60
Bulk Poisson's ratio ν [-]	0.3
Initial crack radius a_0 [µm]	1
Predicted crack radius a [µm]	3
Cohesive zone size l_z [µm]	0.2
Mesh size along the crack plane h [µm]	$0.03/0.05^{\dagger}$

Table 4.1: Model parameters and material properties used in the validation case. *Taken from (Alehossein and Boland, 2004). †Two different mesh sizes used to study the convergence.

The geometry of the numerical model developed for comparison with the analytical solution is depicted in Fig. 4.6. It comprises one quarter of the full space and the crack. The amplitude of the load applied in the model equals to one quarter of the one in the analytical solution. An initial crack of a radius a_0 is pre-inserted (coloured in red). Application of the load $F/4$ should result in the crack extension up to its final radius a predicted by Eq. (4.12). Crack growth is restricted to the horizontal middle plane (coloured in green). Symmetry over the two section planes is established by applying zero out-of-plane displacements. To minimise the boundary effect, height, width and depth of the model are sufficiently large. The dimensions of the model are given in Table 4.1.

Similar to the previous chapter, a high value of $\sigma_t = 4.5$ GPa was chosen to make the size of the cohesive zone significantly smaller than the model and, by this, approach the LEFM solution. Material properties are given in Table 4.1.
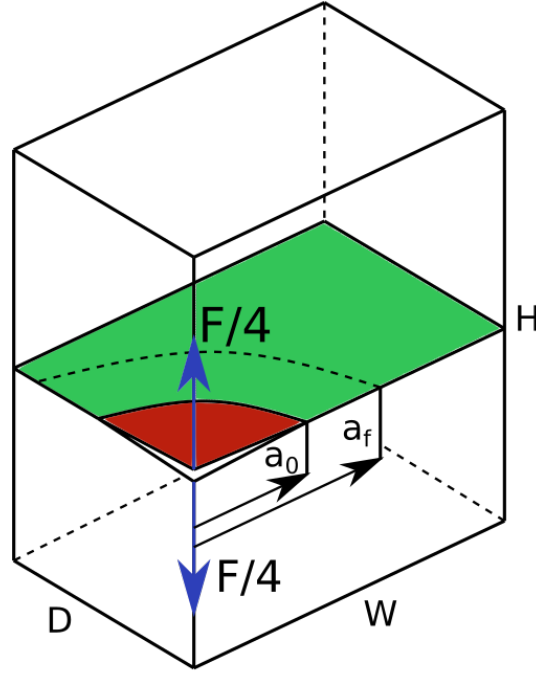
Figure 4.6: Illustration of the numerical model used for the validation.

Comparison of the numerical solution to the analytical prediction is plotted in Fig. 4.7. While the black dotted line represents the analytical prediction, the coloured background defines the numerical cracks. The final positions of the numerical cracks are interpreted through the damage colours: brown corresponds to the fully damaged cohesive elements, blue is for the intact ones. The rainbow-coloured regions correspond to the cohesive zones at the external crack radii. The numerical solutions are obtained for two meshes of different density along the crack plane. In both cases, the results are in a fair agreement with the analytical prediction. While the densest mesh with 0.03 μm element size matches predicted a_f exactly, a coarser mesh ($h = 0.05$ μm) underestimates it by 6.7% which is considered satisfactory.

More insights into the behaviour of the proposed numerical scheme are obtained from the dissipated energy plot in Fig. 4.8. Two families of curves are presented: the curved lines are obtained by the proposed algorithm; the smooth ones are obtained by using the intrinsic cohesive elements approach used in the previous chapter. The latter implies the pre-insertion of all the cohesive elements during mesh generation. The advantage of this approach is the permanent connectivity between elements, which simplifies the solution process. Its drawback is the alteration of the homogenised properties of the cohesive-bulk material mix. The set of curves obtained by the intrinsic method is treated as a benchmark. In addition to the different mesh sizes (0.03 and 0.05 μm), the maximum number of stiffness reductions N is varied between 10 and 20 times (Fig. 4.4 and Algorithm 3).
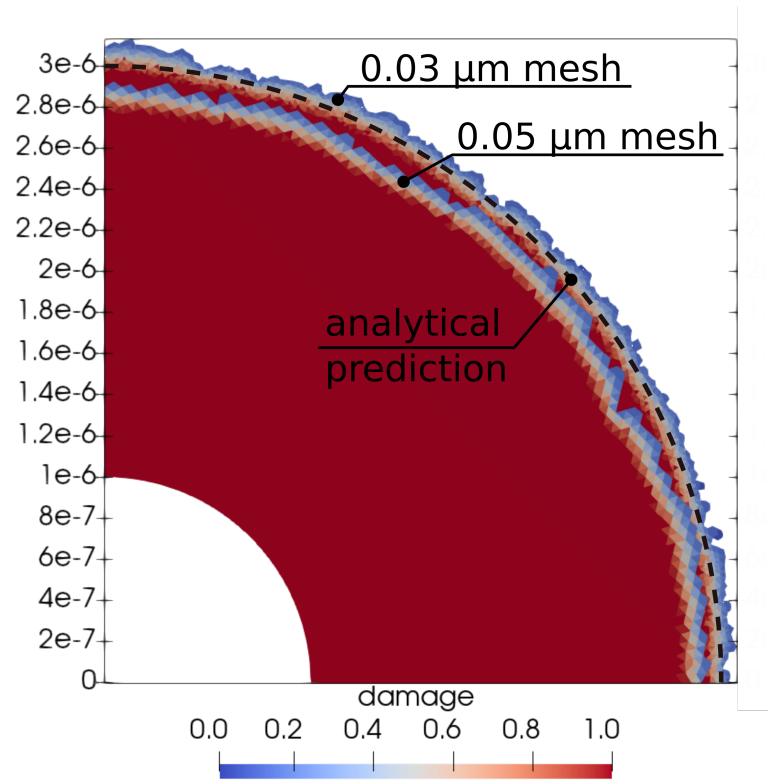
Figure 4.7: Numerical cracks for two different meshes in comparison with the analytical prediction.
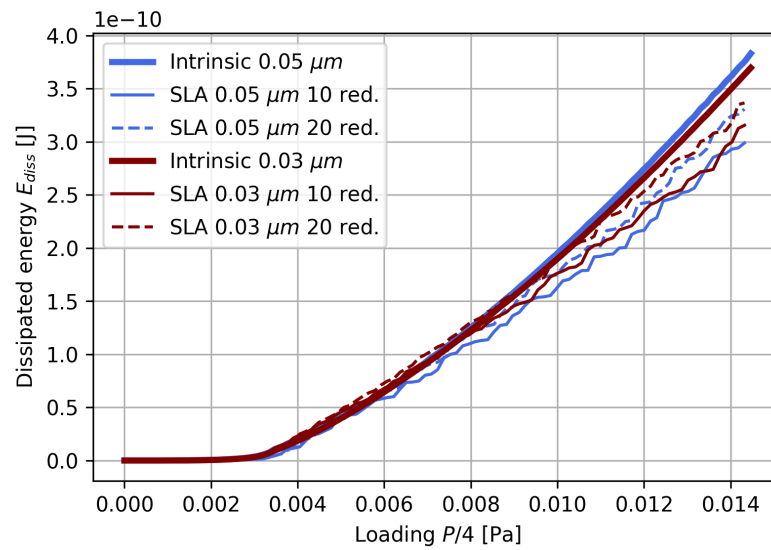
Figure 4.8: Energy dissipation due to the increase in the applied load in the validation study.

Both the mesh refinement and the increase in *N* brings the curves closer to the benchmark. Further mesh refinement and increase in *N* should lead to convergence of the numerical solution. On the other hand, it also extends the computational time. Thus, the final choice of the mesh size and the number of stiffness reductions is a trade-off between model's efficiency and precision.

The dissipated energy serves as a proxy for the crack area. In case of SLA, the energy is not growing monotonously, and so is the crack. Instead, it is advancing in small isles - loops of facets complying with the insertion criteria. This criteria is not met for all the facets in the loop at once, thus a certain time delay is introduced. Similar discontinuous crack growth is also observed experimentally (see (Schmittbuhl and Måløy, 1997)).

4.4   Tomography-based model

The final model used to investigate the crack growth due to the ASR is based on the tomography data obtained by Shakoorioskooie (2021). This data consists of the time sequence of the X-ray tomograms of the ASR-affected concrete specimens. The specimens were prisms of $24.6\,\mathrm{mm} \times 24.6\,\mathrm{mm} \times 100\,\mathrm{mm}$ along the *X*-, *Y*- and *Z*-axes, correspondingly. Starting from the intact state, the tomograms capture the evolution of ASR cracks and the accumulation of ASR products. The current set of scans covers 405 days. The spatial resolution of the tomograms is about $35\,\mu\mathrm{m}$. A central part of the specimen underwent tomography. The tomograms' size is $24.6\,\mathrm{mm} \times 24.6\,\mathrm{mm} \times 24.6\,\mathrm{mm}$. Aggregates, cement paste and pores were segmented due to the difference in voxel values. Cracks and ASR-products were also segmented into independent volumes. This allowed the authors to measure volumes of the cracks and the ASR products and build a statistical database. It includes the volume distributions, local thicknesses and orientations of crack and ASR pockets. Moreover, such macroscopic parameters as the relative length changes, quasi-static Young's modulus, flexural and compressive strength were measured.

The tomograms of the intact concrete were used to build a FE mesh. An algorithm to generate an irregular tetrahedron mesh out of a stack of 2D cross-sections from the tomographed volume was developed. First, it builds a dummy irregular mesh by the Gmsh software (Geuzaine and Remacle, 2009) with the final dimensions of the model. Then, the tomography-based material indexes are assigned to the elements of this mesh. Coordinates of each element's barycentre are used to find a corresponding voxel in the tomogram and choose its material index. Additional smoothing algorithm is applied to remove material isles - single finite elements that have one or no neighbouring element of the same material.

The resolution of the model is $0.2\,\mathrm{mm}$. To reduce the computation load, only a quarter of the full tomogram is modelled. Thus, the final model size is $12.3\,\mathrm{mm} \times$
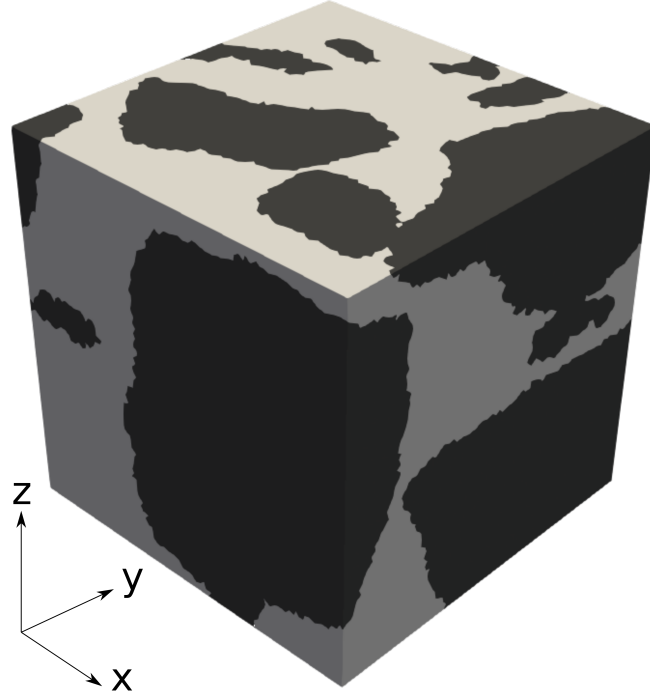
Figure 4.9: Tomography-based FE mesh of concrete. Dark colour denotes the aggregate material and light the cement paste.

12.3 mm × 12.3 mm. The mesh distinguishes between aggregates, cement paste and ITZ, and accounts for internal air voids. The ITZ is defined by the facets shared by the solid elements belonging to aggregates and cement paste. The concrete part is encircled by a layer of a non-damageable buffer to mimic surrounding material. The internal part of the mesh (discarding the buffer) is depicted in Fig. 4.9.

Properties of the two elastic solid materials and three cohesive ones are given in Table 4.2. The values of the tensile strength σ_t are one order of magnitude higher than the ones obtained in the macro-scale experiments (e.g. Alehossein and Boland, 2004). Assigning a higher tensile strength allows constraining the cohesive zone within the specimen and avoid diffused cracking. Natural defects present in all materials are reproduced by spreading the tensile strength σ_t according to a Weibull distribution with the following cumulative distribution function

$$F(\sigma_t) = 1 - e^{\left(-\left(\frac{\sigma_t - \sigma_{t,min}}{\lambda}\right)^k\right)} \tag{4.13}$$

where $\sigma_{t,min}$ is the material quasi-static failure strength, k is the Weibull shape parameter, and λ is the scale parameter. The adopted values are given in Table 4.2.

Material name / parameter	Aggregates	Cement paste	Aggregates (cohesive)	Cement paste (cohesive)	ITZ
Young's modulus E [GPa]	59	25	-	-	-
Poisson's ratio ν [-]	0.2	0.2	-	-	-
Fracture energy G_c [J/m^2]	-	-	66.7*	13†	10
Quasi-static tensile strength $\sigma_{t,min}$ [MPa]	-	-	70	20	20
Weibull shape parameter k [-]	-	-	5	5	5
Scale parameter λ [MPa]	-	-	20	6	6

Table 4.2: Material parameters for the tomography-based simulation. *Taken from (Alehossein and Boland, 2004). †Taken from (Xu and Zhu, 2009).

Parameter / scenario	1	2	3	4	5
Loading rate $\dot{F}$ [N/day]	25	50	12.5	6.25	25
Number of ASR sites	14	7	28	56	14
Loading pressure along z-axis [MPa]	-	-	-	-	-5

Table 4.3: Scenarios of the numerical simulations of the tomography-based model.

4.5   Results

Deformations of the numerical and laboratory specimens are shown in Fig. 4.10. The black lines with error bars are the experimental data. The experimental prisms exhibit initial shrinkage during the first 60 days possibly caused by drying. Shrinkage is followed by the gradual expansion, the rate of which reduces after 250 days. The strain values after 100 days become anisotropic: the expansion along the short prism side X is larger than in the other two directions. This difference could be attributed to different humidity and alkalinity profiles along each direction as well as to the casting process. Discussion on the source of anisotropy in the experimental data is out of the scope.

Numerical simulations were performed according to several scenarios. The results presented in Fig. 4.10 are obtained by the model calibration according to Scenario 1 in Table 4.3. The coloured lines represent mean values and the shaded areas define the range of the obtained results. Three simulations with different initial positions of ASR sites are performed. In this way, randomness of the cracking process is taken into account and statistical representativeness of the numerical output is improved. The abrupt jumps in several curves stem from the simulations that did finalise due to non-convergence. The reason for this is the stiffness alteration between a compressed and tensioned states of cohesive elements. Therefore, when the cracks become abundant, such issue becomes more prominent and hinders the numerical convergence.

The numerical model does not have a preferential direction, thus it demonstrates
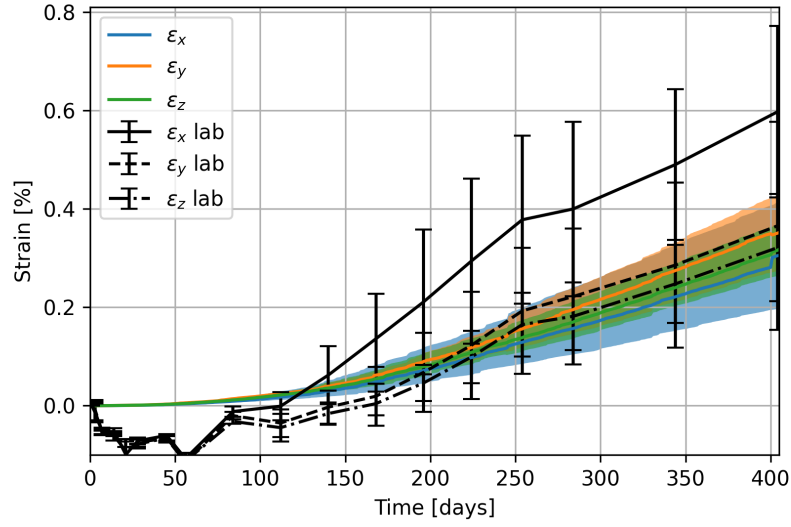
Figure 4.10: Macroscopic deformation of the numerical and laboratory specimens. Solid coloured lines represent mean values from several simulations, and the shaded areas define the range of the obtained results. The black lines and error bars represent the laboratory measurements. The experimental data is taken from (Shakoorioskooie, 2021).

similar expansion values in all three directions. Due to the limited number of simulations, the mean values are far from being statistically representative. If the number of simulations with different concrete meso-structures is much higher, the mean expansions in all three directions shall equalise and the curves shall overlap. The numerical expansion rate is at its maximum in the beginning of the simulation and gradually decreases towards its end, making the expansion almost linear in the last 100 days. Both the absolute values and their increase rates of the numerical expansion fall into the range of values defined by the experiments.

Fig. 4.11 presents two crack distribution maps, one coming from the experiments of Shakoorioskooie (2021) and another one from the simulation. Different colours correspond to the crack numbers associated with the initial numbering of the ASR site. The tomogram level of details is high, which allows having more fine-scale features. The obtained numerical cracks map is qualitatively similar to the experimental cracks distribution in space, as well as in terms of crack shapes and curvatures.

Fig. 4.12a plots the crack volume ratios in different phases. The volume ratio $\tilde{V}_{cracks}$ is computed as

$$\tilde{V}_{cracks,i}(t_j) = \frac{V_{cracks,i}(t_j)}{V_{model}(t_j)}$$

where $V_{cracks,i}(t_j)$ is the volume of cracks at the time step j, $V_{model}(t_j)$ is the current volume of the model without the surrounding buffer, and i defines the crack phase (i.e.
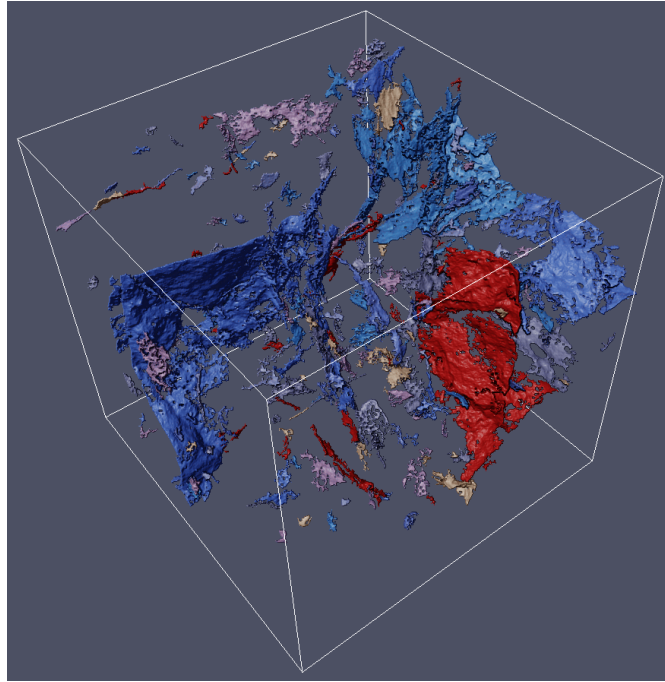
(a)
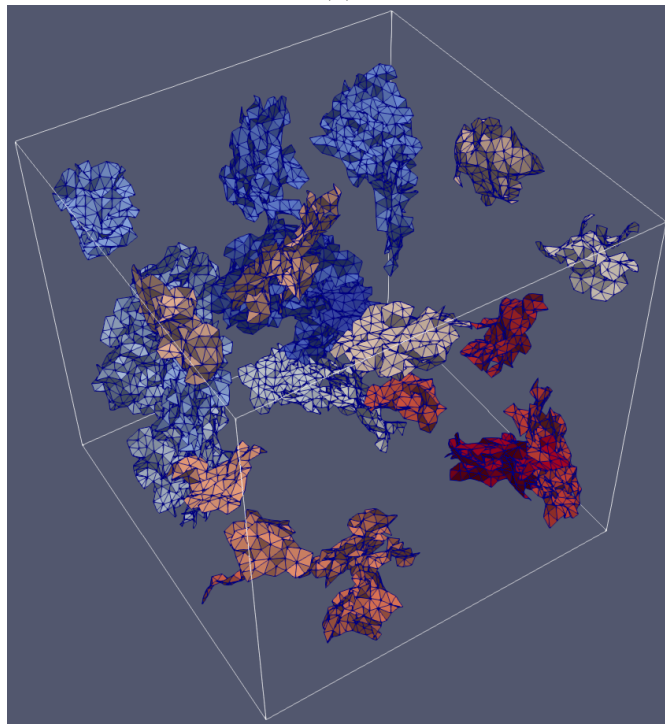
(b)

Figure 4.11: Qualitative comparison between a typical crack map from a) the experiment and b) the numerical simulation. Both snapshots were taken in the middle of the experiment/simulation duration. Tomography data is taken from (Shakoorioskooie, 2021).
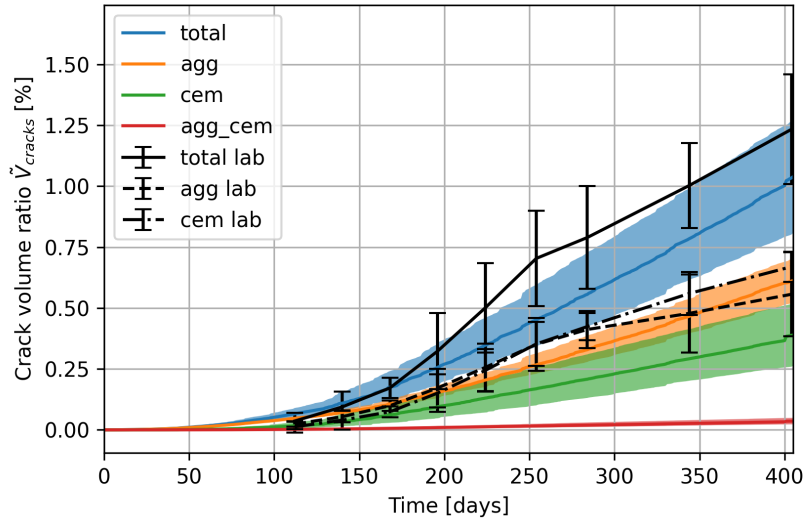
(a)
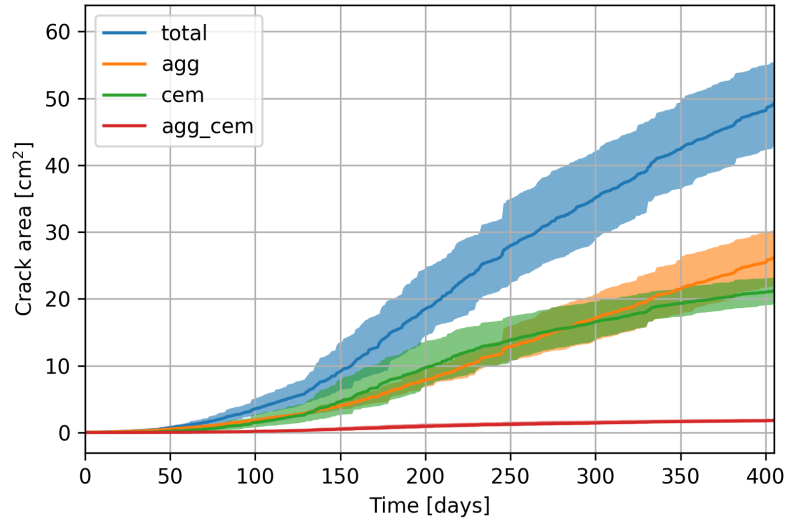
(b)

Figure 4.12: a) Numerical crack-volume ratios and b) areas by different phases (i.e. total volume, aggregates, cement paste and ITZ) compared to the experimental results. Solid coloured lines represent mean values from several simulations, and the shaded areas denote the range of the obtained results. The experimental crack volumes are taken from (Shakoorioskooie, 2021).

total volume, aggregates, cement paste, and ITZ). According to the experiments, nearly the same volume of cracks is present in the aggregates and the cement paste at any time. Their maximum total volume arrives to $\approx 1.2\%$ at 405 days. While the numerical total crack volume is in a fair agreement with its experimental counterpart, the aggregate crack volume is slightly higher than the one in the cement paste.

The simulated crack areas per phase are plotted in Fig. 4.12b. These curves help to interpret the numerical results from the previous plot. Unlike the crack volume that includes the crack extension and opening, the crack area takes into consideration only its elongation. Therefore, the area could be used as an indicator for the newly opened cracks. All the curves in Fig. 4.12b have characteristic asymptotic shape which suggests that the propagation of new cracks is slowing down. Further crack growth is hindered by the non-damageable buffer surrounding the specimen. In the absence of such a buffer, crack growth would be halted by reaching the free external surface. Detailed comparison between the computed crack areas and the experimental ones is complicated due to the spatial resolution of the X-ray tomography. Even though the model can predict thin cracks with few-nanometre width, a CT scanner is not able to resolve such small features.

Although the numerical crack areas in Fig. 4.12b are slowly approaching their asymptotes, the volumes in Fig. 4.12a continue to increase linearly, which is caused by linear increase in the internal loading. Similar phenomenon could also happen in the experimental samples: initially intensive crack growth could reduce due to the crack percolation and reaching the borders. Further volume increase would continue solely due to wider opening of the existing cracks and accumulation of ASR products inside.

Fair agreement between the numerical results and the experimental data suggests that the two made hypotheses are sufficient to reproduce the realistic crack pattern and have similar macroscopic expansion. It does not however disprove different loading mechanisms, e.g. distributed loading along the whole crack area. Neither does it disprove the possibility of nucleation of cracks that are not pressurised from inside (e.g. due to shear stresses, differential expansion of aggregates or even chemical crack formation).

4.5.1   Sensitivity study

A sensitivity study was performed in order to understand the influence of the initial ASR sites number on the macroscopic behaviour. Three additional scenarios with half, double and quadruple number of ASR sites (see Scenarios 2, 3 and 4 in Table 4.3) were simulated. To preserve the global load, the loading rate of a single ASR site was scaled with respect to the original one. Each scenario was simulated three to four times with different random positions of initial ASR cracks. The results of the sensitivity study are presented in Figs. 4.13 and 4.14. As it has been previously seen, the difference between the numerical strains in three directions is small for the free-expansion conditions. This
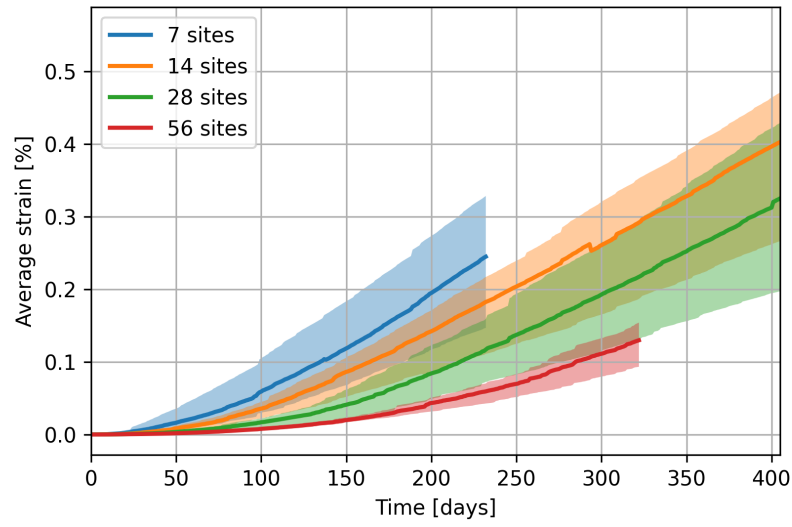
Figure 4.13: Strains averaged over three directions in simulations with different number of the initial ASR sites. The total loading was preserved by scaling the individual force values. Solid lines represent the mean values and shaded areas the range of the output.
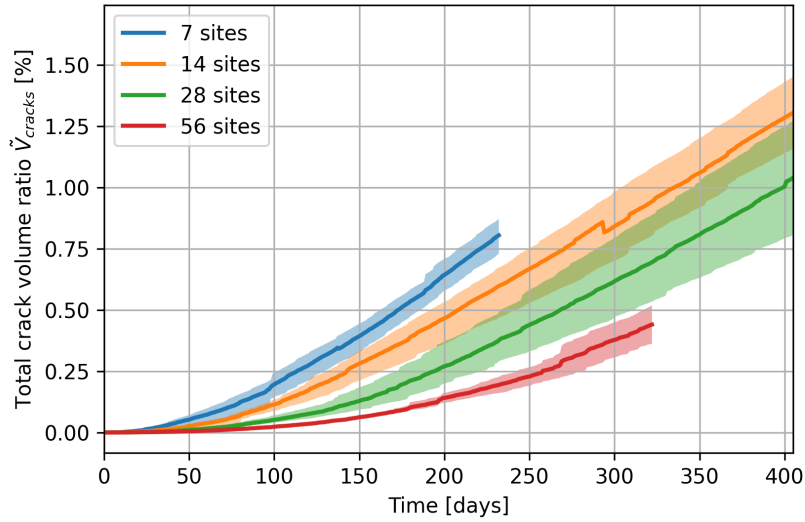
Figure 4.14: Averaged total crack volume ratios in the simulations with different number of the initial ASR sites.

fact permitted us to average strains in all three directions and present a single averaged value per scenario in Fig. 4.13. None of the simulations with 7 and 56 initial ASR sites could reach the final loading due to the convergence issue.

A surprising outcome of this study is the inequality in the final deformations and crack volumes for different number of the initial ASR sites. Expansion of the specimens with more ASR sites starts later and has lower rates, and so does the total crack volumes. It appears that the few initial cracks with high loads are more efficient in causing the ASR expansion and cracks opening. This behaviour is associated to the two main contributors. First, the high loads applied at the few cracks generate higher stress intensities and lead to early crack growth and macroscopic expansion. Second, the inequality of the final crack volumes is attributed to the differences in the crack networks. A few cracks percolate less with their neighbours and the crack pattern remains localised. In contrast, the numerous initial cracks start to percolate early and result in a diffused crack pattern. Application of the same load within a specimen with the few localised cracks and with a diffused crack network has different effects. In the first case, the opening of several cracks will be directly transmitted to the specimen's extremities. In the diffused cracking regime, the loading is partially accommodated by the relative movements of multiple crack segments of the network.

4.5.2 Uniaxial loading

Another study was called to investigate the effect of the uniaxial loading on the crack growth, orientation and percolation. An additional goal was to verify the capacity of the developed model to realistically simulate the loaded ASR experiments. A single simulation of a loaded sample was performed according to Scenario 5 in Table 4.3. The loading was homogeneously applied at the top of the concrete specimen on the border with the surrounding buffer. The loading was applied along the z-axis. Positions of the pre-existing ASR cracks were repeating the ones from the free-expansion simulation. As the experimental campaign did not include the loaded samples, the loading pressure of 5 MPa was chosen rather arbitrarily. A similar value was applied in the ASR experiments by Larive (1997) and Gautam and Panesar (2016). Their results showed reduction of the ASR-related expansion along the loaded direction by $30 - 70\%$ and increase in the perpendicular directions by $10 - 40\%$. All these numbers are approximate and do not take into account the experimental error margins. Moreover, Larive (1997) mentioned that the cracks in the loaded cases are wider than under the free-expansion: the average width of $0.2 - 0.3$ mm under the load and $0.05 - 0.1$ mm in the free samples.

To visualise the results, in Fig. 4.15 crack maps of the free and loaded specimens are plotted. These snapshots were done after 120 days of the simulation time. At the later stages, crack networks spread over the specimens, which complicates the visual perception. An arrow in Fig. 4.15b denotes the loading direction. By comparing the two

(a)   (b)
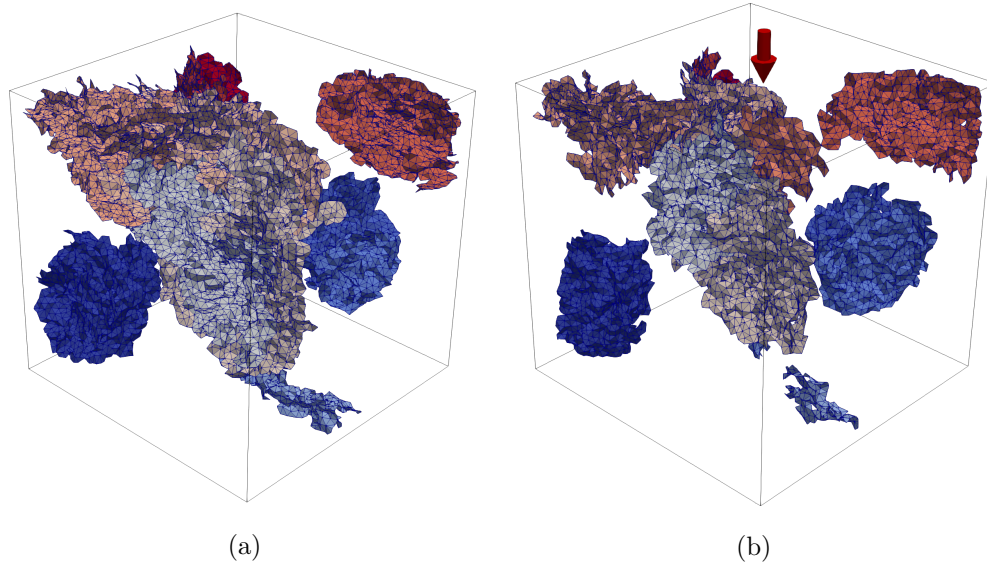
Figure 4.15: Crack maps in a) the free and b) loaded sampes after 120 days. Colours denote the crack numbers. An arrow in the loaded simulation denotes the direction of the applied load.

sets of images, it could be noticed that the crack network of a freely expanding sample is more developed: it has a larger area and more branches. Oppositely, the cracks in the loaded specimen are more planar and localised. To estimate the cracks orientations, probability distributions of the angles between the crack segments represented by cohesive elements and the loading direction are plotted in Fig. 4.16. Both histograms have a normal distribution shape centred around zero degrees (parallel to the z-axis). In both simulations, there are fewer cracks perpendicular to the z-axis than parallel to it. The angle distribution of a loaded specimen is more shrank to zero. This leads to the conclusion that the loaded cracks are more often aligned with the loading direction, while the free cracks are less oriented.

Fig. 4.17 plots the ASR-related strains obtained by subtracting the loading-related deformations from the total ones. Similar to the mentioned experimental results, the loaded model develops smaller ASR strains in the direction of the loading. Difference in ε_z between the two setups is around 25%, which fits the experimental range. Moreover, the strains in the x- and y-directions are higher than in z, which suggests certain redistribution of the ASR expansion between the free directions.

Evolution of the total crack volumes, plotted in Fig. 4.18, shows a smaller value for the loaded sample. As the cracks have a preferential direction to go when loaded, it takes shorter time for them to reach the border. After this moment, a further loading increment is mainly spent on opening the existing cracks rather than generation of new crack surfaces. Oppositely, the internal load in the freely-expanding concrete block is generating a dense network of randomly-oriented cracks. The resulting volume increases
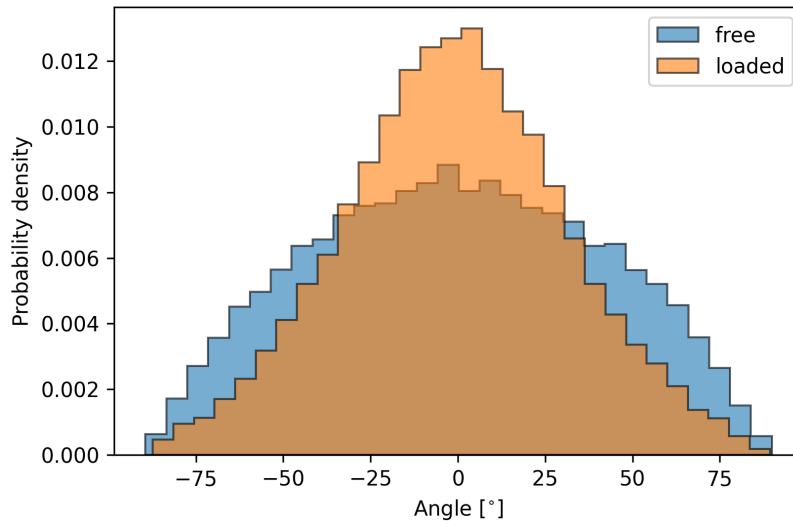
Figure 4.16: Probability densities of the angles between the crack segments and the loading axis at 120 days of the simulation time.
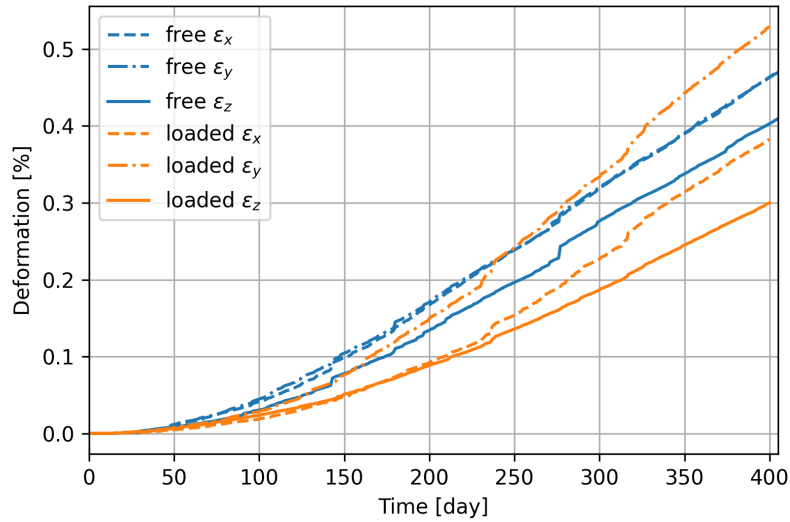
Figure 4.17: Macroscopic strains of the free and loaded specimens.
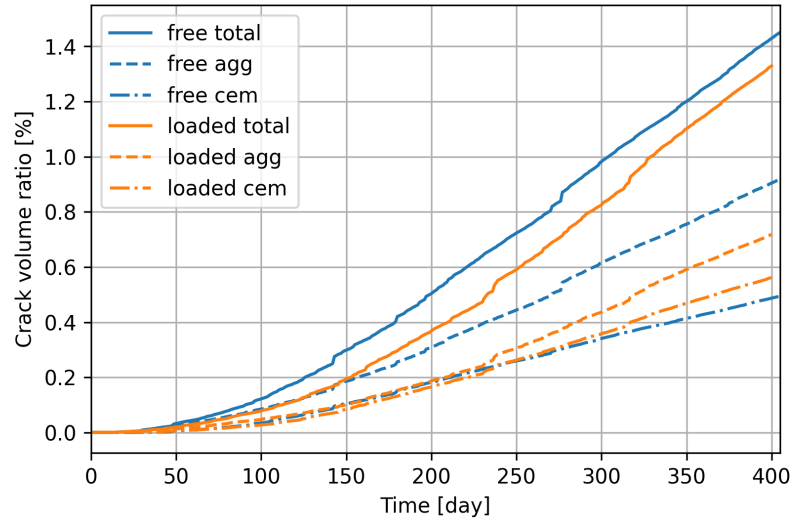
Figure 4.18: Crack volumes by the phase for the loaded and freely-expanding specimens.

simply because of a larger cracks extent. When the diffused network reaches the specimen's borders, further loading increase mostly contributes to opening of the existing cracks. This stage is characterised by almost a linear volume increase observed in both specimens after 200 days.

4.6 Conclusions

A novel 3D meso-scale numerical model for the ASR deterioration of concrete was presented. Owing to the proposed crack insertion algorithm and the numerical solution technique, application of the internal load resulted in a deformed concrete meso-structure permeated by a network of thin cracks. Such an output facilitated qualitative and quantitative comparison with the experimental data, especially with the X-ray tomograms.

Cracks were modelled by cohesive elements. Localisation of the former was facilitated by the insertion algorithm that implies only crack elongation. The cohesive elements were inserted in form of smooth facet loops connecting pairs of neighbouring contour segments.

Ability of the model to simulate multiple deviated cracks simultaneously was provided by adoption of the modified sequentially linear analysis. Within its scope, stiffness of a single cohesive element is reduced in a series of linear steps. It eliminates the need of a tangent stiffness and improves the numerical stability. Stiffness ambiguity between the compressed and tensioned states of the cohesive elements still brings certain complexity to the solution scheme.

The proposed numerical approach was validated by simulating a 3D problem of a penny-shaped crack loaded in its centre. Comparison between the numerical and the analytical predictions yielded a good match. Moreover, the role of some model parameters on the convergence of the numerical solution to the analytical one was investigated.

The final numerical model used for simulating real concrete was built based on the X-ray tomograms. Loading was applied to a number of randomly chosen ASR sites and was linearly increased with time. This led to the evolution of localised cracks and macroscopic expansion of a specimen. The model parameters such as the number of the ASR sites and the loading increase rate were calibrated based on the experimental data. The latter comprised the crack statistics collected from the tomography data as well as the macroscopic deformations.

Agreement between the results has proved two made hypotheses. Both the central crack loading and the crack elongation from its contour were sufficient to reproduce the realistic crack patterns and the macroscopic behaviour. It did not however disprove the idea that ASR products could apply their pressure along the whole crack surface. Neither did it disprove the idea that the ASR could also cause continuous nucleation of new cracks, some of which are not caused by the internal pressure (e.g. shear cracks). This study showed that the proposed hypotheses are valid from the mechanical point of view and should not be ignored in studying the ASR mechanics. To evaluate the impact of different loading mechanisms, additional numerical simulations should be performed. The proposed numerical approach is a perspective tool for further studies.

In the sensitivity study with varying number of the ASR sites, the total loading was preserved by modifying an absolute value of individual forces. The results have shown that few ASR sites with a high load are more efficient in generating new cracks and causing expansion than numerous sites with a moderate loading.

In a simulation of a concrete sample under uniaxial loading, a network of localised, largely oriented cracks has been developed. The smaller crack volume of the loaded specimen was associated to the shorter crack paths to the borders. Macro-scale model behaviour is in accordance with the experimental observations.

The conducted simulations proved the applicability of the developed model to the ASR-expansion experiments. This model is a practical tool to study the complexity of ASR-related mechanics. It allows statistical representation of realistic crack patterns while preserving the physics. It could be used in the future to study different types of ASR loading, e.g. ASR gel distributed along cracks. Moreover, it could be fully coupled with a fluid-flow model, which would mimic accumulation of ASR products and their transport within a crack network.

5 Meso-scale ASR model with continuous damage

The meso-scale ASR model with cohesive-elements representation of cracks proposed in the previous chapter is a powerful tool to predict realistic concrete cracking and expansion. Such a model is indispensable when comparison with the tomography data is at hand. At the same time, fine resolution of a dense crack network comes at the price of the high computational cost. This cost is bearable when several simulations have to be performed, but it becomes unaffordable for tens and hundreds of them. Numerous simultaneous meso-scale simulations become necessary in a computational multi-scale model presented in the following chapter. Therefore, a high computational cost motivates development of a more efficient meso-scale model.

In this chapter, a 2D numerical model with cracks represented by a continuous damage approach is described. The model accounts for the internal structure of concrete including the aggregates and the cement paste. In contrast to the previous developments, the ASR sites are explicitly represented. The adoption of the continuous damage approach increases the computational efficiency and allows conducting Monte Carlo simulation by varying the internal structure of concrete. Two different studies are performed. In the first one, the role of self-contact in cracks in the uniaxially-loaded concrete specimens is evaluated. The self-contact is incorporated by using the orthotropic damage approach. The model succeeds to reproduce the ASR expansion under high uniaxial loads.

In the second study, a simple quasi-static meso-scale model of a viscoelastic strain-softening material is developed. This model can be easily implemented in a standard finite element package. It is based on the combination between the SLA-based approach and the quasi-static solution of a rheological equation. The developed model is used to study the viscoelastic effects in the cement paste on the ASR cracking. The results show that the viscoelastic strain-softening behaviour of the paste causes less damage and lower stiffness reduction than in the linear strain-softening case. The macroscopic expansion also becomes lower than the experimental values. The results of this chapter
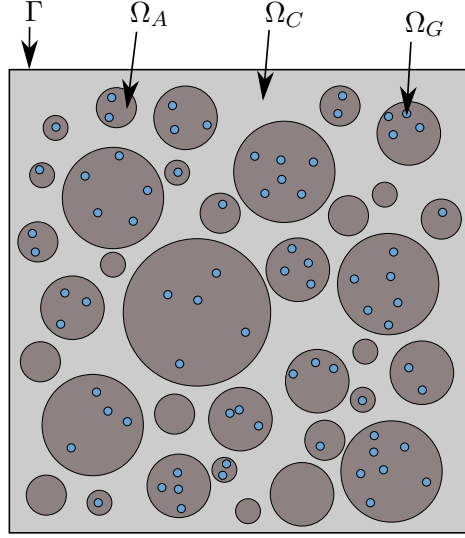
Figure 5.1: Concrete domain with closure Γ and three mutually exclusive phases: cement paste Ω_C, aggregates Ω_A and ASR sites Ω_G.

have been published in (Gallyamov et al., 2020, 2021a).

5.1 ASR meso-scale problem

The meso-scale model presented here is purely mechanical. The dissolution and precipitation processes, which govern the ASR products' evolution, are not modelled. The effect of temperature is taken into account through a phenomenological ASR expansion law. In the following, the basic equations and assumptions constituting this ASR meso-scale model are summarised.

A two-dimensional domain Ω with closure Γ is considered, which represents a block of ASR-affected concrete as shown in Fig. 5.1. Three mutually exclusive phases constitute Ω: the cement paste Ω_C, the aggregates Ω_A, and the ASR sites Ω_G. An isotropic eigenstrain matrix $\boldsymbol{\varepsilon}_{eig}$ is imposed at each ASR site to account for expansion. Eigenstrain is linked to elastic strain $\boldsymbol{\varepsilon}_{el}$ via the following equation:

$$\boldsymbol{\varepsilon} = \boldsymbol{\varepsilon}_{el} + \boldsymbol{\varepsilon}_{eig} \tag{5.1}$$

where $\boldsymbol{\varepsilon}$ is the infinitesimal strain tensor $\boldsymbol{\varepsilon} = \frac{1}{2}\left(\nabla \boldsymbol{u} + \nabla \boldsymbol{u}^{\mathrm{T}}\right)$. Note that the Cauchy stress $\boldsymbol{\sigma}$ depends only on the elastic part of the strain, *i.e.* $\boldsymbol{\sigma} = \boldsymbol{\sigma}(\boldsymbol{\varepsilon}_{el})$.

5.1.1 ASR loading

The volume increase of ASR products is approximated by increasing the imposed eigenstrain at every step of the simulation. In this study, it is assumed that the strain imposed at ASR sites $\boldsymbol{\varepsilon}_{eig}$ is proportional to the total amount of the generated ASR products, which is proportional to the chemical reaction extent ξ. Dependence of the ASR kinetics on temperature and relative humidity was experimentally studied by Larive (1997). As the previously discussed set of experimental data (Shakoorioskooie, 2021) does not account for the loaded experiments, the data published by Multon and Toutlemonde (2006) is used. In order to match this data with the proposed model, an asymptotic expansion law proposed by Ulm et al. (2000) is adopted, which makes the best fit with the majority of accelerated experiments available in the literature. A first-order kinetic law in isothermal conditions results in an explicit equation for the chemical reaction extent ξ:

$$\xi(t,T) = \frac{1 - \exp[-t/\tau_{ch}(T)]}{1 + \exp[-t/\tau_{ch}(T) + \tau_{lat}(T)/\tau_{ch}(T)]} \tag{5.2a}$$

$$\tau_{ch}(T) = \tau_{ch}(T_0)\exp[U_C(1/T - 1/T_0)] \tag{5.2b}$$

$$\tau_{lat}(T) = \tau_{lat}(T_0)\exp[U_L(1/T - 1/T_0)] \tag{5.2c}$$

where t and T are the current time and temperature, τ_{lat} and τ_{ch} are the latency and characteristic times, T and T_0 are the current and the reference temperatures, U_C and U_L are the activation energy constants. Therefore, the phenomenological ASR expansion law reads as

$$\boldsymbol{\varepsilon}_{eig}(t,T) = \varepsilon(\infty)\frac{1 - \exp[-t/\tau_{ch}(T)]}{1 + \exp[-t/\tau_{ch}(T) + \tau_{lat}(T)/\tau_{ch}(T)]}\mathbb{I} \tag{5.3}$$

where $\mathbb{I}$ is the identity matrix and $\varepsilon(\infty)$ is the asymptotic volumetric expansion strain in the stress-free experiment. The latency time τ_{lat}, the characteristic time τ_{ch}, the thermal activation constants U_C and U_L, and the asymptotic strain $\varepsilon(\infty)$ are the calibration parameters of the model. Given a homogeneous temperature of a specimen, the expansion law results in the same eigenstrain values $\boldsymbol{\varepsilon}_{eig}$ at all ASR sites Ω_G.

5.1.2 Solution scheme

Similar to the finite-element procedure described in Chapter 3, quasi-static conditions are assumed. The expression for the virtual work for the current FE model is

$$\delta W = \int_\Omega \mathbb{C}\,(\boldsymbol{\varepsilon} - \boldsymbol{\varepsilon}_{eig}) : \boldsymbol{\varepsilon}(\delta\mathbf{u})\,d\Omega - \int_{\Gamma_t} \boldsymbol{t} \cdot \delta\boldsymbol{u}\,d\Gamma = 0 \tag{5.4}$$

where $\mathbb{C}$ is the global stiffness tensor, $\delta\boldsymbol{u}$ and $\boldsymbol{\varepsilon}$ are the vectors of virtual displacements and associated strains, $\boldsymbol{t}$ is the vector of external forces applied at the corresponding

portion of the boundary Γ_t.

The aggregates and the cement paste are modelled as brittle materials and ASR products as linear elastic. The constitutive behaviours are detailed in Section 5.2.1.

To avoid numerical divergence due to simultaneous propagation of multiple cracks, an SLA-based approach (Rots, 2001; Rots and Invernizzi, 2004) similar to the one used in Chapter 4 is adopted. The main distinction is that here the cracks are modelled by means of continuous damage.

The damaging procedure is also slightly modified. In the damaging algorithm used in the previous chapter (see Algorithm 3), all the integration points (IPs) with stress above the threshold were damaged. It was necessary for speeding up the simulations. Here, the maximum number of simultaneously damaged IPs is limited, which is called to relax the previously imposed condition. This improvement is facilitated by a lower computational cost of the current model, which allows having more iterations per load increment. Damaging single element at a time, as originally envisaged by SLA, is still not feasible due to extremely long simulations. The number of simultaneously damaged IPs is controlled by the threshold parameter ζ. An IP will be damaged if the following conditions hold:

$$\sigma \geq (1 - \zeta)\sigma_{max} \tag{5.5}$$

$$\sigma \geq \sigma_{t,i} \tag{5.6}$$

where σ is the principal tensile stress at this IP, $\sigma_{t,i}$ is its tensile strength and σ_{max} is the maximum principal tensile stress across the whole model. This allows multiple IPs, having stress slightly below the maximum, to be equally damaged. In the current study, ζ was taken equal to 0.01. By reducing this parameter, less and less IPs will be damaged simultaneously.

After each damaging event, mechanical properties at the damaged IP are updated as follows:

$$E_i = E(1 - d_i), \quad \nu_i = \nu(1 - d_i), \quad \mu_i = \mu(1 - d_i) \tag{5.7}$$

where E is the Young's modulus, ν the Poisson's ratio, μ the shear modulus, d_i the damage and i the reduction step. The tensile strength is reduced as

$$\sigma_{t,i} = \varepsilon_u E_i \frac{E_t}{E_i + E_t} \tag{5.8}$$

with the softening slope

$$E_t = \frac{\sigma_t}{\varepsilon_u - (\sigma_t/E)} \tag{5.9}$$

The damaging procedure is illustrated in Fig. 5.2a.
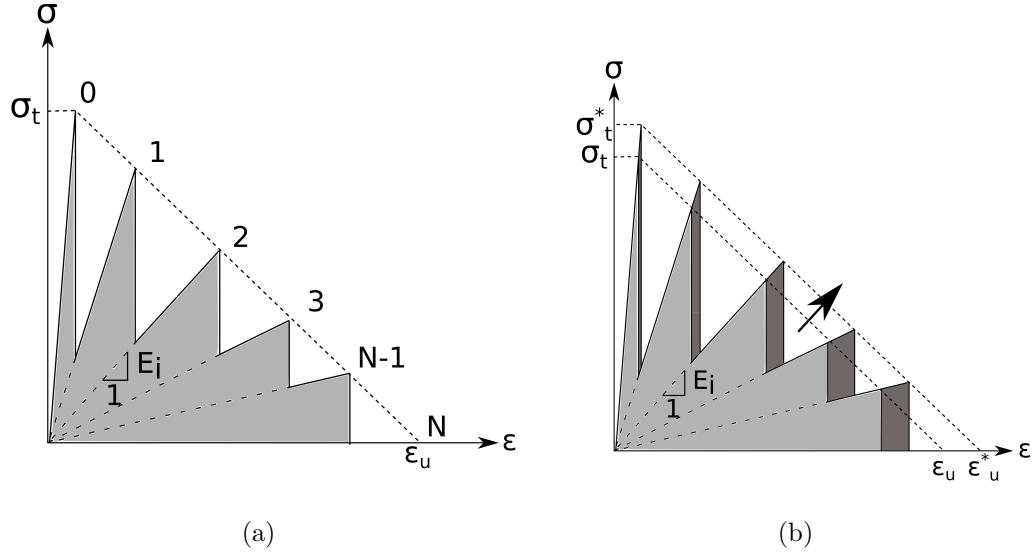
Figure 5.2: Stress-strain curves obtained with SLA: (a) a curve without regularisation and (b) a regularised stress-strain curve.

Due to the discrete reduction of stiffness and strength, the stress-strain curve obtained with SLA differs from the original softening curve shown by the dashed line in Fig. 5.2a. In order to ensure that the dissipated energy equals the fracture energy, different regularisation techniques can be applied (Rots and Invernizzi, 2004). In this work, the combined regularisation technique is used, where the tensile strength σ_t and the ultimate strain ε_u are simultaneously adjusted. The resulting stress-strain curve is illustrated in Fig. 5.2b.

5.2 Role of the self-contact in uniaxial compression experiments

It was previously reported that models with isotropic damage can capture macroscopic expansion of concrete under free boundary conditions and moderate uniaxial loading (Dunant and Scrivener, 2012). However, they fail under high compression by predicting specimen's contraction along the loading direction. Such contraction is never observed in laboratory (Larive, 1997; Gautam and Panesar, 2016; Multon and Toutlemonde, 2006). It is hypothesised that such numerical deficiency is caused by the lack of the self-contact mechanism in existing cracks. Self-contact happens when previously open cracks close and start to transmit compressive loads in the direction perpendicular to their plane. To test the hypothesis, the ability for cracks to come into contact and recover their stiffness is added into the model. Having these features in place, it is verified if the model can efficiently reproduce concrete expansion and cracking under the free-expansion and uniaxially-loaded conditions. By comparing the results of the simulation with the

experimental observations, it is concluded if the made hypothesis was correct.

5.2.1   Constitutive behaviour
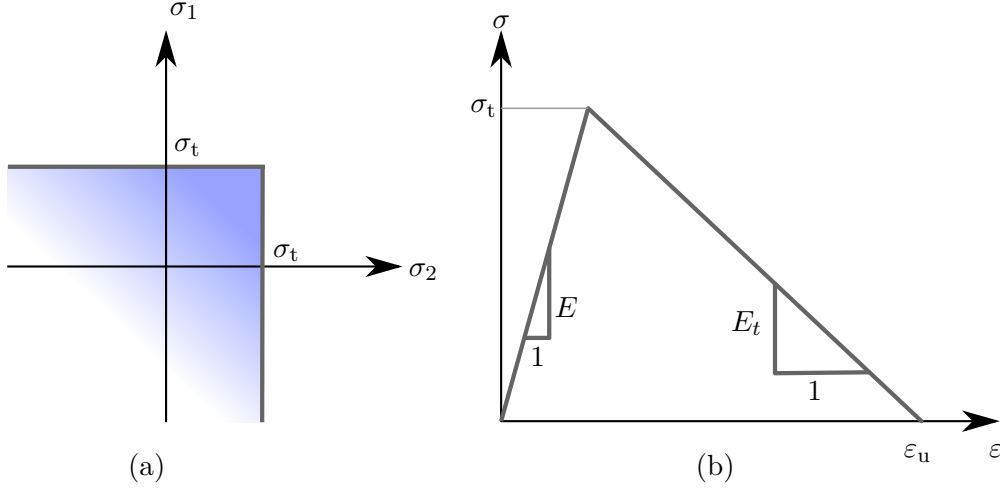
Figure 5.3: a) Failure criterion based on the maximum principal tensile stress. b) Bi-linear constitutive law with an initial elastic loading phase and subsequent linear strain-softening.

As it was shown in Chapter 3, expansion of ASR products causes tensile tangential stresses in the surrounding material. It is valid to assume that the material fails locally always under tension with subsequent linear softening. A bilinear strain-softening curve is plotted in Fig. 5.3b.

Self-contact in cracks and associated stiffness recovery was incorporated into the model by the fixed crack concept (Rots and Blaauwendraad, 1989). In this approach, the continuum is modelled as an elastically softening orthotropic material with its elastic properties degraded in a single direction. This direction is chosen at the first damaging event and kept fixed for the rest of the simulation (see Fig. 5.4). When previously opened crack closes, it goes into self-contact and can again transmit stresses in the perpendicular direction. The crack orientation is decided based on the principal stress criteria:

$$\sigma_i \leq \sigma_t, \text{ with } i = 1, 2, 3 \tag{5.10}$$

where σ_i is the ith principal stress (see Fig. 5.3b). If stress σ_i at any integration point violates Eq. (5.10), the plane perpendicular to the direction of σ_i becomes the crack plane.

Having a single crack passing through an element permits simple energy accounting in a way proposed by Bažant and Oh (1983). The essence of their approach is to smear out existing micro-cracks over the fracture process zone of width w_c, taken equal to the
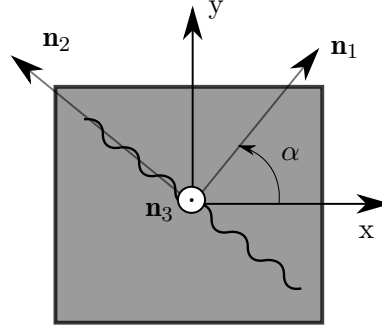
Figure 5.4: Illustration of the fixed crack model. Orientation axes of a crack $\mathbf{n}_1$ and $\mathbf{n}_2$ are rotated with respect to the global coordinate system by an angle α.

average element size. The area under the stress-strain curve in Fig. 5.3b equals the fracture energy G_c divided by the crack band width w_c:

$$\frac{G_c}{w_c} = \int_0^\infty \sigma d\varepsilon^f = \frac{1}{2}\sigma_t^2 \left(\frac{1}{E} - \frac{1}{E_t}\right) \tag{5.11}$$

where ε^f is the fracturing strain, E is the initial material stiffness in the direction perpendicular to the crack, E_t is the softening slope. In all meso-scale simulations, crack band width w_c is taken equal to the average element size. The ultimate strain ε_u becomes a function of the fracture energy, the crack band width, and the material strength in tension:

$$\varepsilon_u = \frac{2G_c}{w_c \sigma_t} \tag{5.12}$$

The stress-strain relation for the orthotropic material in a compact matrix form is

$$\boldsymbol{\sigma} = \mathbf{C}(\boldsymbol{\varepsilon} - \boldsymbol{\alpha}_t \Delta T) \tag{5.13}$$

with $\mathbf{C}$ being the stiffness tensor in the coordinate system associated with the global problem, $\boldsymbol{\alpha}_t$ is the matrix of thermal expansion coefficients, and ΔT is the temperature increase. Multiple works have studied thermal stresses in the vicinity of a crack (Kit et al., 1977; Atkinson and Clements, 1977; Da Yu Tzou, 1990). Among other findings, they have shown that the temperature gradient can cause crack propagation. Factors that play a role in this process include material properties, boundary conditions (both mechanical and thermal), crack shape, its dimensions and a level of insulation. Considering the complexity of the problem and the lack of knowledge of the material and crack properties, the thermo-mechanical aspects of crack growth are ignored and the second term on the right-hand side of Eq. (5.13) is discarded. This is however a simplification, which could be addressed in future work.

An orthotropic material has three perpendicular symmetry planes. Basis vectors are perpendicular to these planes. These vectors could differ from the basis vectors of the global coordinate system. In such a case, transformation from the coordinate system associated with the material symmetry planes to the global coordinate system in matrix form can be expressed as

$$\mathbf{C} = \mathbf{Q} \cdot \mathbf{C}^{(p)} \cdot \mathbf{Q}^T \tag{5.14}$$

where $\mathbf{Q}$ is the transformation matrix and $\mathbf{C}^{(p)}$ is the orthotropic stiffness matrix in the direction of the basis vectors. In the scope of the crack model, the matrix $\mathbf{Q}$ accounts for the angle α between the global coordinate system and the crack plane shown in Fig. 5.4. The stiffness matrix takes the form (Bower, 2009):

$$\mathbf{C}^{(p)} = \begin{bmatrix} c_{11} & c_{12} & c_{13} & 0 & 0 & 0 \\ & c_{22} & c_{23} & 0 & 0 & 0 \\ & & c_{33} & 0 & 0 & 0 \\ & \text{sym} & & c_{44} & 0 & 0 \\ & & & & c_{55} & 0 \\ & & & & & c_{66} \end{bmatrix} \tag{5.15}$$

Its components are related to the elastic moduli through the following equations:

$$c_{11} = E_1(1 - \nu_{23}\nu_{32})\gamma, \qquad c_{22} = E_2(1 - \nu_{13}\nu_{31})\gamma, \qquad c_{33} = E_3(1 - \nu_{12}\nu_{21})\gamma,$$
$$c_{12} = E_1(\nu_{21} + \nu_{31}\nu_{23})\gamma, \quad c_{13} = E_1(\nu_{31} + \nu_{21}\nu_{32})\gamma, \quad c_{23} = E_2(\nu_{32} + \nu_{12}\nu_{31})\gamma,$$
$$c_{44} = \mu_{23}, \qquad\qquad c_{55} = \mu_{13}, \qquad\qquad c_{66} = \mu_{12},$$
$$\gamma = 1/(1 - \nu_{12}\nu_{21} - \nu_{23}\nu_{32} - \nu_{31}\nu_{13} - 2\nu_{21}\nu_{32}\nu_{13})$$

where E_k is the Young's modulus in the direction of the basis vector $\mathbf{n}_k$, ν_{kl} and μ_{kl} are the Poisson's ratio and the shear modulus between directions $\mathbf{n}_k$ and $\mathbf{n}_l$. Symmetry of the stiffness matrix is ensured by satisfying the following equality:

$$\nu_{kl}/E_k = \nu_{lk}/E_l \quad \text{for} \quad k, l = 1, 2, 3 \quad \text{and} \quad k \neq l \quad \text{(no sums).} \tag{5.16}$$

For the undamaged material, all elastic properties are equal to the initial isotropic values:

$$E_k = E, \quad \nu_{kl} = \nu, \quad \mu_{kl} = \mu \tag{5.17}$$

If a crack starts growing along the plane $\mathbf{n}_2\mathbf{n}_3$, as shown in Fig. 5.4, the material properties for the perpendicular direction $\mathbf{n}_1$ are reduced according to:

$$E_1 = E(1 - d), \quad \nu_{12} = \nu_{13} = \nu(1 - d), \quad \mu_{12} = \mu_{13} = \mu(1 - d) \tag{5.18}$$

where d is the damage parameter, which was defined earlier. The material properties in the undamaged directions remain unaltered.

The orthotropic damage approach simplifies modelling of self-contact in cracks and

associated stiffness recovery. For this, the principal strain in the direction perpendicular to the crack is checked. A negative value indicates that the crack segment is closed and its stiffness has to be recovered. In this study, friction is ignored and Young's moduli and Poisson's ratios are fully recovered while the values of shear moduli are kept reduced:

$$E_k = E, \quad \nu_{kl} = \nu, \quad \mu_{kl} = \mu(1 - d)$$

Omission of friction imposes a limitation on the ability of the model to reproduce the real concrete behaviour under the shear load. Accounting for friction should be priority of future work.

5.2.2 Model calibration

The parameters of the ASR expansion law in Eq. (5.3) require calibration with the experimental data. In addition, the number of ASR sites has also to be defined. Calibration is done based on the experimental results of Multon and Toutlemonde (2006), who studied the effects of loading on the macroscopic behaviour of ASR-affected concrete. For this purpose, cylindrical ASR-fostered concrete specimens were either free to expand or loaded longitudinally and radially. Control cylinders without the ASR were set under the same conditions. Their deformations were subtracted from the samples with the ASR as not ASR-related.

The algorithm proposed by Wriggers and Moftah (2006) is used to generate the geometrical models of the concrete specimens and RVEs. In this algorithm, a circular shape is assumed for all aggregates and a Fuller curve is used as a grading curve for the generation of aggregates. The model is not restricted by the shape of the aggregates: any other shape can be incorporated into the proposed model with ease. Subsequently, this geometrical model is discretized with Gmsh (Geuzaine and Remacle, 2009) into a finite element mesh of linear triangular elements with a uniform average element size $h = 0.5$ mm. The resulting numerical concrete samples have a size of 70×70 mm^2, and contain the aggregates with diameters in the range of $1 - 16$ mm (see Fig. 5.5). All the aggregates and sand particles smaller than the mesh size are not resolved. A mix between the small particles and the cement paste is treated as mortar further in the text. The aggregates' packing density is 70%.

The ASR affects a range of scales, varying from nanometre to millimetre. It includes growth of ASR products, opening of micro-cracks, possible transport of products into pores and fissures, change of the products' properties with time and surrounding environment. As it was discussed in Chapter 3, a typical size of an ASR inclusion is of nanometre scale. In the current numerical study, the size of an element is 0.5 mm, which does not resolve individual ASR pockets. Thus, the expansion that is applied at a single finite element to represent the effect of the ASR, should be seen as a homogenised expansion of an aggregate portion comprising several ASR pockets, rather than expan-

	E [GPa]	μ [GPa]	ν [-]	G_c [J/m^2]	$\sigma_{t,min}$ [MPa]
Aggregates	59*	22.6	0.3*	160[†]	10[†]
Mortar	12*	4.6	0.3*	60[‡]	3*
ASR product	11[¶]	4.7	0.18[¶]	-	-

Table 5.1: Material properties. * Taken from (Dunant and Scrivener, 2012). [†] Taken from (Ben Haha, 2006). [‡] Taken from (Xu and Zhu, 2009). [¶] Taken from (Leemann and Lura, 2013).

sion of the ASR product itself. These expanding sites are represented by a number of finite elements that are randomly distributed inside the aggregates and assigned the corresponding mechanical properties.

Similar to the study in Chapter 4, heterogeneity of the underlying micro-structure is taken into account by locally varying the tensile strength of the corresponding finite elements according to a Weibull distribution. A cumulative distribution function of the tensile strength σ_t is computed as follows:

$$F(\sigma_t) = 1 - e^{\left(-\left(\frac{\sigma_t - 0.8\sigma_{t,min}}{\lambda}\right)^k\right)} \tag{5.19}$$

where $\sigma_{t,min}$ is the quasi-static tensile strength, k and λ are the shape and the scale factors of the Weibull distribution, taken equal to 5 and $0.2 \cdot \sigma_{t,min}$ correspondingly.

The intact properties of all material phases are listed in Table 5.1. Shear modulus μ is computed as $\mu = E/[2(1+\nu)]$.

The boundary conditions for the calibration tests are shown in Fig. 5.5. Both free- and loaded-expansion tests are simulated. In the first test type, only the internal load coming from the expanding ASR-sites is present. In the second one, a vertical compression load of 10 MPa is additionally applied on top. Similar to the experiments, both simulation types last 450 days. The time step is taken equal to half a days. This value provides a good time resolution and allows capturing of the gradual evolution of crack networks.

A single-simulation outcome strongly depends on the specific realisation of a concrete specimen (aggregates sizes and positions, spatial distribution of tensile strength, positions of ASR-sites) and may not be representative. To obtain a statistical distribution of results, a Monte Carlo simulation consisting of 200 independent runs is performed for each loading type. The random parameter of the Monte Carlo analysis is the concrete meso-structure. Out of these 200 runs, one hundred has fixed sizes and positions of the aggregates but different distributions of ASR-sites. The second half are performed with the different spatial distribution of the aggregates and, consequently, the ASR-sites. The statistics of the output parameters is plotted in Figures 5.6, 5.8 and 5.9. Mean values

Table 5.2: Parameters of the ASR-expansion law.

Parameter	Value
Ratio of the ASR sites area to the aggregates area [%]	0.1
Asymptotic strain $\varepsilon(\infty)$ [%]	6.5
Latency time $\tau_{lat}(T_0 = 38°)$ [days]	30
Characteristic time $\tau_{ch}(T_0 = 38°)$ [days]	60
Thermal activation constant U_C [°K]	5, 400
Thermal activation constant U_L [°K]	9, 700

in these figures are denoted by letters with an over-line, and standard deviations are denoted by percents in brackets.
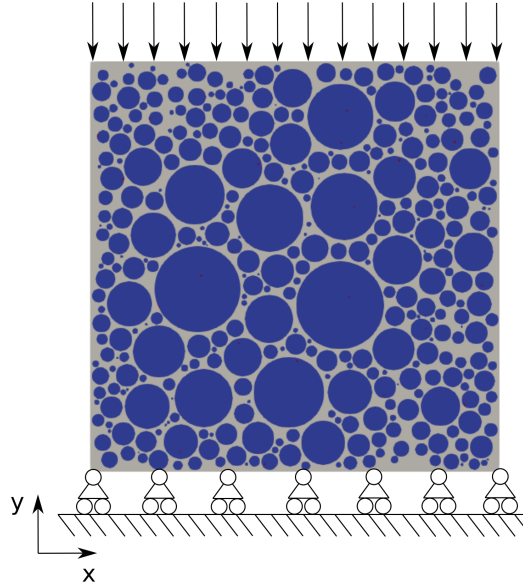
Figure 5.5: Concrete meso-structure and boundary conditions for the calibration tests. The specimens are composed of the aggregates (in blue) surround by the mortar (in grey). Loading is applied on top of the specimen during the compression tests only.

The parameters of the ASR-expansion law and the density of the ASR sites were calibrated on the free expansion experiment and kept constant for the loaded case. Their values are listed in Table 5.2. The total number of ASR sites (or the ratio of their total area to the total area of aggregates) is an important parameter that governs crack distribution across the domain: a small number of sites results in isolated cracks, while a higher number leads to a diffused crack pattern. Currently, experimental quantification of this parameter is a complicated task as there is no unique way of accurately determining the reactive sites. In the simulations, this parameter was chosen in a rather intuitive way.

Results of the calibration tests and the experimental expansion values are plotted in Fig. 5.6. The latter represent the average expansion values over multiple tested specimens. The range of the observed values is marked by the error bars. Both the experimental and the numerical curves account only for the ASR-induced expansion.

In Fig. 5.6a, the numerical expansion curves for the freely-expanding specimens are compared the experimental ones. Both sets of curves have a typical sigmoidal shape and similar asymptotic values. The main discrepancies between the two sets of curves are the faster experimental expansion rate during the first 50 days and the earlier saturation of the numerical expansion (300 days against ~ 370 days in the experiment). To improve the fitting, different thermal law could have been used. However, the choice was made in favour of the one presented in Eq. (5.3) as it is most commonly used in the field of ASR modelling.

In Fig. 5.6a, both the numerical and the laboratory specimens show different strain values depending on the direction. While this difference is insignificant in the simulations, the experimental results show more pronounced separation. In the free-expansion simulation, cracks are overall randomly oriented. However they may have a slight orientation bias due to the aggregates shape and positions, and the ASR-sites placement (see Fig. 5.7a). In the real concrete, the difference in expansions may also be caused by the casting directions, the effect of the self-weight, specific boundary conditions, rock anisotropy, etc (Larive, 1997; Ben Haha, 2006; Gautam and Panesar, 2016). Macroscopic strain curves for both the free-expansion and the loaded conditions have a typical S-shape, as a result of the similar shape of the ASR-product expansion curve. It is important to mention, that in the field conditions, the ASR-affected dams experience continuous swelling during decades (Mauris et al., 2015). The difference in the long-term behaviour of the laboratory specimens with the ASR and the full-scale structures is subject of debate. One of the possible causes of the reduction in experimental expansion is the drop in alkalis concentration due to its leaching (Lindgård et al., 2018; Multon and Sellier, 2016).

Results of the loaded simulations show similar trends as the experimental ones (see Fig. 5.6b). The application of $10\,\text{MPa}$ reduces significantly concrete expansion along the loading direction. The experimental average longitudinal expansion $\varepsilon_{\text{long}}^{\text{exp}}$ is almost null. The numerical average $\bar{\varepsilon}_{\text{long}}^{\text{sim}}$ equals 0.009%. The experimental strain in the stress-free direction $\varepsilon_{\text{lat}}^{\text{exp}}$ is slightly bigger than the average values of the free-expansion case, which is also reproduced in the simulations. However, the proposed model overestimates the lateral expansion $\bar{\varepsilon}_{\text{lat}}^{\text{sim}}$ and results in a wider distribution of the final values. A possible explanation is the two-dimensionality of the model: cracks would have more space to accommodate in a 3D volume, which would reduce the overall expansion. Expanding this model to 3D should improve its fit with the experimental data.

A clear advantage of the proposed model is its capacity to produce positive longitu-

(a)

(b)

(c)
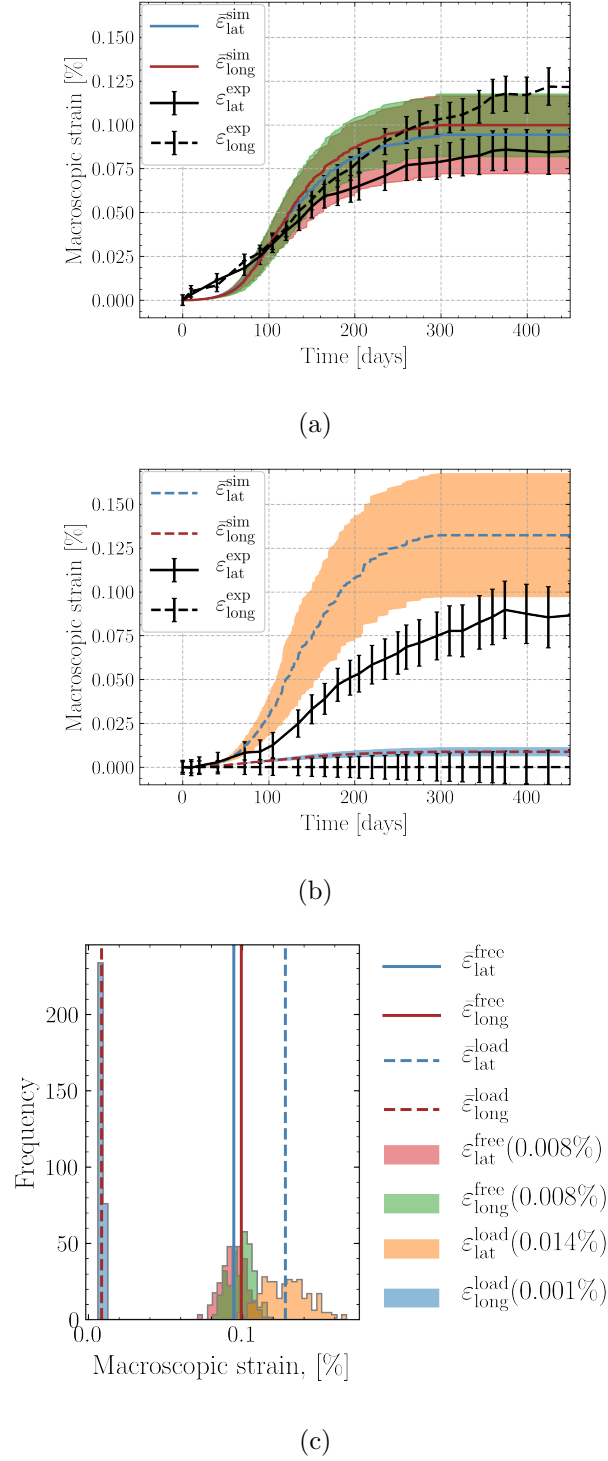
Figure 5.6: Macroscopic strain under a) the free-expansion conditions, b) the uniaxial compression of $10\,\mathrm{MPa}$ compared to the experimental results of Multon and Toutlemonde (2006). Solid lines denote the mean values, and shaded areas bound the range of the output parameter. c) Distributions of the final expansions from the Monte Carlo simulation. Values in brackets are the standard deviations.

dinal expansion under the high-load conditions. This feature was enabled by including self-contact and orthotropic damage in cracks, which was not the case in the previous models.

It is important to mention that the final expansion values shown in Fig. 5.6c have a distribution close to normal. Similar shapes could be also appreciated in Figures 5.8b and 5.9c. Such a uni-variate distribution suggests that varying positions of ASR-sites within fixed aggregates and shuffling aggregates themselves has a similar statistical effect on the final results.

The numerical damage patterns are shown in Figures 5.7a and 5.7b. Colours denote the damage level: blue and grey colours stand for the intact material, red is fully-damaged. The cracks that were earlier open but later closed and recovered normal stiffness do still appear in red. This leads to a certain visual overestimation of the damage amount. Instead of the damage parameter d, Figures 5.7c and 5.7d show additional area of damaged elements. The basic assumption of this plotting way is that, in a damaged element, most of the deformation comes from the crack opening. Then, the crack area of a finite element A^{cr} could be computed as follows

$$A^{cr} = A_0^{el} \cdot \varepsilon_{vol} \tag{5.20}$$

where ε_{vol} is the volumetric strain, A_0^{el} is the initial area of an element. In a 3D-computation, an analogue of the crack area would be the crack volume. This metric is facilitating comparison with the experiments, where crack density is one of the output parameters (it will be discussed later in this section). By a comparison between two sets of figures, one could note that some of the cracks, which are explicit in the damage maps, could not be distinguished in the crack opening plots. This is the effect of the self-contact and stiffness recovery in cracks. Although the cracks open due to tensile loading, their interaction could lead to closure of ones and wider opening of others. Important to mention that the darkest colours in Figures 5.7c and 5.7d correspond to the opening of tens of microns. Cracks of the same size from the real concrete would not be visible with a naked eye.

A real crack pattern coming from the laboratory experiments is plotted in Fig. 5.7e. This image is obtained by X-ray micro-tomography of the ASR-accelerated concrete under free-expansion conditions after 500 days. Similar to the numerical results, the real concrete cracks are present both in aggregates, paste and interfacial transition zone. Their random orientations, broken shapes and homogeneous spread across the cross-section qualitatively resemble those from Fig. 5.7c.

The response of the meso-structure to the load application shows cracks alignment with the load direction, as shown in Figs. 5.7b and 5.7d. The observed crack pattern explains why the horizontal expansion in Fig. 5.6b is higher than the vertical one. Since

multiple coalesced vertical cracks are widely opened in the horizontal direction, the corresponding macroscopic strain $\varepsilon_{\mathrm{lat}}^{\mathrm{num}}$ is larger than the strain in the direction of the load $\varepsilon_{\mathrm{long}}^{\mathrm{num}}$.

Fig. 5.8 plots the crack density λ, which is the ratio between the crack area within a specific phase and the total area of this phase. To compute this parameter, the crack area from Eq. (5.20) is used. The resulting crack density per phase is not exceeding one percent. The tomography studies of the samples in laboratory and field conditions by the colleagues from the Sinergia project (Shakoorioskooie et al., 2019; Leemann et al., 2019) showed the total crack densities of a similar order $(1.8 - 2.6\%)$. The former tomographic analysis showed a very similar crack volume fraction inside the paste and inside the aggregates.

For both loading conditions, one can observe a smaller crack density in the aggregates compared to the mortar caused by the lower strength of the latter. Previous studies on the effect of creep on the ASR show that it helps to accommodate larger strains in the cement paste without damaging it (Giorla et al., 2015; Rezakhani et al., 2021). A model combining isotropic damage with viscoelasticity is described in the following section. The current orthotropic model does not include viscoelastic effects, thus it overestimates the damage amount in the mortar.

The stiffness loss is plotted in Fig. 5.9. The relative stiffness, expressed in per cent, is computed by applying either compressing or extending displacements at the specimen's surfaces. After solving for a new displacement field, internal forces at the nodes on these surfaces are integrated into a scalar. The ratio between the current value of this integral and its initial value serves as an estimator of the specimen's relative stiffness. Pulling a sound piece of concrete would give rise to high reaction forces, whereas in a severely damaged specimen the applied load will only open cracks. In the Monte Carlo simulation, the stiffness was evaluated always in compression. For the comparison purpose, a single simulation with the stiffness computed via tension was performed.

The relative stiffness estimated in compression is higher than the one obtained in tension. This is due to the stiffness recovery of cracks brought into self-contact. Although this phenomenon could still happen while applying tension, its effect is more pronounced during the compression test. Another interesting observation concerns the ratio between the stiffness values into two directions. In the free expansion case the stiffness is almost equally reduced in both directions, whereas the loaded case shows larger stiffness loss in the x-direction. This anisotropy is equally pronounced in both tensile and compressive estimates and is linked to the vertical cracks percolation. When later this meso-scale model is used in the multi-scale framework, the difference between stiffness values estimated via tensile and compressive tests justifies an adaptive homogenisation procedure. According to it, loading directions of virtual tests are chosen based on the stress state of the macroscopic element. In Fig. 5.9a, the grey shaded area denotes the limiting values
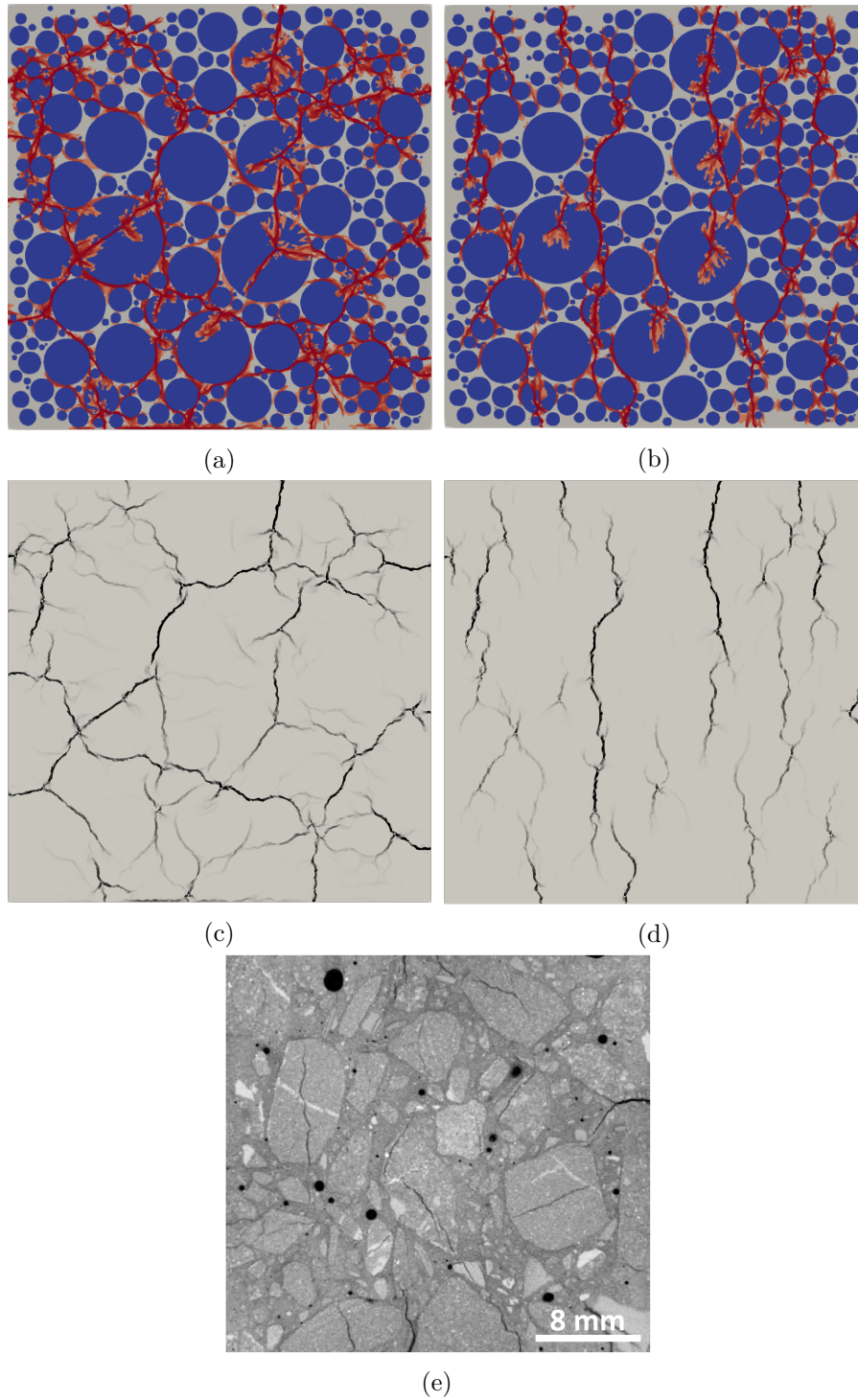
Figure 5.7: Damage map under a) the free expansion and b) the uniaxial loading of 10 MPa. Red colour denotes fully damaged elements ($d = 1$). c,d) Crack opening maps of the same samples. e) Typical X-ray micro-tomography image of ASR-affected concrete (courtesy of the Concrete Technology Group at Empa).
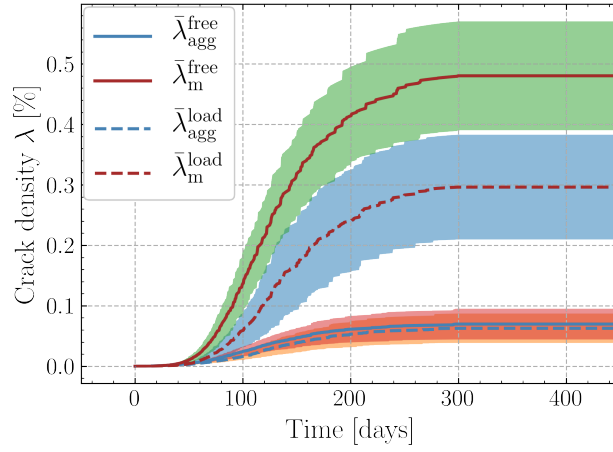
(a)
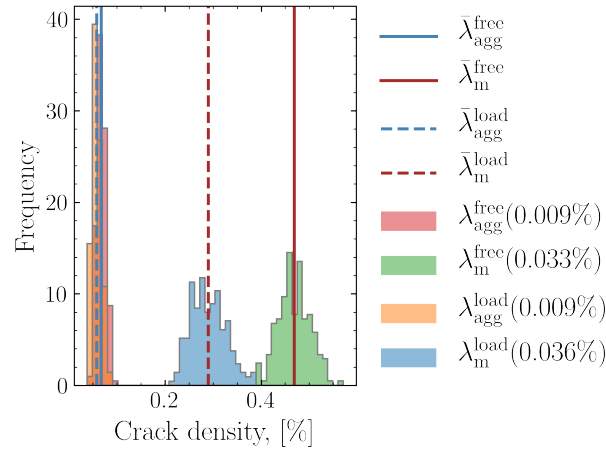
(b)

Figure 5.8: a) Crack density in the aggregates and the mortar for the free-expansion and the loaded ASR simulations. b) Distributions of the final crack density per phase with their mean values and standard deviations (values in brackets) from the Monte Carlo simulation.

of the stiffness in the accelerated free-expansion experiments of Ben Haha (2006). The current model results in the stiffness reduction of $10 - 20\%$, which is very close to the experimental values.

Modelling self-contact and associated stiffness reduction in cracks indeed increases the load-bearing capacity of the numerical sample. Including this phenomenon into the numerical model with the continuous damage representation of cracks solves the problem of the specimens' shrinkage under high uniaxial load, which was previously observed by Dunant and Scrivener (2012). This capacity of the meso-scale model together with its increased computational efficiency allows its integration into the multi-scale numerical model discussed in Chapter 6.

5.3 Role of the viscoelasticity of the cement paste

Earlier, Dunant and Scrivener (2010) have proposed a micro-mechanical model able to simulate brittle concrete deterioration due to the ASR. Later, Giorla et al. (2014) have developed a space-time finite element model, which allowed simulating arbitrarily complex linear viscoelastic behaviour. Finally, the same authors have combined the two approaches in a micro-scale ASR model that accounted for the viscous energy dissipation in the cement paste (Giorla et al., 2015). The authors reported an important effect of creep on the distribution of the damage in the micro-structure. They have also related the low level of damage in the paste to the creep.

The model of Giorla et al. (2015) is unconditionally stable and convergent, and applicable to any rheological model. This model requires elaborate developments associated to the reformulation of the global system of equations and hence can not be easily implemented in a standard FE package. The performed study aimed to develop a simple quasi-static finite element model of viscoelastic strain-softening material, which could be built within a standard FE library. This is done by combining the SLA-based solution technique with the quasi-static solution of a rheological equation.

Having the model ready, the role of the viscoelasticity of cement paste on the deterioration of concrete due to the ASR is evaluated. Viscoelastic strain-softening behaviour of the cement paste is referred as viscous softening further in the text. This behaviour is compared to the paste exhibiting linear strain-softening. To distinguish between these two material behaviours, the latter is referred as elastic softening. Properties of both material laws are calibrated on the experimental data. A free-expansion experiment is simulated in a 2D concrete model comprising either viscously or elastically softening cement paste. Based on the comparison of the two results, conclusions on the role of the viscoelasticity in the concrete damage due to the ASR are derived.

(a)

(b)

(c)
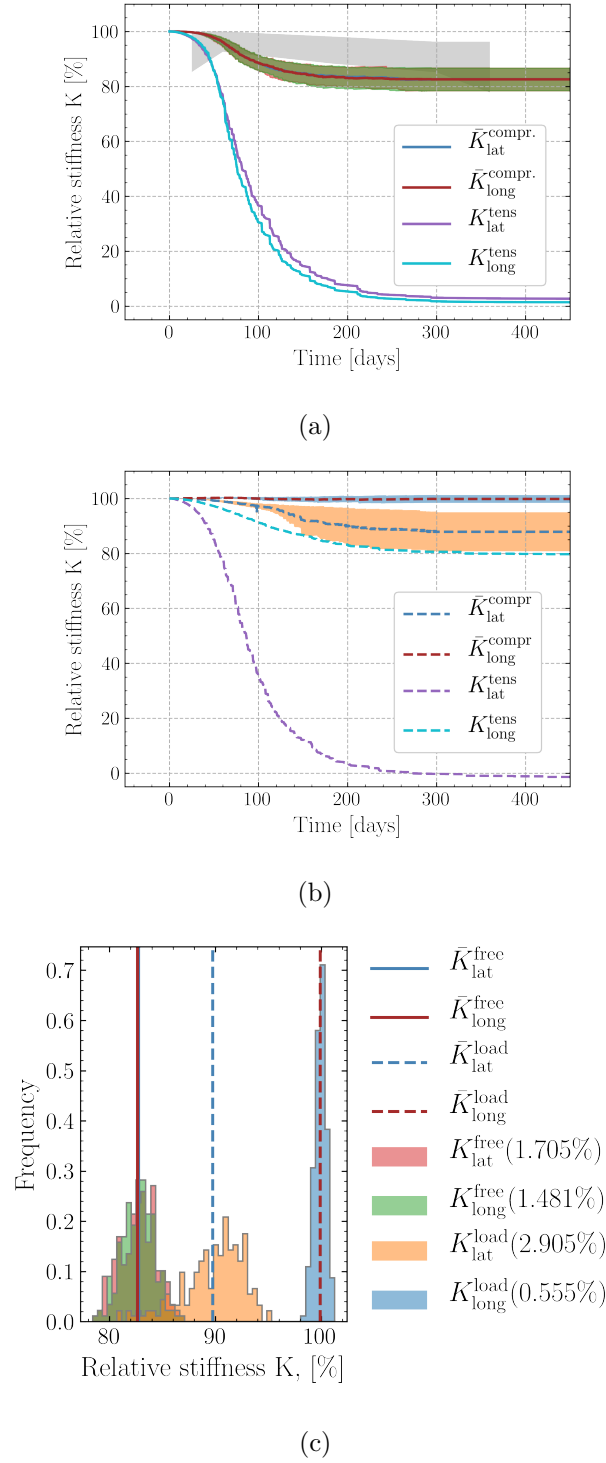
Figure 5.9: Estimation of the stiffness loss via compressive and tensile tests under a) the free expansion and b) the uniaxial loading of 10 MPa. A grey shaded area corresponds to the range of the experimental values reported by Ben Haha (2006). c) Distributions of the final relative stiffness in two directions with mean values and standard deviations (values in brackets) from the Monte Carlo simulation.

$$E_0$$
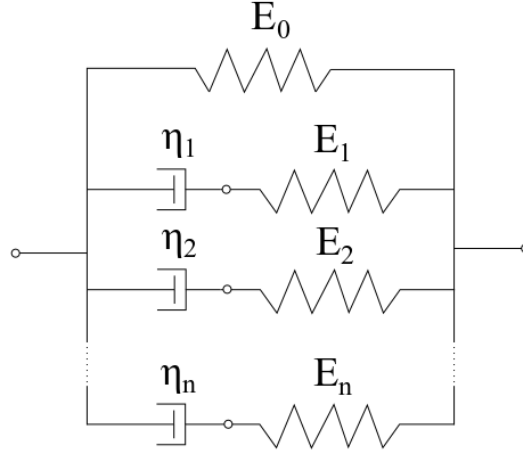
Figure 5.10: Generalised Maxwell chain

5.3.1   Rheological model

To model the viscoelasticity of the cement paste, a generalised Maxwell chain is adopted as the rheological model. It comprises a series of sequential spring-dashpots (Maxwell elements) placed in parallel with a single spring as depicted in Fig. 5.10. Viscosities of the dashpots are marked with η_i, while stiffnesses of the springs are E_i. The relation between stress and strain in the Maxwell chain is described by

$$\sigma(t) = \int_{-\infty}^{t} E(t,\tau)\mathbf{D}\dot{\varepsilon}\,d\tau \tag{5.21}$$

where $E(t,\tau)$ is the time-dependent relaxation function, τ is the loading age, and $\mathbf{D}$ is the dimensionless matrix relating a 3D deformation state to a 1D relaxation function. The latter is expanded in the exponential series

$$E(t,\tau) = E_0 + \sum_{\alpha=1}^{n} E_\alpha e^{-\frac{t-\tau}{\lambda_\alpha}} \tag{5.22}$$

where the relaxation time of each Maxwell element is defined as $\lambda_\alpha = \eta_\alpha/E_\alpha$. Assuming a constant strain rate $\dot{\varepsilon}$ within each time step, analytical integration of the right-hand side of Eq. (5.21), by using the definition of the relaxation function as given in Eq. (5.22), leads to the following form

$$\sigma(t+\Delta t) = E_0\mathbf{D}\varepsilon + \sum_{\alpha=1}^{n} \left(\left(1 - e^{-\frac{\Delta t}{\lambda_\alpha}}\right) \frac{E_\alpha \lambda_\alpha}{\Delta t} \mathbf{D}\Delta\varepsilon + e^{-\frac{\Delta t}{\lambda_\alpha}} \sigma_\alpha(t) \right) \tag{5.23}$$

with $\sigma_\alpha(t)$ being the internal stress within each Maxwell element, defined as

$$\sigma_\alpha(t) = \mathbf{D} \int_0^t E_\alpha e^{-\frac{t-\tau}{\lambda_\alpha}} \dot{\varepsilon} d\tau \qquad (5.24)$$

The first term under the sum sign in Eq. (5.23) could be seen as the effective stiffness of a single Maxwell element multiplied by the matrix $\mathbf{D}$ and the strain increment $\Delta\varepsilon$:

$$E_\alpha^{\mathrm{ef}} = \left(1 - e^{-\frac{\Delta t}{\lambda_\alpha}}\right) \frac{E_\alpha \lambda_\alpha}{\Delta t} \qquad (5.25)$$

The time increment Δt controls rate dependency of the effective stiffness. By limit analysis, the limiting values of the effective stiffness are found equal to E_0 for the infinitely slow loading (Δt tending to infinity) and $E_0 + \sum E_\alpha$ for the infinitely fast (Δt tending to zero). At the end of each converged time step, the internal stress $\sigma_\alpha(t)$ is updated according to

$$\sigma_\alpha(t) = \sigma_\alpha(t - \Delta t)e^{-\frac{\Delta t}{\lambda_\alpha}} + E_\alpha^{\mathrm{ef}} \mathbf{D} \Delta\varepsilon \qquad (5.26)$$

5.3.2 Coupling between the strain-softening and the viscoelasticity

Contrary to the first study of this chapter, a simple isotropic damage law is used. This is done to simplify the coupling of the strain-softening behaviour with viscoelasticity. Damage is affecting the viscoelastic material by reducing both the stiffnesses of the spring elements E_i and the viscosities of the dash-pots η_i by the factor $(1 - d)$. The influence of the temperature on the viscoelasticity is neglected.

Combination of the viscoelasticity with sequential linear analysis is not a trivial task, and to the best of the author's knowledge has not been previously reported in the literature. The major challenge in its implementation is rate-dependency of stresses and hence non-uniqueness of the stress-strain path. To overcome this difficulty, it is assumed that the softening slope is constant and independent of the loading rate. The illustration is in Fig. 5.11. When the softening slope is fixed, a generalised Maxwell chain has two limiting cases: when the loading rate is either infinitely high or infinitely low. The intermediate loading rates will result in a stress-strain curve positioned in-between. This property was used to develop equations for the viscoelastic strain-softening law. The ultimate strain ε_u will now depend on the loading rate $\dot{\varepsilon}$ through the effective stiffness E_α^{ef}:

$$\varepsilon_u = \frac{2G_c}{\sigma_t w_c} - \frac{\sigma_t}{E_0 + \sum E_\alpha} + \varepsilon_0 \qquad (5.27)$$

$$\varepsilon_0 = \frac{\sigma_t}{E_0 + \sum E_\alpha^{\mathrm{ef}}} \qquad (5.28)$$

where E_α^{ef} is connected to the loading rate through the varying time step Δt according to Eq. (5.25). In this way, the decrease in the loading rate will result in the growth of
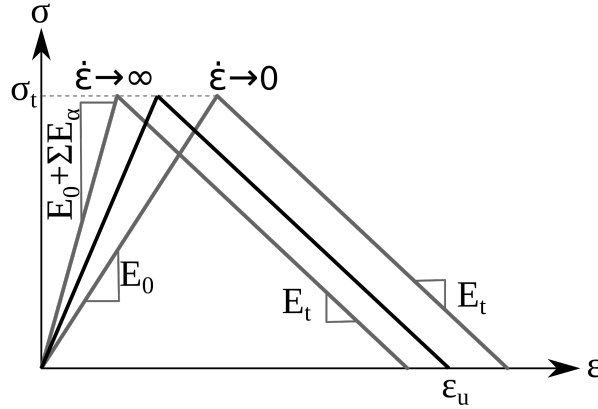
Figure 5.11: Constitutive law combining viscoelasticity with damage. Two cases with the limiting loading rates and the intermediate one.

ε_u with the slope E_t remaining unchanged.

The modified algorithm of the sequentially linear analysis introduced in the previous chapter is applied. The modified SLA supposes that every solution in time is obtained via a direct jump from zero displacements to the current loading. The solution obtained in such manner differs from the one obtained incrementally (using information from the previous steps). It happens because of the proposed scheme not taking into consideration the loading history between the initial and the current step: loading is assumed to increase linearly. This approximate way of solving a viscoelastic problem will introduce a certain error. However, it is argued that for relatively short relaxation times λ this difference will be less pronounced. This is demonstrated in Fig. 5.12. A single finite element of the viscously softening mortar is deformed by strain ε. The element does not experience any damage. Sequential and incremental stress values differ from each other by $5 - 10\%$. In the case of the sigmoidal loading profile in Fig. 5.12a, the sequentially computed stress slightly exceeds the incremental one. In the later stage, it steadily tends towards the incremental curve due to the stronger stress relaxation. This loading profile is of primary interest since it is similar to the one used for the ASR product expansion, which is discussed in Section 5.3.3. It is concluded that the proposed solution technique is approximate and has some error that could be controlled. This model is therefore used for the qualitative study of the viscous-softening behaviour of the mortar.

5.3.3 Simulations of the free-expansion experiments

To study the effects of the viscoelasticity on the damaging process, the ASR deterioration of a freely-expanding concrete specimen is modelled. The same two-dimensional problem introduced in the first study of this chapter is used and depicted in Fig. 5.5. Free expansion boundary conditions are applied. In a same manner, the model comprises the
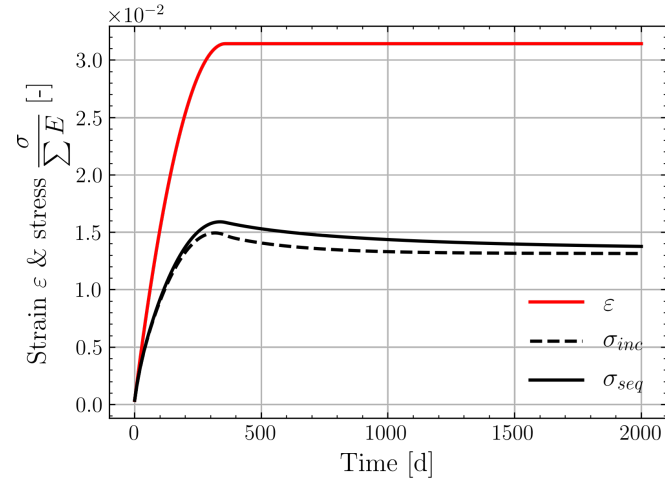
(a)
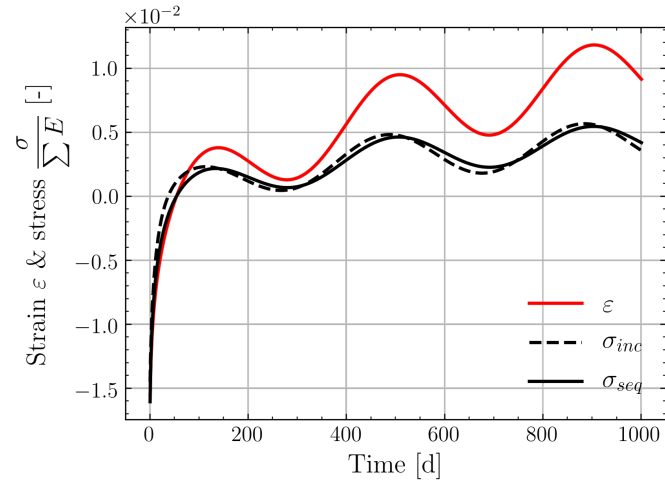
(b)

Figure 5.12: Comparison of stresses in a viscoelastic material computed in the incremental and sequential manners: a) sigmoidal and b) sinusoidal loading.

Property / material	Aggregates	Mortar (elastic softening)	Mortar (viscous softening)	ASR product
Single spring stiffness E_0 [GPa]	60	19	6	11
Maxwell stiffness E_i / relaxation time λ_i [GPa/days]	-	-	5/0.5 6.5/20 1.5/67	-
Poisson ratio ν_i [-]	0.3	0.3	0.3	0.18
Tensile strength σ_t [MPa]	10	4	4	-
Fracture energy G_c [J/m^2]	160	80	80	-

Table 5.3: Material properties of the simulations with elastically and viscously softening mortar.

aggregates and the mortar. The latter accounts for the aggregates and sand particles smaller than the finite elements size ($h = 0.5\,\mathrm{mm}$) and the cement paste. Two simulations with elastically and viscously softening mortar are performed. The material parameters are given in Table 5.3. The viscoelastic properties of the mortar were calibrated on the experiments on uniaxial loading of 28 day-old concrete by L'Hermite et al. (1965). The stiffness of the elastically-softening mortar is chosen to be equal to the sum of the spring stiffnesses in the Maxwell chain of the viscously softening mortar. In this way, the elastic material behaves as if it would be a viscoelastic one under infinitely fast loading. Such a choice of the material properties facilitates fair comparison of two simulations.

Concrete undergoing free ASR expansion was simulated for 450 days at the temperature of $38°C$. The damage patterns obtained in case of the elastically and viscously softening mortar are shown in Fig. 5.13. In both cases, the damage is mainly spread within the mortar due to its lower tensile strength. It is observed that in case of the elastically softening mortar, the damaged area is larger. This becomes evident in Fig. 5.14b, which plots the damage ratio. The latter is computed as the ratio between the damaged area of a concrete phase and its total area. To compute this parameter, area of each damaged element was multiplied by its damage value d, summed all together and divided by the total area of the phase. Damage ratio in the elastically softening mortar is by 5% higher than in its viscoelastic counterpart. The difference in the damage ratio is caused by the lower values of stress within viscously softening material due to the stress relaxation. The damage ratio in aggregates saturates at the value of 2% already at 120 days. This effect is caused by having all the cracks reaching exteriors of aggregates.

Fig. 5.14a shows macroscopic expansion of the numerical specimens, experimental expansion by Multon and Toutlemonde (2006) and expansion of the ASR sites. In this specific distribution of ASR sites, a major crack percolate in the horizontal direction (see Fig. 5.13). It has wide opening in the vertical direction forcing the corresponding
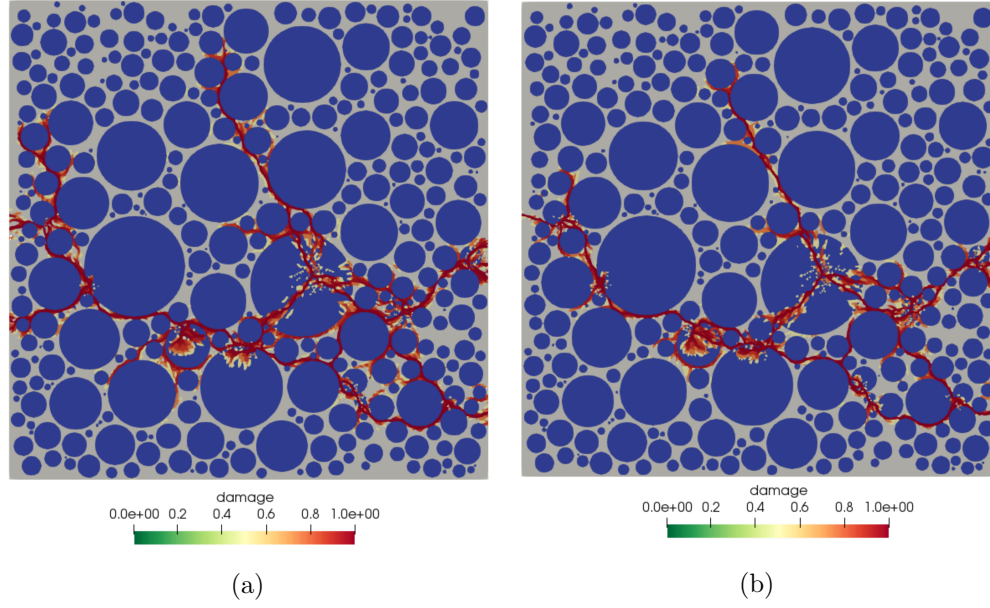
Figure 5.13: Damage patterns in concrete blocks with a) the elastically and b) viscously softening mortar. Colours denote the level of damage.

macroscopic strain ε_y to be larger than the horizontal one ε_x. Although these two curves differ significantly, their mean value is close to the calibration curves. Expansion of the viscously softening mortar in the same figure is similar in the vertical direction but much lower in the horizontal one. This fact is again caused by shorter cracks in the viscously softening paste and hence lower expansion. The average between the horizontal and vertical values becomes lower than the calibration data. The expansion curves follow the behaviour of the ASR product expansion ε_{eig}.

Stiffness reduction estimated in tension is plotted in Fig. 5.15a. Here, one can observe almost total stiffness loss in the vertical direction due to the percolated crack. In the other direction, stiffness drops to $40 - 50\%$ of its initial value due to the vertical cracks yet not reaching the specimen boundaries. Stiffness reduction in the horizontal direction is higher in the elastic-softening case. This is also explained by the elastically-softening mortar having longer cracks in the vertical and close to the vertical directions.

When adding the viscoelasticity to the mortar, a lower stiffness drop is observed. This also results in the reduction of the macroscopic strain due to the shortening of cracks. The reduced strains are lower than the ones observed by the experimentalists. It is suggested that the total damage observed in the concrete (either in mortar or in aggregates) is insufficient to reach the experimental values of expansion. To prove that the damage is the main cause of the macroscopic expansion, two simulations are run, where the mortar is modelled either purely elastically or viscoelastically without any damage. The results are plotted in Fig. 5.15b. The elastic and viscoelastic expansion
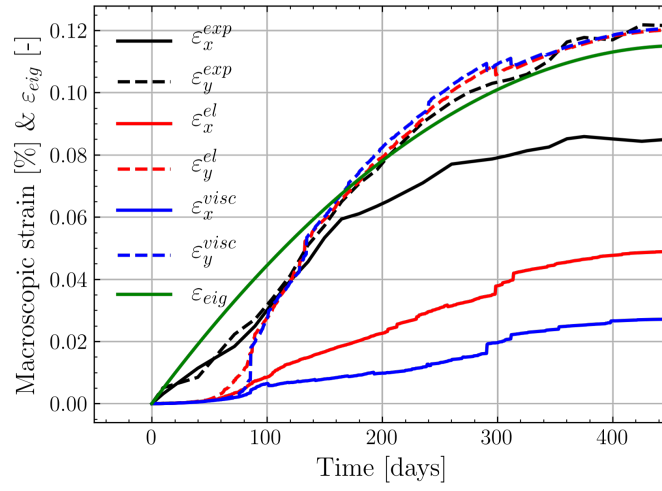
(a)
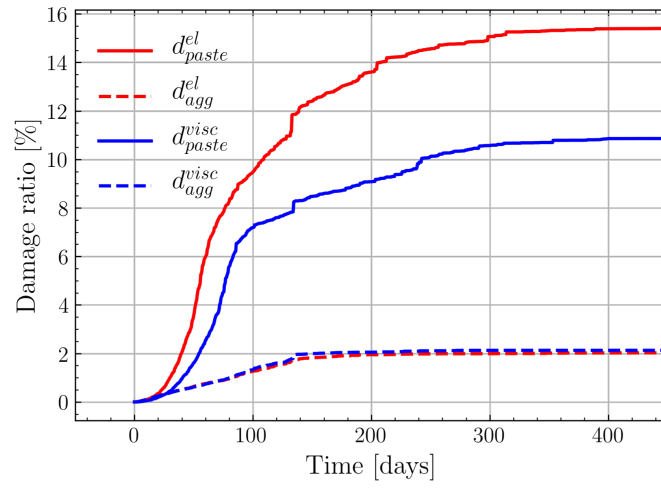
(b)

Figure 5.14: a) Macroscopic expansion of the concrete specimen and b) its damage ratios per phase.
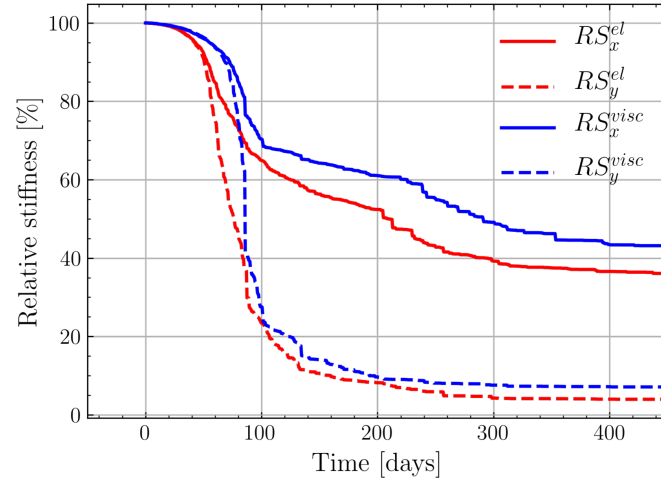
(a)
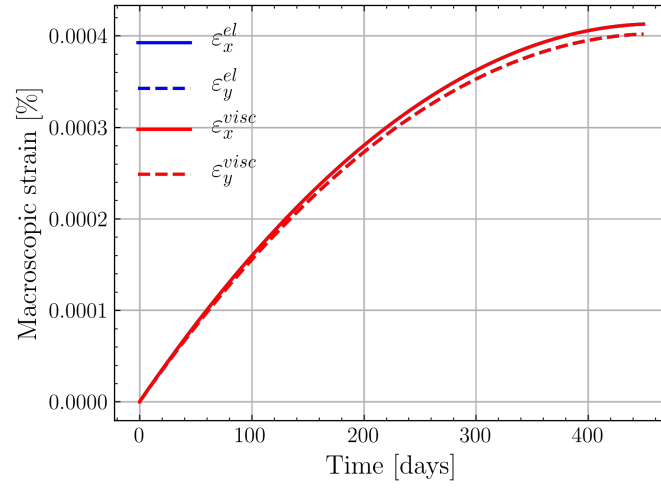
(b)

Figure 5.15: a) Stiffness reduction for the elastic- and viscous-softening cases. b) Macroscopic expansion for the purely elastic and viscoelastic cases without damage.

curves overlap in the absence of damage. The final value of the expansion is three orders of magnitude lower than in the brittle case. This demonstrates that purely (visco-) elastic deformations are not sufficient to bring the macroscopic expansion to the experimental levels. Therefore, the damage is required.

Giorla et al. (2015) also reported little damage in the viscoelastic cement paste which corresponded to the general observations in experiments. However, the macroscopic expansions were lower than the experimental values of Haha et al. (2007). As a possible cause, the authors suggested the fact that the smaller aggregates were not reactive in their simulations. To verify their hypothesis, additional simulations are required.

5.4   Conclusions

The damage-based meso-scale numerical model of concrete deterioration due to the ASR has been presented. Aggregates and mortar are explicitly represented. Two different material laws were introduced in this model. The first one allows orthotropic reduction of elastic properties upon crack nucleation and their recovery upon crack closure and self-contact. The second material law combines isotropic linearly growing damage with viscoelasticity. It was shown that the orthotropic constitutive law better mimics the macroscopic expansion and the stiffness loss observed in the laboratory experiments than a simple isotropic law. The meso-scale model with orthotropic continuous damage is stable and does not pose convergence issues. Its adequate computational efficiency permitted conducting the Monte Carlo simulation with varying concrete meso-structure.

Extension of the elastically-softening material behaviour by viscoelasticity has been formulated and demonstrated on an example. Combination of the generalised Maxwell chain with the sequentially linear analysis resulted in an approximate solution technique permitting qualitative analysis of the ASR problem. The proposed solution algorithm is easily implementable in a standard FE package. To understand the role of the viscoelasticity in the ASR damaging process, simulations with the elastically and viscously softening cement paste were compared. The results are summarised below:

- Macroscopic expansion of the ASR-affected specimens is mainly caused by the crack growth and opening. Direction of the major expansion is orthogonal to the prevailing crack path.

- Macroscopic strain follows the expansion of the ASR sites.

- Viscous-softening behaviour of mortar leads to relaxation of stresses and reduction of damage. It preserves the macroscopic stiffness but also reduces the macroscopic expansion of concrete.

6 Multi-scale modelling of ASR-affected structures

After the mechanics of the ASR at the nano- and meso-scales were studied, the obtained knowledge and the developed models are used to predict the macroscopic behaviour of ASR-affected concrete. One way to pass the information on the important physics from one scale to another is through the multi-scale model, which establishes a link between the meso- and the macro-scales. The development of such a multi-scale model of the ASR-affected concrete, which would naturally capture the expansion anisotropy effect, is the objective of the current chapter. A finite element approach based on the first-order FE^2 homogenisation technique is formulated. It is used to analyse the ASR-induced damage in concrete structures, by linking the concrete degradation at the macro-scale to the reaction extent at the meso-scale. Here, the meso-scale concrete model described in the previous chapter is used. A 2D model of an ASR laboratory specimen is analysed as a proof of concept. The model accounts for the loading applied at the macro-scale and the ASR-product expansion at the meso-scale. The results of this proof-of-concept study have been published by Gallyamov et al. (2020).

The model is used for the analysis of a concrete gravity dam in Western Switzerland. Results of a simulation, calibrated on the field measurements and observations, suggest limited effect of the temperature variation on the ASR advancement in the dam: field displacements could have been reproduced by assigning a constant temperature within an entire dam cross-section. Study of the structural effects shows that the ASR-related expansion anisotropy and cracks alignment is more pronounced along the upstream part and the foundation of the dam. The results of this study of the dam were submitted to a journal and are currently under review.

The future usage of the developed model is meant for scientists, dam engineers and dam owners in order to understand the interplay between the mesoscopic state of concrete and macroscopic behaviour of a structure. The level of details at the meso-scale facilitates visualisation of phenomena at hand, which is hindered by pure macroscopic models. Apart from explaining the current behaviour of an ASR-affected structure, given

enough field measurements for calibration, the model could be used for predictions of the structure's future behaviour. Such opportunity is crucial for the dam owning companies as it allows making well-timed planning and preview necessary interventions.

6.1   ASR multi-scale model

Modelling the ASR at the structural-scale by incorporating the results of the meso-scale simulations is done with the use of a first-order FE^2 homogenisation scheme. This method consists of two coupled finite element problems, one for the macro-scale and the other for the fine scale, *i.e.* the scale of the underlying representative volume element (RVE) that determines the effective material behaviour. Note that in this work, the fine scale of the FE^2 problem is the meso-scale of concrete. The FE^2 method is based on the principle of *separation of scales*, which has been formulated as *"The microscopic length scale is assumed to be much smaller than the characteristic length over which the macroscopic loading varies in space"* by Geers et al. (2010). This assumption is valid for the multi-scale modelling of the ASR, since large concrete structures have several tens of meters of width and height, and a meso-scale RVE is in the centimetre range. The concept of a first-order FE^2 homogenisation scheme for small deformations is illustrated in Fig. 6.1. The first version of this model was developed by Cuba Ramos (2017). It incorporated isotropic damage at the meso-scale and had no iterative procedure in place due to its high computational cost. Instead of the homogenised fine-scale stress, the homogenised eigen strain was transmitted to the macro-scale. Given a small time step, this model permitted modelling macro-scale structures in a stable manner. In the current work, the iterative procedure is introduced into the preceding model, enrich its meso-scale physics and couple mechanical and thermal analyses.

Note that in the following, the subscripts M and m will be used to denote physical quantities at the macro- and the meso-scale, respectively. For instance, $\boldsymbol{\sigma}_M$ is the macroscopic stress for which the mesoscopic counterpart is $\boldsymbol{\sigma}_m$. Every Gauss integration point of the macro-scale FE problem is coupled to a meso-structural RVE of concrete. Quasi-static conditions are assumed at both scales because the advancement of the ASR is slow. The two scales are coupled through the macroscopic deformation gradient $\boldsymbol{F}_M$, the effective stiffness tensor $\mathbb{C}_M$, and the macroscopic stress $\boldsymbol{\sigma}_M$. The boundary conditions of the meso-scale boundary value problem (BVP) are a function of $\boldsymbol{F}_M$. The BVP is solved for the given boundary conditions. Macroscopic temperature T_M is passed to the meso-scale for predicting the ASR product expansion rate. The effective stiffness tensor $\mathbb{C}_M$ and the homogenised mesoscopic stress $\boldsymbol{\sigma}_M$ are then computed and passed back to the macro-scale. The balance between the internal and external forces at the macro-scale is verified. In the case of imbalance, the whole procedure is repeated in the next iteration. As a convergence criterion, the norm of the difference between the internal and external forces, also known as *residual*, is used.

Macro-scale

$\mathbb{C}_M, \sigma_M$

$\mathbf{F}_M, T_M$

Meso-scale

ASR advancement
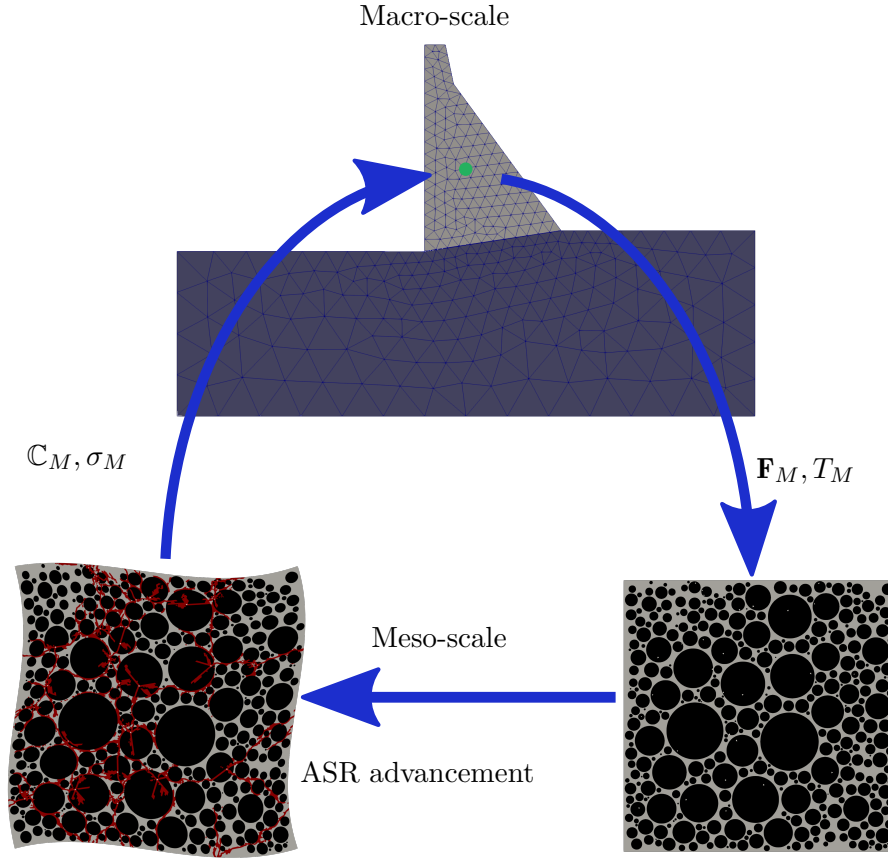
Figure 6.1: Schematic illustration of the numerical homogenisation scheme for the ASR simulations. Every macroscopic computational point is coupled to an underlying RVE. The boundary conditions for the RVE are defined through the macroscopic deformation gradient $\boldsymbol{F}_M$. Macroscopic temperature T_M is passed to the meso-scale for predicting the ASR product expansion rate. After solving the RVE problem, the macroscopic stress $\boldsymbol{\sigma}_M$ and the effective stiffness tensor $\mathbb{C}_M$ are computed.

During the evolution of the ASR within RVEs, cracks may coalesce and therefore violate the separation of scales' principle. The strain localisation limits the concept of homogenisation (Coenen et al., 2012a). The validity of the numerical homogenisation is used for a problem where cracks are evenly distributed over the meso-scale volume. The following model components are called to extend the applicability of the classical homogenisation concept to the ASR case:

- **Extended constitutive model of concrete:** the material model adopted in this study is the continuous orthotropic damage with self-contact in cracks, previously described in Section 5.2.1.

- **Robust stiffness homogenisation procedure:** this measure is called to overcome the ill-posedness of the macro-scale boundary value problem. This is done by an adaptive homogenisation of stiffness either by tension or by compression tests, which produce a non-singular stiffness tensor. The resulting tensors are better suited for the macroscopic stress state, which also improves the convergence rate of the iterative scheme. The homogenisation procedure is described in Section 6.1.4.

One distinctive feature of the current multi-scale model is the fact that the external loading is not only coming from the macro-scale, but also from the fine scale in the form of expanding ASR product. The interplay between these two load scales is interesting both from the physical and the numerical point of view.

The proposed multi-scale model is two-dimensional. This limitation is caused by its high computational cost, which mainly comes from the fine resolution of RVEs and the adopted way of solving the BVP. However, the concept of the proposed approach is universal, and the model could be easily extended to 3D given enough computational powers. Similar to many other 2D multi-scale models, this study aims to investigate the physics at hand while being aware of the possible limitations.

6.1.1 Macro-scale problem

Let Ω_M denote a body of the ASR-affected concrete at the macro-scale. The domain is bounded by Γ_M, which can be decomposed into the Neumann boundary $\Gamma_{M,t}$ and the Dirichlet boundary $\Gamma_{M,u}$, such that the following definitions hold:

$$\Gamma_M = \Gamma_{M,u} \cup \Gamma_{M,t} \tag{6.1}$$

$$\Gamma_{M,u} \cap \Gamma_{M,t} = \emptyset \tag{6.2}$$
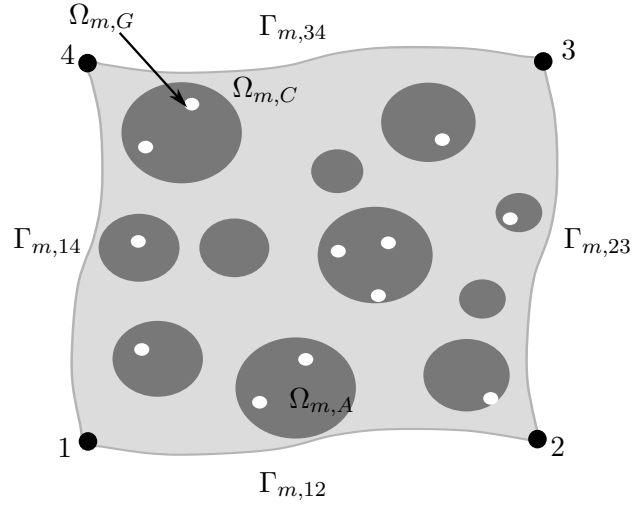
Figure 6.2: Periodically deformed RVE of concrete with three mutually exclusive phases: cement paste $\Omega_{m,C}$, aggregates $\Omega_{m,A}$ and ASR sites $\Omega_{m,G}$. The four edges are denoted by $\Gamma_{m,12}$, $\Gamma_{m,23}$, $\Gamma_{m,34}$ and $\Gamma_{m,14}$.

The principle of virtual work reads as:

$$\delta W_M = \int_{\Omega_M} \boldsymbol{\sigma}_M : \boldsymbol{\varepsilon}_M(\delta \boldsymbol{u}_M) \, d\Omega - \int_{\Omega_M} \boldsymbol{b}_M \cdot \delta \boldsymbol{u}_M \, d\Omega - \int_{\Gamma_{M,t}} \boldsymbol{t}_M \cdot \delta \boldsymbol{u}_M \, d\Gamma = 0 \quad (6.3)$$

where δW_M, $\boldsymbol{b}_M$ and $\boldsymbol{t}_M$ denote the macroscopic virtual work, the macroscopic body-force and traction vectors, and $\boldsymbol{\varepsilon}_M(\delta \boldsymbol{u}_M)$ and $\delta \boldsymbol{u}_M$ the macroscopic virtual-strain and virtual-displacement vectors. No assumptions are introduced regarding $\boldsymbol{\sigma}_M$. Instead, it is obtained directly from the meso-scale computations as explained in Section 6.1.4 and Section 6.1.5.

6.1.2 Meso-scale problem

The meso-scale problem was introduced in the previous chapter. A periodically deformed RVE comprising aggregates, cement paste and ASR sites is depicted in Fig. 6.2. The damage in the aggregates and the cement paste is modelled orthotropically with self-contact in cracks. Viscoelasticity, discussed in the previous chapter, is not taken into account to simplify the computations.

6.1.3 Macro-to-meso transition

The displacement field inside an RVE can be decomposed into two parts:

$$\boldsymbol{u}_m(\boldsymbol{x}) = \boldsymbol{u}_M + \hat{\boldsymbol{u}}(\boldsymbol{x}), \quad (6.4)$$

where $\hat{\boldsymbol{u}}(\boldsymbol{x})$ are the micro-fluctuations. The current macroscopic state enters the RVE computations via the boundary conditions. In this work, periodic boundary conditions are chosen because they give better estimates for the effective stiffness in comparison with the uniform displacement or uniform traction boundary conditions (Coenen et al., 2012a). The periodic boundary conditions are defined as follows:

$$\boldsymbol{u}_{m,i} = (\boldsymbol{F}_M - \boldsymbol{1})\boldsymbol{x}_{m,i} \quad \text{for } i = 1, 2, 3, 4 \tag{6.5a}$$

$$\boldsymbol{u}_{\Gamma_{m,34}} = \boldsymbol{u}_{\Gamma_{m,12}} + \boldsymbol{u}_{m,4} - \boldsymbol{u}_{m,1} \tag{6.5b}$$

$$\boldsymbol{u}_{\Gamma_{m,23}} = \boldsymbol{u}_{\Gamma_{m,14}} + \boldsymbol{u}_{m,2} - \boldsymbol{u}_{m,1} \tag{6.5c}$$

where $\boldsymbol{F}_M$ denotes the deformation gradient at the corresponding macroscopic material point, $\boldsymbol{u}_{m,i}$ is the displacement of the corner node i, and $\Gamma_{m,12}$, $\Gamma_{m,23}$, $\Gamma_{m,34}$ and $\Gamma_{m,14}$ are the boundaries of the RVE (see Fig. 6.2). While the terms $[\boldsymbol{u}_{m,4} - \boldsymbol{u}_{m,1}]$ and $[\boldsymbol{u}_{m,2} - \boldsymbol{u}_{m,1}]$ represent the macroscopic component of displacement, $\boldsymbol{u}_{\Gamma_{m,12}}$ and $\boldsymbol{u}_{\Gamma_{m,14}}$ are the periodic micro-fluctuations at the boundary pairs ($\Gamma_{m,12}$ and $\Gamma_{m,34}$) and ($\Gamma_{m,14}$ and $\Gamma_{m,23}$), correspondingly.

6.1.4 Meso-to-macro transition

The stress distribution inside an RVE is obtained through the solution of the meso-scale boundary value problem. For the macro-scale, the average stress response of an RVE needs to be determined. This can be done using the *Hill-Mandel* macro-homogeneity condition (Hill, 1963)

$$\frac{1}{\Omega_m} \int_{\Omega_m} \boldsymbol{\sigma}_m : \boldsymbol{\varepsilon}_m \, \mathrm{d}\Omega_m = \boldsymbol{\sigma}_M : \boldsymbol{\varepsilon}_M \tag{6.6}$$

Note that $\boldsymbol{\sigma}_m$ and $\boldsymbol{\varepsilon}_m$ are coupled to their macroscopic counterparts via the following equations:

$$\boldsymbol{\sigma}_m = \boldsymbol{\sigma}_M + \hat{\boldsymbol{\sigma}} \tag{6.7}$$

$$\boldsymbol{\varepsilon}_m = \boldsymbol{\varepsilon}_M + \hat{\boldsymbol{\varepsilon}} \tag{6.8}$$

where $\hat{\boldsymbol{\sigma}}$ and $\hat{\boldsymbol{\varepsilon}}$ are the micro-fluctuations of the stress and the strain fields, respectively. The *Hill-Mandel* macro-homogeneity condition implies that the work of the stress fluctuations $\hat{\boldsymbol{\sigma}}$ on the strain fluctuations $\hat{\boldsymbol{\varepsilon}}$ vanishes, *i.e.*

$$\frac{1}{\Omega_m} \int_{\Omega_m} \hat{\boldsymbol{\sigma}} : \hat{\boldsymbol{\varepsilon}} \, \mathrm{d}\Omega_m = 0 \tag{6.9}$$

Therefore, $\hat{\boldsymbol{\sigma}}$ and $\hat{\boldsymbol{\varepsilon}}$ must be orthogonal to each other. The macroscopic stress can be expressed in terms of traction along the boundaries of the RVE:

$$\boldsymbol{\sigma}_M = \int_{\Gamma_m} \boldsymbol{t}_m \otimes \boldsymbol{x}_m \, \mathrm{d}\Gamma_m \tag{6.10}$$

It was shown by Suquet (1987) that the boundary conditions presented in Section 6.1.3 fulfil the *Hill-Mandel* condition and yield equivalence between the macroscopic stress and volume average of the mesoscopic stresses inside the RVE:

$$\boldsymbol{\sigma}_M = \int_{\Gamma_m} \boldsymbol{t}_m \otimes \boldsymbol{x}_m \, \mathrm{d}\Gamma_m = \frac{1}{\Omega_m} \int_{\Omega_m} \boldsymbol{\sigma}_m \, \mathrm{d}\Omega_m \tag{6.11}$$

The above equation is used for the stress homogenisation at the meso-scale.

For the macro-scale analysis, a tangent stiffness tensor is required at each integration point. The effective stiffness tensor is defined by the effective stress-strain relation

$$\boldsymbol{\sigma}_M = \mathbb{C}_M \boldsymbol{\varepsilon}_M. \tag{6.12}$$

Both, $\boldsymbol{\sigma}_M$ and $\boldsymbol{\varepsilon}_M$ are symmetric second-order tensors with three independent components in 2D. There are multiple methods of stiffness homogenisation available in the literature. The one proposed by Kouznetsova et al. (2001) comprises rearrangement of the full RVE stiffness tensor and its condensation with the help of position vectors of the fixed corner nodes. Miehe (1996) has suggested a method based on a forward difference approximation. In the present work, the virtual-tests approach is adopted, the mathematical formulation of which is thoroughly described by Fritzen (2011). In the scope of this method, the results of three virtual loading tests, linearly independent from each other, are required to determine the symmetric fourth-order tensor $\mathbb{C}_M$.

For a specimen with isotropic stiffness reduction in cracks and no self-contact, tensile and compressive loading tests would result in the same tensor $\mathbb{C}_M$. However, a material with orthotropic damage and stiffness recovery will behave differently under tension than under compression, as it was previously demonstrated in Section 5.2. While pulling a specimen would only open the cracks perpendicular to the load, its compression will close them and cause stresses in the bulk. This is however a simplification of a problem. In reality, cracks could be oriented in different directions, and the opening of one crack could be accompanied by the closing of another. In general, the stiffness obtained via compression is higher than the one computed via tension. The effect of the test type on the stiffness reduction is described in Section 5.2.2.

Since the homogenised stiffness is used to solve the macro-scale problem for displacements, the better it approximates the stiffness of the meso-scale structure, the faster the multi-scale scheme converges. Providing low tensile stiffness for an element which undergoes compression would result in an underestimation of its stress level and thus slow

convergence of the iterative scheme. Similarly, providing high compressive stiffness for a tensioned element will result in a similar issue. In order to avoid this nonconformity, the direction of the stiffness homogenisation tests is decided based on the stress sign. For this, the hydrostatic part is extracted from the averaged mesoscopic RVE stresses, and its value is used to judge on the stress state of the macroscopic element. If the hydrostatic stress is positive, then two uniaxial tensile tests are done, if it is negative - two compression tests. The uniaxial tests are performed in the horizontal and vertical direction. Additionally to the uniaxial tests, one pure shear test is done.

For each virtual-loading test, the effective stress and strain can be computed. Using a normalised Voigt basis $\{\boldsymbol{B}^\alpha\}_{\alpha=1,\dots,3}$ and the notation introduced in Fritzen (2011) yields the following system of linear equations:

$$\hat{C}_M \hat{E} = \hat{\Sigma} \qquad \text{with} \tag{6.13a}$$

$$\hat{E}_{\alpha\beta} = \boldsymbol{B}^\alpha \cdot \overline{\boldsymbol{\varepsilon}}^\beta \tag{6.13b}$$

$$\hat{\Sigma}_{\alpha\beta} = \boldsymbol{B}^\alpha \cdot \overline{\boldsymbol{\sigma}}^\beta \tag{6.13c}$$

$$\hat{\hat{C}}_{\alpha\beta} = \mathbb{C}_M \cdot \boldsymbol{B}^\alpha \otimes \boldsymbol{B}^\beta \tag{6.13d}$$

6.1.5   Nested multi-scale approach

As discussed in Section 6.1.3, the boundary conditions for the RVEs are prescribed in terms of the macroscopic deformation gradients. The macroscopic displacements, however, are not known *a priori* and depend on the deformation process inside the RVEs. In the multi-scale approach adopted here, a deformation-driven iterative procedure is applied, where an initial macroscopic deformation is imposed and a series of solve steps are performed until reaching convergence. Subsequently, both the macroscopic and mesoscopic loads can be increased, and the next iteration starts.

The homogenised mesoscopic stress passed to the macro-scale serves both to judge on the convergence of iterations and also to update the displacements at the macro-scale. The global macroscopic stiffness matrix, composed of the homogenised stiffness matrices of the underlying RVEs, is used at the macro-scale to compute the increment of displacements. The algorithm for the current multi-scale implementation, executed by every processor, is detailed in Algorithm 4.

Algorithm 4 Multi-scale algorithm for the ASR-affected concrete

---
1: **for** every integration point at the macro-scale
2:     Generate an RVE
3: **for** every time step i
4:     Apply boundary conditions at the macro-scale
5:     **for** every RVE
6:         Compute ASR products expansion value
7:         Impose expansion at the ASR sites
8:     **while** solution is not converged
9:         Solve the macro-scale problem
10:         **for** every RVE
11:             Collect deformation gradient from the macro-scale
12:             Apply it as boundary conditions
13:             **while** finite elements are damaged
14:                 Solve the meso-scale problem
15:                 Reduce material properties of the damaged elements (SLA)
16:             Homogenise stress
17:             Determine hydrostatic component of the homogenised stress
18:             Homogenise the RVE stiffness
19:         Assemble global stiffness matrix
20:         Assemble macro-scale internal force
21:         Check for convergence
22:     Output results

6.1.6 Parallel implementation

The current ASR multi-scale model was implemented into the open-source finite-element library Akantu (Richart and Molinari, 2015; Cuba Ramos, 2017). The coding developments were carried out under the premise that the meso-scale computations for a single RVE are executed in serial. Therefore, the FE meshes of the RVEs must be small in size, which is the case for two-dimensional numerical concrete samples containing only the coarse aggregates. The parallel computation scheme of the multi-scale model is illustrated in Fig. 6.3. At the beginning of the simulation, the macro-scale FE mesh is partitioned among all available processors. Every processor generates an RVE per each integration point belonging to macroscopic finite elements.
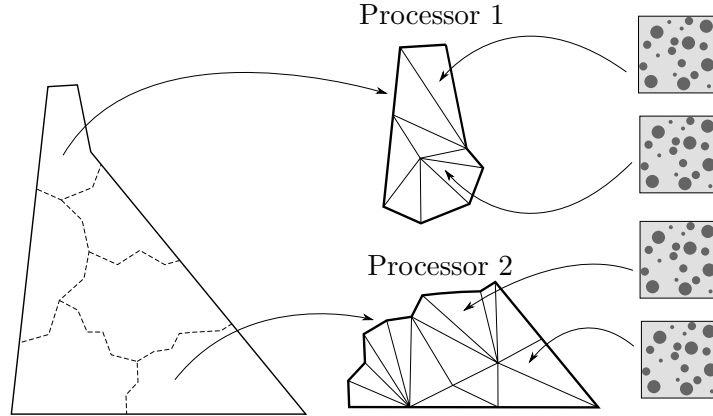
Figure 6.3: Parallel computation scheme for the multi-scale ASR simulations: the macroscopic finite-element mesh is partitioned among all available processors. Each processor generates RVEs for the elements it owns. The RVEs are then used for the meso-scale computations. Inspired by Cuba Ramos (2017).

6.2   Multi-scale model verification

The meso-scale model was previously calibrated in Section 5.2.2 with the material and expansion law parameters listed in Table 5.1. Here, the predictive capacities of the multi-scale model are validated. The test case is based on the previously-used laboratory experiments by Multon and Toutlemonde (2006) as a macro-scale structure. This allows us to verify the ASR multi-scale model and to provide the proof of concept for the method. Although the separation of scales concept does not hold anymore, this choice allows a direct comparison between the results of the FE^2-simulation and the experimental measurements. Another advantage of this setup is its simple stress state, which is not the case for a large operating structure such as a dam or a bridge pier. By applying a load at the macro-scale, one can directly observe how it is balanced by the internal forces at the meso-scale. Fig. 6.4 shows the multi-scale setup used for the validation test. The size of the numerical macro-scale specimen is 140×280 mm^2, while the RVE size is kept the same as the one used previously (70×70 mm^2). In the present case, each finite element at the macro-scale is linked to an underlying RVE, which represents the heterogeneous structure of concrete at the meso-scale. The total number of RVEs corresponds to the number of finite elements in the macroscopic FE mesh because each macroscopic finite element contains only one integration point. The macro-scale mesh is coarsely discretised in order to keep the macro-element size larger or equal to the RVE size, in partial accordance with the separation of scales concept. From the computational point of view, the macro-scale problem could be easily discretized by a much denser mesh.

The laboratory experiments of Multon (2004) were performed at 38°C temperature. Since the temperature field is homogeneous within the specimen, a constant single value
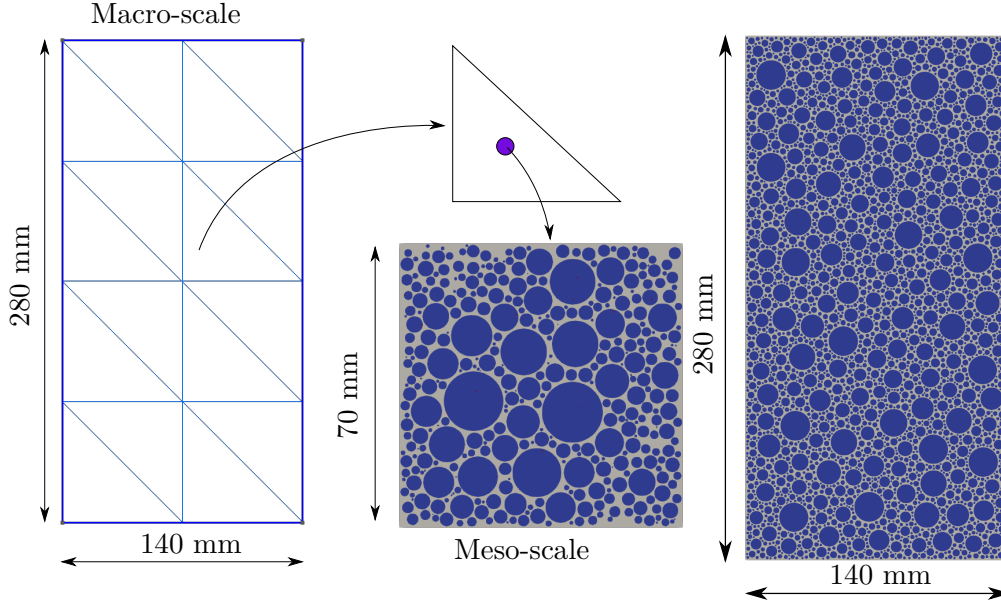
Figure 6.4: Meshes used for the multi-scale simulation. Each of 16 macroscopic finite elements has a square concrete RVE at the meso-scale.

Figure 6.5: Mesh for the detailed macro-scale simulation used for the comparison with FE^2.

T_M is passed to all RVEs during the entire simulation.

For comparison, fully detailed simulations of the macro-scale structure were performed. The mesh for these simulations is shown in Fig. 6.5. In both models, the density of the ASR sites and the parameters of the ASR product expansion law from the calibration tests are used (see Table 5.2). The two following tests were performed: free expansion and uniaxial compression with 10 MPa. These two stress values were chosen as the limiting values of the possible stress variation in a massive concrete structure undergoing the ASR. As the statistical distributions of the output parameters were studied in the previous chapter, here, the study is limited to a single realisation of both the multi-scale and the fully detailed models.

Expansion curves from the multi-scale simulations are plotted in Fig. 6.6 next to the ones coming from the fully detailed macro-scale model. The multi-scale expansion values were obtained by averaging the individual strain values at the macro-scale integration points. One can see a good match between the two sets of curves in both simulations. Naturally some differences remain between the multi-scale and detailed macro-scale simulations. Similar to the calibration simulations, there is a gap between the numerical lateral expansion value and its experimental counterpart.

The average crack density of the multi-scale simulations is plotted in Fig. 6.7, where
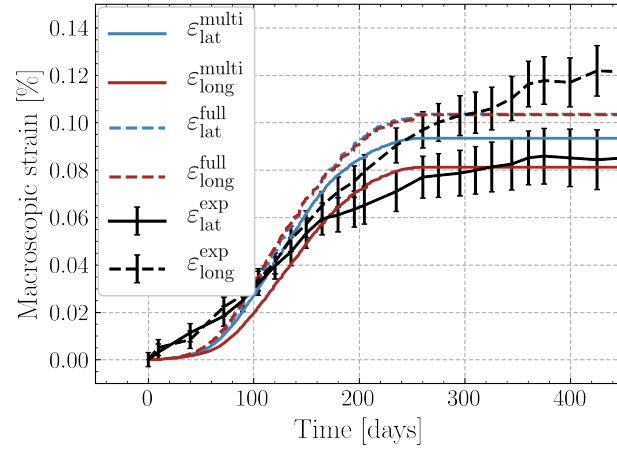
(a)
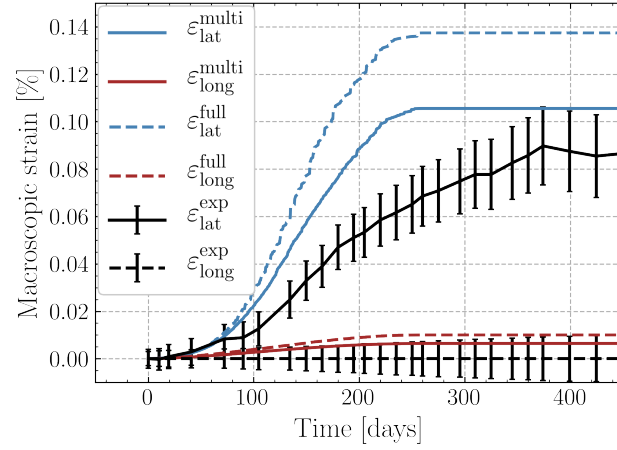
(b)

Figure 6.6: Expansion curves of the macroscopic specimen obtained by the multi-scale and fully resolved macro-scale simulations: a) the free-expansion experiment; b) the uniaxial compression by $10\,\mathrm{MPa}$. The experimental expansion curves are plotted for comparison.

the averaging was done over all RVEs. The FE^2 simulation of 10 MPa compression has the lowest crack area both in the aggregates and the mortar (0.05% and 0.29% correspondingly). It is followed by the free-expansion experiment with 0.07% of the aggregates and 0.42% of the mortar occupied by cracks.
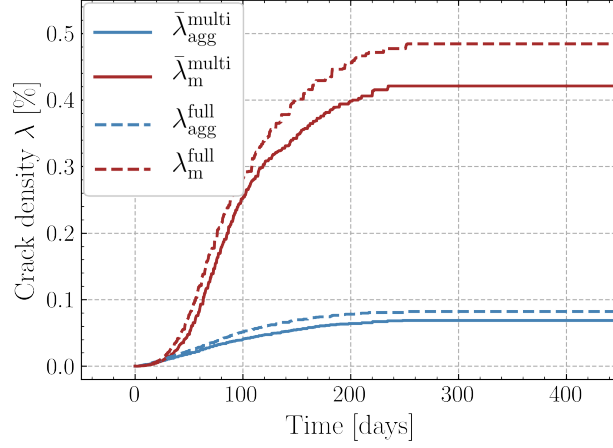
(a)
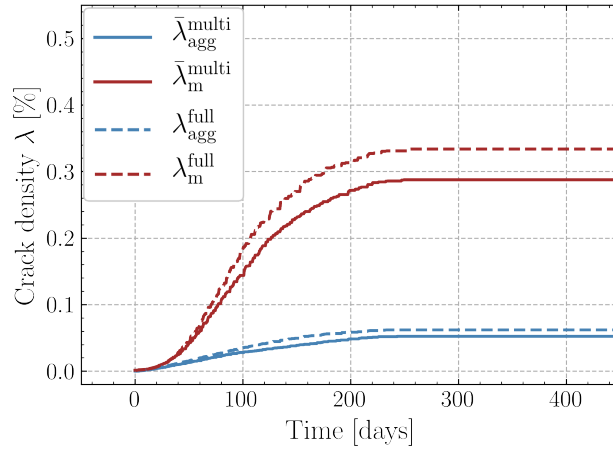
(b)

Figure 6.7: Average crack density for the a) the free and b) the loaded multi-scale simulations.

RVEs crack opening maps are shown in Figs. 6.8a and 6.8b. For comparison, similar images in the detailed macro-scale simulations are given in Figs. 6.8c and 6.8d. A similar amount of cracks and matching orientations in each pair of simulations are evident. The difference in crack volumes between the two loading cases is somehow expected. Compressive load pushes the stress state of each finite element further from the tensile failure envelop. In such case, the cracks are strongly localised and follow the direction

perpendicular to the maximum principal stress. In the case of the free-expansion experiment, the stress state is closer to the limits, therefore the cracks appear earlier and grow longer. The periodic boundary conditions applied at the RVEs cause cracks continuity across the borders. Artificial perpendicularity of the cracks to the periodic boundaries is a well-known issue, which also brings bias into the homogenised stiffness tensor. A possible solution was proposed by Coenen et al. (2012b), who proposed to align boundaries with the evolving localisation bands, enabling crack bands to grow slantwise to the boundaries directions. In future, this method could be adopted in the current model to enhance the crack patterns and stiffness estimation.

6.3 Macro-scale simulation of an ASR-affected dam

The objective of the current section is the analysis of the structural effects of the ASR within a dam by solving the concrete deterioration problem at the meso-scale level. The study aims at understanding the interplay between the macroscopic state of a dam (stresses, deformations and their anisotropy) and the mesoscopic state of concrete (amount of cracks, their percolation, opening and orientation). Moreover, the role of the seasonal temperature variation across the dam in the advancement of the ASR is studied. The model sensitivity to the temperature fluctuations in the field and laboratory conditions is compared. A 2D thermo-mechanical multi-scale model of a dam with a concrete meso-structure resolved numerically is employed. A unique set of continuous 67 years-long field measurements from an ASR-affected gravity dam in Western Switzerland allows for an improved model calibration and quantitative interpretation of the results.

The presented model is thermo-mechanical at the macroscopic scale and purely mechanical at the RVE level. However, the effect of temperature enters RVEs through the ASR-product expansion law. To facilitate the reading, the previously described equations of the expansion law are listed below:

$$\boldsymbol{\varepsilon}_{eig}(t,T) = \boldsymbol{\varepsilon}(\infty)\frac{1 - \exp[-t/\tau_{ch}(T)]}{1 + \exp[-t/\tau_{ch}(T) + \tau_{lat}(T)/\tau_{ch}(T)]}\mathbb{I} \tag{6.14a}$$

$$\tau_{ch}(T) = \tau_{ch}(T_0)\exp[U_C(1/T - 1/T_0)] \tag{6.14b}$$

$$\tau_{lat}(T) = \tau_{lat}(T_0)\exp[U_L(1/T - 1/T_0)] \tag{6.14c}$$

where t and T are the current time and temperature, τ_{lat} and τ_{ch} are the latency and characteristic times, T and T_0 are the current and the reference temperatures, U_C and U_L are the activation energy constants, $\mathbb{I}$ is the identity matrix and $\boldsymbol{\varepsilon}(\infty)$ is the asymptotic volumetric expansion strain in the stress-free experiment. The moisture diffusion process, which governs the evolution of the chemical reaction, is not taken into account, and it is assumed that the dam is fully saturated. Previous study by Comi et al. (2012) showed that, for the particular environmental conditions and water-reservoir level, this assumption is valid and only a thin layer of concrete in contact with air of about

(a)

(b)

(c)

(d)
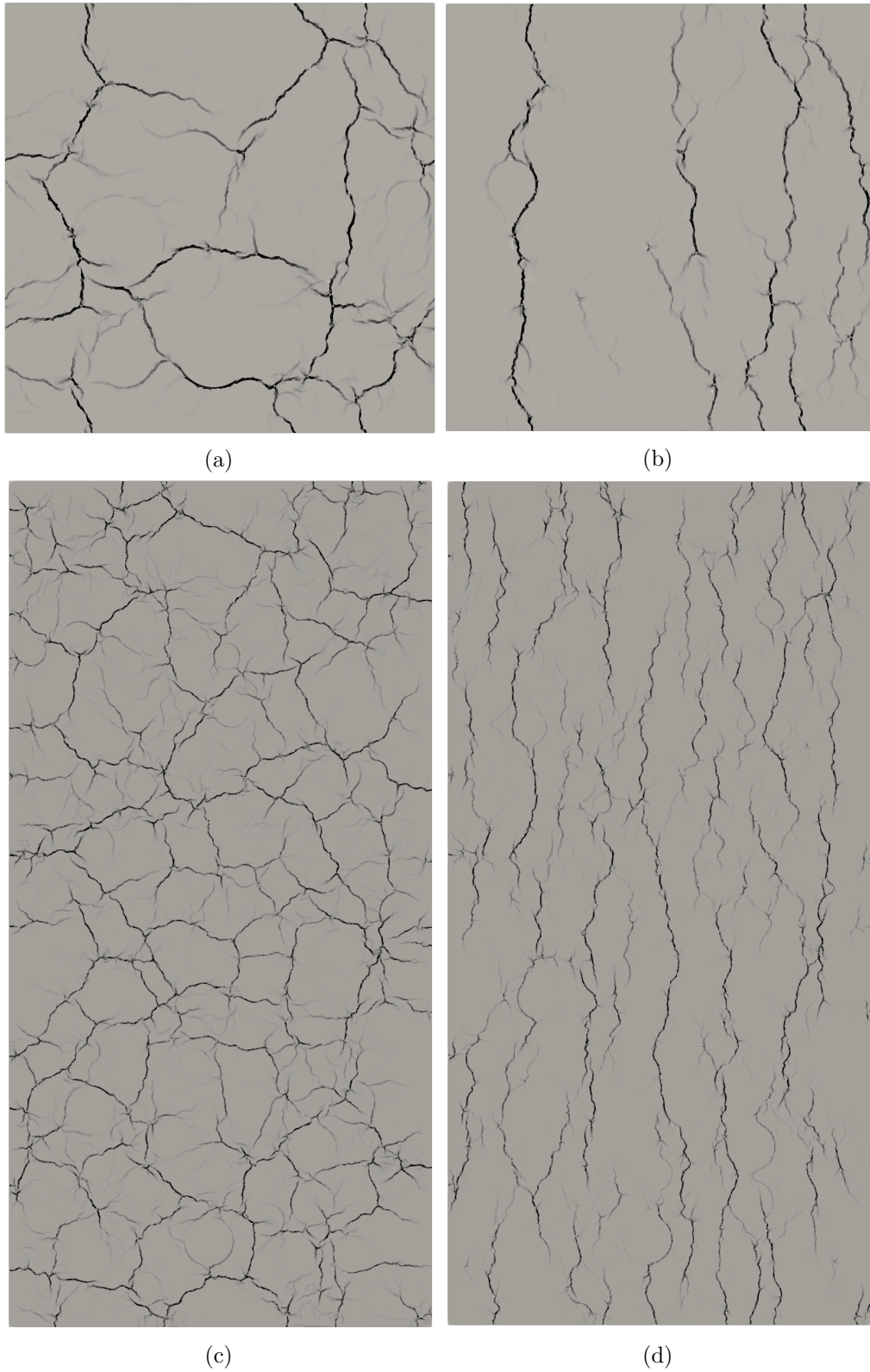
Figure 6.8: Crack opening patterns within typical RVEs under a) the free expansion conditions and b) the uniaxial compression stress of 10 MPa. c,d) Similar images from the full macro-scale model.

40 cm is dry.

Thermo-elastic expansion is ignored both at the macro- and meso-scales. At the macroscopic scale, this is done mainly to separate displacements of a dam due to yearly temperature fluctuations from continuous ASR-caused drift. For more details on this subject, readers can refer to the comprehensive study of the dam deformations due to the thermo-elastic expansion by Aniskin and Shaytanov (2020). At the meso-scale, assuming that the thermo-elastic properties of the damaged material are similar to the undamaged ones, the thermo-elastic expansion should not cause any difference in the results due to the homogeneous temperature across an entire RVE. This is however a simplification that should be addressed in future work.

6.3.1   Macroscopic heat transfer model

Assuming no mass transfer or radiation, the energy conservation equation for a non-uniform isotropic medium is written as

$$\rho c_p \frac{\partial T}{\partial t} - \nabla \cdot (k \nabla T) = b \qquad (6.15)$$

with T being the scalar temperature field, c_p the specific heat capacity, ρ the material density, k the thermal conductivity, and b the volumetric heat-source. The first term in the equation above is responsible for the heat accumulation, the second for its diffusion to a colder area, and the right-hand side for the heat generation.

Similar to the mechanical part, the heat transfer problem is discretized by the finite element method. Accounting for the dynamical nature of the heat transfer problem, Eq. (6.15) is solved implicitly, which makes the solution unconditionally stable and does not limit the time step size.

In the current study, a one-way coupling scheme is adopted. The heat transfer model affects the mechanical one by altering the ASR-product growth rate (Eq. (6.14)), while the reverse influence of the stress and damage states on the thermal parameters in Eq. (6.15) is omitted.

At each time step, first, the heat transfer model is solved for the given boundary conditions. Then, the updated temperature field is passed to the macro-scale model, which, in its turn, transfers local temperatures to the corresponding RVEs. After that, the mechanical multi-scale problem is solved iteratively.

Thermal properties of concrete are specified in Table 6.1. Due to the unknown geological situation and a wide range of possible thermal rock properties (Robertson, 1988), the latter were taken equal to the concrete ones.

Parameter	Value
Thermal conductivity k [W/(mK)]	1
Specific heat capacity c_p [kJ/(kgK)]	1

Table 6.1: Thermal properties of the concrete and the rock in the multi-scale simulation.

6.3.2 Macro-scale problem

A cross-section of the Salanfe gravity dam is chosen to study the mechanical behaviour of an ASR-affected dam and the role of temperature on it. The Salanfe dam, owned by Alpiq Suisse SA, is located near Martigny of canton Valais in Switzerland and was built in 1952. Irreversible upstream deformations have been reported for the first time in the early 1970's. In 2001, petrographic and SEM analysis finally proved that the dam is affected by the ASR. Slot cutting, as a rehabilitation measure, was carried out on the dam in 2012 (Droz et al., 2013).

A cross-section in the middle of a long straight segment of the dam was chosen as the reference to minimise the 3D effect. Actual drawings of the dam as well as the field measurements of displacements, temperature and reservoir level were provided by the dam owner.

The 2D finite-element mesh of the dam's cross-section is shown in Fig. 6.9 and consists of 250 triangular finite elements. Each finite element at the macro-scale (3 m size, on average) is linked to a single underlying RVE (70×70 mm^2), which represents the heterogeneous structure of concrete at the meso-scale. The total number of RVEs corresponds to the number of finite elements in the macroscopic FE mesh because each macroscopic finite element contains only one integration point. The total number of degrees of freedom in the FE^2 analysis is about $25,000,000$ and the simulation was run on 280 processors.

The real foundation shape of the reference cross-section has a rough profile due to the rock topology. The latter changes significantly from one joint to another. For simplification, the numerical model has a planar inclined foundation resembling the actual shape. To allow for certain relative movement of the dam bottom with respect to the underlying rock, a layer of interface finite elements was placed in-between. Its shear stiffness is adjusted to test different rigidities. For the basic case, its value was set to 4 MPa. The effect of the shear stiffness on the overall dam behaviour will be discussed further in the text.

The mechanical boundary conditions at the macro-scale are shown in Fig. 6.10. Two types of loads are acting on the dam: the load of the water and the load due to the self-weight. One component of the water load is applied along the upstream face with the hydrostatic distribution starting from the reservoir level down to the bottom. The second component acts upon the dam bottom as the hydrostatic uplift. Field data on
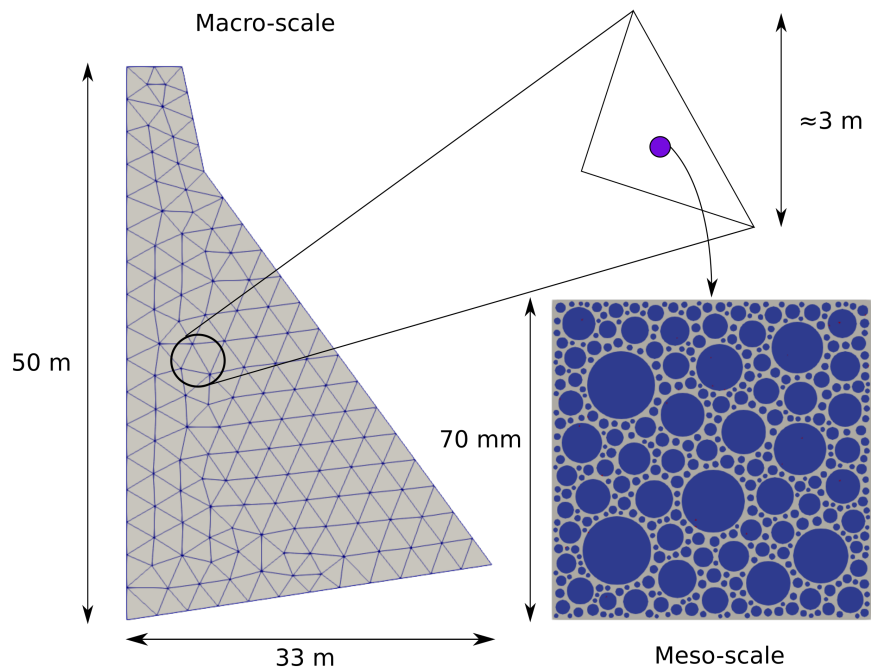
Figure 6.9: Macroscopic finite element mesh of the cross-section of the dam and the underlying concrete RVE.

the water pressure under the dam is not available, thus the following pressure profile was suggested: pressure linearly reduces from the value of the reservoir bottom pressure to one third of it at the grout curtain position (≈ 5 m from the upstream face in the downstream direction); later it linearly reduces to zero at the downstream side.
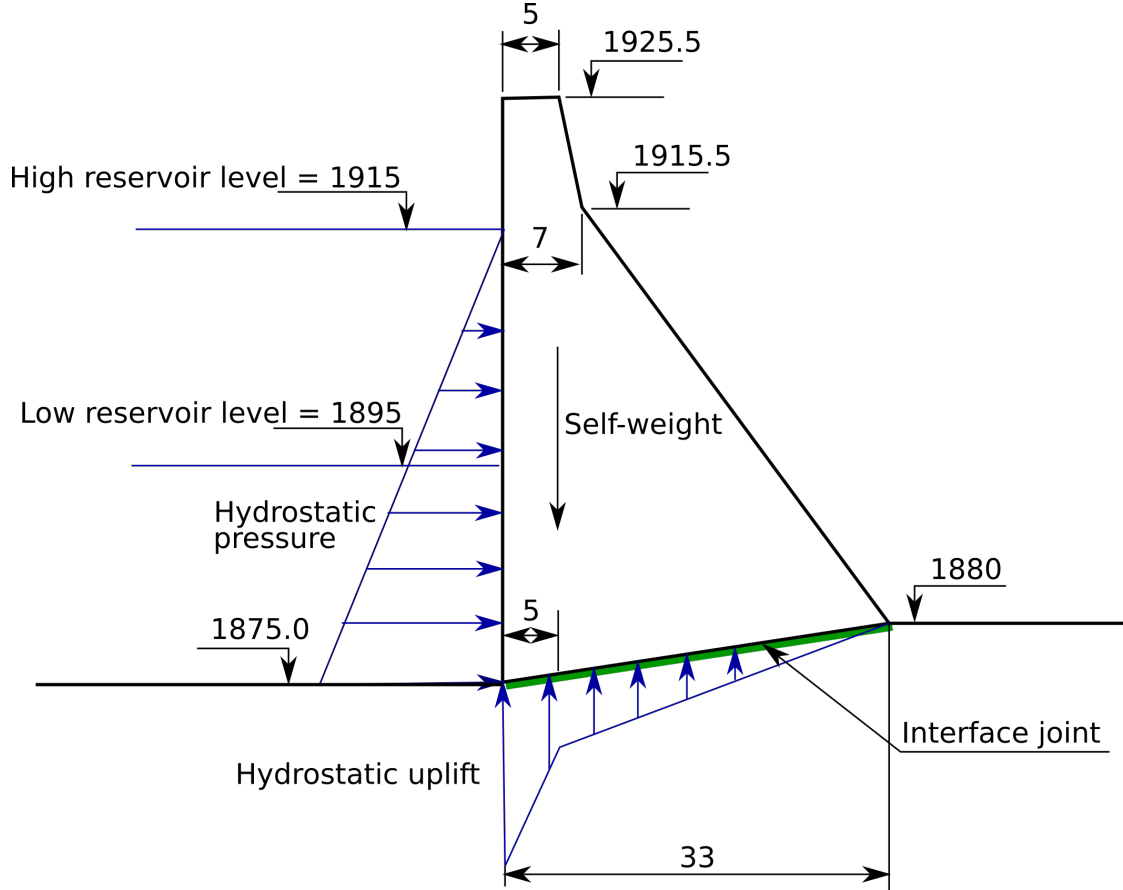
Figure 6.10: Altitudes and dimensions of the dam and mechanical boundary conditions for the 2D model of the Salanfe dam. Dimension are given in metres.

The water level in the reservoir is not constant within a year. It is at its maximum in the winter months and at its minimum in summer. The intermittent field measurements of the water level were approximated by the continuous periodic parabolic curve shown in Fig. 6.11.

The boundary conditions for the heat transfer problem are illustrated in Fig. 6.12. They consist of either prescribing the temperature (Dirichlet type) or the temperature gradient (Neumann type) at the model's contour. Actual record of the air temperature in surroundings of the Salanfe dam was used to establish its continuous sinusoidal approximation (see Fig. 6.13). The temperature prescribed at the concrete surface comprises the effect of the air temperature and the solar radiation. It is known that exposure to
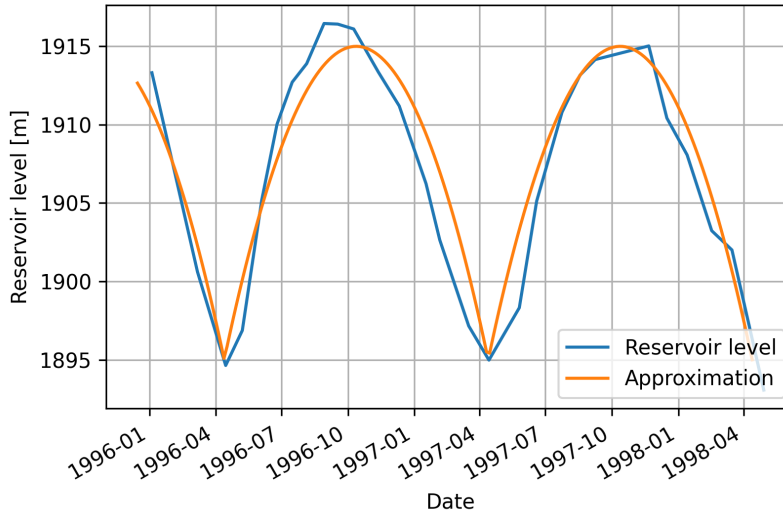
Figure 6.11: Real reservoir level fluctuations within two consequent years and its numerical approximation.

the sunlight can increase the temperature of structures significantly. Such an increase, computed based on the building code SP 20.13330.2016 (in Russian), for this specific dam location and its orientation, equals 7.9°C added on top of the daily mean temperature during the warm season. The above-mentioned code suggests the same total solar radiation for vertical surfaces facing West or East. Although the lower part of the downstream face is inclined and thus attracts more solar radiation, this additional increment is not taken into account for simplicity. According to the meteorological reports, total annual sunshine in Western Switzerland is about 50%. To account for this information, the annual surface temperature curve was built based on the air temperature curve by shifting the highest temperature value by the radiation increase and keeping the low value similar to the original one. To verify the correctness of such approach, the proposed curve was integrated over one year and compared to the integral of a curve with 180 days with a constant radiation increase and other 180 days with normal air temperature. The final difference between the two integrals was less than one percent, which proves the applicability of the proposed adjustment.

Temperature at the soil top was assumed to be equal to the air temperature, and the radiation effect was discarded. The constant rock temperature of 6°C was assumed at the 40 m depth based on the data of Huang and Pietruszczak (1999) . Left and right borders of the rock mass were assigned the homogeneous Neumann boundary condition ($\nabla T = 0$). Reservoir temperatures were taken from the field measurements of Vieux Emosson dam situated in the Salanfe's neighbouring valley. Temperature at the top of the reservoir is fluctuating between 0°C and 10°C. Fluctuations penetrate down to 15 m depth, after which a constant temperature of 6° is applied and maintained down to

Figure 6.12: Boundary conditions for the macroscopic heat transfer problem.

the bottom of the reservoir.

6.4 Results

6.4.1 Field measurements

Performed numerical simulations were compared to the field data provided by the dam owner. This data includes horizontal displacements in the upstream-downstream (U-D) and left-right (L-R) directions as well as vertical (Z) movement of the crest. Horizontal displacements are available both at the level of the crest and at the base and are measured by direct and inverted pendulums correspondingly. Available data is shown in Fig. 6.14. Since the numerical model is two-dimensional, the left-right displacement of the crest is ignored. The rest of the data is used for the comparison. The upstream-downstream movement of the crest has the longest historical track beginning right after the dam construction in 1953. The rest of the data (crest Z and base U-D movements) start its record in 1993. While the base movements are almost zero, the crest has substantial uplift. As there are no available data during preceding 40 years, the Z curve does not provide the absolute values of displacement, but rather the uplift rate. This plot shows that in the field conditions, the ASR expansion continues for already 68 years and it still goes on. In the subsequent figures, the initial offset of 13 mm was subtracted from the whole U-D curve as being not ASR-related. If the frequency of

Figure 6.13: Approximations for the temperature fluctuations of the air, top of the soil, the concrete surface and top of the reservoir within a year.
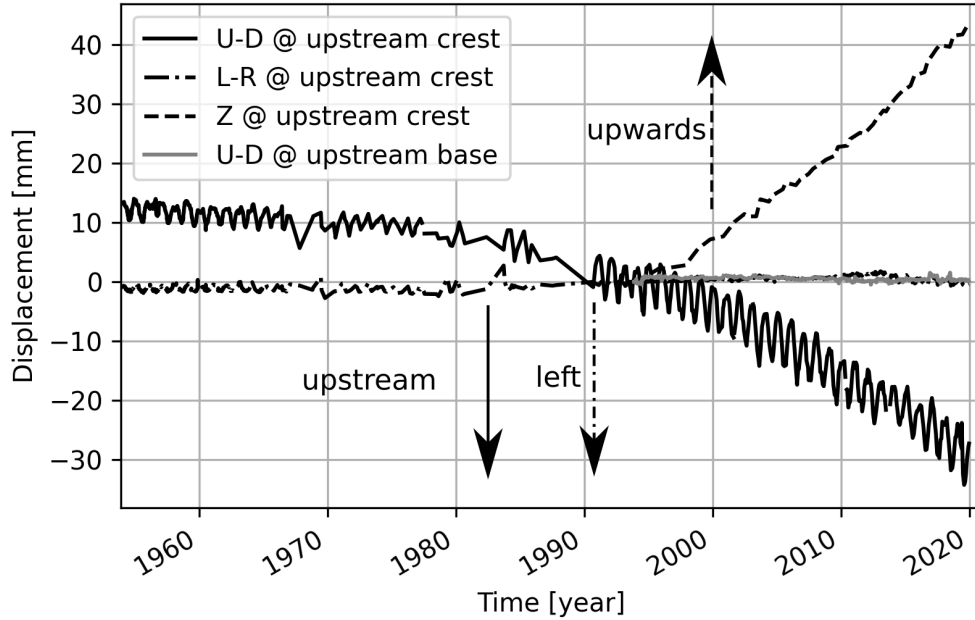
Figure 6.14: Field measurements of the Salanfe displacements in the reference cross-section. U-D stands for the upstream-downstream direction, L-R for the left-right direction, and Z for the vertical direction.

112

the horizontal displacement varies between one to four measurements per month, the vertical displacement data is much more scarce and is measured only two to three times per year.

Extra to the displacement measurements, the dam owner performs yearly inspections. One of the outcomes is the updated crack map of the surface. The latter is not presented here due to privacy reasons. It could have been observed that, in the block of interest, almost all the cracks are concentrated in the upper half of the upstream face with most of them following the axis of the dam (horizontal lines on the upstream face). The latter makes the approach of 2D modelling of a cross-section valid: all the numerical cracks in a 2D model take form of infinite planes propagating along the dam axis when extrapolated to 3D.

6.4.2 ASR parameters

Simulation of the dam behaviour with the parameters of the expansion law in Table 5.2, calibrated on the accelerated laboratory experiments, results in the premature dam expansion and the reaction stop within the first ten years after construction, which does not correspond to the field observations, as can be seen in Fig. 6.15. In order to match
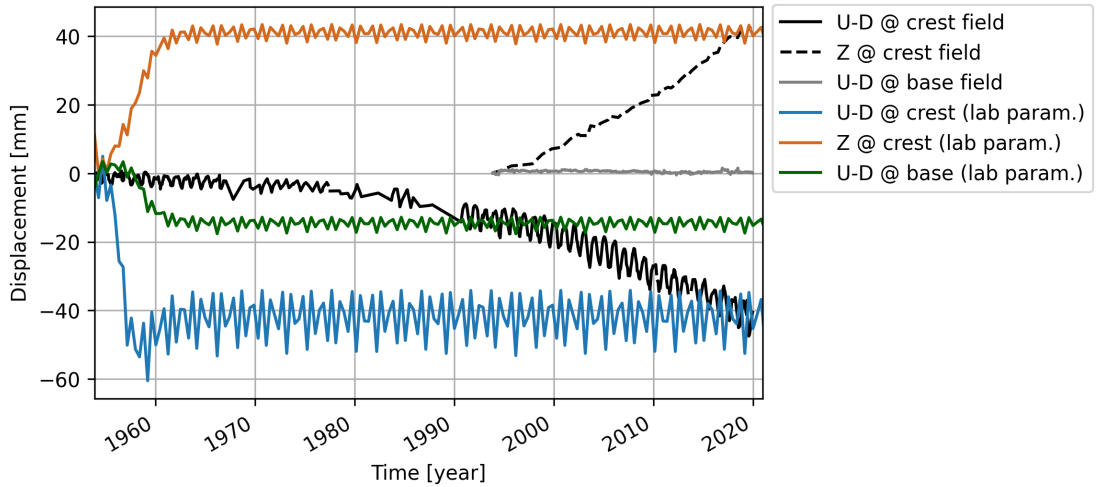
Figure 6.15: Displacements at the crest and the bottom of the dam obtained by employing the expansion law parameters calibrated on the accelerated laboratory experiments.

the numerical results with the field data, parameters of the ASR expansion law had to be re-calibrated. The updated set of parameters is given in Table 6.2. The energy constant U_C got eliminated by making the characteristic time τ_{ch} in Eq. (6.14) independent of the temperature and equal to the reference value $\tau_{ch}(T_0)$, and the reference temperature was reduced to 0°C. The actual values of the latency and characteristic times are not unique: both lower and higher values could have been chosen. The main purpose of taking such

Parameter	Value
Ratio of the ASR sites area to the aggregates area [%]	0.1
Asymptotic strain $\varepsilon(\infty)$ [%]	37
Latency time τ_{lat} [years]	120.5
Characteristic time τ_{ch} [years]	123.29
Reference temperature T_0 [°C]	0
Energy constant U_C [°K]	-
Energy constant U_L [°K]	400

Table 6.2: Updated parameters of the ASR-expansion law.

large numbers is to make the expansion linear within the studied time period. The minimum values of τ_{lat} and τ_{ch} for which the expansion curve stays linear are of order of 43 years.

The numerical outcome is plotted next to the field data in Fig. 6.16. Displacements of the crest are measured at the top upstream point. Numerical results have a good agreement both with the vertical movement and the upstream drift of the crest. Similar to the field data, numerical horizontal drift curves have yearly fluctuations caused by the reservoir level change. While the rate of the simulated horizontal drift is matching
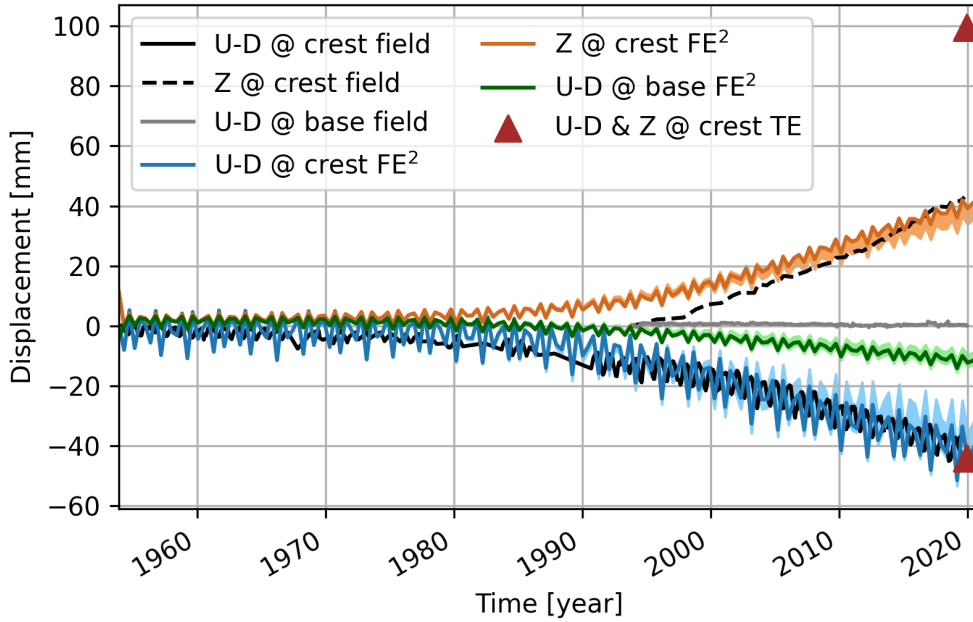
Figure 6.16: Comparison of the field measurements of the dam movement with the numerical results. Shaded areas represent variation between three simulations with different RVEs. TE stands for the isotropic thermo-elastic simulation.

the measured one perfectly, its vertical counterpart is by 25% slower than the field rate. This difference could possibly be explained by the 3D effect, which is not captured by the model. High out-of-plane stress might play a role on the ASR-related expansion by hindering it in the dam-axis direction and boosting it in the other two. The horizontal drift of the upstream bottom point is not exactly zero as measurements indicate. The behaviour of the foundation is dictated by the shear stiffness of the interface between concrete and rock, which will be demonstrated further in the text.

The macroscopic results depend on a specific RVE meso-structure and on the positions of the ASR sites. For a better statistics, an ensemble of multi-scale simulations with different RVE meso-structures shall be run. The result of the Monte Carlo simulation would be a family of displacement curves forming a statistical distribution. The mean curve shall match the field measurements. Otherwise, the expansion law parameters have to be adjusted and the statistics updated. The described procedure is extremely computationally expensive and could not be performed within the scope of the current study. To obtain a better statistical representation, two additional FE^2 simulations with different positions of ASR sites and distributions of tensile strength σ_t within RVEs were conducted. The ranges of displacements between the three simulations are defined in Fig. 6.16 as shaded areas. As there is no significant variation between these three simulations, the results of the first simulation will be used further in the text. We do not expect qualitatively different results from the full Monte Carlo simulation.

The final set of the expansion law parameters substantially differs from the ones based on the laboratory experiments. Employment of a less reactive concrete with a lower alkali content could cause an increase in the τ_{lat} and τ_{ch}. However, this argument does not seem to be legit for their thousandth increase as the construction data does not have any track of ASR-mitigating additives used in the Salanfe dam. The energy constant U_L was reduced significantly compared to the one identified by Ulm et al. (2000). More than that, U_C had to be fully eliminated. Overall, the newly identified parameters made the thermal law less sensitive to the temperature variation and narrowed the gap between expansion rates of the coldest and the warmest parts of the dam. Moreover, the macroscopic expansion became linear with no sign of slowing down.

To obtain similar results, there is no need in the asymptotic expansion law of Eq. (6.14). Instead, a linear Arrhenius-inspired law could be formulated as follows:

$$\frac{\partial \varepsilon_{eig}(t,T)}{\partial t} = k e^{-(E_a/RT)} \tag{6.16}$$

where k is some pre-exponential constant, E_a is the ASR activation energy, R is the universal gas constant and T is the temperature. E_a has a double functionality: it defines the expansion rate as well as the sensitivity to the temperature difference. k is a scaling factor for the final curve. To get the feeling of the role of E_a, a short limit analysis is performed. The ratio between the expansion values for two different

temperatures equals

$$\frac{\varepsilon_{eig}(T_1)}{\varepsilon_{eig}(T_2)} = e^{\frac{E_a}{R}\left(\frac{1}{T_2} - \frac{1}{T_1}\right)} \tag{6.17}$$

Taking E_a infinitely small would result in the exponential taking value of 1, which means equality between the expansion values $\varepsilon_{eig}(T_1)$ and $\varepsilon_{eig}(T_2)$ no matter how different temperatures T_1 and T_2 are. Oppositely, an increase in E_a would separate the two expansion values. Experimentally, E_a for the ASR was identified in a wide range of $10 - 50$ kJ/mole (Larive, 1997; Ben Haha, 2006; Mukhopadhyay et al., 2006; Ghanem et al., 2010).

To match the field data, the following parameters of the expansion law in Eq. (6.16) were used: the pre-exponential constant $k = 9.3\text{e}{-}6$ and the activation energy $E_a = 3$ kJ/mole. The displacement curves obtained with the Arrhenius equation are plotted in Fig. 6.17. The results obtained with Eq. (6.14) and Eq. (6.16) match each other. Similar
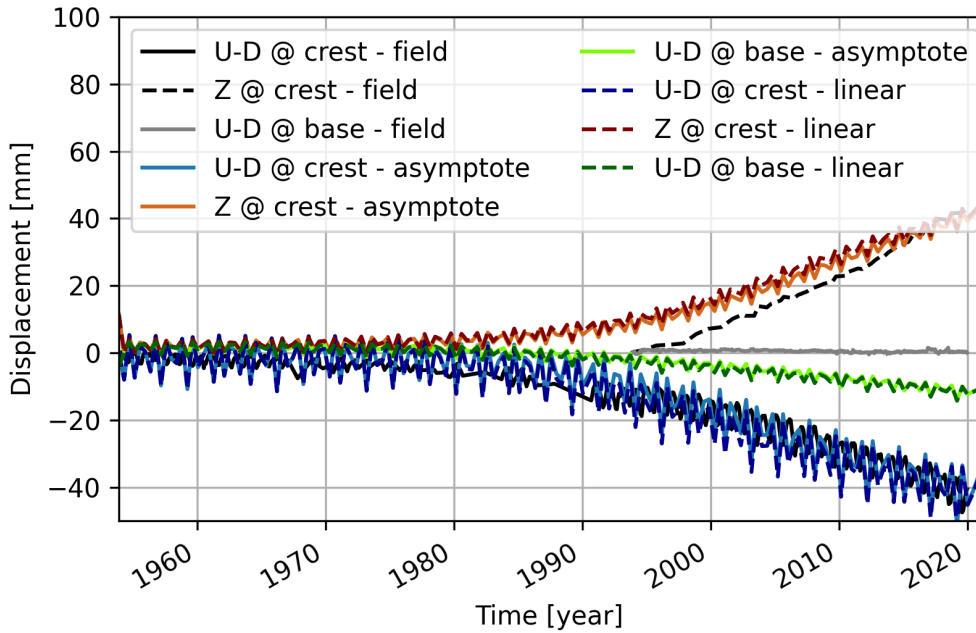
Figure 6.17: Comparison between the results obtained by the asymptotic expansion law from Eq. (6.14) and the linear one from Eq. (6.16).

to the previous case, the energy constant had to be reduced by more than ten times. Although the low value of E_a generally suggests high reactivity of aggregates, the reason for reducing E_a in the developed model was to minimise the difference in expansion values within the operational temperature range. To counteract the increase in expansion due to the reduction of E_a, a small value of k had to be adopted. Equilibrium between the values of E_a and k allowed us to keep the expansion rate low and close to the

measurements.

The identified mismatch between the laboratory and field-based parameters suggests that there is a certain gap between two conditions. The issue of predicting field behaviour based on the accelerated tests was repeatedly discussed in the literature (i.e. Ideker et al. (2012a,b); Fournier et al. (2009); Durand and Fournier (2016)). Expansion results obtained in the accelerated mortar bar test at 80°C (AMBT), concrete prism test at 38°C (CPT) and exposure field sites for the same concrete are not monotonous (Ideker et al., 2012b). Fournier et al. (2016) pointed at the progressive loss of correlation between the concrete prism expansion under 38°C and relative humidity > 95% and the 15-year expansions in concrete blocks stored outdoors. A recent study by Borchers et al. (2016) proved that accelerated tests are useful for determining the reactivity of aggregates, however correlation of the expansion magnitude between the laboratory experiments and the field exposure sites is complicated.

One possible reason for such discrepancy is the difference in the temperature regimes. The laboratory temperature range at which the expansion law was calibrated does not cover the field conditions, and this results in a change in environmental conditions. Most of the accelerated ASR tests are done at temperatures above 20°C (Ulm et al., 2000; Larive, 1997; Ben Haha, 2006; Gautam and Panesar, 2016; Multon and Toutlemonde, 2006), which is above the upper limit of the current field range in Switzerland. The obtained results suggest that the ASR experiments at elevated temperatures result in a different ASR dynamics than what happens in the field conditions. Moreover, the rates of the chemical and mechanical processes can not be exponentially extrapolated from the accelerated experiments by employing the Arrhenius law.

Given a relative model's simplicity, it has its limitations. The latter are summarised in the following list:

- not modelling the long-term deformations in the dam due to the creep;

- the two-dimensionality of the model not capturing the 3D effects in the dam;

- the relative humidity (RH) of a dam differing from the assumed full saturation conditions: the reduced RH would slow the ASR down;

- not accounting for the alkalis transport and the ASR products migration within cracks and pores.

In order to evaluate the possible contribution of these factors, the proposed model has to be expanded and additional simulations to be performed. It also requires extensive additional field measurements (e.g. typical displacements of a dam only due to the creep effect, RH and displacement measurements of the dam as a 3D structure, etc.)

Meanwhile, the author of the thesis hopes that the highlighted mismatch will trigger further discussions in the scientific and engineering committees.

6.4.3   Temperature effect

When the calibration is completed, the focus is on the ASR effects within the dam structure. ASR products' strain ε_{eig} accumulated at the end of simulation is plotted in Fig. 6.18a. There is a slight increase of the ASR products' strain from the upstream

(a)   (b)
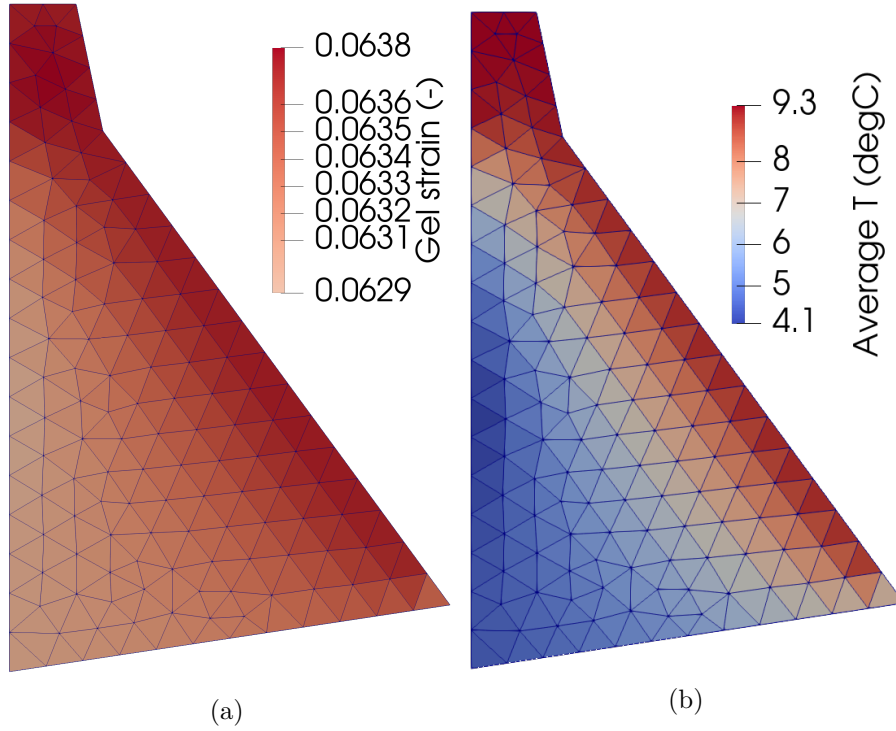
Figure 6.18: a) Accumulated ASR products' strain at the end of the last time step. b) Macroscopic temperature averaged over the simulation time.

underwater part towards downstream and the crest. This gradient is caused by the upstream having in average lower temperature during the year than the downstream. The lowest ASR products' strain values are concentrated in the middle upstream zone, as temperatures there could take values between 0 and 6°C in winter. The two extreme ASR products' strain values differ insignificantly (0.062 and 0.063 for the minimum and the maximum values).

To have a clear understanding on the contribution of this ASR products' strain difference to the overall dam displacement an additional multi-scale simulation was performed. The latter comprised no heat flow simulation, but only a mechanical FE^2 model with a constant temperature applied across the entire dam. The temperature value was obtained by spatial and temporal averaging within the dam cross-section and was equal

to 8°C. The parameters of the ASR-expansion law were kept the same. The results are plotted in Fig. 6.19. All the displacement curves are exactly matching the results of the thermo-mechanical multi-scale simulation. This study proves that the homogeneous
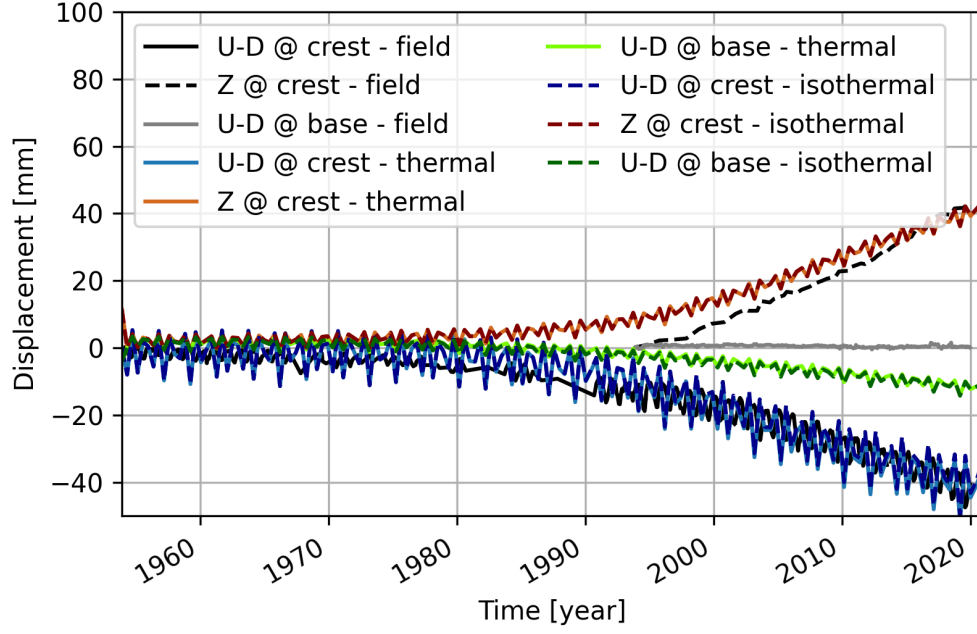
Figure 6.19: Results of the isothermal simulation with average temperature applied across the dam compared to the full thermo-mechanical model and field measurements.

ASR products' strain results in the same deformation profile of the dam as in the non-homogeneous case with small ASR products' strain variation. Therefore, the numerical model suggests that, within the specific environmental conditions (specific temperature range, dam geometry and reservoir fluctuations), the temperature difference has a negligible effect on the ASR evolution within the structure.

The macroscopic temperature averaged over the simulation time is presented in Fig. 6.18b. ASR products' strain accumulation for the minimum and the maximum average temperatures, which are 4.1°C and 9.3°C correspondingly, is plotted in Fig. 6.20. These curves were obtained from Eq. (6.14) by applying constant temperature values and the parameters from Table 6.2. One can observe that the original curves have a very small gap in-between which illustrates low sensitivity to the temperature variation within considered temperature window. To understand how higher sensitivity (therefore higher energy constants) would affect model behaviour, two additional simulations were performed. The parameters of the expansion law were modified to have a larger expansion difference between the cold and warm areas. This resulted in the constant-temperature curves plotted in Fig. 6.20 (by stars and circles). First set of parameters
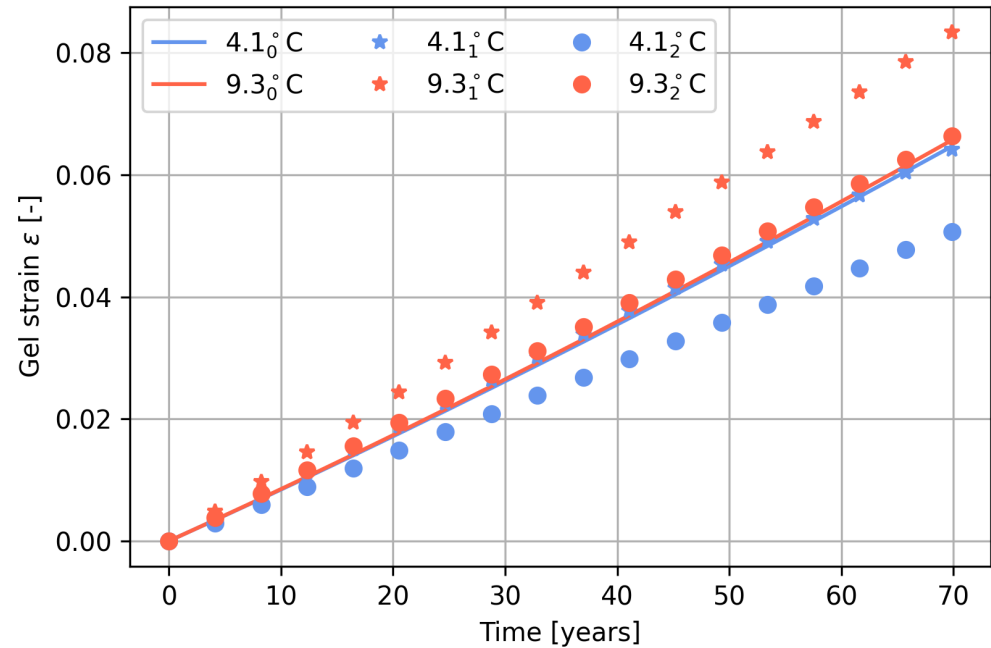
Figure 6.20: ASR products' strain evolution for two extreme temperatures for original parameters of the expansion law (solid line) and two sets of curves for modified parameters.

($\tau_{lat} = 41.1$ year, $\tau_{ch} = 230$ year, $U_L = 4500$ K) produces the same ASR products' strain for low temperature and a higher strain for 9.3° C. The second set ($\tau_{lat} = 41.1$ year, $\tau_{ch} = 298.6$ year, $U_L = 4500$ K) has an opposite effect. In physical terms, the first set would increase the ASR expansion in the warmer part compared to the simulation presented below, while the second set would reduce the expansion in the cold part. The rest of the parameters were kept unchanged with respect to Table 6.2. Multi-scale simulations were performed with these two sets of parameters. The results are plotted in Fig. 6.21. The first set of parameters, as expected, results in premature U-D and Z crest
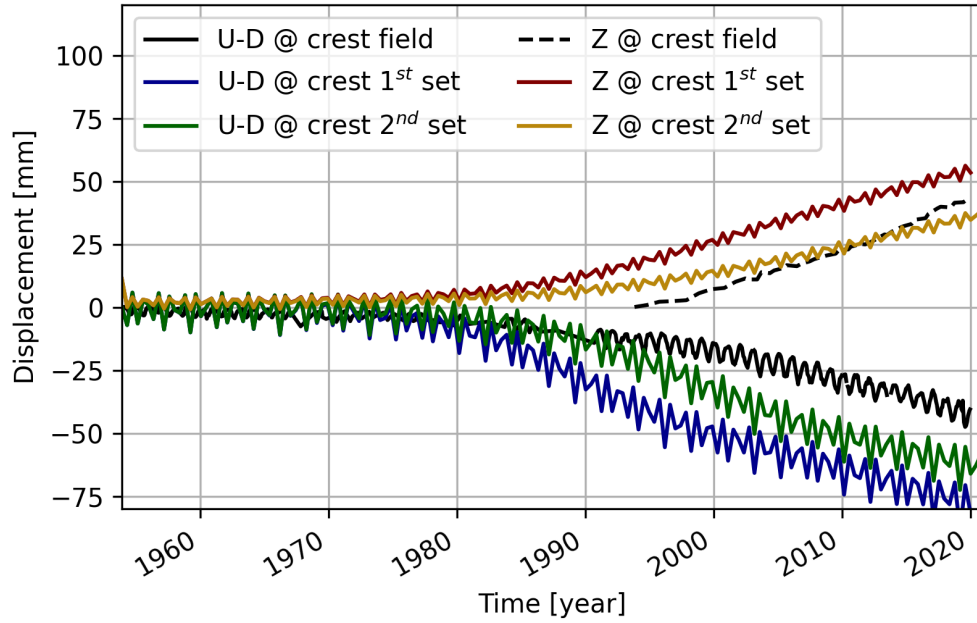
Figure 6.21: Crest displacements for two sets of the expansion law parameters compared to the field data. Displacements at the base are omitted for brevity.

displacements due to the "warm" area accumulating higher ASR strain. The results of the second set are somehow intriguing: although the "cold" area is producing less ASR products' strain, the U-D displacement of the crest still starts earlier and goes above the field measurements. This is happening because of the difference in the ASR strain values of the "warm" and "cold" zones: the "warm" area will produce an additional "push" of the crest in the upstream direction due to the expansion advantage over the "cold" one, independently of the absolute values. Contrary to the case with different expansion values, having the same expansions across the entire cross section minimises the U-D drift and brings it close to the observations.

Oppositely to the horizontal displacements, expansion magnitude is directly linked to the vertical crest displacement: higher ASR strains across the dam cause higher crest

uplift. These two additional simulations demonstrate that the model does not have to be sensitive to the temperature variations within the considered temperature gap in order to match the available field measurements. The constant expansion across the dam has to be high enough to cause the sufficient uplift.

6.4.4 Measurements frequency

The field data on temperature has relatively a low frequency (one datapoint per month), so that it had to be replaced by the continuous sinusoidal curve. Therefore, a question on a sufficient data density persists. Engineers in the field may wonder what is the lowest frequency of the temperature measurements which would not affect the numerical model results significantly. In order to answer this question, an additional set of simulations was performed. The idea behind it was to take a real high-density temperature data from the field and run the thermal simulation with different time steps: starting with the smallest one and steadily increasing it. Then, the accumulated ASR products' strain (ε_{eig} in Eq. (6.14)) distribution across the dam cross-section is compared between the simulations with the different time steps. This comparison is done by computing the difference between the ASR products' strain distributions of a simulation with the shortest time step (the most precise) and all the other simulations.

Since in the proposed approach computation of the ASR products' strain depends only on the temperature, there is no need to include the mechanisms of actual ASR expansion and crack growth. Therefore, only transient thermal analysis was run and the ASR products' strain was updated at each time step. The macroscopic mesh was further densified.

As the temperature measurements from the Salanfe dataset were not dense enough to convey this study, a different set of data was used. A record of the air temperature in Vancouver, Canada taken every hour between 10/2012 and 10/2017 (Beniaguev, 2017) was used as the basis. This five year-long basis was looped to form a 70 year-long continuous record.

Simulations were performed with following time steps: 0.25, 0.5, 1, 10, 20, 50, 100 and 200 days. Results of all the simulations were compared to the one with the shortest time step. The comparisons were done at the final time of 70 years. Results are shown in Figs. 6.22 and 6.23. A typical distribution of the ASR products' strain is shown in Fig. 6.22a. There is a front-like reduction of ε_{eig} from the warmest (downstream wall and crown) towards the coldest area (contact with water). The difference between the extreme values of strain is about 1e−3. The error between 6 hours and 200 days time-step simulations is plotted in Fig. 6.22b. Here, one could note the two major error zones: the negative error on the upstream face in the area of the reservoir level fluctuation and the positive error in the rest of the dam. The error sign does not play a role, however it helps

to distinguish two different error sources. The positive zone, with maximum values at the dam extremities, is due to skipping the details on the temperature within a long time step. The extreme value of such error is 0.0045% which is fairly low. The negative error zone is due to the combined effect of the temperature and the reservoir level fluctuation. A large time step not only skips details on the temperature, but also on the water level which changes dynamically during the year (see Fig. 6.11). Within 200 days the reservoir is depleted and refilled again. Skipping this data leads to the application of the average reservoir level and assigning the corresponding temperature profile on the upstream face. This type of averaging causes a higher relative error of 0.47%. The evolution of

(a)　　　　　　　　　　　　　　　　(b)
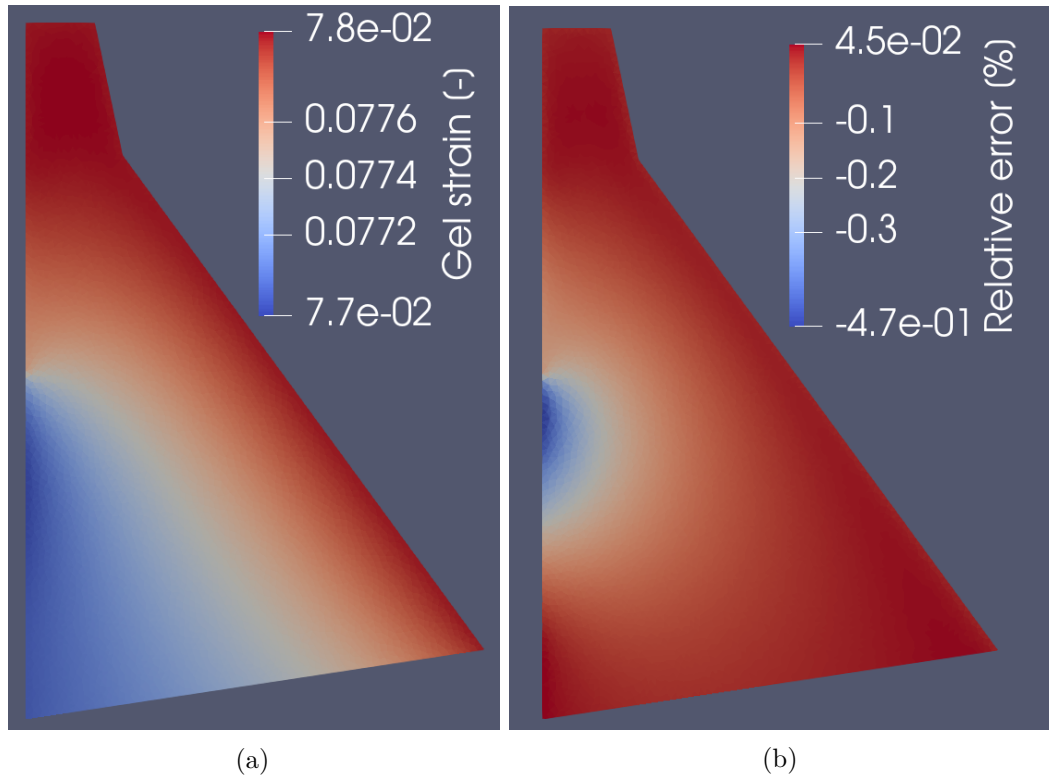
Figure 6.22: a) Cumulative ASR products' strain distribution within the dam after 70 years computed with the time step of 6 hours. b) ASR products' strain error of the 200 days time-step simulation compared to the 6 hours one normalised by the absolute ASR products' strain value.

the two types of error with the time step size could be appreciated in Fig. 6.23. The error in the upstream face develops non-monotonously which might be explained by the combination of the specific water fluctuation periodicity and the time step. The change in the error sign serves as evidence of the faster evolution of water-level related error than the temperature-fluctuations related one. Such a low error due to the time skipping owes to the low sensitivity of the ASR-expansion law in Eq. (6.14) to the temperature high-frequency fluctuations. While the expansion law has been more sensitive with the previously-identified parameters in Table 5.2, their updated version in Table 6.2 has

increased the "thermal inertia".
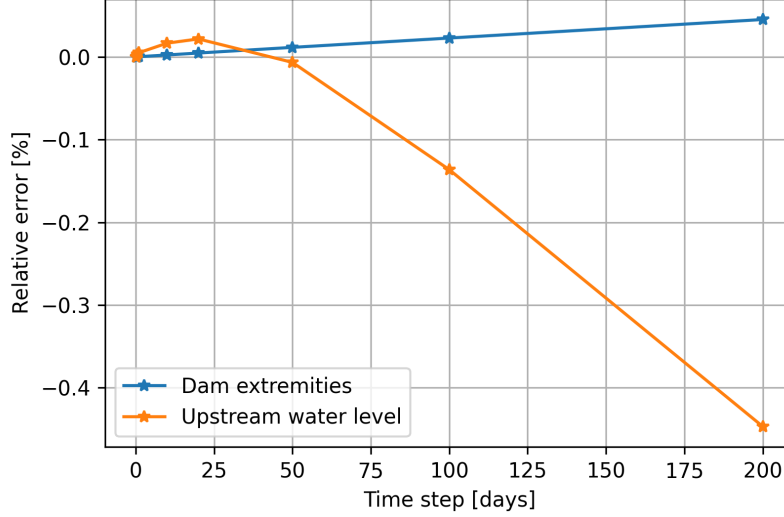
Figure 6.23: Evolution of the ASR products' strain relative error with the time-step growth.

6.4.5 Expansion anisotropy

It is of great importance to state that the homogeneous ASR products' strain distribution does not cause homogeneous expansion within the cross-section. The so called ASR-expansion anisotropy manifests itself in the form of the load-dependent expansion. The current numerical model successfully reproduces ASR-related anisotropy, which was demonstrated in the previous chapter. To highlight the ASR-anisotropy effect in the dam simulation, the multi-scale results are compared to the thermo-elastic simulation with no damage in it. In the latter, expansion is caused by applying homogeneous hydrostatic eigenstrain ε_{eig} across the dam cross-section (similar to the thermo-elastic expansion). The eigenstrain value is chosen in a way to match the horizontal crest drift. The final vertical and horizontal displacement values are plotted in Fig. 6.16 by triangles. The elastic crest uplift is by 140% higher than the multi-scale one. Such difference owes to the expansion anisotropy present in the FE^2 simulation. This result should raise awareness between the dam engineers on modelling the ASR as the thermal expansion. The results indicate that not including the anisotropy into ASR models could lead to the unrealistic predictions.

Comparison of the full thermo-mechanical multi-scale model with its homogeneous-temperature modification have shown that the difference in the ASR products' strain is not sufficient to cause the horizontal drift. However, there are two other causes for the

latter:

- orthogonal triangle shape of the dam;

- different levels of expansion anisotropy at the upstream and downstream dam faces.

The geometrical component could be identified directly from the thermo-elastic simulation (see Fig. 6.16). Having the same expansion values of the vertical upstream and the inclined downstream faces, the latter is longer, which results in a bigger length increase. The difference in extensions between two dam faces makes the whole structure extend upwards and bend upstream (see Fig. 6.24c). Following this logic, a dam having an isosceles triangle shape would have only a vertical uplift due to the homogeneous ASR extent.

The second contributor to the horizontal drift is the non-homogeneous expansion anisotropy across the dam cut. This is illustrated in Fig. 6.24a. Black segments here denote the principal strains at the integration points. Their directions correspond to the principal directions. Sizes of the segments were obtained by multiplying the actual principal strain values by some scaling factor to make them visible. Principal strains and their directions were computed by the eigenvalue analysis of the small strain tensor ε. Although there is certain rotation taking place, its contribution to the deformation gradient is negligible. This eliminates the need to compute more complex deformation measures (such as right or left Cauchy-Green tensors) and allows operating the simple strain ε. All the values of the principal strain are positive. The maximum extension corresponding to the maximum segment size is 0.12%. Coloured background denotes the ratio between two principal strain values. While the warm shades indicate the expansion state close to isotropic, the cool ones denote the areas with orthotropic expansion. The downstream wall and the crest are primarily expanding isotropically as they are not constrained nor heavily loaded. The foundation is restrained by the underlying rock, thus its horizontal movement is limited, which minimises its horizontal strain. The red area in the right bottom corner has the most isotropic state. It could be explained by the transition between the restrained lower boundary and the free downstream side. The most interesting observation about this plot concerns the slightly blue area on the upstream side of the dam. In this zone, the principal strain directions are close to horizontal and vertical. The horizontal strain is 1.3 times larger than the vertical one. The reason for this could be deduced from Fig. 6.24b where the principal stresses are plotted. Colours here denote the amplitudes of the highest principle stress. The load coming from the self-weight and the reservoir pressure generates compressive stresses, which transition from being nearly vertical in the upper part to almost horizontal at the base. Such transition is due to the following factors: the presence of the horizontal load from the reservoir, which is transmitted to the underlying rock; the horizontal constraint at the bottom, which gives rise to the high compressive stresses in response to the expansion of concrete. The highest principal stresses pass through the area next to

(a)

(b)

(c)

(d)
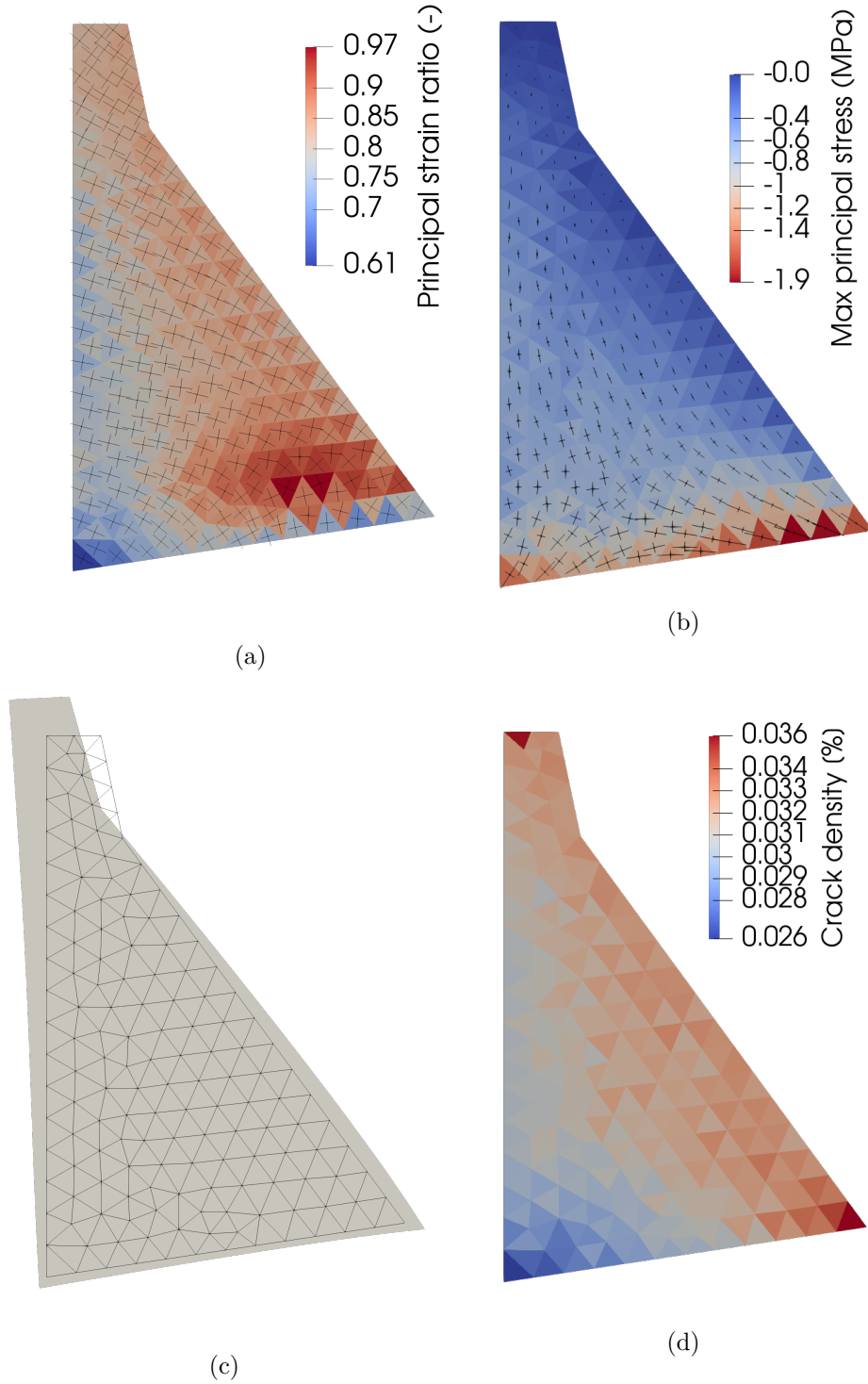
Figure 6.24: a) Ratio between the principal strains in colour. Segments denote the directions and the amplitudes of the principal strains at each integration point. b) Coloured background represents the crack density. The principal stresses are denoted by segments. c) Deformed shape of the dam in comparison with the initial configuration (amplification factor of 100). d) Crack density map quantifying the ratio between the total crack opening area and the RVE area.

the upstream wall and impose compressive forces on the corresponding RVEs. Although the stress values are relatively small ($\approx 0.4 - 1.0$ MPa), it is sufficient to partially hinder the vertical ASR expansion.

To further illustrate the loading effect, a crack density map in Fig. 6.24d and crack opening maps in Fig. 6.25 are given. The crack density map is visualising the ratio

<div align="center">(a)   (b)</div>
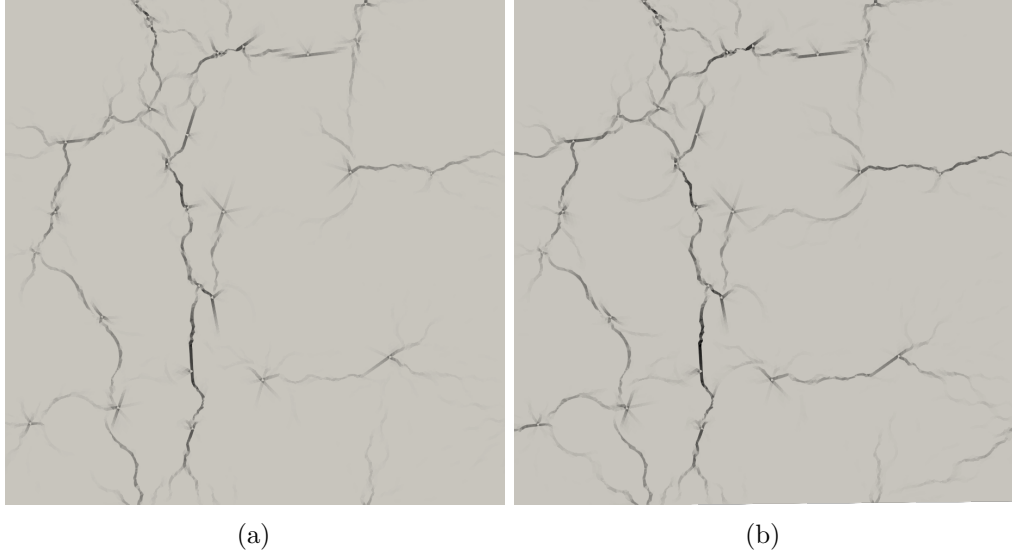
Figure 6.25: Crack opening maps of the RVEs on a) the upstream and b) downstream sides at the age of 42 years.

between the total crack area and the area of an RVE. Indeed, the RVEs on the upstream side have slightly lower area of cracks in comparison to the downstream side. Two typical RVEs on the upstream and downstream sides at the age of 42 years are plotted in Fig. 6.25. The reason for choosing this intermediate step is the possibility to clearly distinguish the difference between two patterns. At the end of the simulation it becomes complicated due to the abundance of cracks. The intensity of grey here denotes the crack opening. The darkest shade corresponds to an opening of 40 μm. Such crack is difficult to distinguish by visual inspection. The downstream RVE has more horizontally oriented cracks. Moreover, the horizontal cracks present in both RVEs are more open in the downstream RVE. Since expansion in the proposed model comes mainly from the propagation and opening of cracks, two typical crack maps explain why the expansion is orthotropic on the upstream side and close to isotropic on the downstream one. Expansion is never exactly isotropic due to its dependence on a specific RVE meso-structure and ASR positions.

While the simulation results show variations in the crack density from the upstream to the downstream face, the field observations show more developed cracking in the upper part of both faces. A possible explanation for such discrepancy could be the 3D effect not captured by the model.

6.4.6 The concrete-rock interface

The effect of the interface between the dam and the rock was investigated by modifying its shear stiffness. If in the original simulation its value was 4 MPa, which allowed for substantial displacement, here it was increased to 4 GPa, bringing it into the range of rock-like materials. For a better match in the upstream-downstream displacement of the crest, the latency time τ_{lat} of Eq. (6.14) had to be reduced to 109.6 years.

Results of this simulation are plotted in Fig. 6.26. While the crest displacements were not significantly affected by this change, the horizontal drift at the base was almost eliminated, which brings it even closer to the field data. Therefore, the stiffness of the concrete-rock interface is controlling the foundation's horizontal displacement.
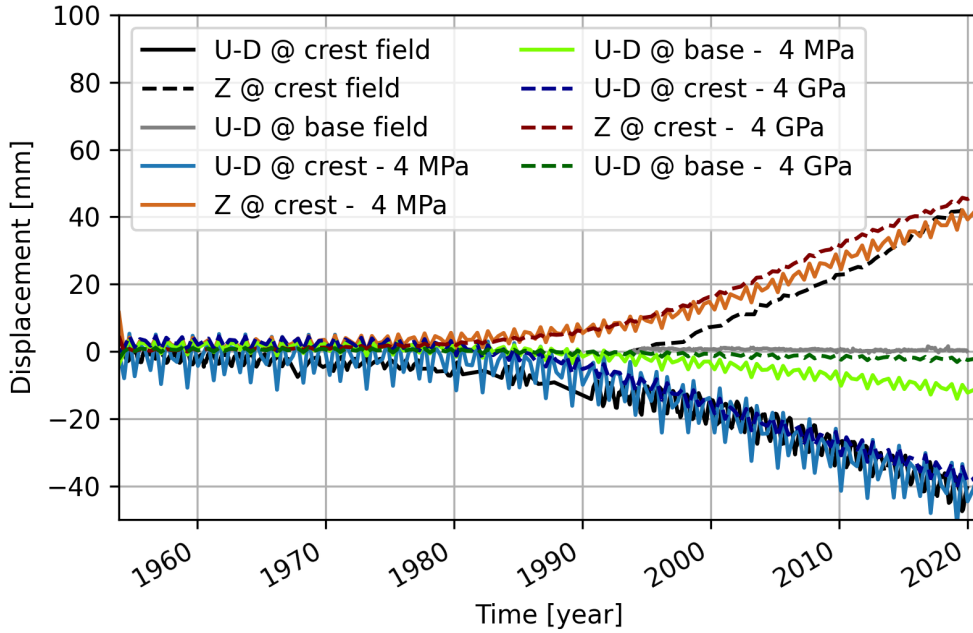
Figure 6.26: Crest and bottom displacements of the dam with two different shear stiffness values of the concrete-rock interface.

More consequences of the stiff interface could be observed in Fig. 6.27. Due to the rigidity of the dam's foundation, the horizontal expansion is constrained and the principal strain ratio reduces down to the $0.2 - 0.3$ range. Two bottom corners show negative strain ratio due to the highest stress concentrations. The reduced horizontal expansion comes at the cost of high compressive stresses shown in Fig. 6.27b. The range of the principal stress values along the foundation is $3 - 10$ MPa, which is few times higher than the stresses caused by the self-weight of the structure (see Fig. 6.24b). Two

(a)   (b)
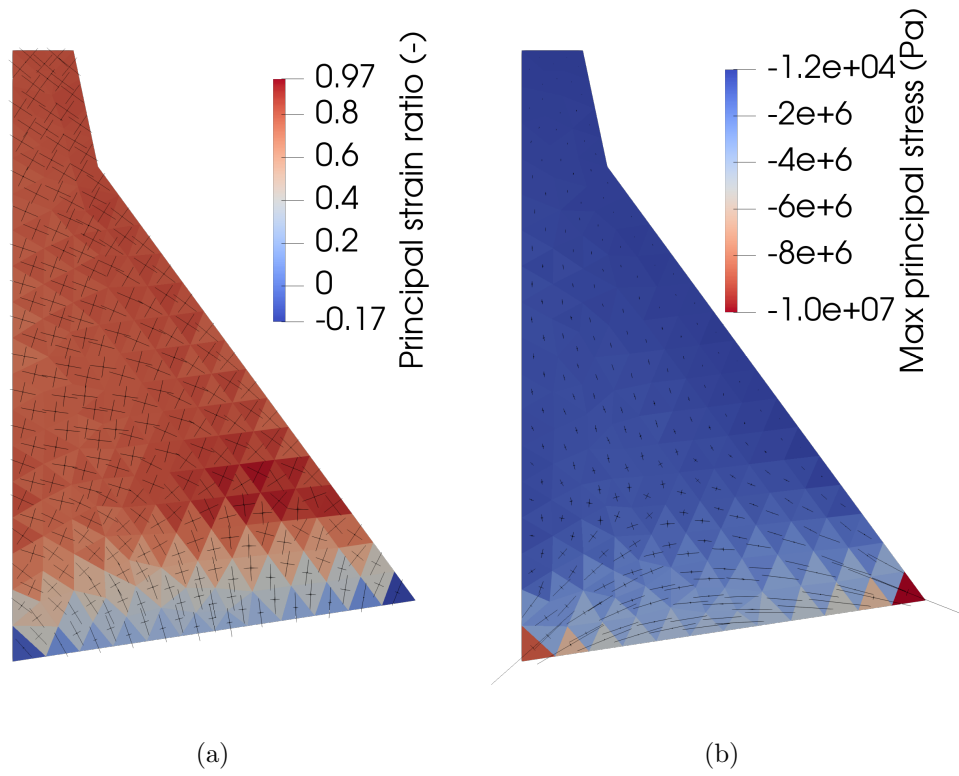
Figure 6.27: a) Principal strains (segments) and ratios between them (colour) for the stiff concrete-rock interface simulation. b) Compressive principal stresses for the same simulation.

RVEs, one from the bottom and one from the crest, are compared at the end of the simulation in Fig. 6.28. Cracks in the bottom RVE are predominantly horizontal, while the crest ones have random orientations. This horizontal cracks alignment is due to the strong uniaxial compression setting the preferable crack orientation.

(a)   (b)

Figure 6.28: Crack opening maps of the RVEs at a) the bottom and b) the crest at the age of 70 years.

Important to discuss that the high compressive stresses in the foundation are partially caused by the idealistic elastic modelling of the underlying rock. The latter develops tensile stress in response to the expansion of the foundation. Thus, compression in the foundation is equilibrated by the tension in the rock. In reality, the underlying rock is far from being a continuous elastic material: it has pre-existing fissures and also can fracture. The full tensile strain applied to the rock will be partially accumulated by the rock mass movement, while the rest of it will contribute to the stress evolution. Additionally, the tensile strength of the rock is also imposing a cap on the maximum possible tensile stress. For most of the rock types used as foundations, its value is in $5-14$ MPa range (Demirdag et al., 2019). Therefore, the developed model with the stiff interface gives an approximate upper estimate for the stresses in the foundation. Better prediction could be obtained by using more sophisticated rock model, e.g. Hoek-Brown. For this, more field data on the underlying rock is necessary (GSI, RMR, tensile strength and stiffness).

6.5   Conclusions

A multi-scale finite-element method for simulating the mechanical consequences of the ASR in large concrete structures has been presented. The multi-scale approach is advan-

tageous because the macroscopic material behaviour is governed by the mesoscopic ASR phenomena. Consequently, no drastic assumptions on how the mesoscopic damage evolution affects the effective stiffness of the concrete are required. The multi-scale model has been implemented in the parallel open-source library Akantu. Meso-scale laboratory experiments of Multon and Toutlemonde (2006) are numerically simulated as a proof of concept. The model is able to simultaneously account for the loading due to the boundary conditions on the macro-scale and for the loading due to the ASR expansion at the meso-scale. The results, furthermore, demonstrate that the macroscopic stress state influences the orientation of damage inside the underlying RVEs. The effective stiffness becomes anisotropic in cases where the cracks are aligned. Comparison of the multi-scale and the fully detailed macro-scale model shows a fair agreement of results both for the free and the loaded tests. Although the evolution of the percolated crackbands within RVEs is evident, their diffused patterns make the classical homogenisation concept still applicable.

The performed validation of the multi-scale model suggests its applicability for the detailed studies of real concrete structures affected by the ASR. Thus, the model was applied to simulate the behaviour of the ASR-affected Salanfe dam in Western Switzerland. The parameters of the expansion law were re-calibrated to match the field measurements. The obtained set of parameters substantially differs from the one matching the accelerated laboratory experiments. A possible reason for the gap between the two sets could be the different dynamics of the ASR (both in chemistry and physics) happening in the low temperature range compared to the accelerated laboratory tests. Moreover, the expansion saturation, commonly seen in laboratory experiments, could not be observed in the field data, where the expansion is predominantly linear. This fact also suggests that there is a gap between the laboratory conditions and field. Otherwise, the model could underestimate the role of temperature in the ASR expansion due to certain factors not being accounted. The latter comprise the visco-elastic effects, variations in the relative humidity and ion concentrations within across the dam, etc. To evaluate the possible contribution of these factors, additional simulations of an expanded numerical model and supplementary field measurements are necessary.

The structural analysis of the dam revealed some interesting insights. The upstream drift and the vertical uplift at the level of the dam crest were attributed to the difference in length between the upstream and the downstream faces rather than the different ASR products' strains within a structure. Having the same level of expansion, the longer downstream face pushes the crest in the upstream direction.

Although the ASR is advanced to the same level within the whole cross-section, concrete strain is only partially isotropic. The most of isotropic expansion is happening along the downstream face, while the bottom upstream part has more pronounced horizontal expansion. Such behaviour was attributed to the sensitivity of the ASR expansion to the external load: the self-weight of the structure partially hinders the evolution

of horizontal cracks in corresponding RVEs reducing the vertical expansion. Another anisotropically-expanding area of the dam is its foundation. The vertical strains there prevail over the horizontal ones due to the restraining effect of the rock below. Given a competent rock, such expansion constraints could lead to the evolution of compressive stresses few times larger than the ones coming from the self-weight. Given all the evidence of the ASR anisotropy within a dam, it could be concluded that the common engineering approach of modelling the ASR through the thermal expansion dictates unrealistic behaviour to the structure.

7 Conclusions & outlook

7.1 Conclusions

The current thesis has presented the analytical and numerical studies on the mechanics of the alkali-silica reaction in concrete performed in the scope of the multi-disciplinary inter-institutional Sinergia project. These studies were conducted in collaboration with other Sinergia sub-projects and were partially based on their experimental findings. Three different scales of concrete were considered: nano, meso and macro. The points of interest concerned the nature of the ASR loading, the mechanisms responsible for the initiation and propagation of cracks, the evolution of the effective properties of concrete. Moreover, the dialogue between the macroscopic behaviour of an affected structure and its mechanical state at the meso-scale was studied. The final question was asked on the role of the temperature variation in the progression of the ASR in field conditions.

First, an overview of the existing mechanisms of the ASR expansion available in the literature was presented. They vary from relatively simple ones, like the osmotic pressure due to the water uptake by ASR products, to very complex ones, like the theory of electrical double-layer repulsion forces on the surface of the ASR-gel particles. Yet, modern science does not have a definitive answer to the question, "Which exact mechanism causes the ASR expansion and the cracking of concrete?"

Further, a literature review of the existing numerical methods used to model the ASR at the meso- and macro-scales was given. At the meso-scale, these models were categorised by the source of the expansion, while at the structural level, the models were either phenomenological or based on the principles of poromechanics.

In the first study of a single ASR pocket of a nanometer-size, the hypothesis that the 100% volume increase could lead to the evolution of surrounding cracks was investigated. This value was provided by the colleagues from the Sinergia and was based on their extensive studies of different ASR products. To analyse this problem, a semi-analytical

model of an expanding ellipsoidal inclusion encircled by a ring-shaped crack was employed. An analytical solution was used to estimate the stresses outside the inclusion in the absence of a crack. When the crack was added, the stress intensity factor was estimated by integrating the product between the stresses and the specific weight function over the crack area. This stress intensity factor was used to estimate the maximum crack radius.

Between all possible inclusion shapes, a spheroid with 1/4 height-radius ratio and a sphere were distinguished. Given the same expansion, the former causes the highest stress intensity factor and the latter produces the longest crack. The size of the inclusion played a crucial role on the crack growing potential. For an inclusion of 1 μm radius under the expansion of 100%, all spheroidal shapes with aspect ratios above 1/10 were likely to grow a crack. Flatter shapes caused either a short crack or no crack at all. A critical inclusion radius was identified, below which no crack growth was expected for any inclusion's shape. This size depends on the material parameters and the expansion value. A further increase in the inclusion size suggested a power-law dependence between the inclusion size and the maximum crack radius. Independently of the spheroidal shape or the expansion value, a power-law exponent was about 4/3.

The results of the analytical predictions were verified by the finite element model. First, the elastic stresses in the inclusion's vicinity were reproduced by an elastic 3D model. Then, a crack was added to the model by means of cohesive elements. The numerical crack size fairly matched the one predicted by the semi-analytical model for the case of a sphere and a 1/4-spheroid but failed for a penny-shaped inclusion by predicting no crack evolution. The latter was associated to the interference from the inclusion.

When the initial stage of the ASR expansion and cracking was studied, the thesis has proceeded to a more advanced ASR stage, namely the evolution of a crack network. This phenomenon is considered at the intermediate scale of concrete - the meso-scale. For this, meso-scale structure of concrete was resolved, distinguishing between the aggregates, the cement paste and the interfacial transition zone. To represent cracks numerically, two different approaches were adopted: one used zero-thickness interface elements following a cohesive law, while the second one modelled cracks by the continuum damage approach.

The goal of the first meso-scale study employing the cohesive zone model was to investigate the nature of the propagation and percolation of the ASR cracks in a realistic meso-scale structure of concrete. This study was done in collaboration with the colleagues from the Sinergia Sub-project V from Concrete Technology Group at Empa in Switzerland, who performed laboratory experiments resulting in a set of time-evolving X-ray tomograms of ASR-affected concrete. The latter captured the evolution of the displacement field accounting for opening and elongation of cracks as well as accumulation of ASR products. The tomograms were used to build a numerical mesh. Two hypothe-

ses on ASR-loading and cracking mechanisms were made. The first one stated that the ASR loading is applied pointwise inside cracks, while the second one stated that the new crack area is produced due to the elongation of the pre-existing cracks rather than the nucleation of the new ones. These hypotheses were tested by including them into the model and verifying their sufficiency in reproducing realistic crack networks. The time-dependent internal loading was represented by the pairs of oppositely-oriented forces of equal magnitudes applied at the randomly chosen initial ASR sites, which coincided with the pre-existing micro-cracks. The latter were modelled by the loops of the pre-inserted cohesive elements. Application of the pulling forces led to the crack growth. A novel crack-extension mechanism comprised insertion of cohesive elements at the contours of existing cracks. New cohesive elements were inserted in smooth loops connecting every two neighbouring segments of the crack contour. Choice of the elements in a loop was based on finding the shortest smooth path. The proposed insertion algorithm ensured the development of a network of localised cracks similar to the ones observed in the tomograms.

For comparison with the tomographic data, crack statistics and macroscopic strains were computed. The numerical concrete samples exhibited a gradual expansion increase followed by the continuous linear expansion growth, which was attributed to the further opening of the existing cracks and a slowdown in generation of the new ones. A similar mechanism was suggested to happen in the laboratory specimens. The calibrated numerical model had a good match with the experimental data regarding the expansion, the crack statistics and patterns. The hypotheses made on the loading and cracking mechanism were sufficient to reproduce the ASR processes at the meso-scale.

A sensitivity study varying the number of the initial ASR sites and the loading rate produced interesting results. It appeared that the few initial ASR sites with a high load are more efficient in growing a crack network and causing macroscopic expansion than the multiple cracks with a small load. It was attributed to the higher stress concentrations and hence earlier crack growth and expansion. More than that, the crack networks in the specimens with fewer initial sites were more localised. In contrast, the specimens with numerous ASR sites had very diffused crack patterns. It was suggested that a very diffused crack network could partially accommodate the internal loading and hence cause less macroscopic expansion.

An additional simulation of a concrete block under uniaxial compression showed a reduction in the ASR-related expansion along the loading direction. Moreover, a statistical distribution of the crack-segment orientations showed that the cracks in the loaded specimen are more aligned with the loading direction. Both these observations are in fair agreement with the experimental studies available in the literature.

Although the cohesive elements permit realistic representation of the ASR cracks and facilitate comparison with the tomography data, they have a substantial computational

cost and could lead to non-convergence. When multiple simulations have to be performed (e.g. within a Monte Carlo simulation or in a multi-scale framework), the efficiency and stability of computations play a crucial role. A need in numerous simulations is explained by the development of a multi-scale model presented in Chapter 6. To improve the computational characteristics of the meso-scale model, a different modelling approach was adopted.

In the second meso-scale study, cracks were represented by means of the continuous damage approach. Not only it was done to make the model computationally cheaper and more stable, but also to investigate the role of the crack growth on the macroscopic behaviour of concrete specimens. Namely, the difference in the representation of cracks by isotropic and orthotropic damage was investigated, and how it affected the macroscopic strain. Another question to be answered was on the role of the viscoelasticity on the damage extent and the homogenised elastic properties of concrete.

To reach the defined goals, two sub-studies were conducted in Chapter 5. In the first one, a material law with orthotropic damage was introduced. This development allowed modelling of thin cracks with the stiffness recovery upon self-contact. A 2D model of a concrete meso-structure was calibrated on the free-expansion laboratory experiments by matching the macroscopic expansion. This was followed by modelling the uniaxial-loading experiment. In the direction of the load, the specimen developed positive expansion, whose values depended on the loading magnitude. Such behaviour reproduced the laboratory experiments much better than the earlier models with isotropic damage, which predicted substantial specimen shrinkage under the load. The numerical cracks were aligned with the loading direction, which is commonly observed in experiments. The developed model was relatively slow but stable, which made it possible to include it into the multi-scale framework discussed in Chapter 6.

In the second sub-study, a simple quasi-static FE model of viscoelastic strain-softening material, which could be easily implemented in a standard FE package, was developed. This model combined the isotropic continuous damage and viscoelasticity in the cement paste. The smallest aggregates together with the cement paste were treated as mortar. A generalised Maxwell chain was adopted as a rheological model and was integrated in the modified sequentially linear analysis. The resulting approximate solution differed insignificantly with respect to the exact one, which permitted us to analyse the results qualitatively. To understand the role of the viscoelasticity in the ASR damaging process, the behaviours of specimens with elastic and viscoelastic strain-softening mortars were compared. It was shown that adding the viscoelasticity to the mortar leads to the relaxation of stresses and consequent reduction of the damage. The latter, in its turn, reduces the overall expansion of the specimens. A possible way to increase the macroscopic expansion of concrete without significant damage increment in the mortar is to have more reactive ASR sites in the aggregates, including the small ones. To test this hypothesis, additional numerical simulations resolving smaller aggregates are necessary.

Finally, the macroscopic behaviour of ASR-affected structures was studied in Chapter 6. The thesis aimed to understand how it was related to the local state of concrete, namely its level of cracking and expansion. Moreover, the role of the seasonal temperature variations in the ASR evolution in a structure was questioned. To link the two scales (meso and macro), the numerical multi-scale approach was adopted. At the meso-scale, the finite element model with the orthotropic damage representation of cracks was employed. At the macro-scale, no damage was modelled and the elastic properties of concrete were extracted from the meso-scale through the numerical homogenisation procedure. The developed model was verified by simulating the free-expansion and the loaded laboratory experiments. The model simultaneously accounted for the external loading due to the boundary conditions at the macro-scale and for the internal loading due to the ASR expansion at the meso-scale. The results showed that the macroscopic stress influenced the orientations of the cracks inside the underlying RVEs. The effective stiffness has become anisotropic in cases where the cracks were aligned.

The developed multi-scale model was used to simulate a cross-section of an ASR-activated dam. Extra to the mechanical simulations, the heat flow problem was solved at the macro-scale. The information on the concrete temperature was used to compute the temperature-dependent ASR-expansion rate. For this study, Salanfe dam in Western Switzerland was considered. It experiences continuous ASR-related deformations since it was constructed. The parameters of the ASR-expansion law were calibrated based on the field data comprising the displacements, the air and the reservoir temperatures, and the reservoir fluctuations. The identified parameters suggested limited or no effect of the temperature variations in the cross-section of the dam on the difference in the ASR expansion. To match the field displacements, almost the same ASR expansion was applied at all RVEs. The field measurements of the upstream drift and uplift at the level of the crest were reproduced by the model due to the difference in extension of the long downstream and short upstream faces. The identified parameters significantly differed from the ones that were previously calibrated on the accelerated laboratory experiments. Such a difference could be explained by the different ASR dynamics happening at low temperatures. The obtained results suggested that the ASR rates observed in the accelerated laboratory experiments could not be exponentially extrapolated to the low-temperature range according to Arrhenius law. Otherwise, the model could underestimate the role of the temperature on the ASR dynamics due to the several factors that were not accounted for. The latter comprised the viscoelastic deformations, the 3D nature of the dam displacements, the variations in the relative humidity and alkalis concentration. To evaluate the contribution of these factors, additional model developments and simulations, as well as the field measurements are required.

Strain at the macro-scale was partially anisotropic, which was related to the difference in the crack patterns at the meso-scale. The bottom upstream part and the dam foundation had the strongest anisotropic expansion and also showed crack alignments. These specific areas were affected by the self-weight and the underlying rock causing a

constraint that led to the disturbance of the isotropic expansion state. Moreover, the dam foundation developed high compressive horizontal stresses due to the competent dam-rock interface. The obtained results had a clear indication that the ASR anisotropy was significant in massive concrete structures. The conducted study demonstrated that the common engineering practice of modelling the ASR as thermal expansion was misleading as it did not represent the real complexity of the ASR stress-dependence.

7.2 Outlook

In the current section, we analyse the possible further improvements and the follow-up work that could be performed based on the presented developments.

The study of the crack growing potential of an expanding nanoscopic ASR inclusion had certain limitations, which could be addressed in future work. First, the small-strain theory was considered, limits of which were exceeded by assigning a 100% expansion on the inclusion. Although the small strain theory still permits a qualitative analysis, more quantitatively-precise estimates could be obtained by adopting the finite deformations theory. However, its combination with the principles of linear elastic fracture mechanics could be complicated.

Moreover, the adopted model assumed that the ASR product remained solid and did not redistribute upon the crack extension and opening. While this is true for a mature crystallised ASR product, it might be wrong for the amorphous one. In that case, the opening of a crack would cause the ASR-product to flow and to reduce the original pressure. Both analytical and numerical models could be developed for this scenario. The numerical model would comprise a classical hydro-fracking problem of petroleum engineering, where the fluid-solid interaction and the mass conservation is taken into account. As the crack is never full with the ASR products, the two-phase flow shall be modelled, where one phase would be the ASR gel and another one the air.

Moving one scale above, a cohesive-zone meso-scale model of concrete was considered. The proposed model succeeded to simulate the growth of cracks in a localised manner. Nevertheless, the numerical scheme was very sensitive to the changes in the loading. While a simulation was stable for the loads applied at the one-time-defined positions, it was diverging if a new loading force was introduced. Such instability partially came from the stiffness jumps between the opened and closed states of the cohesive elements, which is particularly inconvenient when different loading scenarios are to be tested. Another issue of the proposed method is its high computational cost due to the sequentially linear analysis, which requires numerous elastic solutions within a single loading step. Therefore, both the stability and efficiency of the solution scheme shall be improved. One way of doing so is to use more complex iterative solver. In the current work, the Newton-Raphson algorithm is employed. Instead, Broyden–Fletcher–Goldfarb–Shanno

(BFGS) algorithm could be tested. Its advantage over the conventional methods is the approximated Hessian matrix, which does not require assembly and inversion of the global stiffness matrix at each iteration. This fact is expected to improve both the stability and the efficiency of the model.

If the convergence is improved, different loading scenarios could be tested. A point-wise application of the load could be compared with the case where the load is partially redistributed along the newly opened crack. Comparison of the crack patterns developed in these two scenarios is called to shed light on the real nature of the ASR loading.

A more ambitious step would be to model the full fluid-structure interaction problem, where the fluid would be the ASR gel that expands and flows within the crack network. This direction was partially explored by the author of this thesis by developing a model based on the Poiseuille flow equation. While the flow was taking place within the crack network, the fluid pressure was passed to the surrounding solid in the form of external forces. The fluid and solid parts were modelled separately and later were linked by a staggered scheme. The solutions were obtained in an explicit dynamic manner, which imposed a limiting time-step size on both models. Further developments in this direction were hindered by the few-orders-of-magnitude difference between the time steps of the fluid and solid problems. One thousand steps of the fluid-flow model corresponded to a single step of the solid on. A possible way to overcome this problem is the modification in the solution scheme. For instance, instead of explicitly solving the fluid flow, one could solve it implicitly. Otherwise, a numerical stabilisation technique could be used (e.g. Meyer et al., 2012).

For the continuous damage model, the study on the role of viscoelasticity has a potential extension to account for a larger reaction extent in smaller aggregates. The conducted study showed that the viscoelasticity is reducing the damage extent in the cement paste. This reduction is also affecting the macroscopic behaviour of concrete by reducing its expansion. It was suggested that in order to reach the experimental values of expansion, more damage and expansion should happen in the aggregates. Although this hypothesis seems to be convincing, it is not clear if the local damage and expansion of isolated aggregates could be transmitted to the specimen's borders. Numerical simulations of the concrete meso-structures with different packing densities could be tested. Smaller aggregates, which were previously homogenised into the mortar, could also be resolved. Given a larger extent of the ASR expansion over the aggregates, the damage extent and the macroscopic expansion should be compared to the laboratory measurements. This will verify the correctness of the made hypothesis.

Finally, at the macro-scale, there was a major question that was risen by the results of the dam simulation. It concerned the difference between the parameters of the expansion law calibrated on the accelerated laboratory experiments and the field measurements. The model predicted no difference in the reaction extent at its warm and cold areas.

It has been suggested that the results of the accelerated laboratory tests could not be exponentially extrapolated to the low-temperature operational range by the Arrhenius equation. However, zero difference in the ASR extent across the dam still seems counterintuitive and contradicts the general field observations. One possible reason is the fact that the model does not account for the creep effects in the cement paste. It is possible that the long-term creep is slowly moving the dam's crest in the downstream direction and counteracts the ASR-related upstream movement. In this manner, the difference in the ASR extent between the warm and cold areas could be larger. It could be also due to the non-homogeneous distribution of the ASR within the cross-section of the dam, or due to the variations in the relative humidity or alkali concentration, or due to the two-dimensionality of the proposed model. To test any of these hypotheses, additional numerical simulations are required. The simplest one would be adding the viscoelasticity at the meso-scale. It still requires a smart coupling between the orthotropic damage law and the rheological model. Otherwise, the isotropic viscous-softening behaviour introduced in Section 5.3 could be used. Extension of the multi-scale model to three dimensions depends fully on the available computational capacities. A 3D model of a dam would require numerous three-dimensional RVEs to be solved simultaneously. To reduce the computational burden, one possible strategy would be to create a database of RVE states which would relate the input and the output RVE parameters. The input parameters are the temperature and the deformation of an RVE coming from the macro-scale. These two quantities fully define the RVE response expressed in a form of homogenised RVE stress and stiffness, which are the output parameters mentioned above. Creation of a database of unique input-output pairs could be done before the actual simulation and thus could be called "database training". This training could employ machine learning algorithms. When the database is ready, the RVEs are not necessary anymore and the macroscopic structure could be efficiently computed. Once constructed, the database could be kept for the future simulations. Adding more variables to the model (e.g. relative humidity and alkali concentration) would extend the parametric space of the database and increase the training time.

Bibliography

Akantu (Version 4.0.0), Aug. 2021. URL https://akantu.ch/.

H. Alehossein and J. N. Boland. Strength, toughness, damage and fatigue of rock. In *Structural Integrity and Fracture: Proceedings of the International Conference, SIF 2004*, page 8, 2004.

M. E. Almenar, F. López Rivarola, N. A. Labanda, and G. J. Etse. An RVE-Based Multi-Scale Approach for Concrete Affected by Alkali–Silica Reaction. 2017. URL http://sedici.unlp.edu.ar/handle/10915/99158. ISSN: 2591-3522.

M. Alnaggar, G. Cusatis, and G. D. Luzio. Lattice Discrete Particle Modeling (LDPM) of Alkali Silica Reaction (ASR) deterioration of concrete structures. *Cement and Concrete Composites*, 41:45–59, Aug. 2013. ISSN 09589465. doi: 10.1016/j.cemconcomp. 2013.04.015. URL https://linkinghub.elsevier.com/retrieve/pii/S0958946513000802.

M. H. Anders, S. E. Laubach, and C. H. Scholz. Microfractures: A review. *Journal of Structural Geology*, 69:377–394, Dec. 2014. ISSN 0191-8141. doi: 10.1016/j.jsg.2014.05. 011. URL https://www.sciencedirect.com/science/article/pii/S0191814114001151.

N. A. Aniskin and A. M. Shaytanov. Assessment of Temperature Effect on the Stress-Strain Behavior of a Concrete Gravity Dam. *Power Technol Eng*, 54(2):154–159, July 2020. ISSN 1570-145X, 1570-1468. doi: 10.1007/s10749-020-01183-1. URL http://link.springer.com/10.1007/s10749-020-01183-1.

C. Atkinson and D. Clements. On some crack problems in anisotropic thermoelasticity. *International Journal of Solids and Structures*, 13(9):855–864, 1977. ISSN 00207683. doi: 10.1016/0020-7683(77)90071-3. URL https://linkinghub.elsevier.com/retrieve/ pii/0020768377900713.

F. Bangert, D. Kuhl, and G. Meschke. Chemo-hygro-mechanical modelling and numerical simulation of concrete deterioration caused by alkali-silica reaction. *Int. J. Numer. Anal. Meth. Geomech.*, 28(78):689–714, June 2004. ISSN 0363-9061, 1096-9853. doi: 10.1002/nag.375. URL http://doi.wiley.com/10.1002/nag.375.

Bibliography

G. Barenblatt. The Mathematical Theory of Equilibrium Cracks in Brittle Fracture. In *Advances in Applied Mechanics*, volume 7, pages 55–129. Elsevier, 1962. ISBN 978-0-12-002007-2. doi: 10.1016/S0065-2156(08)70121-2. URL https://linkinghub.elsevier.com/retrieve/pii/S0065215608701212.

Z. P. Bažant. Size Effect in Blunt Fracture: Concrete, Rock, Metal. *Journal of Engineering Mechanics*, 110(4):518–535, Apr. 1984. ISSN 0733-9399, 1943-7889. doi: 10.1061/(ASCE)0733-9399(1984)110:4(518).

Z. P. Bažant and B. H. Oh. Crack band theory for fracture of concrete. *Matériaux et Construction*, 16:155–177, 1983.

M. Ben Haha. *Mechanical effects of alkali silica reaction in concrete studied by sem-image analysis*. PhD thesis, EPFL, Lausanne, Switzerland, 2006.

D. Beniaguev. Historical Hourly Weather Data 2012-2017, 2017. URL https://kaggle.com/selfishgene/historical-hourly-weather-data.

Y. Benveniste. A new approach to the application of Mori-Tanaka's theory in composite materials. *Mechanics of Materials*, 6(2):147–157, June 1987. ISSN 0167-6636. doi: 10.1016/0167-6636(87)90005-6. URL https://www.sciencedirect.com/science/article/pii/0167663687900056.

I. Borchers, J. Lindgård, and C. Muller. Evaluation of laboratory test methods for assessing the alkali-reactivity potential of aggregates by field site tests. In *First Book of Proceedings of the 16th ICAAR*, volume 1, pages 699–710, 2016.

A. F. Bower. *Applied Mechanics of Solids*. CRC Press, 0 edition, Oct. 2009. ISBN 978-1-4398-0248-9. doi: 10.1201/9781439802489. URL https://www.taylorfrancis.com/books/9781439802489.

H. F. Bueckner. Novel principle for the computation of stress intensity factors. *Zeitschrift fuer Angewandte Mathematik & Mechanik*, 50(9), Sept. 1970. URL https://trid.trb.org/view/3976.

G. Camacho and M. Ortiz. Computational modelling of impact damage in brittle materials. *International Journal of Solids and Structures*, 33(20-22):2899–2938, Aug. 1996. ISSN 00207683. doi: 10.1016/0020-7683(95)00255-3. URL https://linkinghub.elsevier.com/retrieve/pii/0020768395002553.

B. Capra and J.-P. Bournazel. Modeling of Induced Mechanical Effects of Alkali-Aggregate Reactions. *Cement and Concrete Research*, 28(2):251–260, Feb. 1998. ISSN 00088846. doi: 10.1016/S0008-8846(97)00261-5. URL https://linkinghub.elsevier.com/retrieve/pii/S0008884697002615.

B. Capra and A. Sellier. Orthotropic modelling of alkali-aggregate reaction in concrete structures: numerical simulations. *Mechanics of Materials*, 35(8):817–830,

Aug. 2003. ISSN 01676636. doi: 10.1016/S0167-6636(02)00209-0. URL https://linkinghub.elsevier.com/retrieve/pii/S0167663602002090.

R. Charlwood and I. Sims. A Review of the Effectiveness of Strategies to Manage Expansive Chemical Reactions in Dams and Hydro Projects. In *Swelling Concr. Dams Hydraul. Struct.*, pages 3–39, 2017.

S. Chatterji. Mechanisms of alkali- silica reaction and expansion. In *Proceedings of the 8th International Conference on Alkali-Aggregate Reaction*, Kyoto, Japan, 1989.

S. Chatterji and N. Thaulow. Some fundamental aspects of alkali-silica reaction. In *Proc., 11th AAR Inter. Conf., Québec, Canada*, pages 21–29, 2000.

E. Coenen, V. Kouznetsova, and M. Geers. Multi-scale continuous–discontinuous framework for computational-homogenization–localization. *Journal of the Mechanics and Physics of Solids*, 60(8):1486–1507, Aug. 2012a. ISSN 00225096. doi: 10.1016/j.jmps.2012.04.002. URL https://linkinghub.elsevier.com/retrieve/pii/S0022509612000749.

E. Coenen, V. Kouznetsova, and M. Geers. Novel boundary conditions for strain localization analyses in microstructural volume elements: BCS FOR LOCALIZATION ANALYSIS IN MICROSTRUCTURES. *Int. J. Numer. Meth. Engng*, 90(1):1–21, Apr. 2012b. ISSN 00295981. doi: 10.1002/nme.3298. URL http://doi.wiley.com/10.1002/nme.3298.

W. F. Cole and C. J. Lancucki. Products formed in an aged concrete the occurrence of okenite. *Cement and Concrete Research*, 13(5):611–618, Sept. 1983. ISSN 0008-8846. doi: 10.1016/0008-8846(83)90049-2. URL https://www.sciencedirect.com/science/article/pii/0008884683900492.

I. Comby-Peyrot, F. Bernard, P.-O. Bouchard, F. Bay, and E. Garcia-Diaz. Development and validation of a 3D computational tool to describe concrete behaviour at mesoscale. Application to the alkali-silica reaction. *Computational Materials Science*, 46(4):1163–1177, Oct. 2009. ISSN 09270256. doi: 10.1016/j.commatsci.2009.06.002. URL https://linkinghub.elsevier.com/retrieve/pii/S0927025609002572.

C. Comi, R. Fedele, and U. Perego. A chemo-thermo-damage model for the analysis of concrete dams affected by alkali-silica reaction. *Mechanics of Materials*, 41(3):210–230, Mar. 2009. ISSN 01676636. doi: 10.1016/j.mechmat.2008.10.010. URL https://linkinghub.elsevier.com/retrieve/pii/S0167663608001464.

C. Comi, B. Kirchmayr, and R. Pignatelli. Two-phase damage modeling of concrete affected by alkali–silica reaction under variable temperature and humidity conditions. *International Journal of Solids and Structures*, 49(23-24):3367–3380, Nov. 2012. ISSN 00207683. doi: 10.1016/j.ijsolstr.2012.07.015. URL https://linkinghub.elsevier.com/retrieve/pii/S0020768312003009.

Bibliography

A. I. Cuba Ramos. *Multi-Scale Modeling of the Alkali-Silica Reaction in Concrete*. PhD thesis, EPFL, Lausanne, Switzerland, 2017.

A. I. Cuba Ramos, C. Roux-Langlois, C. F. Dunant, M. Corrado, and J.-F. Molinari. HPC simulations of alkali-silica reaction-induced damage: Influence of alkali-silica gel properties. *Cement and Concrete Research*, 109:90–102, July 2018. ISSN 00088846. doi: 10.1016/j.cemconres.2018.03.020. URL https://linkinghub.elsevier.com/retrieve/pii/S000888461731150X.

Da Yu Tzou. The singular behavior of the temperature gradient in the vicinity of a macrocrack tip. *International Journal of Heat and Mass Transfer*, 33(12):2625–2630, Dec. 1990. ISSN 00179310. doi: 10.1016/0017-9310(90)90198-4. URL https://linkinghub.elsevier.com/retrieve/pii/0017931090901984.

R. Dähn, A. Arakcheeva, P. Schaub, P. Pattison, G. Chapuis, D. Grolimund, E. Wieland, and A. Leemann. Application of micro X-ray diffraction to investigate the reaction products formed by the alkali–silica reaction in concrete structures. *Cement and Concrete Research*, 79:49–56, Jan. 2016. ISSN 0008-8846. doi: 10.1016/j.cemconres.2015.07.012. URL https://www.sciencedirect.com/science/article/pii/S0008884615002094.

L. De Ceukelaire. The determination of the most common crystalline alkali-silica reaction product. *Materials and Structures*, 24(3):169–171, May 1991. ISSN 1359-5997, 1871-6873. doi: 10.1007/BF02472981. URL http://link.springer.com/10.1007/BF02472981.

S. Demirdag, K. Tufekci, N. Sengun, T. Efe, and R. Altindag. Determination of the Direct Tensile Strength of Granite Rock by Using a New Dumbbell Shape and its Relationship with Brazilian Tensile Strength. *IOP Conf. Ser.: Earth Environ. Sci.*, 221:012094, Mar. 2019. ISSN 1755-1315. doi: 10.1088/1755-1315/221/1/012094. URL https://doi.org/10.1088/1755-1315/221/1/012094. Publisher: IOP Publishing.

S. Diamond. ASR - Another look at mechanisms. In *Proceedings of the 8th International Conference on Alkali-Aggregate Reaction*, Kyoto, Japan, 1989.

R. Dron. Thermodynamique de la réaction alcali-silice. *Bulletin de liaison des Laboratoires des Ponts et Chaussées*, 1990.

R. Dron, F. Brivot, and T. Chaussadent. Mécanisme de la réaction alcali-silice. *BULLETIN-LABORATOIRES DES PONTS ET CHAUSSEES*, pages 61–68, 1998.

P. Droz, O. Vallotton, T. Menouillard, and R. Leroy. Slot cutting an AAR-affected dam: case study of the Salanfe dam. *Hydropower and Dams*, page 4, 2013.

D. Dugdale. Yielding of steel sheets containing slits. *Journal of the Mechanics and Physics of Solids*, 8(2):100–104, May 1960. ISSN 00225096. doi: 10.1016/0022-5096(60)90013-2. URL https://linkinghub.elsevier.com/retrieve/pii/0022509660900132.

C. F. Dunant and K. L. Scrivener. Micro-mechanical modelling of alkali–silica-reaction-induced degradation using the AMIE framework. *Cement and Concrete Research*, 40 (4):517–525, Apr. 2010. ISSN 00088846. doi: 10.1016/j.cemconres.2009.07.024. URL https://linkinghub.elsevier.com/retrieve/pii/S0008884609001847.

C. F. Dunant and K. L. Scrivener. Effects of uniaxial stress on alkali–silica reaction induced expansion of concrete. *Cement and Concrete Research*, 42(3):567–576, Mar. 2012. ISSN 00088846. doi: 10.1016/j.cemconres.2011.12.004. URL https://linkinghub.elsevier.com/retrieve/pii/S0008884611003267.

B. Durand and B. Fournier. 20-year results of an in-situ monitoring study of large concrete electrical tower foundations affected by alkali-silica reaction (ASR). In *ICAAR 15 Proceedings*, page 10, July 2016.

J. D. Eshelby. The determination of the elastic field of an ellipsoidal inclusion, and related problems. *Proc. R. Soc. Lond. A*, 241(1226):376–396, Aug. 1957. ISSN 0080-4630, 2053-9169. doi: 10.1098/rspa.1957.0133. URL https://royalsocietypublishing.org/doi/10.1098/rspa.1957.0133.

J. D. Eshelby. The elastic field outside an ellipsoidal inclusion. *Proc. R. Soc. Lond. A*, 252 (1271):561–569, Oct. 1959. ISSN 0080-4630, 2053-9169. doi: 10.1098/rspa.1959.0173. URL https://royalsocietypublishing.org/doi/10.1098/rspa.1959.0173.

R. Esposito and M. A. N. Hendriks. A multiscale micromechanical approach to model the deteriorating impact of alkali-silica reaction on concrete. *Cement and Concrete Composites*, 70:139–152, July 2016. ISSN 0958-9465. doi: 10.1016/j.cemconcomp.2016.03.017. URL https://www.sciencedirect.com/science/article/pii/S0958946516300555.

T. Fett and G. Rizzi. Weight Functions and Stress Intensity Factors for Ring-shaped Cracks, 2007.

F. Feyel and J.-L. Chaboche. FE2 multiscale approach for modelling the elastoviscoplastic behaviour of long fibre SiC/Ti composite materials. *Computer Methods in Applied Mechanics and Engineering*, 183(3-4):309–330, Mar. 2000. ISSN 00457825. doi: 10.1016/S0045-7825(99)00224-8. URL https://linkinghub.elsevier.com/retrieve/pii/S0045782599002248.

B. Fournier, J. H. Ideker, K. J. Folliard, M. D. Thomas, P.-C. Nkinamubanzi, and R. Chevrier. Effect of environmental conditions on expansion in concrete due to alkali–silica reaction (ASR). *Materials Characterization*, 60(7):669–679, July 2009. ISSN 10445803. doi: 10.1016/j.matchar.2008.12.018. URL https://linkinghub.elsevier.com/retrieve/pii/S1044580308003513.

B. Fournier, R. Chevrier, A. Bilodeau, P.-C. Nkinamubanzi, and N. Bouzoubaa. Comparative field and laboratory investigations on the use of supplementary cementing materials (SCMS) to control alkali-silica reaction (ASR) in concrete. page 10, 2016.

Bibliography

F. Fritzen. *Microstructural modeling and computational homogenization of the physically linear and nonlinear constitutive behavior of micro-heterogeneous materials.* PhD thesis, KIT, Karslruhe, Germany, 2011.

F. Gaboriaud, A. Nonat, D. Chaumont, and A. Craievich. Aggregation Processes and Formation of Silico-calco-alkaline Gels under High Ionic Strength. *Journal of Colloid and Interface Science*, 253(1):140–149, Sept. 2002. ISSN 0021-9797. doi: 10.1006/jcis.2002.8522. URL https://www.sciencedirect.com/science/article/pii/S002197970298522X.

E. Gallyamov, A. Cuba Ramos, M. Corrado, R. Rezakhani, and J.-F. Molinari. Multiscale modelling of concrete structures affected by alkali-silica reaction: Coupling the mesoscopic damage evolution and the macroscopic concrete deterioration. *Int J Solids Struct*, 207:262–278, Dec. 2020. ISSN 00207683. doi: 10.1016/j.ijsolstr.2020.10.010. URL https://linkinghub.elsevier.com/retrieve/pii/S0020768320303942.

E. Gallyamov, R. Rezakhani, M. Corrado, and J.-F. Molinari. Meso-scale modelling of ASR in concrete: effect of viscoelasticity. In *Proceedings of the 16 th International Conference on Alkali-Aggregate Reaction in Concrete*, volume 1, page 10, 2021a.

E. R. Gallyamov, A. Leemann, B. Lothenbach, and J.-F. Molinari. Predicting damage in aggregates due to the volume increase of the alkali-silica reaction products, 2021b. URL arXiv:2110.05276[cond-mat.mtrl-sci].

E. Garcia-Diaz, J. Riche, D. Bulteel, and C. Vernet. Mechanism of damage for the alkali–silica reaction. *Cement and Concrete Research*, 36(2):395–400, Feb. 2006. ISSN 0008-8846. doi: 10.1016/j.cemconres.2005.06.003. URL https://www.sciencedirect.com/science/article/pii/S000888460500150X.

B. P. Gautam and D. K. Panesar. A new method of applying long-term multiaxial stresses in concrete specimens undergoing ASR, and their triaxial expansions. *Mater Struct*, 49(9):3495–3508, Sept. 2016. ISSN 1359-5997, 1871-6873. doi: 10.1617/s11527-015-0734-z. URL http://link.springer.com/10.1617/s11527-015-0734-z.

M. Geers, V. Kouznetsova, and W. Brekelmans. Multi-scale computational homogenization: Trends and challenges. *Journal of Computational and Applied Mathematics*, 234(7):2175–2182, Aug. 2010. ISSN 03770427. doi: 10.1016/j.cam.2009.08.077. URL https://linkinghub.elsevier.com/retrieve/pii/S0377042709005536.

G. Geng, Z. Shi, A. Leemann, K. Glazyrin, A. Kleppe, D. Daisenberger, S. Churakov, B. Lothenbach, E. Wieland, and R. Dähn. Mechanical behavior and phase change of alkali-silica reaction products under hydrostatic compression. *Acta Crystallogr B Struct Sci Cryst Eng Mater*, 76(4):674–682, Aug. 2020. ISSN 2052-5206. doi: 10.1107/S205252062000846X. URL https://scripts.iucr.org/cgi-bin/paper?S205252062000846X.

C. Geuzaine and J.-F. Remacle. Gmsh: A 3-D finite element mesh generator with built-in pre- and post-processing facilities: THE GMSH PAPER. *Int. J. Numer. Meth. Engng.*, 79(11):1309–1331, Sept. 2009. ISSN 00295981. doi: 10.1002/nme.2579. URL http://doi.wiley.com/10.1002/nme.2579.

H. Ghanem, D. Zollinger, and R. Lytton. Predicting ASR aggregate reactivity in terms of its activation energy. *Construction and Building Materials*, 24(7):1101–1108, July 2010. ISSN 0950-0618. doi: 10.1016/j.conbuildmat.2009.12.033. URL https://www.sciencedirect.com/science/article/pii/S0950061809004449.

A. Giorla, K. Scrivener, and C. Dunant. Finite elements in space and time for the analysis of generalised visco-elastic materials. *International Journal for Numerical Methods in Engineering*, 97(6):454–472, 2014. ISSN 1097-0207. doi: 10.1002/nme.4598. URL https://onlinelibrary.wiley.com/doi/abs/10.1002/nme.4598. _eprint: https://onlinelibrary.wiley.com/doi/pdf/10.1002/nme.4598.

A. B. Giorla, K. L. Scrivener, and C. F. Dunant. Influence of visco-elasticity on the stress development induced by alkali–silica reaction. *Cement and Concrete Research*, 70:1–8, Apr. 2015. ISSN 00088846. doi: 10.1016/j.cemconres.2014.09.006. URL https://linkinghub.elsevier.com/retrieve/pii/S0008884614002531.

L. S. D. Glasser. Osmotic pressure and the swelling of gels. *Cement and Concrete Research*, 9(4):515–517, July 1979. ISSN 0008-8846. doi: 10.1016/0008-8846(79)90050-4. URL https://www.sciencedirect.com/science/article/pii/0008884679900504.

A. A. Griffith. The phenomena of rupture and flow in solids. *Phil. Trans. R. Soc. Lond. A*, 221(582-593):163–198, Jan. 1921. ISSN 0264-3952, 2053-9258. doi: 10.1098/rsta.1921.0006. URL https://royalsocietypublishing.org/doi/10.1098/rsta.1921.0006.

E. Grimal, A. Sellier, S. Multon, Y. Le Pape, and E. Bourdarot. Concrete modelling for expertise of structures affected by alkali aggregate reaction. *Cement and Concrete Research*, 40(4):502–507, Apr. 2010. ISSN 00088846. doi: 10.1016/j.cemconres.2009.09.007. URL https://linkinghub.elsevier.com/retrieve/pii/S0008884609002476.

R. M. Gunn, K. L. Scrivener, and A. Leemann. The Identification, Extent and Prognosis of Alkali-Aggregate Reaction Related to Existing Dams in Switzerland. In *Swelling Concr. Dams Hydraul. Struct.*, pages 117–143, 2017.

M. B. Haha, E. Gallucci, A. Guidoum, and K. Scrivener. Relation of expansion due to alkali silica reaction to the degree of reaction measured by SEM image analysis. *Cement and Concrete Research*, 37(8):1206–1214, Aug. 2007. ISSN 00088846. doi: 10.1016/j.cemconres.2007.04.016. URL https://linkinghub.elsevier.com/retrieve/pii/S000888460700107X.

D. Healy. Elastic field in 3D due to a spheroidal inclusion—MATLAB™ code for Eshelby's solution. *Computers & Geosciences*, 35(10):2170–2173, Oct. 2009. ISSN

00983004. doi: 10.1016/j.cageo.2008.11.012. URL https://linkinghub.elsevier.com/retrieve/pii/S0098300409001356.

A. Hilaire, A. B. Giorla, C. F. Dunant, L. Sofia, and K. L. Scrivener. Behavior of Concrete Deteriorated by ASR under Triaxial Load. In *Swelling Concr. Dams Hydraul. Struct.*, pages 55–74, 2017.

R. Hill. Elastic properties of reinforced solids: Some theoretical principles. *Journal of the Mechanics and Physics of Solids*, 11(5):357–372, Sept. 1963. ISSN 00225096. doi: 10.1016/0022-5096(63)90036-X. URL https://linkinghub.elsevier.com/retrieve/pii/002250966390036X.

A. Hillerborg, M. Modéer, and P.-E. Petersson. Analysis of crack formation and crack growth in concrete by means of fracture mechanics and finite elements. *Cement and Concrete Research*, 6(6):773–781, Nov. 1976. ISSN 00088846. doi: 10.1016/0008-8846(76)90007-7. URL https://linkinghub.elsevier.com/retrieve/pii/0008884676900077.

M. Huang and S. Pietruszczak. Modeling of Thermomechanical Effects of Alkali-Silica Reaction. *Journal of Engineering Mechanics*, 125(4):476–485, Apr. 1999. ISSN 0733-9399, 1943-7889. doi: 10.1061/(ASCE)0733-9399(1999)125:4(476).

Y. Huang, Z. Yang, W. Ren, G. Liu, and C. Zhang. 3D meso-scale fracture modelling and validation of concrete based on in-situ X-ray Computed Tomography images using damage plasticity model. *International Journal of Solids and Structures*, 67-68:340–352, Aug. 2015. ISSN 0020-7683. doi: 10.1016/j.ijsolstr.2015.05.002. URL https://www.sciencedirect.com/science/article/pii/S0020768315002127.

T. Ichikawa and M. Miura. Modified model of alkali-silica reaction. *Cement and Concrete Research*, 37(9):1291–1297, Sept. 2007. ISSN 0008-8846. doi: 10.1016/j.cemconres.2007.06.008. URL https://www.sciencedirect.com/science/article/pii/S0008884607001329.

J. H. Ideker, T. Drimalas, A. Bentivegna, K. J. Folliard, B. Fournier, M. D. Thomas, R. D. Hooton, and C. Rogers. The importance of outdoor exposure site testing. In *ICAAR 12 Proceedings*, Austin, Texas, USA, 2012a.

J. H. Ideker, K. J. Folliard, M. Juenger, and A. Bentivegna. Do Current Laboratory Test Methods Accurately Predict Alkali-Silica Reactivity? *MJ*, 109(4), 2012b. ISSN 0889-325X. doi: 10.14359/51683914. URL http://www.concrete.org/Publications/ACIMaterialsJournal/ACIJournalSearch.aspx?m=details&ID=51683914.

T. Iskhakov, J. J. Timothy, and G. Meschke. Expansion and deterioration of concrete due to ASR: Micromechanical modeling and analysis. *Cement and Concrete Research*, 115:507–518, Jan. 2019. ISSN 00088846. doi: 10.1016/j.cemconres.2018.08.001. URL https://linkinghub.elsevier.com/retrieve/pii/S0008884618301509.

T. Iskhakov, C. Giebson, J. J. Timothy, H. M. Ludwig, and G. Meschke. Deterioration of concrete due to ASR: Experiments and multiscale modeling. *Cement and Concrete Research*, 149:106575, Nov. 2021. ISSN 0008-8846. doi: 10.1016/j.cemconres.2021.106575. URL https://www.sciencedirect.com/science/article/pii/S0008884621002246.

T. N. Jones. New interpretation of alkali-silica reaction and expansion mechanisms in concrete. *Chemistry and industry*, pages 40–4, 1988.

J. W. Ju and L. Z. Sun. A Novel Formulation for the Exterior-Point Eshelby's Tensor of an Ellipsoidal Inclusion. *Journal of Applied Mechanics*, 66(2):570–574, June 1999. ISSN 0021-8936, 1528-9036. doi: 10.1115/1. 2791090. URL https://asmedigitalcollection.asme.org/appliedmechanics/article/66/ 2/570/445956/A-Novel-Formulation-for-the-ExteriorPoint-Eshelbys.

J. W. Ju and L. Z. Sun. Effective elastoplastic behavior of metal matrix composites containing randomly located aligned spheroidal inhomogeneities. Part I: micromechanics-based formulation. *International Journal of Solids and Structures*, page 19, 2001.

L. M. Kachanov. *Introduction to continuum damage mechanics*, volume 10 of *Mechanics of Elastic Stability.* Springer Netherlands, Dordrecht, 1986. ISBN 978-90-481-8296-1 978-94-017-1957-5. doi: 10.1007/978-94-017-1957-5. URL http://link.springer.com/ 10.1007/978-94-017-1957-5.

G. S. Kit, Y. K. Nechaev, and O. V. Poberezhnyi. Determination of the stress intensity factors in a plate subjected to heat transfer. *Soviet Applied Mechanics*, 13(4):365–369, Apr. 1977. ISSN 0038-5298, 1573-8582. doi: 10.1007/BF00882935. URL http: //link.springer.com/10.1007/BF00882935.

V. Kouznetsova, W. A. M. Brekelmans, and F. P. T. Baaijens. An approach to micro-macro modeling of heterogeneous materials. *Computational Mechanics*, 27(1):37–48, Jan. 2001. ISSN 0178-7675, 1432-0924. doi: 10.1007/s004660000212. URL http: //link.springer.com/10.1007/s004660000212.

C. Larive. *Apports combinés de l'expérimentation et de la modélisation à la compréhension de l'alcali-réaction et de ses effets mécaniques.* PhD thesis, l'École Nationale des Ponts et Chaussées, 1997.

A. Leemann. Impact of different alkalis on concrete expansion due to ASR. In *Proceedings of the 16 th International Conference on Alkali-Aggregate Reaction in Concrete*, volume 1, Lisboa, Portugal, 2021.

A. Leemann and P. Lura. E-modulus of the alkali–silica-reaction product determined by micro-indentation. *Construction and Building Materials*, 44:221–227, July 2013. ISSN 09500618. doi: 10.1016/j.conbuildmat.2013.03.018. URL https://linkinghub.elsevier. com/retrieve/pii/S0950061813002237.

Bibliography

A. Leemann and B. Münch. The addition of caesium to concrete with alkali-silica reaction: Implications on product identification and recognition of the reaction sequence. *Cement and Concrete Research*, 120:27–35, June 2019. ISSN 00088846. doi: 10.1016/j.cemconres.2019.03.016. URL https://linkinghub.elsevier.com/retrieve/pii/S0008884619300730.

A. Leemann, T. Katayama, I. Fernandes, and M. A. T. M. Broekmans. Types of alkali–aggregate reactions and the products formed. *Proceedings of the Institution of Civil Engineers - Construction Materials*, 169(3):128–135, June 2016. ISSN 1747-650X, 1747-6518. doi: 10.1680/jcoma.15.00059. URL http://www.icevirtuallibrary.com/doi/10.1680/jcoma.15.00059.

A. Leemann, I. Borchers, M. Shakoorioskooie, M. Griffa, C. Müller, and P. Lura. Microstructural analysis of ASR in concrete – accelerated testing versus natural exposure. In *SMSS 2019*, page 10, Rovinj, Croatia, 2019.

A. Leemann, Z. Shi, and J. Lindgård. Characterization of amorphous and crystalline ASR products formed in concrete aggregates. *Cement and Concrete Research*, 137: 106190, Nov. 2020. ISSN 00088846. doi: 10.1016/j.cemconres.2020.106190. URL https://linkinghub.elsevier.com/retrieve/pii/S0008884620304324.

E. Lemarchand, L. Dormieux, and F.-J. Ulm. Micromechanics investigation of expansive reactions in chemoelastic concrete. *Philosophical Transactions of the Royal Society A: Mathematical, Physical and Engineering Sciences*, 363(1836):2581–2602, Nov. 2005. doi: 10.1098/rsta.2005.1588. URL https://royalsocietypublishing.org/doi/10.1098/rsta.2005.1588. Publisher: Royal Society.

R. G. L'Hermite, M. Mamillan, and C. Lefèvre. Nouveaux résultats de recherches sur la déformation et la rupture du béton. *Annales de l'Institut Techn. du Bâtiment et des Travaux Publics*, 18(207-208):325, 1965.

J. Liaudat, I. Carol, and C. M. López. Model for alkali-silica reaction expansions in concrete using zero-thickness chemo-mechanical interface elements. *International Journal of Solids and Structures*, 207:145–177, Dec. 2020. ISSN 0020-7683. doi: 10.1016/j.ijsolstr.2020.09.019. URL https://www.sciencedirect.com/science/article/pii/S0020768320303619.

J. Lindgård, T. Østnor, B. Fournier, Ø. Lindgård, T. Danner, G. Plusquellec, and K. De Weerdt. Determining alkali leaching during accelerated ASR performance testing and in field exposed cubes using cold water extraction (CWE) and µXRF. *MATEC Web Conf.*, 199:03004, 2018. ISSN 2261-236X. doi: 10.1051/matecconf/201819903004. URL https://www.matec-conferences.org/10.1051/matecconf/201819903004.

R. P. Martin, O. O. Metalssi, and F. Toutlemonde. Modelling of concrete structures affected by internal swelling reactions: couplings between transfer properties, alkali leachning and expansion. page 9, 2012.

F. Mauris, F. Martinot, J.-P. Fabre, P. Bourgey, and J. Sausse. Synthesis of hydraulic structures behavior: lessons learned from monitored dams of EDF in France. page 9, Nanjing, China, Oct. 2015.

C. D. Meyer, D. S. Balsara, and T. D. Aslam. A second-order accurate Super TimeStepping formulation for anisotropic thermal conduction: Super TimeStepping scheme for TC. *Monthly Notices of the Royal Astronomical Society*, 422(3):2102–2115, May 2012. ISSN 00358711. doi: 10.1111/j.1365-2966.2012.20744.x. URL https://academic.oup.com/mnras/article-lookup/doi/10.1111/j.1365-2966.2012.20744.x.

C. Miehe. Numerical computation of algorithmic (consistent) tangent moduli in large-strain computational inelasticity. *Computer Methods in Applied Mechanics and Engineering*, 134(3-4):223–240, Aug. 1996. ISSN 00457825. doi: 10.1016/0045-7825(96)01019-5. URL https://linkinghub.elsevier.com/retrieve/pii/0045782596010195.

C. Miehe, J. Schröder, and J. Schotte. Computational homogenization analysis in finite plasticity Simulation of texture development in polycrystalline materials. *Computer Methods in Applied Mechanics and Engineering*, 171(3-4):387–418, Apr. 1999. ISSN 00457825. doi: 10.1016/S0045-7825(98)00218-7. URL https://linkinghub.elsevier.com/retrieve/pii/S0045782598002187.

Ministry. SP 20.13330.2016 [in Russian]. Technical report, Ministry of Construction and Housing and Communal Services of the Russian Federation, 2016.

T. Miura, S. Multon, and Y. Kawabata. Influence of the distribution of expansive sites in aggregates on microscopic damage caused by alkali-silica reaction: Insights into the mechanical origin of expansion. *Cement and Concrete Research*, 142:106355, Apr. 2021. ISSN 0008-8846. doi: 10.1016/j.cemconres.2021.106355. URL https://www.sciencedirect.com/science/article/pii/S0008884621000041.

A. K. Mukhopadhyay, C.-S. Shon, and D. G. Zollinger. Activation Energy of Alkali–Silica Reaction and Dilatometer Method. *Transportation Research Record*, 1979(1):1–11, Jan. 2006. ISSN 0361-1981, 2169-4052. doi: 10.1177/0361198106197900102. URL http://journals.sagepub.com/doi/10.1177/0361198106197900102.

S. Multon. *Evaluation expérimentale et théorique des effets mécaniques de l'alcali-réaction sur des structures modèles*. PhD thesis, Laboratoire central des ponts et chaussées, 2004.

S. Multon and A. Sellier. Multi-scale analysis of alkali–silica reaction (ASR): Impact of alkali leaching on scale effects affecting expansion tests. *Cement and Concrete Research*, 81:122–133, Mar. 2016. ISSN 00088846. doi: 10.1016/j.cemconres.2015.12.007. URL https://linkinghub.elsevier.com/retrieve/pii/S0008884615300168.

S. Multon and F. Toutlemonde. Effect of applied stresses on alkali–silica reaction-induced expansions. *Cement and Concrete Research*, 36(5):912–920, May 2006. ISSN 00088846.

Bibliography

doi: 10.1016/j.cemconres.2005.11.012. URL https://linkinghub.elsevier.com/retrieve/pii/S0008884605002838.

S. Multon, A. Sellier, and M. Cyr. Chemo–mechanical modeling for prediction of alkali silica reaction (ASR) expansion. *Cement and Concrete Research*, 39(6):490–500, June 2009. ISSN 00088846. doi: 10.1016/j.cemconres.2009.03.007. URL https://linkinghub.elsevier.com/retrieve/pii/S0008884609000702.

T. Mura. *Micromechanics of defects in solids.* Martinus Nijhoff Publishers, 1987. ISBN: 9789400934894 OCLC: 1158181484.

O. Omikrine Metalssi, J.-F. Seignol, S. Rigobert, and F. Toutlemonde. Modeling the cracks opening–closing and possible remedial sawing operation of AAR-affected dams. *Engineering Failure Analysis*, 36:199–214, Jan. 2014. ISSN 13506307. doi: 10.1016/j.engfailanal.2013.10.009. URL https://linkinghub.elsevier.com/retrieve/pii/S1350630713003208.

T. Pan, C. Chen, and Q. Yu. Microstructural and multiphysics study of alkali-silica reaction in Portland cement concrete. *Structural Concrete*, 19(5):1387–1398, 2018. ISSN 1751-7648. doi: 10.1002/suco.201700164. URL https://onlinelibrary.wiley.com/doi/abs/10.1002/suco.201700164. _eprint: https://onlinelibrary.wiley.com/doi/pdf/10.1002/suco.201700164.

M. Pari, A. V. Van de Graaf, M. A. N. Hendriks, and J. G. Rots. A multisurface interface model for sequentially linear methods to analyse masonry structures. *Engineering Structures*, 238:112123, July 2021. ISSN 0141-0296. doi: 10.1016/j.engstruct.2021.112123. URL https://www.sciencedirect.com/science/article/pii/S014102962100273X.

H. Petroski and J. Achenbach. Computation of the weight function from a stress intensity factor. *Engineering Fracture Mechanics*, 10(2):257–266, Jan. 1978. ISSN 00137944. doi: 10.1016/0013-7944(78)90009-7. URL https://linkinghub.elsevier.com/retrieve/pii/0013794478900097.

R. Pignatelli, C. Comi, and P. J. Monteiro. A coupled mechanical and chemical damage model for concrete affected by alkali–silica reaction. *Cement and Concrete Research*, 53:196–210, Nov. 2013. ISSN 00088846. doi: 10.1016/j.cemconres.2013.06.011. URL https://linkinghub.elsevier.com/retrieve/pii/S0008884613001567.

A. B. Poole. Alkali-silica reactivity mechanisms of gel formation and expansion. In *Proceedings of the 9th International Conference on Alkali-Aggregate Reaction, London (England)*, volume 104, pages 782–789. Concrete Society Publications CS, 1992. Issue: 1.

M. Prezzi, P. J. Monteiro, and G. Sposito. The alkali–silica reaction: Part I. Use of the double-layer theory to explain the behavior of reaction-product gels. *ACI materials journal*, 94(1):10–17, 1997.

W. Puatatsananon and V. Saouma. Chemo-Mechanical Micromodel for Alkali-Silica Reaction. *ACI Materials Journal*, page 12, 2013.

J. Renard. Etude de l'initiation de l'endommagement dans la matrice d'un materiau composite par une methode d'homogenisation. *Aerosp. Sci. Technol.*, 6:37–51, 1987.

R. Rezakhani, M. Alnaggar, and G. Cusatis. Multiscale Homogenization Analysis of Alkali–Silica Reaction (ASR) Effect in Concrete. *Engineering*, 5(6):1139–1154, Dec. 2019. ISSN 20958099. doi: 10.1016/j.eng.2019.02.007. URL https://linkinghub. elsevier.com/retrieve/pii/S209580991830938X.

R. Rezakhani, E. Gallyamov, and J. Molinari. Meso-scale finite element modeling of Alkali-Silica-Reaction. *Constr Build Mater*, 278:122244, Apr. 2021. ISSN 09500618. doi: 10.1016/j.conbuildmat.2021.122244. URL https://linkinghub.elsevier. com/retrieve/pii/S0950061821000040.

J. R. Rice. Some remarks on elastic crack-tip stress fields. *International Journal of Solids and Structures*, 8(6):751–758, June 1972. ISSN 00207683. doi: 10.1016/0020-7683(72) 90040-6. URL https://linkinghub.elsevier.com/retrieve/pii/0020768372900406.

N. Richart and J. Molinari. Implementation of a parallel finite-element library: Test case on a non-local continuum damage model. *Finite Elements in Analysis and Design*, 100:41–46, Aug. 2015. ISSN 0168874X. doi: 10.1016/j.finel.2015.02.003. URL https: //linkinghub.elsevier.com/retrieve/pii/S0168874X15000153.

R. O. Ritchie. The conflicts between strength and toughness. *Nature Mater*, 10(11): 817–822, Nov. 2011. ISSN 1476-4660. doi: 10.1038/nmat3115. URL https://www. nature.com/articles/nmat3115. Bandiera_abtest: a Cg_type: Nature Research Journals Number: 11 Primary_atype: Reviews Publisher: Nature Publishing Group Subject_term: Mechanical properties Subject_term_id: mechanical-properties.

E. Robertson. Thermal properties of rock. Open-File Report 88-441, United States Department of the Interior Geological Survey, 1988. Series: Open-File Report.

F. A. Rodrigues, P. J. Monteiro, and G. Sposito. The alkali-silica reaction: The surface charge density of silica and its effect on expansive pressure. *Cement and Concrete Research*, 29(4):527–530, 1999. Publisher: Elsevier.

J. G. Rots. Sequentially linear continuum model for concrete fracture. *Fracture Mechanics of Concrete Structures*, page 9, 2001.

J. G. Rots and J. Blaauwendraad. Crack models for concrete: discrete or smeared? Fixed, Multi-directional or rotating? *HERON*, 34(1), 1989.

J. G. Rots and S. Invernizzi. Regularized sequentially linear saw-tooth softening model. *Int. J. Numer. Anal. Meth. Geomech.*, 28(78):821–856, June 2004. ISSN 0363-9061, 1096-9853. doi: 10.1002/nag.371. URL http://doi.wiley.com/10.1002/nag.371.

Bibliography

J. G. Rots, B. Belletti, and S. Invernizzi. Robust modeling of RC structures with an "event-by-event" strategy. *Engineering Fracture Mechanics*, 75(3-4):590–614, Feb. 2008. ISSN 00137944. doi: 10.1016/j.engfracmech.2007.03.027. URL https://linkinghub.elsevier.com/retrieve/pii/S0013794407001518.

V. Saouma and L. Perotti. Constitutive Model for Alkali-Aggregate Reactions. *ACI Materials Journal*, page 9, 2006.

SCD. Concrete swelling of dams in Switzerland. Report of the Swiss Committee on Dams on the state of concrete swelling in Swiss Dams, Swiss Committee on Dams, 2017.

E. Schlangen and O. Copuroglu. Modeling of expansion and cracking due to ASR with a 3D lattice model. In *Proceeding of the conference on Fracture Mechanics of Concrete and Concrete Structures 2010*, page 7, Seoul, Korea, 2010.

J. Schmittbuhl and K. J. Måløy. Direct Observation of a Self-Affine Crack Propagation. *Phys. Rev. Lett.*, 78(20):3888–3891, May 1997. ISSN 0031-9007, 1079-7114. doi: 10.1103/PhysRevLett.78.3888. URL https://link.aps.org/doi/10.1103/PhysRevLett.78.3888.

M. Shakoorioskooie. *The alkali-silica reaction damage in concrete at the mesoscale: characterization by X-ray tomography.* PhD thesis, ETH Zurich, 2021.

M. Shakoorioskooie, A. Leemann, M. Griffa, R. Zboray, and P. Lura. Characterization of alkali-silica reaction damage in concrete by X-ray tomography. In *Proceedings of the 2019 International Conference on Tomography of Materials & Structures*, Cairns, Australia, July 2019.

M. Shakoorioskooie, M. Griffa, A. Leemann, R. Zboray, and P. Lura. Alkali-silica reaction products and cracks: X-ray micro-tomography-based analysis of their spatial-temporal evolution at a mesoscale. *Cement and Concrete Research*, 150:106593, Dec. 2021a. ISSN 0008-8846. doi: 10.1016/j.cemconres.2021.106593. URL https://www.sciencedirect.com/science/article/pii/S0008884621002428.

M. Shakoorioskooie, M. Griffa, A. Leemann, R. Zboray, and P. Lura. Supplementary data/materials for the article: "Alkali-silica reaction products and cracks: X-ray micro-tomography-based analysis of their spatial-temporal evolution at a mesoscale". *Zenodo*, May 2021b. doi: 10.5281/zenodo.5206839. URL https://zenodo.org/record/5206839.

Z. Shi, G. Geng, A. Leemann, and B. Lothenbach. Synthesis, characterization, and water uptake property of alkali-silica reaction products. *Cement and Concrete Research*, 121:58–71, July 2019. ISSN 00088846. doi: 10.1016/j.cemconres.2019.04.009. URL https://linkinghub.elsevier.com/retrieve/pii/S0008884619301139.

Z. Shi, S. Park, B. Lothenbach, and A. Leemann. Formation of shlykovite and ASR-P1 in concrete under accelerated alkali-silica reaction at 60 and 80 °C. *Cement and Concrete Research*, 137:106213, Nov. 2020. ISSN 0008-8846. doi: 10.1016/j.cemconres.2020.106213. URL https://www.sciencedirect.com/science/article/pii/S0008884620304622.

P. M. Suquet. Introduction. In: Sanchez-Palencia E., Zaoui A. (eds) Homogenization Techniques for Composite Media. Lecture Notes in Physics. In E. Sanchez-Palencia and A. Zaoui, editors, *Homogenization Techniques for Composite Media*, volume 272, pages 193–198. Springer Berlin Heidelberg, Berlin, Heidelberg, 1987. ISBN 978-3-540-17616-9 978-3-540-47720-4. doi: 10.1007/3-540-17616-0_15. URL http://link.springer.com/10.1007/3-540-17616-0_15. Series Title: Lecture Notes in Physics.

A. Suwitoa, W. Jinb, Y. M. Xia, and C. Meyerc. A Mathematical Model for the Pessimum Size Effect of ASR in Concrete. 2003.

R. N. Swamy. *Alkali-silica reaction in concrete*. Blackie and Son ; Taylor and Francis e-Library, Glasgow, England; New York, New York, 2003. ISBN 978-0-203-20033-9. URL https://www.taylorfrancis.com/books/0203036638. OCLC: 1132080496.

H. Tada, P. C. Paris, and G. R. Irwin. *The stress analysis of cracks handbook*. ASME Press, New York, 3rd ed edition, 2000. ISBN 978-0-7918-0153-6.

P. S. M. Thilakarathna, K. S. Kristombu Baduge, P. Mendis, V. Vimonsatit, and H. Lee. Mesoscale modelling of concrete – A review of geometry generation, placing algorithms, constitutive relations and applications. *Engineering Fracture Mechanics*, 231:106974, May 2020. ISSN 0013-7944. doi: 10.1016/j.engfracmech.2020.106974. URL https://www.sciencedirect.com/science/article/pii/S0013794420300291.

S. Timoshenko and J. N. Goodier. *Theory of Elasticity*. McGraw-Hill, 3 edition, 1951. ISBN 978-0-07-085805-3.

F.-J. Ulm, O. Coussy, L. Kefei, and C. Larive. Thermo-Chemo-Mechanics of ASR Expansion in Concrete Structures. *J. Eng. Mech.*, 126(3):233–242, Mar. 2000. ISSN 0733-9399, 1943-7889. doi: 10.1061/(ASCE)0733-9399(2000)126:3(233).

D. Vo, S. Multon, P. Morenon, A. Sellier, E. Grimal, B. Masson, and P. Kolmayer. Evaluation of structures affected by Alkali-Silica reaction (ASR) using homogenized modelling of reinforced concrete. *Engineering Structures*, 246:112845, Nov. 2021. ISSN 0141-0296. doi: 10.1016/j.engstruct.2021.112845. URL https://www.sciencedirect.com/science/article/pii/S0141029621009950.

M. Vocialta, N. Richart, and J.-F. Molinari. 3D dynamic fragmentation with parallel dynamic insertion of cohesive elements: 3D DYNAMIC FRAGMENTATION WITH COHESIVE ELEMENTS IN PARALLEL. *Int. J. Numer. Meth. Engng*, 109(12):1655–1678, Mar. 2017. ISSN 00295981. doi: 10.1002/nme.5339. URL http://doi.wiley.com/10.1002/nme.5339.

Bibliography

H. Wang and J. E. Gillott. Mechanism of alkali-silica reaction and the significance of calcium hydroxide. *Cement and Concrete Research*, 21(4):647–654, July 1991. ISSN 0008-8846. doi: 10.1016/0008-8846(91)90115-X. URL https://www.sciencedirect.com/science/article/pii/000888469190115X.

P. Wriggers and S. O. Moftah. Mesoscale models for concrete: Homogenisation and damage behaviour. *Finite Elements in Analysis and Design*, 42(7):623–636, Apr. 2006. ISSN 0168-874X. doi: 10.1016/j.finel.2005.11.008. URL https://www.sciencedirect.com/science/article/pii/S0168874X05001563.

T. Wu, İ. Temizer, and P. Wriggers. Multiscale hydro-thermo-chemo-mechanical coupling: Application to alkali–silica reaction. *Computational Materials Science*, 84: 381–395, Mar. 2014. ISSN 09270256. doi: 10.1016/j.commatsci.2013.12.029. URL https://linkinghub.elsevier.com/retrieve/pii/S0927025613007799.

S. Xu and Y. Zhu. Experimental determination of fracture parameters for crack propagation in hardening cement paste and mortar. *Int J Fract*, 157(1-2):33–43, May 2009. ISSN 0376-9429, 1573-2673. doi: 10.1007/s10704-009-9315-x. URL http://link.springer.com/10.1007/s10704-009-9315-x.

Z.-J. Yang, B.-B. Li, and J.-Y. Wu. X-ray computed tomography images based phase-field modeling of mesoscopic failure in concrete. *Engineering Fracture Mechanics*, 208: 151–170, Mar. 2019. ISSN 0013-7944. doi: 10.1016/j.engfracmech.2019.01.005. URL https://www.sciencedirect.com/science/article/pii/S0013794418313122.

Curriculum Vitae

Emil Rinatovich Gallyamov (Эмиль Ринатович Галлямов) was born in Ufa, Bashkortostan, USSR, on 4 July 1988. He graduated summa cum laude with Diploma in Civil Engineering from Ufa State Petroleum Technological University, Russia, in 2010. In his thesis, supervised by Dr. Rinat Sakhibgareyev, Emil focused on the development of technological processes for the construction of high-rise buildings from cast-in-place concrete. During his studies, Emil took an active role in the university's social life: he was representing his groupmates in a student union, publishing a faculty magazine as editor-in-chief, and acting in theatre plays. While being at the university, Emil did several industrial internships starting from working at construction sites to performing geotechnical calculations.

After graduation, Emil began his international engineering career in the oil and gas service company Schlumberger. During $2010 - 2012$, he has been working as a Measurements While Drilling engineer at the oil fields of Russia and Bolivia. His responsibilities comprised installing and calibrating a system of sensors and receivers, programming and assembling the downhole equipment, running the measurements, recording the data and performing troubleshooting. In addition, this role implied the preliminary interpretation of raw geophysical data in cooperation with an on-site geologist. During the following two years, Emil was working as a Directional Driller at the on-shore sites in Cuba and off-shore platforms in the Gulf of Mexico. His new responsibilities included assembling the downhole drilling equipment and navigating the deviated, horizontal and extended-reach wells. Apart from the technical role, Emil was managing the Schlumberger team at the offshore facilities, representing the company to the platform manager and being in charge of the onsite logistics of the drilling and logging equipment. Emil was further promoted to the position of Drilling Engineer, which he occupied up to June 2015. During this office assignment, he was in charge of the offshore wells design and safety analysis, and the real-time support of the field operations. This job involved extensive cooperation with the client's engineering and operational departments.

In times of the oil crisis, Emil decided to invest to his education and started an M.Sc. in Geotechnical Engineering at Delft University of Technology in the Netherlands. Being interested in programming, he has done a graduation work on numerical methods under

the supervision of TU Delft Associate Professor Dr. Denis Voskov and Stanford Senior Scientist Dr. Timur Garipov. Emil has developed a numerical model for the fluid-driven fracture growth in a poroelastic medium. The results of this work were later published in a peer-reviewed journal and presented in SIAM Conference on Mathematical and Computational Issues in the Geosciences. For his contribution to the subject of the reservoir simulations, he has received the Xodus - Sergio Ottochian Scholarship. During the second year of studies, Emil has undertaken an industrial internship in the finite-element software company DIANA FEA B.V. He has used the FE package to study different hydro-mechanical coupling schemes and tested newly added functions. In 2017, Emil has graduated cum laude.

Being attracted to science, Emil decided to pursue a Ph.D. in Mechanical Engineering at École Polytechnique Fédérale de Lausanne in Switzerland under the supervision of Professor Jean-François Molinari. The objective of Emil's research was to improve the understanding of the mechanical deterioration of concrete due to the alkali-silica reaction (ASR) by developing analytical and numerical models. The investigations were part of a multi-disciplinary inter-institutional Sinergia project, which implied collaborations and joint publications with different laboratories and researchers from several Swiss research institutes. To get access to the field measurements of ASR-affected structures, Emil has established direct links with the Swiss Federal Office of Energy, energy services provider Alpiq Suisse SA and engineering consultancy Stucky SA, which resulted in a fruitful collaboration. Emil has served as one of the developers of the open-source finite-element library Akantu, in which he has coded numerical approaches developed in the course of his Ph.D. He has published several articles and given talks at international conferences on the problems of ASR, fractures in concrete and computational mechanics. He has received the Best Poster Award at the 2020 SWICCOMAS General Assembly in Zurich, Switzerland. Apart from conducting research, Emil has devoted considerable time to teaching activities. He was a teaching assistant for the courses in Continuum Mechanics and Scientific Programming and supervised several semester student's projects.

As for extracurricular activities, Emil participated in the association of Russian-speaking EPFL students and organised several thematic cinemas screenings, where he has presented the historical background of the movies. He has also organised and participated in three editions of SciFilmIt - science filmmaking hackathon, where he has been directing, filming and editing short scientific movies.

Publications and Conferences

List of Publications

- E.R. Gallyamov, A. Leemann, B. Lothenbach, J.-F. Molinari. Predicting damage in aggregates due to the volume increase of the alkali-silica reaction products. Submitted, Under Review, Pre-print at arXiv:2110.05276 [cond-mat.mtrl-sci], 2021.

- E.R. Gallyamov, M. Corrado, J. Fauriel, J.-F. Molinari. Long-term behaviour of a dam affected by alkali-silica reaction studied by a multi-scale model. Submitted, Under Review, 2021.

- R. Rezakhani, E. Gallyamov, J.-F. Molinari. Meso-scale finite element modeling of Alkali-Silica-Reaction. Construction and Building Materials 278 (2021) 122244.

- E.R. Gallyamov, M. Shakoorioskooie, J.-F. Molinari. Study on the internal crack network of the ASR-affected concrete by the tomography-based numerical model. In Preparation, 2021.

- A. Leemann, M. Bagheri, B. Lothenbach, K. Scrivener, S. Barbotin, E. Boehm-Courjault, G. Geng, F. Marafatto, R. Dähn, E. Wieland, Z. Shi, M. Shakoorioskooie, M. Griffa, R. Zboray, P. Lura, E.R. Gallyamov, R. Rezakhani, J.-F. Molinari. Alkali-silica reaction - a multidisciplinary approach. Submitted, Under Review, 2021.

- E.R. Gallyamov, A.I. Cuba Ramos, M. Corrado, R. Rezakhani, J.-F. Molinari. Multi-scale modelling of concrete structures affected by alkali-silica reaction: Coupling the mesoscopic damage evolution and the macroscopic concrete deterioration. International Journal of Solids and Structures 207 (2020) 262-278.

- E.R. Gallyamov, T. Garipov, D. Volkov, P. Van den Hoek. Discrete fracture model for simulating waterflooding processes under fracturing conditions. International Journal for Numerical and Analytical Methods in Geomechanics 42 (2018) 1445-1470.

- E. Gallyamov. Hydraulic fracture propagation model for porous media. Master thesis. TU Delft, 2017. Available at http://resolver.tudelft.nl/uuid:43692e45-66e5-4e9c-bcbd-98dde1cfd886

Conference Talks

- E.R. Gallyamov, M. Corrado, J.-F. Molinari. Multi-scale model to study the long-term mechanical behaviour of a dam affected by alkali-silica reaction. COMPLAS XVI International Conference on Computational Plasticity. Fundamentals and Applications. Barcelona, Spain, September 7-9, 2021.

- E.R. Gallyamov, R. Rezakhani, M. Corrado, J.-F. Molinari. Meso-scale modelling of ASR in concrete: effect of viscoelasticity. ICAAR 16th International Conference on Alkali-Aggregate Reaction in Concrete. Lisboa, Portugal, 2020-2022.

- E.R. Gallyamov, M. Corrado, R. Rezakhani, J.-F. Molinari. FraMCoS-X Fracture Mechanics of Concrete and Concrete Structures. Experiments-based multi-scale modeling of the alkali-silica reaction in concrete. Bayonne, France, June 23-26, 2019.

- R. Rezakhani, E.R. Gallyamov, J.-F. Molinari. Keynote: Meso-scale finite element modeling of Alkali-Silica-Reaction (ASR) effect in concrete. FraMCoS-X Fracture Mechanics of Concrete and Concrete Structures. Bayonne, France, June 23-26, 2019.

- E.R. Gallyamov, T. Garipov, D. Voskov, P. Van den Hoek. Fully coupled fluid flow and geomechanical model for reservoir fracturing accounting for poroelastic effects. SIAM Conference on Mathematical and Computational Issues in the Geosciences. Erlangen, Germany, September 11—14, 2017.